Hybrid functionals approach for the study of the properties of complex materials for photovoltaic applications

Fabien Lafond

Fabien Lafond. Hybrid functionals approach for the study of the properties of complex materials for photovoltaic applications. Chemical Sciences. Université de Lorraine, 2019. English. NNT : 2019LORR0308 . tel-02860746

HAL Id: tel-02860746
https://hal.univ-lorraine.fr/tel-02860746v1

Submitted on 8 Jun 2020

École doctorale C2MP

Thèse

pour l'obtention du grade de
Docteur de l'Université de Lorraine

présentée par

Fabien LAFOND

Hybrid functionals approach for the study of the properties of complex materials for photovoltaic applications

---

Défendue le 16 décembre 2019 à Metz

Composition du jury

Hong XU *Professeur, Université de Lorraine*	Présidente
Mébarek ALOUANI *Professeur, Université de Strasbourg*	Rapporteur
Ludger WIRTZ *Professeur, Université du Luxembourg*	Rapporteur
Jéléna SJAKSTE *Chargée de recherche CNRS, École Polytechnique*	Examinateur
Michael SPRINGBORG *Professeur, Université de la Sarre*	Examinateur
Andrei POSTNIKOV *Professeur, Université de Lorraine*	Directeur de thèse

Thèse préparée sous l'encadrement de Philippe BARANEK
(EDF R&D) au Laboratoire de Chimie et de Physique – Approche
Multi-échelles des Milieux Complexes (LCP–A2MC) et à
l'Institut du Photovoltaïque d'Île de France (IPVF)

Acknowledgement

This thesis would not have been possible without the help of my PhD director, Andrei Postnikov, and my supervisor at EDF R&D, Philippe Baranek. Thank you for your time and advice.

My sincere thanks to all the members of my doctoral committee, for the time they spent reading and reviewing my work and for their thoughtful questions and remarks during my defence.

This acknowledgement also addresses my managers at EDF, Matthieu Versavel, Cédric Guérard, Stéphanie Muller and with a special thought to Jean-Christophe Gault.

I would also like to thank all the EDF R17 team, especially Mireille, for her help for all the administrative tasks, and the close-knit group of PhD students.

A big thank you to the rest of my colleagues from IRDEP, IPVF and LCP-A2MC.

About the financial aspect, I would like to thank the ANRT for its support within the CIFRE agreement 2016/0608.

Heartfelt thanks go to all my friends, who have always been a major source of support and motivation. From Böen to Sherbrooke through Le Mans, thank you for your valued presence in my life.

I also express my profound gratitude to all my family members. Who I have become is due to the hard work of my parents who help me and my two sisters to push our limits everyday.

Finally, I could not thank Clara-Victoria enough for sharing her life with me. She has done so many things for me that if she wants the moon, she can just say the word, and I'll throw a lasso around it and pull it down.

Contents

Introduction

The electrical properties of semiconductors, such as concentrations and mobilities of charge careers, are strongly influenced by the types of dopants and defects inserted or formed during the synthesis of materials (Mahajan, 2000; Holt and Yacobi, 2007). In the field of photovoltaics, the objective of device is to convert the sunlight into electricity via charge separation on a p-n junction. When photons are absorbed by the material, they excite the minority charge carriers, i.e., holes in n-type and electrons in p-type semiconductors, creating a electron-hole pair, which subsequently flows into the solar cell's electrical contacts. In this process, the structural defects inevitably present in the semiconductor result in various obstacles, such as phase stability's perturbation, supplementary energy level appearing in the band gap, etc. and can degrade the efficiency and durability of solar cells (Sopori, 1999; Carr and Chaudhary, 2013). The understanding of these effects is thus a priority for solar cell development in order to increase the efficiency and the lifetime of the cell. Experimental process and characterisation techniques are widely used, yet the defects remain hard to identify and to characterise (Seeger, 1974; Saarinen *et al.*, 1997). Theoretical study and simulation works are then complementary to experimental technics. They can describe concentration too low to be characterised, or probe a system under specific conditions not experimentally achievable. When dealing with material properties and behaviour, different length and time scales of study are possible, from atomic to macroscopic.

At the atomistic scale, speaking specifically about first-principles simulation, different theories and approximations exist but the calculation are usually done within, or with, the Hartree-Fock (HF) approximation (Hartree, 1928a,b) or the density functional theory (DFT) (Hohenberg and Kohn, 1964). Among the practical issues important for modelling the materials in photovoltaics are the ability of calculation schemes to predict the equilibrium structure and the optical properties, or, at least, the magnitude and the character (direct vs indirect) of the optical gap. The "straightforward" determination of the band gap (estimated from the electron band structures) turns out to be largely overestimated, as compared to experimental values, when using the HF and underestimated in the DFT. Therefore, more justified methods like the configuration interaction method (CI) and the GW approximation should be used but these requires a big amount of time and computational resources. One possible alternative can be the use of hybrid functional within the DFT framework. This pragmatic approach combined results from both HF and DFT, thus using their drawbacks for more accurate description of the electronic properties of the system.

In any case, temperature is not taken into account in first-principles calculations. Classical molecular dynamics simulations deal with evolution of the temperature, but electronic structures are not explicit variables in the model. As both of these aspect are primordials, the quasi-harmonic approximation (QHA) can be used by bringing *a posteriori* the temperature in the model via the vibrational modes of the crystal.

At mesoscopic or macroscopic scale of simulation, transport properties are very important in order to understand the behaviour of the material. However, these are properties intrinsic to the material and deeply linked to its composition, doping or the presence of other defects. These properties like the conductivity are accessible via the Boltzmann transport equation that describes the non equilibrium behaviour of charge carriers by statistically averaging over all possible quantum states.

The main problematic of this work is the development of a pragmatic method that would permit a quick and accurate description of realistic complex system depending on temperature. The objective here is to be able to understand the behaviour of system under the influence of changing the alloy concentration, modification of the level of doping by impurities, or creation of other types of point defects. The context of photovoltaic imposes the correct description of the electronic and transport properties in particular. This method will be applied to the analysis of two groups of materials common for applications in photovoltaics, namely chalcopyrite-type $\mathrm{Cu(III)(VI)_2}$ compounds and crystalline silicon.

The first species represents a family of compounds which can be ternary, quaternary or penternary, depending of the composition. In this work, we are interested in the copper-based chalcopyrite (Coughlan *et al.*, 2017; Abou-Ras *et al.*, 2017), of which the most general form is $\mathrm{CuGa}_x\mathrm{In}_{1-x}(\mathrm{S}_y\mathrm{Se}_{1-y})_2$. These materials are conventionally referred to in shorthand notation, depending of the atoms present. For exemple, CIGSSe is the general form, CIGS correspond to the quaternary $\mathrm{CuIn}_{1-x}\mathrm{Ga}_x\mathrm{S}_2$, and CGSe to the ternary CuGaSe_2. This direct band gap material have high absorption properties that allows high efficiency for thin-film solar cells. Various properties of CIGSSe are directly linked to its compositions. A broad range of band gap, lattice parameter values and other properties can be obtained within this family of materials, especially with a new type of dopant, alkali metals. This is why its application in tandem solar cell, e.g., with silicon, is considered. In a solar cell, the absorber that captures phonons is sensible to a certain range of photon energy and thus can only absorb a part of the sunlight. In order to increase the number of photons captured, the stacking of more than one solar cell is called a multijunction or tandem solar cell. A typical tandem structure can be found in figure 1. The optimised efficiency for tandem solar cell have been calculated in the literature (Meillaud *et al.*, 2006). The maximum efficiency range corresponds to a bottom cell having the band gap of around 1 eV and the top cell having the band gap of 1.5 – 1.7 eV. The objective for the study on chalcopyrites is then to determine the composition or doping that would lead to a band gap in the desired area.

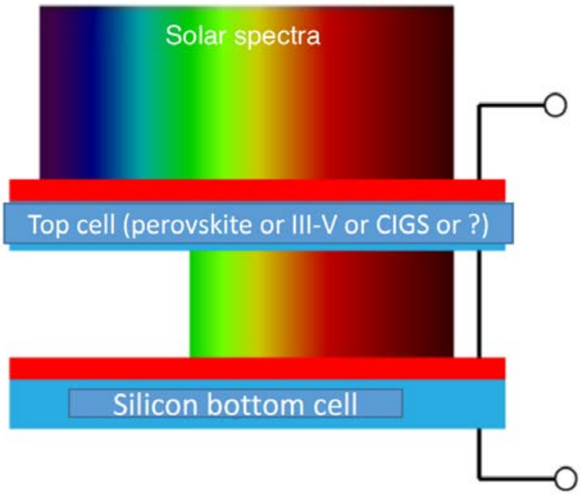

Figure 1 Tandem solar cell device with silicon bottom cell under sunlight irradiation.

For silicon, the situation is different. Silicon is the main semiconductor used in the photovoltaic market, and its properties are well known. However, with new type of cell architecture, different type of degradation induced by light and elevated temperature (LID and LeTID) appeared (Osterwald *et al.*, 2002; Ramspeck *et al.*, 2012). This deterioration of the performance seems to be linked to hydrogen defect (Wenham *et al.*, 2018), that is however not yet well understood. A special attention in the present work is then brought on silicon point defects, especially hydrogen.

The manuscript is organised as follows. In the first part of this thesis, the theoretical background of different concepts, approximations and methods used throughout this whole work is introduced. In the second part, the methodology developed to correctly describe complex system is outlined. The accurate electronic properties are then obtained by the use of optimised hybrid functional, whereas the temperature and transport properties are incorporated via the quasi-harmonic approximation and the Boltzmann transport equation. This method chosen undergoes tests on pure compounds used in the photovoltaic field, and the results of such tests are compared to experimental data and other theoretical works. In the third part, chalcopyrite-type compounds are investigated with the aim to find compositions suitable for tandem application. Two different studies are undertaken. Firstly, a mapping of electronic, structural and thermodynamic properties for all the concentration of CIGSSe is carried out. Secondly, an insertion of alcali metal atoms to substitute copper is simulated, with corresponding effect on lattice relaxation and electronic properties. The experimentally apparent improvement of the cell efficiency via alkali metal admixture is not yet well understood. The variation of properties under Li, Na, K, Rb ans Cs doping of ternary chalcopyrite-type compounds is calculated. Finally, in the last part of this work, hydrogen, iron and boron point defect in silicon are simulated. This preliminary works takes place within the frame of a larger project devoted to the ageing of silicon solar cells.

Chapter 1

Theoretical background

Before diving into their practical use, the different methods and procedures applied during this thesis are described theoretically. The Hartree-Fock (HF) and density functional theory (DFT) are summarised before the introduction of the hybrid approach. In order to deal with the effect of temperature, the theory behind the quasi-harmonic approximation is explained. Finally, the derivation of the electrical conductivity and other transport properties from the Boltzmann transport equation (BTE) are demonstrated.

1.1 First-principles calculations

In this section, the first-principles approaches are presented. They are based on the resolution of the time-independent Schrödinger equation,

$$\hat{\mathrm{H}}\Psi = E\Psi, \tag{1.1}$$

where the Hamiltonian operator $\hat{\mathrm{H}}$ is

$$\hat{\mathrm{H}} = -\frac{1}{2}\sum_{i}\nabla_i^2 + \sum_{i}\frac{1}{2M_A}\nabla_A^2 - \sum_{i,A}\frac{\mathrm{Z}_A}{r_{iA}} + \sum_{A,B}\frac{\mathrm{Z}_A\mathrm{Z}_B}{R_{AB}} + \sum_{i>j}\frac{1}{r_{ij}}, \tag{1.2}$$

with i, j refering to electrons and A, B to nuclei. In order to simplify this equation, the adiabatic or Born-Oppenheimer approximation (Born and Oppenheimer, 1927) decouples the motion of nuclei and electrons, adopting the following form of the wavefunction:

$$\Psi_{\{\mathbf{R}\}}(\mathbf{r}) = \Psi_{electron}(\mathbf{r};\mathbf{R})\Psi_{nuclei}(\mathbf{R}), \tag{1.3}$$

where the nuclei positions $\{\mathbf{R}\}$ are entering as parameters. The remaining task is to solve the electronic part of the Schrödinger equation with the following Hamiltonian:

$$\begin{aligned} \hat{H}_e &= -\frac{1}{2}\sum_{i}\nabla_i^2 - \sum_{i,A}\frac{\mathrm{Z}_A}{r_{iA}} + \sum_{i>j}\frac{1}{r_{ij}} && (1.4)\\ &= T + V_{eN} + V_{ee}, && (1.5) \end{aligned}$$

with T being the operator of the kinetic energy of the electrons, V_{eN} the operator of interaction between electron and nuclei and V_{ee} the operator of interaction between electrons.

The later term is a sum over N independent particles difficult to evaluate. This equation is not exactly solvable for more than two particles. Different methods to tackle this problem exist as we briefly explain in the following sections.

1.1.1 Hartree-Fock approximation

The first method we evoke is the Hartree-Fock (HF) approximation (Hartree, 1928a,b; Fock, 1930). The objective of HF approximation is to find the wavefunction of the fundamental state via a variational method. It is a purely mono-electronic model where one electron is under the influence of the mean field of all others. In order to satisfy the Pauli's exclusion principle, we assume that the many-electron wavefunction takes the form of a Slater determinant of single-electron wavefunctions (Slater, 1929):

$$\Psi = \frac{1}{\sqrt{N!}} \begin{vmatrix} \varphi_1(r_1) & \cdots & \varphi_N(r_1) \\ \vdots & & \vdots \\ \varphi_1(r_N) & \cdots & \varphi_N(r_N) \end{vmatrix}. \tag{1.6}$$

In this context, each electron is associated to a wavefunction φ_i and the mono-electronic Hamiltonians for the i-th electron can be written as follows:

$$\hat{h}_i = -\frac{1}{2}\nabla_i^2 - \sum_A \frac{Z_A}{r_{iA}} + \frac{1}{2}\sum_j \left[\hat{J}_j(r_i) + \hat{K}_j(r_i)\right] \tag{1.7}$$

$$\hat{h}_i = \hat{T} + \hat{V}_{eN} + \hat{J}[\rho(\mathbf{r})] + \hat{K}[\rho(\mathbf{r},\mathbf{r}')], \tag{1.8}$$

where $\hat{J}_j$ the Coulombian operator between electrons and $\hat{K}_j$ the exchange operator defined as

$$\hat{J}_j(r_i)\varphi_i(r_i) = \left[\int \varphi_j^*(r_j)\frac{1}{r_{ij}}\varphi_j(r_j)\right]\varphi_i(r_i) \tag{1.9}$$

and

$$\hat{K}_j(r_i)\varphi_i(r_i) = \left[\int \varphi_j^*(r_j)\frac{1}{r_{ij}}\varphi_j(r_i)\right]\varphi_i(r_i). \tag{1.10}$$

One of the big drawbacks of this method is that it fails to represent the correlation between electrons beyond the Pauli's exclusion principle. The correlation is defined as the difference between the real ground state energy of the system and the one determined by HF method:

$$E_c = E_{TOT}^{real} + E_{HF}. \tag{1.11}$$

The lack of correlation here means that an electron at a position $\mathbf{r}$ has no influence on the position $\mathbf{r}'$ of another electron other than Coulomb interaction. That leads to an overestimation of the ionic character of the system. The band gaps of semiconductors and insulators are thus highly overestimated. The J and K

operators lead to a calculation time proportional to N^4, with N the number of electrons in the system. From a computational point of view, the system is either 0D (molecules), 1D (chains, or polymers), 2D (surfaces) or 3D (periodic crystals). In our case, we deal with 3D cells with periodic boundary conditions.

1.1.2 Density Functional Theory

Driven by a motivation to grasp the electron correlation within a practical theory, Hohenberg and Kohn put foundation to what is nowadays known as the density functional theory (DFT) (Hohenberg and Kohn, 1964). They proved that the ground state energy is a functional of the electronic density and that the minimum of this functional is the true electronic density:

$$E_0 \leq E[\rho_0] = \min_{\rho} \left(\min_{\Psi} \left[F[\rho] + \int \rho(r) v_{eN}(r) d^3 r \right] \right). \tag{1.12}$$

In the Kohn-Sham DFT (Kohn and Sham, 1965), the wavefunction-based theory (WFT) is abandoned and the real density is mimicked by a density of non-interacting particles under the influence of an external potential V_{xc}. In this context, the Hamiltonian of the mono-electronic equation is

$$\hat{h}_i = \hat{T} + \hat{V}_{eN} + \hat{J}[\rho(\mathbf{r})] + \hat{v}_{xc}(\mathbf{r}). \tag{1.13}$$

The terms are the same as for equation (1.8) except for the exchange-correlation functional $\hat{v}_{xc}$. The external potential is defined such that the electronic density of non-interacting electrons equals the one of the real system:

$$\rho(\mathbf{r}) = \sum_{i=1}^{N} |\psi_i(\mathbf{r})|^2. \tag{1.14}$$

The only problem is that the form of the exchange-correlation functional is unknown and we need to use some approximations. The simplest is the local density approximation (LDA) where the exchange-correlation energy E_{xc} is the one of an uniform electron gas:

$$E_{xc}^{LDA} = \int \epsilon_{xc} \rho(\mathbf{r}) d^3\mathbf{r}, \tag{1.15}$$

where ϵ_{xc} is the exchange-correlation energy per particle of an uniform electron gas of density ρ. When density undergoes rapid spatial variations, LDA fails and the semi-local generalised gradient approximation (GGA) is used. It takes into account the density and its gradient with position $\nabla\rho(\mathbf{r})$. As these methods are based on the assumption that the electron distribution is more delocalised and homogeneous like in metal, it thus underestimates the band gap. This method is even faster than HF as it is proportional to N^3(Leach, 2001).

1.1.3 Beyond HF and DFT

Both HF and DFT suffer from drawbacks, especially their inevitable error on the determination of the band gap of semiconductors. Further methods called post-HF and -DFT were created to correct some of these issues. In the WFT, a many-electrons wavefunction corresponds to a particular electronic configuration where the electrons are assigned to specific orbitals. The HF wavefunction corresponds to the ground state configuration where electrons filled the lowest orbitals. The configuration interaction (CI) method (Hehre *et al.*, 1986) takes advantage of all these configurations. Its wavefunction is a sum of Slater determinants of wavefunctions corresponding to specific electron configurations:

$$\Psi = c_0\Psi_0 + c_1\Psi_1 + c_2\Psi_2 + \cdots . \tag{1.16}$$

In this framework, the correlation is taken into account, including also the excited states. However, this method can be very time consuming (proportional to N^{12}) and the full CI where all the configurations are investigated can only be done for small systems.

Within the DFT, the many-body GW approximation correct the electronic structures determined by LDA or GGA. It takes advantage of Green's functions describing the photoemission process, and the screen-Coulomb interaction to approximate the exact exchange self-energy (Aryasetiawan and Gunnarsson, 1998; Reining, 2018): This method thus increases the description of the electron's interaction with its environment. CI and GW are not the only methods available to reach more accurate results from HF and DFT. However, all of these methods require important computational time. The time necessary for GW calculations scales with the system size as N^8. For a quick but reliable description of semiconductors properties, *hybrid functionals* are a good alternative.

1.1.4 Hybrid functionals

In order to correct the drawback of DFT and HF, hybrid functionals were introduced by Becke (1993b). It is a pragmatic approach which combines the exact exchange of HF with DFT exchange-correlation term, since both methods give error of the opposite sign when compared to the experimental data. The simplest form corresponds to full-range hybrid functionals which is a linear combination of the HF and DFT exchange:

$$E_{xc}^{PBE0} = \alpha \times E_x^{HF} + (1-\alpha) \times E_x^{PBE} + E_c^{PBE}, \tag{1.17}$$

with α being the *exchange mixing ratio*. This notation should not be mixed up with the similar labelling of the thermal expansion coefficient in the subsequent chapters. In the case of the PBE0 functional, 25% of HF exact exchange are mixed with the PBE exchange (Adamo and Barone, 1999); this exchange mixing ratio is not empirical but based on a model (Perdew *et al.*, 1996b). Because of the potentially very demanding computational time of the exact exchange for long distance interactions, it is decomposed into short (sr) and long (lr) range parts. This is done by splitting the Coulomb interaction as

$$\frac{1}{r} = \frac{\mathrm{erfc}(\omega r)}{r} + \frac{\mathrm{erf}(\omega r)}{r}, \tag{1.18}$$

where r is the interatomic distance between $\mathbf{r}$ and $\mathbf{r}'$, and ω is the screening parameter that defines the range separation. When the screening parameter is zero, equation (1.18) is equivalent to equation (1.17). One of the most used hybrid defined this way is HSE06 (Heyd *et al.*, 2003, 2006). It is a short range hybrid functional where the exchange energy is written as

$$E_{xc}^{HSE06} = 0.25 \times E_x^{HF,sr,\mu} + 0.75 \times E_x^{PBE,sr,\mu} + E_x^{PBE,lr,\mu} + E_c^{DFT}. \tag{1.19}$$

In this case, the μ parameter is defined empirically. The performance of hybrid functionals will be discussed more thoroughly in section 2.1.

1.2 Computational details

1.2.1 Basis set

In a vast majority of calculation methods in practical use, either one or the other of two families of functions serve as basis sets in order to represent the wavefunction, or the electron density.

The first family of *localised basis sets* is the Gaussian-type orbitals (GTO). A Gaussian-type orbital (Boys, 1950), centered at some site and possessing the angular symmetry $Y_{lm}(\theta, \phi)$ around it, can be expressed by equation (1.20), whereby the parameter α gives control over the desired extension (more or less diffuse character) of the radial part:

$$g_{l,m}(\mathbf{r}) = B(l, \alpha) r^l \exp(-\alpha r^2) Y_{lm}(\theta, \phi). \tag{1.20}$$

This type of basis set is easily tuned. As the product of two Gaussians is another Gaussian, the two-center and other multicenter integrals involving these functions can be expressed analytically and thus easy to compute. The wavefunction is expressed as a linear combinaison of GTOs. One drawback of this type of orbital is that, for metallic system, the number of diffuse GTOs required can be quite important.

The second family is the *plane-waves basis sets*. A plane-wave (PW) is written as

$$p(\mathbf{r}) = \frac{1}{\Omega} \exp(i\mathbf{G} \cdot \mathbf{r}), \tag{1.21}$$

with $\mathbf{G}$ a vector of the reciprocal lattice. The drawback here is that a large number of plane-wave functions is required for a good description of system with inhomogeneous electronic clouds.

Since the HF exact exchange is difficult to determine in the PW framework (Betzinger, 2007; Dziedzic *et al.*, 2013), some codes such as VASP (Paier *et al.*, 2005) propose an approximative way to do it but do not allow to have a self-consistent description of the system. In general, the optimisation of the geometry is done within LDA or GGA approximation. The determination of the electronic structure is further on done at a fixed geometry with the hybrid functional. As GTOs do not suffer from this problem, all calculations done during this thesis have been performed with the GTO-oriented `CRYSTAL17` code (Dovesi *et al.*, 2018). The description of the basis sets used can be found in the appendix A.

1.2.2 The `CRYSTAL` code

`CRYSTAL17` is based on the linear crystalline atomic orbital (LCAO) theory where the wave function is described as a sum of one-electron crystalline orbitals that are solutions of the one-particle equation:

$$\hat{h}_i \varphi_{k_i} = \varepsilon_{k_i} \varphi_{k_i}. \tag{1.22}$$

The one-particle Hamiltonian $\hat{h}_i$ is the one explicit for HF and KS in the equations (1.8) and (1.13) respectively. These one-electron crystalline orbitals are in turn expressed as a sum of Bloch function ϕ_i build from local Gaussians:

$$\varphi_i(\mathbf{r}, \mathbf{k}) = \sum_j c_{ij}(\mathbf{k}) \phi_j(\mathbf{r}, \mathbf{k}). \tag{1.23}$$

In order to computationally solve it, the one-electron Schrödinger equation can be written in a form of matrix equation (Dovesi *et al.*, 2005):

$$\mathbf{H}(\mathbf{k})\mathbf{C}(\mathbf{k}) = \mathbf{S}(\mathbf{k})\mathbf{C}(\mathbf{k})\mathbf{E}(\mathbf{k}), \tag{1.24}$$

with $\mathbf{S}(\mathbf{k})$ being the overlap matrix and $\mathbf{C}(\mathbf{k})$ the matrix of coefficients from equation (1.23). In CRYSTAL, the self-consistent field (SCF) observes the following steps (Dovesi *et al.*, 2005). After creating the basis sets and evaluating the overlap matrix and the Fock matrix (corresponding to the single electron operator $\hat{h}_i$) in direct space, these matrices are then Fourier-transformed into the reciprocal space. The Schrödinger equation is then solved at every k-point, and the Fermi energy is calculated. After that, the density matrix is determined and Fourier-transformed back into the direct space. At the end on this procedure, the total energy of the system is calculated. This is the cornerstone of every other calculations. Once we know how to solve the Schrödinger equation for a given nuclei geometry thanks to the different theories and approximations, various properties can be obtained from different types of calculations. Below, we outline the quasi-harmonic approximation and the transport properties calculations as two important parts of this work.

1.3 Quasi-harmonic approximation

Geometry optimisations, once performed, lead to the equilibrium position in the potential energy surface where the other types of calculations can take place. However in a real crystal, the lattice is not rigid and each atom moves around its equilibrium position. The effect of temperature on the crystal vibrational properties can be taken into account via the crystal vibrational properties. When looking for small variations around the equilibrium position, the Taylor expansion, see -equation (1.25), comes in handy:

$$f(x) = f(x_0) + (x - x_0) \cdot \frac{df(x_0)}{dx} + \frac{(x - x_0)^2}{2} \cdot \frac{df^2(x_0)}{d^2x} + \cdots \tag{1.25}$$

By definition, the first derivative of energy over displacements at the equilibrium position is zero so that the first assumption is to consider only the quadratic term. This would correspond to the harmonic approximation for atomic vibrations. The Hessian or dynamic matrix is obtained by the finite displacement technique, whereby the atoms are shifted one by one from their equilibrium positions. The dynamical equations which contain the Hessian are then diagonalised, yielding the phonon eigenvalues (frequencies squared) and eigenvectors (displacement patterns within each mode). By default in CRYSTAL, the phonon calculation is done at the Γ point. In order to take phonons with other (commensurate) wavevectors into account, one can resort to constructing a supercell which would accommodate the vibration wave in question. The phonon calculation is e.g., useful for checking the dynamical stability of presumably equilibrium structure. An instability could be identified by detecting an imaginary phonon frequency, that means that a combined displacement pattern exists which would lower the total energy on displacement from the equilibrium. Once the phonon frequencies are calculated in the harmonic approximation, the energy levels of corresponding quantum oscillators can be artificially populated with Bose-Einstein distribution for a specific temperature. Even as this would allow the calculation of different thermodynamic properties, a major drawback of such approach is that it does not provide a mechanism that would relate the variation of interatomic distances with temperature. That means for example that there is no thermic expansion of the crystal or that the thermal conductivity will be infinite.

This problem can be tackled down via the incorporation of inharmonic terms but this requires to solve more complex equation. A simpler solution is the quasi-harmonic approximation (QHA) that keeps the harmonic expression but adds an explicit dependence of vibration phonon frequencies on volume.

The quasi-harmonic approximation has been implemented in `CRYSTAL17` (Erba, 2014). An automated algorithm computes the influence of the temperature and pressure on different structural and thermodynamic properties. The procedure needs to start from an optimised geometry at 0 K, either from a previous work or done at the beginning of the calculation. Depending of the chosen parameters, the algorithm performes structural optimisation and phonon calculation for different contracted or expanded systems around the zero-temperature equilibrium position. Once all those structures have been computed, their volume and energy can be used to fit the purely electronic internal energy as a function of volume via different equations-of-state (EOS) from the literature. CRYSTAL proposes different EOS but uses the third-order Birch-Murnaghan (Birch, 1947; Murnaghan, 1944) for further thermodynamic calculations. Volume dependence of each phonon frequency is then individually fitted with second or third-order polynomes.

For a given temperature, the Helmholtz free energy is calculated thanks to the following equations :

$$F^{QHA}(T,V) = U_0(V) + F_{vib}^{QHA}(T,V), \tag{1.26}$$

$$F_{vib}^{QHA}(T,V) = E_0^{ZP}(V) + k_B T \sum_{\mathbf{k}p} \left[\ln \left(1 - e^{-\frac{\hbar\omega_{\mathbf{k}p}(V)}{k_B T}} \right) \right] \tag{1.27}$$

and

$$E_0^{ZP}(V) = \sum_{\mathbf{k}p} \hbar\omega_{\mathbf{k}p}(V)/2. \tag{1.28}$$

For each temperature, the Helmholtz free energy is minimised in order to obtain the equilibrium structure. In that way, the temperature dependence of the volume can be plotted. As several properties depend on the derivative of the volume's variation with the temperature, the number of temperature steps must be sufficiently large.

Once the geometry has been fitted at each temperature, the band gap can be calculated for this fixed geometry.

1.4 Electrical transport properties

1.4.1 Boltzmann transport equation

In order to study the classical transport of charge carrier in the bulk, the Boltzmann transport equation (BTE) is used that deals with the local concentration of carriers in the state **k** close to the point **r** and describes how this concentration changes in time (Allen, 1996). Even though the transport properties need, in principle, to be calculated by taking into account the phonon contribution, only the electronic contribution will be considered in this thesis. Three different effects should be indicated in what concerns the charge carriers' distribution.

- The first one is their diffusion. If the velocity of a carrier in state **k** is denoted $\mathbf{v_k}$, the carrier will travel a distance $t\mathbf{v_k}$ in an interval t, with the velocity:

  $$v_\alpha\left(i, \mathbf{k}\right) = \frac{1}{\hbar}\frac{\partial \varepsilon_{i,\mathbf{k}}}{\partial k_\alpha}. \tag{1.29}$$

  Thanks to Liouville's theorem, which states that "*the phase-space distribution function is constant along the trajectories of the system*", we can write for the probability density function f:

  $$f_\mathbf{k}(\mathbf{r}, t) = f_\mathbf{k}(\mathbf{r} - t\mathbf{v_k}, 0), \tag{1.30}$$

  so that :

  $$\left[\frac{\partial f_\mathbf{k}}{\partial t}\right]_{diff} = -\mathbf{v_k}\frac{\partial f_\mathbf{k}}{\partial \mathbf{r}} = -\mathbf{v_k}\nabla_r f_\mathbf{k}. \tag{1.31}$$

- The second effect concerns constant external fields that change the vector **k** at a rate of

  $$\frac{d\mathbf{k}}{dt} = \frac{e}{\hbar}\left(\mathbf{E} + \frac{1}{c}\mathbf{v_k} \wedge \mathbf{H}\right). \tag{1.32}$$

  This corresponds to the velocity in k-space so that by analogy with equation (1.30), the impact of the field is

  $$\left[\frac{\partial f_\mathbf{k}}{\partial t}\right]_{field} = -\frac{e}{\hbar}\left(\mathbf{E} + \frac{1}{c}\mathbf{v_k} \wedge \mathbf{H}\right)\nabla_\mathbf{k} f_\mathbf{k}. \tag{1.33}$$

- The last one is the scattering effect. It is more complicated to express and we generally stay in the scope of elastic scattering.

The BTE states that the net rate of change of $f_{\mathbf{k}}(\mathbf{r})$ with time is zero :

$$\left[\frac{\partial f_{\mathbf{k}}}{\partial t}\right]_{diff} + \left[\frac{\partial f_{\mathbf{k}}}{\partial t}\right]_{field} + \left[\frac{\partial f_{\mathbf{k}}}{\partial t}\right]_{scatt.} = 0. \tag{1.34}$$

The distribution function can be seen as the perturbation, $g_{\mathbf{k}}(\mathbf{r})$, of the equilibrium Fermi-Dirac distribution function defined at spatially variable temperature $T(\mathbf{r})$:

$$f_{\mathbf{k}}(T(\mathbf{r})) = f^0_{\mathbf{k}}(T(\mathbf{r})) + g_{\mathbf{k}}(\mathbf{r}), \tag{1.35}$$

with:

$$f^0_{\mathbf{k}} = \frac{1}{e^{\frac{\varepsilon_k-\mu}{k_{\mathrm{B}}T}}+1}. \tag{1.36}$$

In the absence of temperature gradients ($\nabla_r f_{\mathbf{k}} = 0$) and for an external force consisting only of a low electric field $\mathbf{E}$ ($\mathbf{H} = 0$), the equation (1.34) becomes:

$$\left(\frac{\partial f_{\mathbf{k}}(T)}{\partial t}\right)_s = e\mathbf{E}\mathbf{v}_{\mathbf{k}}\left(-\frac{\partial f^0_{\mathbf{k}}(T)}{\partial \varepsilon}\right). \tag{1.37}$$

1.4.2 Relaxation Time approximation

In order to solve the BTE, the scattering effect term must be explicated. However, instead of defining every possible scattering effects, the following assumption is made:

$$\left[\frac{\partial f_{\mathbf{k}}}{\partial t}\right]_{scatt.} = -\frac{1}{\tau}\cdot g_{\mathbf{k}}, \tag{1.38}$$

with τ the relaxation time needed for a system without the influence of external fields to go back to its equilibrium. This can also be seen as

$$g_{\mathbf{k}}(t) = g_{\mathbf{k}}(0)e^{-\frac{t}{\tau}}. \tag{1.39}$$

By replacing equation (1.38) in equation (1.37), we obtain

$$g_{\mathbf{k}} = -\tau\mathbf{v}_{\mathbf{k}}\cdot e\mathbf{E}\left(-\frac{\partial f^0_{\mathbf{k}}(T)}{\partial \varepsilon}\right). \tag{1.40}$$

Even though the relaxation time depends on the band index and the vector direction, it is usually taken as a constant in the constant relaxation time approximation (CRTA).

1.4.3 Electrical conductivity

The number of carriers in the volume $d\mathbf{k}$ is $\frac{g(\mathbf{k})d\mathbf{k}}{4\pi^3}$ so that we can write the current density in the band n as

$$\mathbf{J}_n = -e\int\frac{1}{4\pi^3}\mathbf{v}_{n,\mathbf{k}}g_{n,\mathbf{k}}d\mathbf{k}. \tag{1.41}$$

As the electrical conductivity is the sum of the contribution of each band $\mathbf{J}_n = \boldsymbol{\sigma}_n \mathbf{E}_n$,

$$\boldsymbol{\sigma} = \sum_n e^2 \int \frac{1}{4\pi^3} \tau_n \mathbf{v}_{n,\mathbf{k}} \mathbf{v}_{n,\mathbf{k}} \left(-\frac{\partial f^0_{\mathbf{k}}(T)}{\partial \varepsilon} \right) d\mathbf{k}, \tag{1.42}$$

and the inverse mass tensor,

$$M^{-1}_{\beta u}(i, \mathbf{k}) = \frac{1}{\hbar^2} \frac{\partial^2 \varepsilon_{i,\mathbf{k}}}{\partial k_\beta \partial k_u}, \tag{1.43}$$

the different transport properties can be written :

$$[\sigma]_{i,j}(T;\mu) = e^2 \int \Sigma_{i,j}(\varepsilon) \left[-\frac{\partial f(\mu, E, T)}{\partial E} \right] dE, \tag{1.44}$$

$$[\sigma S]_{ij} = \frac{e}{T} \int \Sigma_{i,j}(\varepsilon) \left[-\frac{\partial f(\mu, E, T)}{\partial E} \right] (E-\mu) dE, \tag{1.45}$$

and

$$[\kappa_e]_{i,j}(T;\mu) = \frac{1}{T} \int \Sigma_{i,j}(\varepsilon) \left[-\frac{\partial f(\mu, E, T)}{\partial E} \right] (E-\mu)^2 dE, \tag{1.46}$$

with the transport distribution function defined as

$$\Sigma_{ij}(E) = \frac{1}{V} \sum_{n,k} v_i(n,k) v_j(n,k) \tau_{n,k} \delta(E - E_{n,k}). \tag{1.47}$$

1.4.4 Computational approaches

During the last decade, different codes were developed in order to calculate the transport properties from the BTE. The underlying theory is usually the same.

First, the rigid band approximation (RBA) implies that the band structure does not change under the influence of temperature or chemical potential.

The different packages principally differ in their way to interpolate the band structure. One of the most famous package is `BoltzTraP` (Madsen and Singh, 2006) that uses a Fourier expansion to interpolate the band. This numerical interpolation offers the advantage of directly obtaining the group velocity and the inverse mass tensor from the derivative with the finite-difference procedure. The problem with this method is the potential band crossing at the boundaries. In this case, a very fine k-grid needs to be used to correctly describe the phenomena. To avoid that, Scheidemantel *et al.* (2003) calculated the group velocities with the momentum matrix , also called the intraband optical matrix element:

$$\mathbf{v}_{n,\mathbf{k}} = \frac{1}{m} \mathbf{p}_{n,\mathbf{k}} = \frac{1}{m} \langle \Psi_{n,\mathbf{k}} | \hat{\mathbf{p}} | \Psi_{n,\mathbf{k}} \rangle . \tag{1.48}$$

The new version of BoltzTraP, simply called `BoltzTraP2` (Madsen *et al.*, 2018), had implemented the momentum matrix approach. Another method consists in using Wannier functions as in `BoltzWann` (Pizzi *et al.*, 2014). This analytical method uses the localised Wannier functions on a coarse k-point grid to avoid the finite-difference methods. Boltzmann transport equation has also been implemented in `CRYSTAL17` within the RBA and RTA.

Until now, all the codes cited performed calculations under the constant relaxation time approximation (CRTA). However, this is not a necessary limitation. For example, one can abandon the CRTA by varying the relaxation time with the energy. Another possible way is to take into account different types of scattering process. This is the case for the work of Faghaninia (Faghaninia *et al.*, 2015; Faghaninia, 2016) who suggested an *abinitio* model for calculating mobility and Seebeck coefficient using the Boltzmann transport (`aMoBT`) which was implemented in the `AMSET` (Faghaninia *et al.*, 2015, 2017) script. This Python module approximates scattering effects via different properties such as the phonon frequencies and the dielectric constant. The acoustic deformation potential, ionised impurity, piezoelectric and polar optical phonon differential scattering rates are available in this code.

In this thesis, we tested `BoltzTraP2` and `CRYSTAL17` . As we used `CRYSTAL17` for all the type of calculation, we first calculated the transport properties of the build-in module of `CRYSTAL17` . The calculation works smoothly for the material tested in a within a bearable time. A defective system of 32 atoms with low symmetry takes less than three hours. However, the important number of integrals to calculate and store during the time of simulation results in creating files of several gigabytes of data. For one simulation, 1.2 Tb of temporary data have been accumulated. This is problematic because of the limit of memory of the computer. Even if the jobs are launched sequentially, one heavy file can stop the program due to a memory error. This is why we turned to the second solution, the python module `BoltzTraP2`. It is not configured for `CRYSTAL17` output but we created the necessary interface. `BoltzTraP2` can be used in command line or as a python library. Here, only the command line function was used.

1.5 Summary and conclusion

All these methods are complementary and can be used to reach different types of properties. The hybrid functionals are a pragmatic way to correct the band gap problem of Hartree-Fock and density functional theory and prevent the computational cost of more sophisticated methods. Quasi-harmonic approximation and Boltzmann transport equation enable us to access the temperature dependence of various properties and the transport properties of our material. We explained the underlying theory in this chapter and their practical use and optimisation will be developed in the next one. The properties calculated from the quasi-harmonic approximation and the transport properties will be compared to experimental data and the performance of different functionals.

Chapter 2

Hybrid functional performances

The main objective of this thesis is to access macroscopic properties of defective materials in the context of photovoltaic applications. In this thesis, hybrid functionals have been optimised to reproduce the experimental value of the studied materials' band gap. This method will first be explained before comparing the optimised hybrid functionals to the theoretical and experimental works of literature for perfect compounds in order to verify the reliability of this method. Once these are obtained, the temperature effect will be tested via the quasi-harmonic approximation. Finally, the Boltzmann transport equation will be solved for the determination of macroscopic transport properties. The methodology introduced in this chapter is tested for pure compounds and its results are compared with the experimental and computational works from literature.

2.1 Hybrid functionals

2.1.1 Hamiltonian optimisation

State-of-the-art

As we saw in section 1.1.4, hybrid functionals were created to correct the "band gap problem" of density functional theory and Hartree-Fock approximation. They could be an interesting alternative to accurate but time-consuming methods such as GW. In the full-range hybrid functionals, a percentage of the HF exact exchange, called α, see equation (1.17), is incorporated into the DFT functionals. Other parameters such as the screening parameter are used in short- and long-range hybrid functionals but we limit ourselves to the full-range hybrid functionals in this thesis. In the early years of hybrid functionals, different Hamiltonians were created with a fixed value of the exchange mixing ratio. For example, PBE0 (Adamo and Barone, 1999) uses a PBE functional (Perdew *et al.*, 1996a) with 25% of exact exchange from HF. This value was obtained without any experimental considerations (Perdew *et al.*, 1996b). Nevertheless, PBE0 is known to overestimate the band gap of low band gap materials and underestimate the one of high band gap materials (Alkauskas *et al.*, 2011). It is more a compromise than an absolute and perfect value. Since the middle of the 2000s, discussions about the optimised amount of exact exchange to incorporate in DFT functionals have been set. This value can be system-dependent but its determination must be done in preliminary calculation. Alkauskas *et al.* (2008) tuned the exchange mixing ratio to reproduce the experimental band gap for the determination of band offsets at silicon-based semiconductors interface. They found that the lineup of bulk reference levels is practically independent of α. In the same year, the same group observed a linear impact of α on the evolution of the valence- and conduction-band edges of Si and Ge (Broqvist *et al.*, 2008). In both cases, the DFT functional chosen was PBE and the optimised values of α were 0.11, 0.15 and 0.15 for Si, Ge and SiC respectively. Moreover, they observed that the optimised value of the exchange mixing is related to an effective static screening of the long-range interaction (Alkauskas *et al.*, 2008). The link between the optimised value and the high frequency dielectric constant (ε_∞) has also been found by Shimazaki and Asai (2008) at the same period. The relation is

$$\alpha \simeq \frac{1}{\varepsilon_\infty}. \tag{2.1}$$

This can be explained by observing the similarity with GW approximation (Alkauskas and Pasquarello, 2011). The non-local exchange-correlation potential of hybrid functionals can be seen as the many-electron exchange-correlation self-energy in the GW approximation. In this approximation, the long-range interaction can be compared to a screened exchange whose asymptotic is the inverse of the dielectric constant times the distance between $\mathbf{r}$ and $\mathbf{r}'$. As the DFT, semi-local, terms of the hybrid functional are short-ranged, the long-range interactions are fully covered by the non-local, HF exact exchange $\alpha/|\mathrm{r}-\mathrm{r}'|$. Since the cited observation of Alkauskas and Pasquarello, numerous works used the inverse of the dielectric constant as an approximation for the exchange mixing ratio (Alkauskas *et al.*, 2011; Marques *et al.*, 2011; Conesa, 2012; Hinuma *et al.*, 2017; Shimazaki and Nakajima, 2014; Fritsch *et al.*, 2017). In order to automatise the process, some self-consistent methods have been proposed (Shimazaki and Asai, 2009; Skone *et al.*, 2014). They suggest to calculate the dielectric constant self-consistently until convergence by changing at each iteration the value of alpha. The method proposed by Skone *et al.* (2014) was implemented in `CRYSTAL17` (Erba, 2017). The procedure is exposed in figure 2.1. In this algorithm, the dielectric constant is calculated via a coupled-perturbed Kohn-Sham or HF (CPKS or CPHF) calculation (Ferrero *et al.*, 2008) at each iteration for a given value α defined as in equation (2.1).

Band gap optimised hybrid functional

For tandem applications, the band gaps of the two absorbers need to be complementary to capture as much of the incident light as possible. In order to have a qualitative and quantitative description of the electronic properties such as the band structure, we adjusted α in order to define a hybrid functional that leads to a band gap which matches its experimental value for each material. A fully automated algorithm for the determination of the optimal fraction was developed.

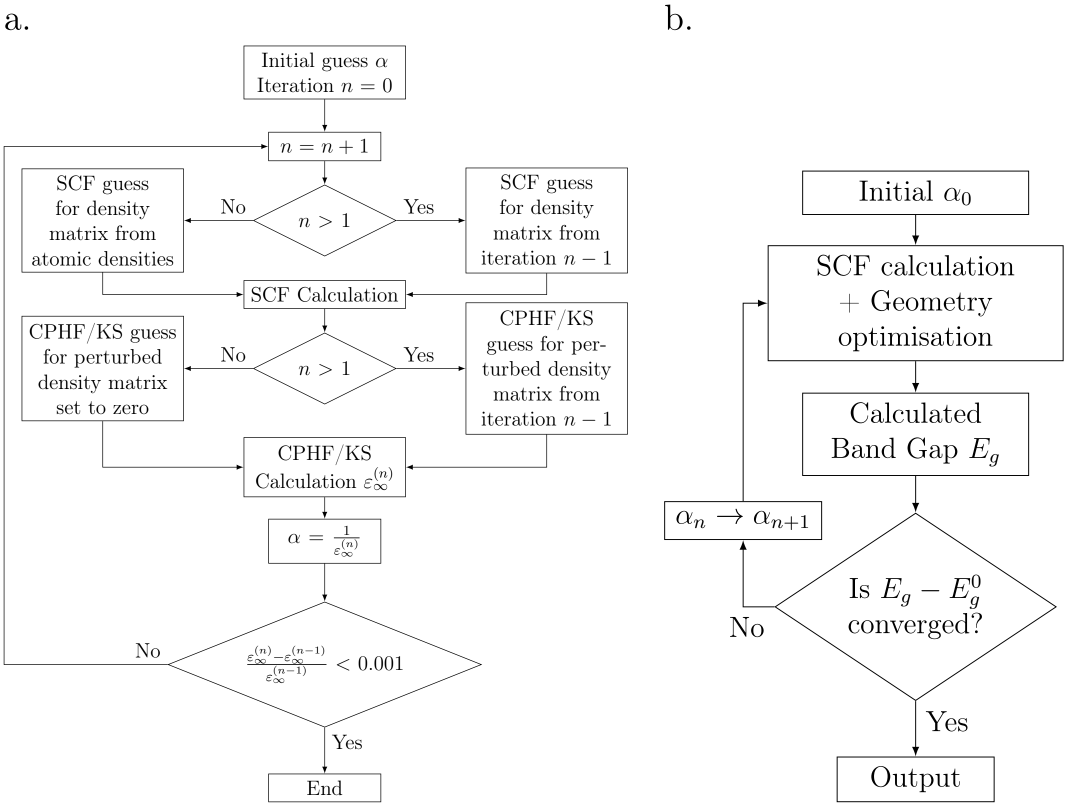

Figure 2.1 Flow charts of the automated algorithm for the system-specific definition of self-consistent hybrid functionals (a)as implemented into the `CRYSTAL17` program (Erba, 2017) (b) as done in this work for an accurate description of the band gap.

In a self-consistent way it allows, from the knowledge of the experimental band gap, to obtain α as seen in figure 2.1.

PBE and PBEsol functionals (Perdew *et al.*, 2008), corresponding to the revised PBE improving the description of the equilibrium properties of solids, were chosen as DFT basis for our hybrid functionals because of their important use in the solid state physic field. Materials used to test our hybrid Hamiltonians are zinc blend semiconductors, important in the photovoltaic area, namely silicon (Si), germanium (Ge), silicon-germanium (SiGe) and the III–V family with III = Ga, Al, In and V = P, As, Sb, and four ternary chalcopyrites, $CuGaS_2$, $CuGaSe_2$, $CuInS_2$ and $CuInSe_2$.

The effect of α on the electronic properties

As it has been explained in chapter 1.1, HF overestimates the band gap value (by more than 100%) whereas DFT underestimates it (by around 50%). Since these two limits are far from each other, the variation of the HF exact exchange can then lead to a significant variation of the band gap. This is illustrated in figure 2.2 which displays the variation of the band gap and the dielectric constant with the percentage of the HF exact exchange in the hybrid functional for different materials. The variation is practically linear for the band gap whereas as it has been already indicated by Broqvist *et al.* (2008). The dielectric constant varies as the inverse of the percentage of the exact exchange. For a small gap material like germanium, the PBE functional converges to a metallic solution, leading to an infinite value of the dielectric constant. Here, an inclusion of at least 10% of the exact exchange are then necessary for the system to converge on a semiconductor solution. When varying the α parameter, a change of 0.01% leads to a variation of the band gap of 0.001 eV. Thus in order to obtain a band gap of 1.17 eV for silicon, the hybrid made from PBEsol must include 12.3% of the exact exchange. This is sufficient for a precision on the second decimal of the band gap. The underlying DFT description used for the exchange-correlation, be it PBE or

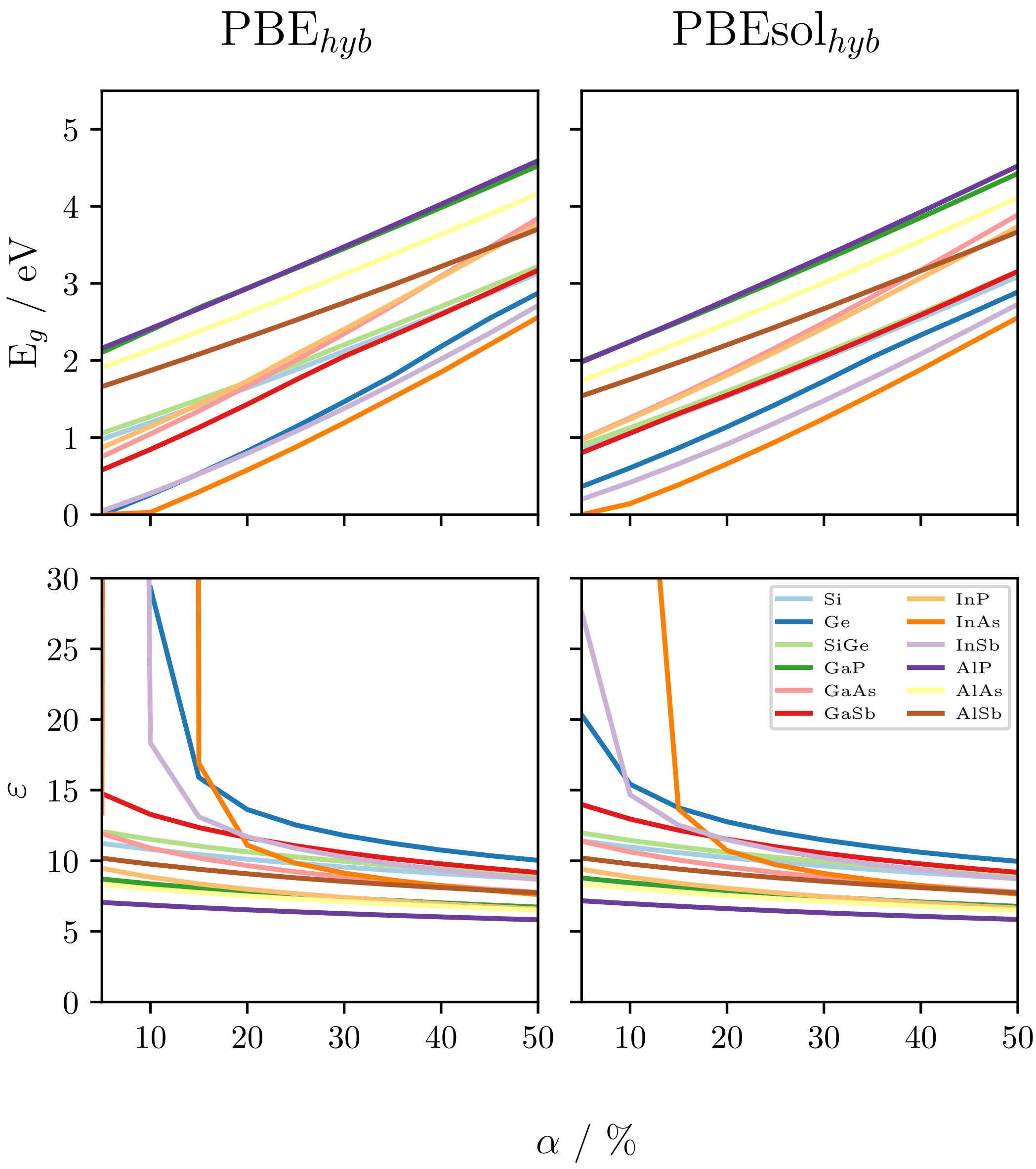

Figure 2.2 Calculated band gap values (upper panels) and the electron dielectric function ε_∞ (lower panels) for different semiconductors, depending on the mixing parameter α in the hybrid exchange-correlation functional based on the PBE (left panels) and PBEsol (right panels) prescriptions for the exchange-correlation.

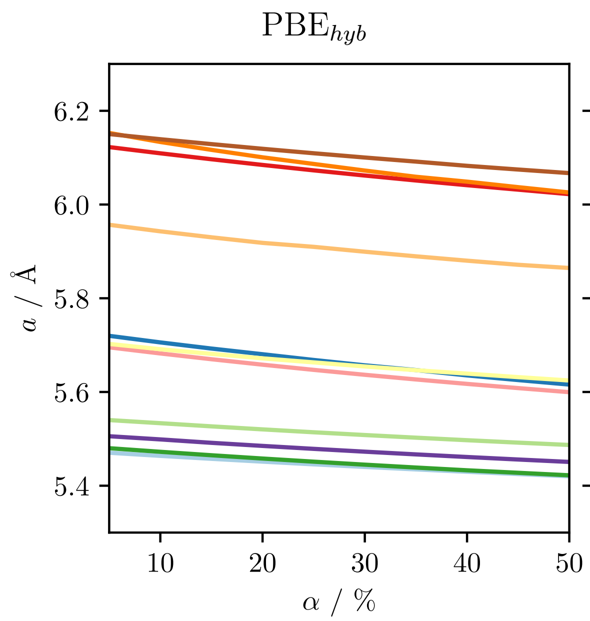

Figure 2.3 Influence of the percentage of exact exchange in the hybrid functional on the structural parameters for different materials.

PBEsol, hardly makes a noticeable difference. Moreover, as their impact on the final result decreases with the increase of α, they tend to the same HF limit.

Impact on the structural properties

Even though we are interested here in the correct description of the band gap, the other parameters are of significant importance. The structural properties have also a key role for tandem application where the lattice parameters of the two compounds must be similar to avoid lattice mismatch and thus growth and adhesion problems. According to literature, α does not have a strong influence on the structural properties (Deák *et al.*, 2005; Paier *et al.*, 2006; Heyd *et al.*, 2005). Figure 2.3 shows the variation of the lattice parameter a for Si, Ge, SiGe, GaP, GaAs and GaSb. Similar to the behaviour of the band gap, the lattice parameter can be seen at first approximation as linear with the percent α. However, unlike the variation of the band gap, the lattice parameter decreases for higher α. The relative variation of each one is of the order of magnitude of 0.1 for the whole range of percentage of exact exchange studied.

If we turn this differently, in an attempt to optimise our hybrid not according to the band gap but to the lattice parameter, the percentage would need to be changed drastically for a very small change of the lattice parameter. Thus, the corresponding value of the band gap might happen to be too far from the experimental value.

Optimised HF exact exchange percentage

Figure 2.4 shows the values of the mixing parameter α, optimised by the procedure described in figure 2.1, and grouped as function of calculated band gap values (left column) and depending on the calculated values of the electron static dielectric constant (right column), for the PBE (upper row) and PREsol (bottom row) exchange-correlation functionals. In the right column moreover, the inverse function of the dielectric constant is traced, to illustrate that the mixing values α do indeed follow its trend closely enough. For the rest of this thesis, the general optimised hybrid functionals are named as H_{hyb}, with H the name of the original Hamiltonian, *i.e.* PBE_{hyb}. For a material-specific optimised hybrid, it will be named similarly as H_x with x the percentage of exact exchange. The hybrid $\mathrm{PBEsol}_{12.3}$ is then based on PBEsol exchange-correlation with 12.3% of HF exact exchange. For the material studied, the optimised percentages of exact exchange are contained between 5% and 25% for both PBE and PBEsol hybrid functionals. Only SiGe for the PBE_{hyb} has a exchange mixing ratio inferior to 5%. When looking at the variation of α with the band gap, different trends can be observed. The ternary chalcopyrites have the highest percentage of exact exchange between 20% and 25%. The III-V semiconductors are divided into three different categories,

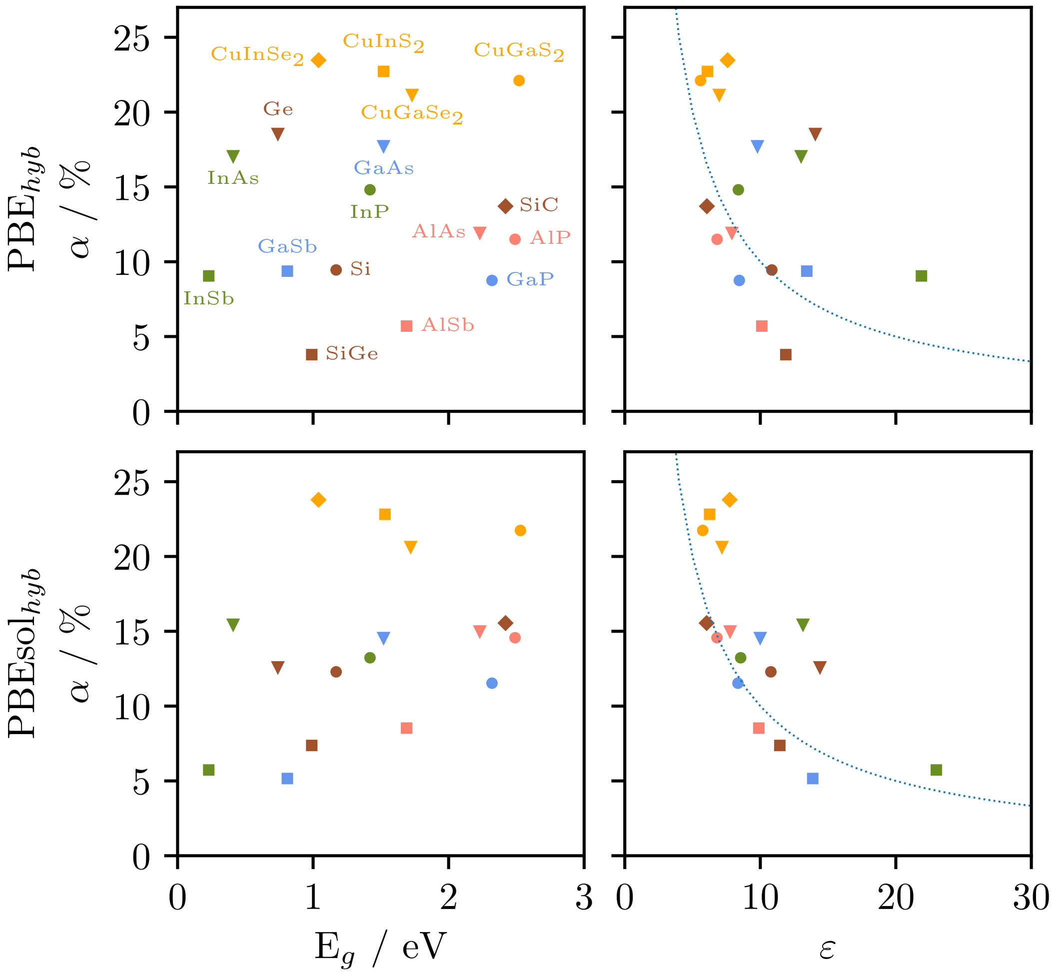

Figure 2.4 Optimal exchange mixing ratio α versus the calculated band gap (left) and dielectric constant (right) for the PBE_{hyb} (top) and PBEsol_{hyb} (bottom) functionals. The dashed curve corresponds to the inverse of the dielectric constant.

for which the value of α is dictated by the V's atoms. Phosphide-based materials are in the same range of percentage, just as arsenide-based and antimonide-based materials. This is true for both PBE and PBEsol hybrid functionals. SiGe is not in the middle of a line between Si and Ge even though its band gap is comprised between their values. In general, two materials with the same approximate band gap do not have the same optimised α. AlSb and $CuGaSe_2$ each have a band gap around 1.70 eV but their optimised exchange mixing ratio differs from more than 10% for PBEsol-based and more than 15% for PBE-based hybrid functional. On the contrary, different materials with various band gap may have practically the same optimised exchange mixing ratio. This is the case for InSb, GaSb, Si and GaP for a PBE_{hyb} optimised with 10% of exact exchange for band gaps going from 0.23 eV to 2.32 eV. Thus, there is no direct correlation between the optimised amount of exact exchange to incorporate into DFT functionals and the band gap of the material. Other parameters like the chemical nature of the compound might have an influence.

For the dielectric, our results are in accordance with equation (2.1). The global description of α by the inverse dielectric constant is well reproduced for PBEsol functional and to a lesser extent for PBE where there is more dispersion. However, even though the description of α by the inverse dielectric constant can be a first good approximation, some difference arise. As for the band gap, two materials with the same dielectric constant do not have the same optimised α. This is true for both PBE and PBEsol-based hybrids.

Comparison with the performance of the hybrid functionals optimised using Skone's method

Here, we will compare our Hamiltonians with functionals optimised with Skone's method that have been implemented in `CRYSTAL17`. Table 2.1 shows the performance of the two types of hybrid functionals on the structural, dielectric and electronic properties. The first column for each material corresponds to the percentage of exact exchange incorporated in the functional. The values of α are sensitively different for both methods in numerous cases. In Ge, for example, when our hybrids have α equal to 19 % and 13 % for PBE_{hyb} and PBEsol_{hyb}, the dielectric dependent functionals have 6 % and 4 % respectively. This leads to different calculated values for the band gap. For PBE and PBEsol-based dielectric dependent hybrid Hamiltonian, the band gap is underestimated. $\text{PBE}_{\varepsilon_\infty}$ even gives a nearly disappearing band gap (0.04 eV). The same test was made for the ternary compound and $\text{PBEsol}_{\varepsilon_\infty}$ converged, for $CuInSe_2$, to a solution with closing band gap. The hybrid functionals optimised taking into account the calculated values of the dielectric constant are not well suited for an accurate description of the band gap. The description of the dielectric constant is not better compared to the one obtained with PBE_{hyb} and PBEsol_{hyb}. The performances are globally the same, except for the band gap. Hence, our hybrids are more adapted for photovoltaic applications where the electronic properties are of most interest.

Table 2.1 Comparison of the performance of two type of self-consistent hybrid Hamiltonians in reproducing the various properties of semiconductors.

	Si				Ge				SiGe			
	α	a	ε	E_g	α	a	ε	E_g	α	a	ε	E_g
PBE$_{E_g}$	9.45	5.464	10.85	1.17	18.57	5.684	14.06	0.74	3.79	5.542	11.87	0.99
PBEsol$_{E_g}$	12.29	5.432	10.78	1.17	12.62	5.625	14.40	0.74	7.37	5.485	11.43	0.99
PBE$_{\varepsilon_\infty}$	9.1848	5.465	10.88	1.16	5.86	5.717	17.05	0.04	8.52	5.517	11.73	1.13
PBEsol$_{\varepsilon_\infty}$	9.0464	5.434	11.05	1.02	3.69	5.637	27.07	0.30	8.61	5.463	11.60	0.99
Others		5.46	11.76	0.99			15.65	0.71				
Exp.		5.430	11.4	1.17		5.652	15.36	0.74		5.537	13.95	0.99
	GaP				GaAs				GaSb			
	α	a	ε	E_g	α	a	ε	E_g	α	a	ε	E_g
PBE$_{E_g}$	8.75	5.474	8.45	2.32	17.75	5.663	9.79	1.52	9.37	6.111	13.43	0.81
PBEsol$_{E_g}$	11.53	5.418	8.35	2.32	14.58	5.606	9.99	1.52	5.16	6.045	13.87	0.81
PBE$_{\varepsilon_\infty}$	12.06	5.469	8.29	2.51	8.78	5.686	11.38	0.94	6.91	6.107	14.47	0.78
PBEsol$_{\varepsilon_\infty}$	11.99	5.418	8.34	2.34	9.23	5.613	10.83	1.18	7.37	6.032	13.57	0.97
Others												
Exp.		5.447	8.46	2.31		5.648	10.58	1.52		6.096	13.80	0.81
	InP				InAs				InSb			
	α	a	ε	E_g	α	a	ε	E_g	α	a	ε	E_g
PBE$_{E_g}$	14.81	5.931	8.38	1.42	17.08	6.110	13.01	0.41	9.05	6.516	21.89	0.23
PBEsol$_{E_g}$	13.23	5.877	8.55	1.42	15.47	6.047	13.15	0.41	5.73	6.445	22.99	0.23
PBE$_{\varepsilon_\infty}$	11.26	5.940	8.88	1.21								
PBEsol$_{\varepsilon_\infty}$	11.36	5.880	8.80	1.32								
Others												
Exp.		5.866	9.56	1.42		6.058	11.78	0.41		6.479	16.76	0.23
	AlP				AlAs				AlSb			
	α	a	ε	E_g	α	a	ε	E_g	α	a	ε	E_g
PBE$_{E_g}$	11.50	5.497	6.81	2.49	11.96	5.687	7.90	2.23	5.70	6.149	10.11	1.69
PBEsol$_{E_g}$	14.57	5.463	6.80	2.49	15.02	5.643	7.77	2.23	8.53	6.093	9.89	1.69
PBE$_{\varepsilon_\infty}$	14.90	5.491	6.71	2.67	12.62	5.689	7.92	2.26	10.20	6.151	9.80	1.88
PBEsol$_{\varepsilon_\infty}$	14.71	5.463	6.79	2.50	12.61	5.647	7.93	2.10	10.21	6.102	9.79	1.77
Others			7.23	2.37								
Exp.		5.464	9.8	2.50		5.660	8.2	2.23		6.136	9.88	1.69

Table 2.2 Calculated mean absolute relative error (MARE) in percent for each tested Hamiltonians for the structural properties (a), the bulk modulus (B), the band gap (E_g), the dielectric constant (ε), the Gamma phonon frequencies (ω), the average of all the properties (MARE$_{tot}$) and all except the band gap (MARE$_0$)).

Hamiltonian	a	B	E_g	ε	ω	MARE$_{tot}$	MARE$_0$
HF	1.05	36.95	350.80	34.76	10.92	86.90	20.92
PBE	0.52	12.09	43.00	30.6	0.39	17.32	10.90
PBE0	1.34	22.46	31.49	11.23	5.89	14.48	10.23
PBEsol	0.14	20.30	19.69	40.56	2.59	16.66	15.90
PBEsol0	0.64	33.02	52.45	15.98	7.56	21.93	14.30
LDA	0.47	18.77	41.01	14.96	4.22	15.89	9.61
B3LYP	1.22	14.36	8.19	34.30	1.37	11.89	12.81
HSE06	1.29	21.20	18.14		5.18	11.45	9.22
HSEsol	0.56	31.49	20.85		6.95	14.96	13.00
M06	1.10	18.95	18.20		3.26	10.38	7.77
M06L	1.07	16.21	55.48		1.20	18.49	6.16
HISS	1.65	28.50	29.46		8.68	17.07	12.94
PBE$_{hyb}$	0.45	20.24	2.15	3.80	3.11	5.95	6.90
PBEsol$_{hyb}$	0.40	27.47	0.26	3.69	5.29	7.42	9.21

2.1.2 Hamiltonian benchmark

Method

Once the hybrid functionals were optimised to accurately describe the experimental band gap, we tested and compared them against the other Hamiltonians from literature. Several exchange-correlation functionals were used for the comparison. The local density approximation (LDA) is represented by a Dirac-Slater exchange (Dirac, 1930) plus a Vosko-Wilk-Nusair correlation potential (Vosko *et al.*, 1980). The varieties of the GGA used were the Perdew-Burke-Ernzerhof (PBE) exchange-correlation functional (Perdew *et al.*, 1996a), and PBEsol (Perdew *et al.*, 2008). Different hybrid HF/KS functionals were also considered: three global, B3LYP (Becke, 1993a; Lee *et al.*, 1988), PBE0 (Adamo and Barone, 1999) and PBEsol0, three range-separated, HSE06 (Heyd *et al.*, 2003, 2006), HSEsol (Schimka *et al.*, 2011; Perdew *et al.*, 2008) and HISS (Henderson *et al.*, 2007, 2008), and two meta-GGA, M06 (Zhao and Truhlar, 2006) and M06L (Zhao and Truhlar, 2008). All those Hamiltonian were tested by comparing their equilibrium geometry a (Å), Gamma phonon frequency ω (cm^{-1}), elastic C_{ij} and B (GPa) as well as the dielectric properties ε_∞ and direct and indirect band gap $E_{g_{d,i}}$ (eV), with experimental data. The dielectric properties are calculated via the coupled-perturbed HF/KS which option, however, is not yet implemented for HSE06, HSEsol, M06, M06L and HISS. The tables 2.3 to 2.8 regroup the different calculated values for each material and the corresponding relative error with the experimental data are shown in the figures 2.5 to 2.11.

Results

Several patterns can be pointed out in the different tables. The first one is the direct or indirect behaviour of the band gap. For GaP, GaSb and AlAs, the calculated band gaps converge to the wrong solution for functionals such as B3LYP or M06. For the second one, as LDA and GGA underestimate the band gap, small band gap semiconductors are sometimes seen as metal by some LDA or GGA. This is the case here for Ge, InaS, InSb and $CuInSe_2$ which become metallic for several Hamiltonians. Finally, some calculated band gaps are really close to zero. This leads to an infinite dielectric constant, as for InSb with the PBEsol functional with its 0.01 eV. All these problems are linked to the electrical properties. With the optimised hybrid functionals, those types of problems disappear.

Relative error from experimental data

In order to have a general point of view of the different error with experimental data, these errors are quantified in table 2.2. In this table, the mean absolute relative error (MARE) was calculated for each family of properties. The mean value regrouping the different lattice parameters a, c and u can be found in the first column, noted a. For every functional, it has been obtained by taking the average value of the mean absolute relative value for all the material. For the structural properties, different constants are calculated. We then took the average value of

Table 2.3 Si, SiGe and Ge equilibrium lattice constant a (Å), Gamma phonon frequency ω (cm^{-1}), elastic C_{ij}, B (GPa), dielectric constant ε, and band gap, direct E_{g_d} and indirect E_{g_i} (eV) calculated with different Hamiltonians compared with experimental data.

	Hamilt.	a	ω	C_{11}	C_{12}	C_{44}	B	ϵ	E_{g_d}	E_{g_i}
Si	HF	5.513	583.	196.	62.	101.	107.	7.32	8.65	6.44
	PBE	5.477	515.	157.	59.	78.	91.	11.70	2.55	0.77
	PBE0	5.446	544.	174.	66.	85.	102.	9.82	3.84	1.88
	PBEsol	5.441	522.	162.	65.	78.	87.	11.91	2.51	0.62
	PBEsol0	5.423	548.	177.	69.	86.	105.	9.92	3.81	1.78
	LDA	5.410	527.	167.	67.	80.	100.	11.91	2.53	0.60
	B3LYP	5.498	528.	165.	54.	85.	91.	9.87	3.72	1.92
	HSE06	5.449	540.	172.	65.	85.	100.		3.29	1.31
	HSEsol	5.425	545.	176.	69.	85.	104.		3.26	1.21
	M06	5.459	539.	171.	66.	83.	102.		4.07	2.20
	M06L	5.428	542.	176.	64.	89.	102.		2.91	1.20
	HISS	5.427	558.	185.	69.	90.	107.		3.67	1.56
	PBE$_{9.45}$	5.464	527.	163.	61.	81.	95.	10.85	3.02	1.17
	PBEsol$_{12.29}$	5.432	535.	169.	67.	82.	101.	10.78	3.13	1.17
	Exp.	5.430^{a}	$520.^{\mathrm{b}}$	$168.^{\mathrm{c,d}}$	$65.^{\mathrm{c,d}}$	$80.^{\mathrm{c,d}}$	$99.^{\mathrm{c,d}}$	11.4^{e}	4.19^{f}	1.17^{g}
SiGe	HF	5.599	487.	191.	60.	100.	104.	7.58	8.12	6.45
	PBE	5.547	433.	152.	57.	76.	89.	12.34	1.88	0.85
	PBE0	5.514	458.	170.	64.	85.	99.	10.03	3.51	1.95
	PBEsol	5.489	442.	161.	65.	79.	97.	12.25	2.16	0.68
	PBEsol0	5.476	463.	176.	69.	87.	104.	10.03	3.70	1.84
	LDA	5.446	447.	168.	69.	82.	102.	12.23	2.23	0.63
	B3LYP	5.577	441.	159.	53.	83.	88.	10.59	2.57	1.96
	HSE06	5.519	454.	168.	63.	84.	98.		2.97	1.40
	HSEsol	5.480	459.	174.	68.	86.	103.		3.15	1.28
	M06	5.522	444.	161.	70.	76.	100.		2.75	1.94
	M06L	5.541	440.	159.	60.	80.	93.		2.38	1.16
	HISS	5.487	469.	182.	67.	91.	105.		3.67	1.61
	PBE$_{3.79}$	5.542	437.	155.	58.	78.	90.	11.87	2.11	0.99
	PBEsol$_{7.37}$	5.485	449.	165.	66.	81.	99.	11.43	2.59	0.99
	Exp.	5.537^{h}	$407.^{\mathrm{i}}$	$147.^{\mathrm{j}}$	$56.^{\mathrm{j}}$	$73.^{\mathrm{j}}$	$86.^{\mathrm{j}}$	13.95^{j}	2.77^{j}	0.99^{k}
Ge	HF	5.727	349.	161.	48.	91.	85.	8.91	5.30	
	PBE	5.734	300.	115.	38.	64.	64.	19.34		
	PBE0	5.669	328.	136.	44.	75.	75.	12.54	1.14	
	PBEsol	5.643	316.	126.	44.	69.	72.	93.09	0.14	
	PBEsol0	5.610	333.	144.	49.	78.	81.	12.03	1.43	
	LDA	5.581	320.	134.	49.	73.	77.	35.68	0.23	
	B3LYP	5.757	308.	121.	36.	69.	65.		0.02	
	HSE06	5.677	324.	133.	43.	74.	73.		0.74	
	HSEsol	5.617	330.	141.	48.	77.	79.		1.01	
	M06	5.681	323.	130.	60.	62.	83.		0.67	
	M06L	5.758	308.	115.	41.	62.	66.		0.06	
	HISS	5.631	335.	147.	48.	81.	81.		1.41	
	PBE$_{18.57}$	5.684	323.	131.	43.	73.	72.	14.06	0.74	
	PBEsol$_{12.62}$	5.625	325.	135.	47.	74.	76.	14.40	0.74	
	Exp.	5.652^{l}	$301.^{\mathrm{m,n}}$	$131.^{\mathrm{o}}$	$49.^{\mathrm{o,p}}$	$68.^{\mathrm{o}}$	$76.^{\mathrm{o,p}}$	15.36^{q}	0.74^{r}	

[a]Staroverov *et al.* (2004), [b]Parker *et al.* (1967), [c]Hall (1967), [d]McSkimin and Andreatch (1972), [e]Faulkner (1969), [f]Aspnes and Studna (1972), [g]Bludau *et al.* (1974), [h]Dismukes *et al.* (1964), [i]Alonso and Winer (1989), [j]Levinshtein *et al.* (2001), [k]Weber and Alonso (1989), [l]Staroverov *et al.* (2004), [m]Parker *et al.* (1967), [n]Olego and Cardona (1982), [o]Fine (1955), [p]McSkimin and Andreatch (1972), [q]Faulkner (1969), [r]Kittel (2004)

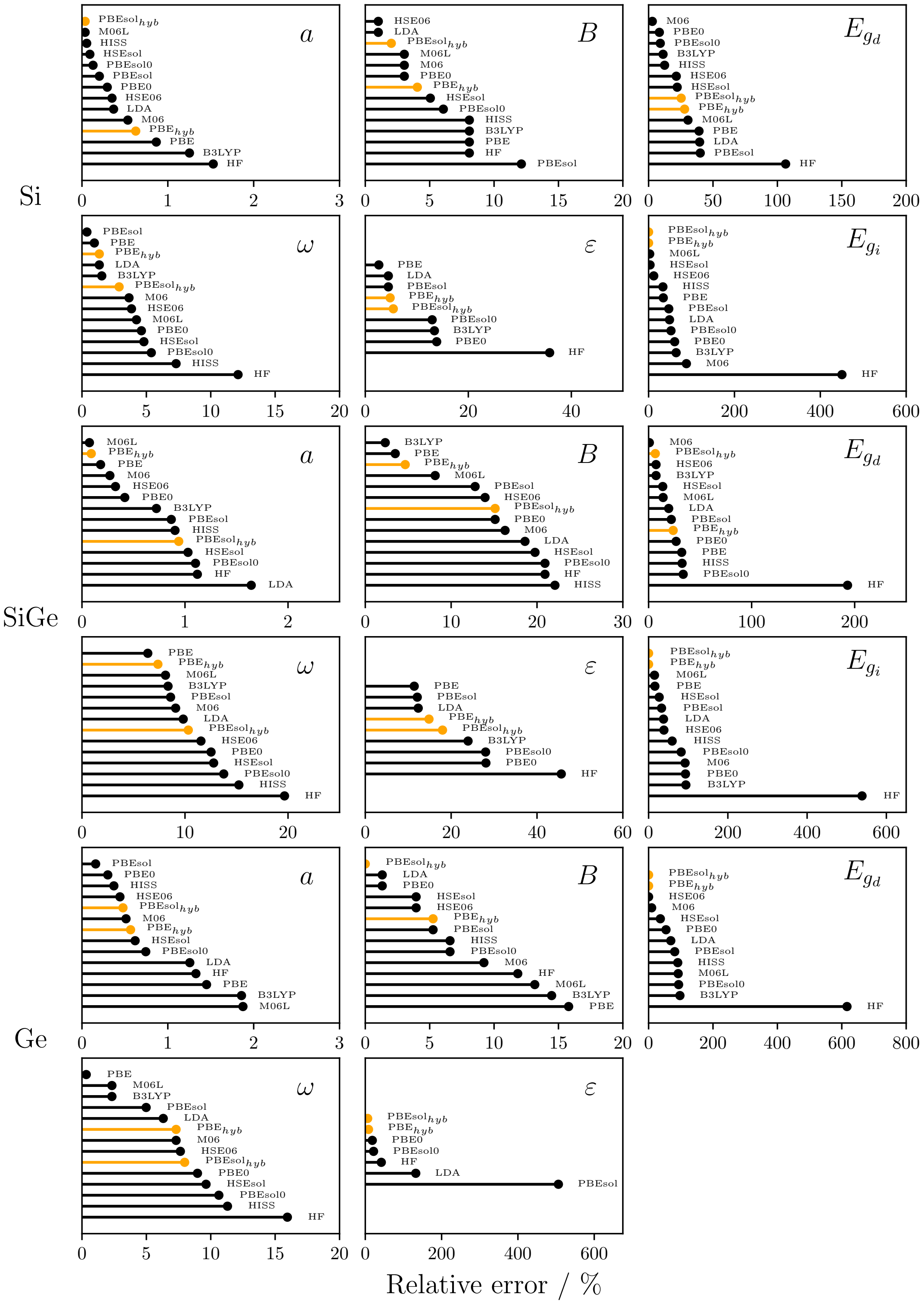

Figure 2.5 Absolute value of the relative error between calculated and experimental properties of Si, SiGe and Ge for each Hamiltonian. Hybrid functionals optimised for the material are displayed in orange.

Table 2.4 GaP, GaAs and GaSb equilibrium lattice constant a (Å), Gamma phonon frequency ω (cm^{-1}), elastic C_{ij}, B (GPa), dielectric constant ε, and band gap, direct E_{g_d} and indirect E_{g_i} (eV) calculated with different Hamiltonians compared with experimental data.

	Hamilt.	a	ω	C_{11}	C_{12}	C_{44}	B	ϵ	E_{g_d}	E_{g_i}
GaP	HF	5.536	392.	167.	66.	85.	100.	5.79	8.56	7.83
	PBE	5.488	362.	132.	60.	64.	84.	9.10	1.94	1.83
	PBE0	5.452	382.	149.	68.	72.	95.	7.58	3.59	3.19
	PBEsol	5.425	374.	141.	68.	66.	92.	9.16	2.12	1.75
	PBEsol0	5.411	389.	155.	73.	73.	100.	7.66	3.69	3.03
	LDA	5.379	381.	149.	72.	69.	97.	9.24	2.17	1.67
	B3LYP	5.519	365.	138.	56.	70.	84.	7.99	2.79	
	HSE06	5.457	380.	148.	67.	71.	94.		3.02	2.59
	HSEsol	5.415	387.	154.	72.	73.	99.		3.13	2.43
	M06	5.471	363.	142.	66.	66.	91.		2.88	
	M06L	5.467	365.	143.	68.	69.	91.		2.68	2.36
	HISS	5.423	392.	161.	73.	77.	102.		3.76	2.84
	PBE$_{8.75}$	5.474	370.	139.	63.	67.	88.	8.45	2.49	2.32
	PBEsol$_{11.53}$	5.418	382.	148.	70.	70.	96.	8.35	2.82	2.32
	Exp.	5.447[a,b]	367.[c,d]	144.[e]	65.[e]	71.[e]	91.[e]	8.46[f]	2.87[g]	2.31[h]
			366.[i]	141.[j]	63.[j]	70.[j]	89.[j]			
GaAs	HF	5.716	289.	141.	55.	76.	83.	6.56	6.73	
	PBE	5.709	263.	105.	44.	56.	64.	13.69	0.48	
	PBE0	5.647	280.	124.	54.	65.	77.	9.14	2.00	
	PBEsol	5.625	275.	115.	53.	59.	73.	12.26	0.72	
	PBEsol0	5.594	287.	131.	59.	67.	83.	9.09	2.16	
	LDA	5.567	282.	123.	58.	63.	79.	12.30	0.74	
	B3LYP	5.734	265.	111.	43.	60.	65.	10.39	1.10	
	HSE06	5.655	278.	121.	52.	64.	75.		1.54	
	HSEsol	5.600	285.	129.	58.	66.	81.		1.69	
	M06	5.670	273.	121.	55.	61.	77.		1.64	
	M06L	5.705	263.	110.	47.	59.	67.		1.10	
	HISS	5.612	287.	134.	58.	70.	83.		2.22	
	PBE$_{17.75}$	5.663	275.	118.	51.	62.	73.	9.79	1.52	
	PBEsol$_{14.58}$	5.606	282.	124.	56.	64.	79.	9.99	1.52	
	Exp.	5.648[k]	273.[l,m]	123.[n]	57.[n]	60.[n]	79.[n]	10.58[o]	1.52[p]	
				121.[q]	55.[q]	60.[q]	77.[q]	10.92[r]		
GaSb	HF	6.141	265.	125.	49.	60.	75.	7.69	6.19	5.92
	PBE	6.136	238.	92.	42.	43.	58.	19.11	0.34	
	PBE0	6.073	253.	107.	48.	49.	68.	11.00	1.75	
	PBEsol	6.052	246.	99.	47.	45.	65.	15.49	0.57	
	PBEsol0	6.018	259.	112.	52.	51.	72.	10.91	1.90	1.80
	LDA	5.996	251.	104.	51.	47.	69.	15.63	0.58	
	B3LYP	6.164	240.	96.	40.	47.	59.	12.83	0.81	
	HSE06	6.083	251.	105.	47.	49.	66.		1.32	1.31
	HSEsol	6.026	256.	110.	51.	50.	71.		1.48	1.33
	M06	6.113	250.	100.	51.	43.	67.		1.31	
	M06L	6.155	240.	95.	43.	44.	60.		0.78	
	HISS	6.037	260.	115.	51.	53.	72.		1.67	
	PBE$_{9.37}$	6.111	244.	98.	44.	45.	62.	13.43	0.81	
	PBEsol$_{5.16}$	6.045	249.	102.	48.	46.	66.	13.87	0.81	
	Exp.	6.096[s]	231.[t]	91.[u]	41.[u]	44.[u]	58.[u]	13.80[t]	0.809[v]	
			227.[w]						0.813[x]	

[a]Deus *et al.* (1983b), [b]Reeber and Wang (1995), [c]Krishnan and Krishnamurthy (1965), [d]Tiginyanu (1999), [e]Boyle and Sladek (1975), [f]Barker (1968), [g]Vurgaftman *et al.* (2001), [h]Lorenz *et al.* (1968), [i]Mooradian and Wright (1966), [j]Weil and Groves (1968), [k]Staroverov *et al.* (2004), [l]Mooradian and Wright (1966), [m]Hass and Henvis (1962), [n]Garland and Park (1962), [o]Moore and Holm (1996), [p]Sturge (1962), [q]Cottam and Saunders (1973), [r]Rode (1970), [s]Straumanis and Kim (1965), [t]Rode (1970), [u]Boyle and Sladek (1975), [v]Muñoz *et al.* (2000), [w]Sekine *et al.* (1976), [x]Wu and Chen (1992)

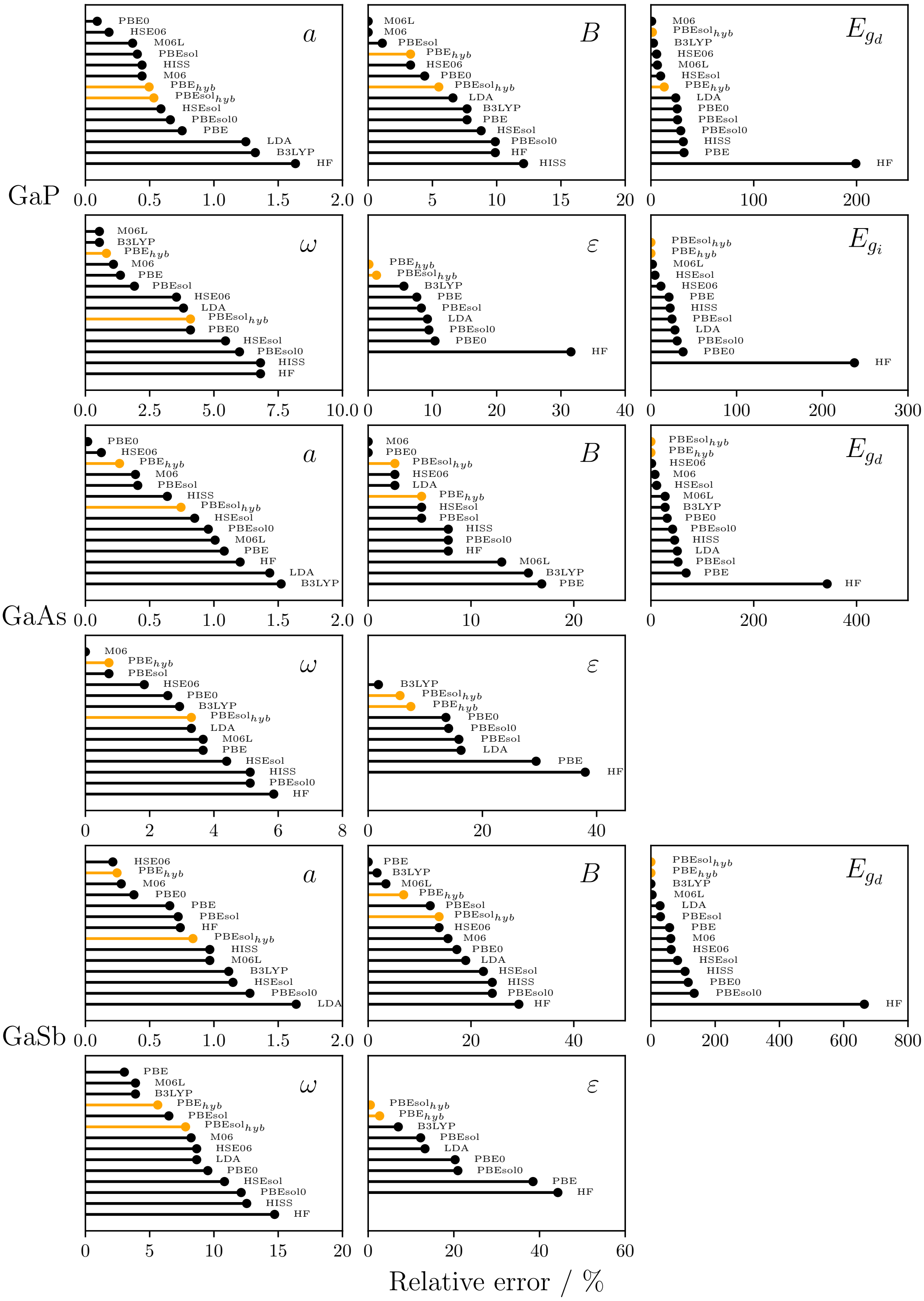

Figure 2.6 Absolute value of the relative error between calculated and experimental properties of GaP, GaAs and GaSb for each Hamiltonian.Hybrid functionals optimised for the material are displayed in orange.

Table 2.5 InP, InAs and InSb equilibrium lattice constant a (Å), Gamma phonon frequency ω (cm^{-1}), elastic C_{ij}, B (GPa), dielectric constant ε, and band gap, direct E_{g_d} and indirect E_{g_i} (eV) calculated with different Hamiltonians compared with experimental data.

	Hamilt.	a	ω	C_{11}	C_{12}	C_{44}	B	ϵ	E_{g_d}
InP	HF	5.974	327.	126.	61.	61.	83.	10.41	6.70
	PBEXC	5.971	297.	93.	48.	44.	63.	7.67	0.61
	PBE0	5.910	316.	109.	58.	50.	75.	10.16	2.08
	PBESOLXC	5.897	309.	100.	55.	45.	70.	7.74	0.72
	PBESOL0	5.864	324.	114.	62.	51.	79.	10.32	2.11
	SVWN	5.851	315.	105.	59.	47.	74.	8.49	0.70
	B3LYP	5.995	300.	98.	48.	48.	64.	8.57	1.32
	HSE06	5.915	315.	107.	57.	50.	73.		1.54
	HSESOL	5.869	322.	112.	61.	50.	78.		1.59
	M06	5.941	306.	103.	57.	44.	72.		1.55
	M06L	5.957	289.	97.	53.	44.	69.		1.25
	HISS	5.874	326.	118.	62.	54.	81.		2.13
	PBE$_{14.81}$	5.931	309.	102.	54.	48.	70.	8.38	1.42
	PBEsol$_{13.23}$	5.877	317.	108.	59.	49.	75.	8.55	1.42
	Exp.	5.866[a]	308.[b]	102.[c]	58.[c]	46.[c,d]	73.[c]	9.56[e]	1.42[f,g]
				101.[d]	56.[d]		71.[d]		
InAs	HF	6.136	226.	108.	52.	55.	69.	6.24	5.47
	PBEXC	6.171	204.	75.	39.	36.	50.	15.29	
	PBE0	6.087	222.	91.	48.	43.	61.	9.83	0.88
	PBESOLXC	6.077	214.	83.	46.	38.	57.	14.39	
	PBESOL0	6.030	228.	97.	53.	45.	66.	9.72	0.94
	SVWN	6.020	220.	89.	50.	40.	62.	14.67	
	B3LYP	6.186	210.	81.	38.	41.	51.	97.39	0.10
	HSE06	6.096	220.	89.	47.	42.	60.		0.46
	HSESOL	6.038	227.	95.	51.	44.	65.		0.52
	M06	6.133	220.	88.	46.	40.	59.		0.55
	M06L	6.198	201.	75.	40.	36.	50.		
	HISS	6.047	228.	99.	52.	47.	66.		0.99
	PBE$_{17.08}$	6.110	217.	86.	45.	41.	58.	13.01	0.41
	PBEsol$_{15.47}$	6.047	224.	92.	50.	42.	63.	13.15	0.41
	Exp.	6.058[h]	220.[i]	90.[j]	50.[j]	39.[j]	63.[j]	11.78[k]	0.41[l]
				83.[m]	45.[m]	40.[m]			
InSb	HF	6.524	211.	102.	47.	47.	63.	7.20	5.39
	PBEXC	6.548	186.	71.	37.	31.	47.	16.42	
	PBE0	6.468	202.	85.	44.	37.	56.	10.87	1.08
	PBESOLXC	6.457	194.	77.	42.	33.	52.		0.01
	PBESOL0	6.410	206.	89.	47.	38.	60.	10.77	1.19
	SVWN	6.402	197.	81.	44.	34.	56.	15.92	
	B3LYP	6.571	191.	76.	36.	35.	48.	17.35	0.29
	HSE06	6.478	200.	83.	43.	36.	55.		0.71
	HSESOL	6.418	205.	88.	46.	37.	58.		0.81
	M06	6.544	200.	77.	43.	31.	53.		0.61
	M06L	6.590	189.	72.	38.	31.	48.		0.14
	HISS	6.426	207.	92.	47.	40.	60.		1.22
	PBE$_{9.05}$	6.516	194.	77.	40.	33.	50.	21.89	0.23
	PBEsol$_{5.73}$	6.445	199.	80.	43.	34.	54.	22.99	0.23
	Exp.	6.479[n]	182.[o]	67.[p]	34.[p]	31.[p,q]	45.[p]	16.76[r]	0.23[s]
				69.[q]	38.[q]				

[a] Reeber and Wang (1995), [b] Mooradian and Wright (1966), [c] Hickernell and Gayton (1966), [d] Nichols *et al.* (1980), [e] Rode (1970), [f] Pavesi *et al.* (1991), [g] Varshni (1967) [h] Ioffe Institute (2019), [i] Carles *et al.* (1980), [j] Gerlich (1964), [k] Rode (1970), [l] Fang *et al.* (1990), [m] Gerlich (1963) [n] Straumanis and Kim (1965), [o] Kiefer *et al.* (1975), [p] Potter (1956), [q] Slutsky and Garland (1959), [r] Rode (1970), [s] Zollner *et al.* (1991)

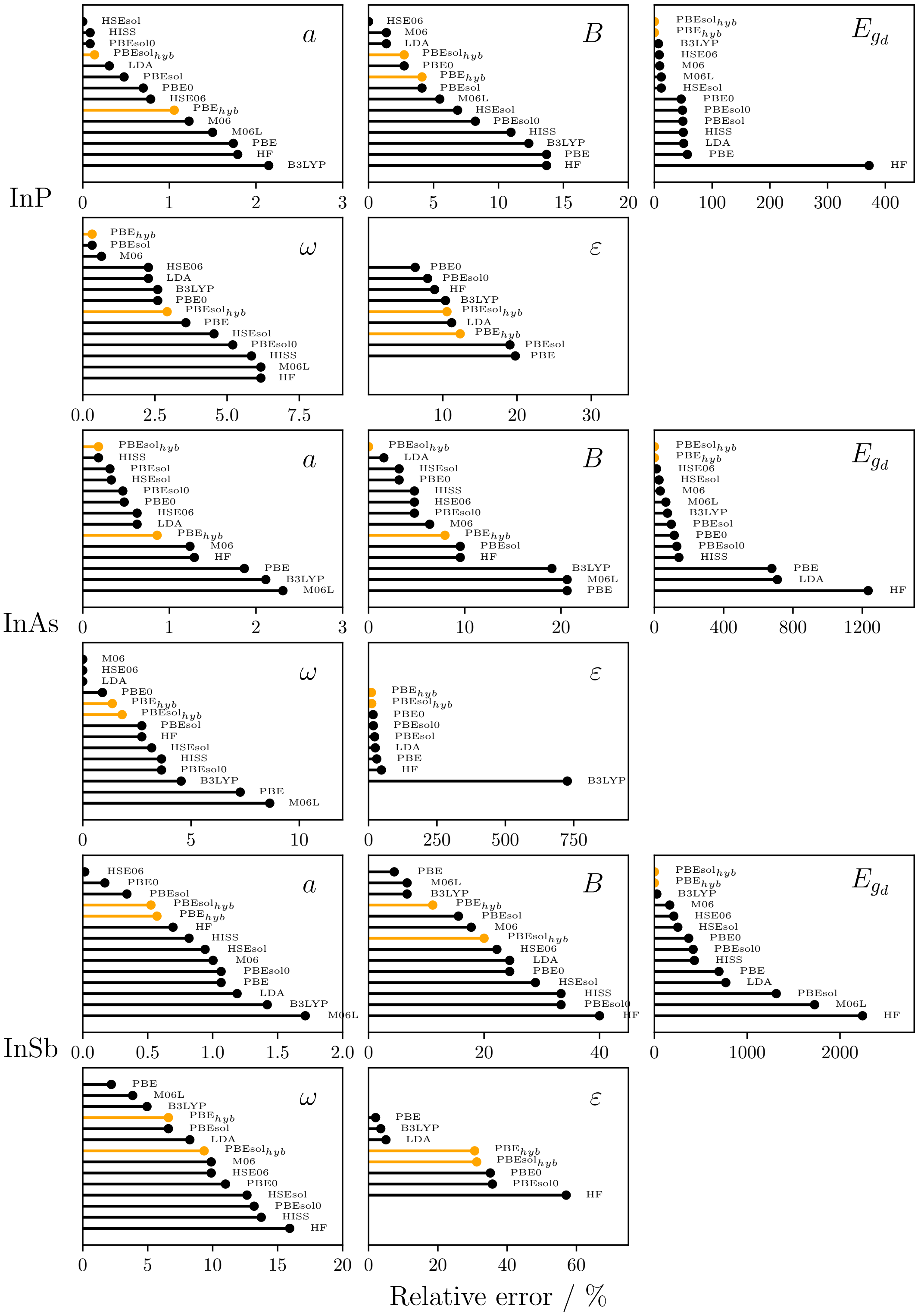

Figure 2.7 Absolute value of the relative error between calculated and experimental properties of InP, InAs and InSb for each Hamiltonian. Hybrid functionals optimised for the material are displayed in orange.

Table 2.6 AlP, AlAs and AlSb equilibrium lattice constant a (Å), Gamma phonon frequency ω (cm^{-1}), elastic C_{ij}, B (GPa), dielectric constant ε, and band gap, direct E_{g_d} and indirect E_{g_i} (eV) calculated with different Hamiltonians compared with experimental data.

	Hamilt.	a	ω	C_{11}	C_{12}	C_{44}	B	ϵ	E_{g_d}	E_{g_i}
AlP	HF	5.540	474.	162.	68.	83.	99.	5.07	10.30	8.10
	PBEXC	5.513	440.	129.	62.	62.	84.	7.26	3.19	1.91
	PBE0	5.479	459.	143.	69.	68.	93.	6.38	4.90	3.20
	PBESOLXC	5.476	448.	132.	67.	61.	88.	7.41	3.25	1.72
	PBESOL0	5.455	463.	145.	72.	67.	96.	6.46	4.91	3.07
	SVWN	5.440	453.	137.	69.	63.	92.	7.43	3.32	1.68
	B3LYP	5.529	444.	138.	60.	69.	86.	6.40	4.46	3.23
	HSE06	5.482	457.	142.	68.	67.	92.		4.28	2.58
	HSESOL	5.457	462.	144.	71.	67.	95.		4.31	2.44
	M06	5.489	429.	138.	67.	64.	90.		4.46	3.26
	M06L	5.456	452.	145.	71.	69.	95.		4.20	2.30
	HISS	5.459	470.	151.	72.	72.	99.		4.97	2.88
	$\text{PBE}_{11.50}$	5.497	449.	136.	65.	64.	89.	6.81	3.91	2.49
	$\text{PBEsol}_{14.57}$	5.463	457.	140.	70.	64.	93.	6.80	4.14	2.49
	Exp.	5.464[a]	440.[b]	133.[c]	63.[c]	62.[c]	86.[c]	7.54[d]	3.6[e]	2.50[f]
										2.52[g]
AlAs	HF	5.710	380.	142.	58.	75.	86.	5.49	8.48	7.48
	PBEXC	5.714	355.	109.	50.	54.	69.	8.66	1.83	1.68
	PBE0	5.663	372.	123.	57.	61.	79.	7.30	3.44	2.87
	PBESOLXC	5.661	363.	113.	55.	55.	74.	8.69	1.95	1.50
	PBESOL0	5.631	377.	126.	61.	61.	82.	7.32	3.51	2.74
	SVWN	5.616	369.	118.	58.	57.	78.	8.68	2.00	1.47
	B3LYP	5.720	358.	117.	48.	62.	71.	7.42	2.86	
	HSE06	5.668	370.	122.	57.	61.	78.		2.89	2.28
	HSESOL	5.635	376.	125.	60.	61.	81.		2.96	2.15
	M06	5.673	361.	122.	56.	60.	77.		3.25	3.06
	M06L	5.674	362.	118.	54.	60.	75.		2.55	1.92
	HISS	5.637	380.	131.	61.	65.	84.		3.55	2.52
	$\text{PBE}_{11.96}$	5.687	363.	116.	53.	58.	74.	7.90	2.45	2.23
	$\text{PBEsol}_{15.02}$	5.643	372.	121.	59.	59.	79.	7.77	2.77	2.23
	Exp.	5.660[h]	360.[i]	120.[j]	57.[j]	59.[j]	78.[j]	8.2[k]	3.13[l]	2.23[m]
AlSb	HF	6.166	367.	123.	50.	58.	72.	6.55	7.90	6.67
	PBEXC	6.162	333.	93.	43.	41.	58.	10.67	1.71	1.46
	PBE0	6.109	350.	105.	48.	46.	66.	8.79	3.21	2.52
	PBESOLXC	6.105	340.	96.	47.	41.	62.	10.67	1.86	1.33
	PBESOL0	6.072	354.	107.	51.	46.	68.	8.80	3.31	2.43
	SVWN	6.061	343.	99.	49.	42.	64.	10.66	1.89	1.30
	B3LYP	6.177	337.	99.	42.	46.	59.	9.01	2.57	2.39
	HSE06	6.115	348.	104.	48.	46.	65.		2.70	1.97
	HSESOL	6.077	352.	106.	50.	45.	68.		2.80	1.88
	M06	6.130	342.	100.	50.	41.	65.		2.78	2.40
	M06L	6.138	340.	99.	46.	44.	62.		2.23	1.60
	HISS	6.079	358.	111.	51.	49.	70.		3.31	2.17
	$\text{PBE}_{5.70}$	6.149	338.	96.	44.	42.	60.	10.11	1.97	1.69
	$\text{PBEsol}_{8.53}$	6.093	345.	100.	48.	43.	64.	9.89	2.27	1.69
	Exp.	6.136[n]	318.[o]	89.[p]	44.[p]	41.[p]	59.[p]	9.88[q]	2.21[r]	1.69[s]

[a] Singh (1992), [b] Beer *et al.* (1968), [c] Vurgaftman *et al.* (2001), [d] Yu and Cardona (2010), [e] Yu and Cardona (2010), [f] Monemar (1973), [g] Lorenz *et al.* (1970) [h] Singh (1992), [i] Azuhata *et al.* (1995), [j] Adachi (1985), [k] Lockwood *et al.* (2005), [l] Yu and Cardona (2010), [m] Monemar (1973) [n] Singh (1992), [o] Isaenko *et al.* (2003), [p] Bolef and Menes (1960), [q] Lockwood *et al.* (2005), [r] Cardona *et al.* (1966), [s] Palmer (2019)

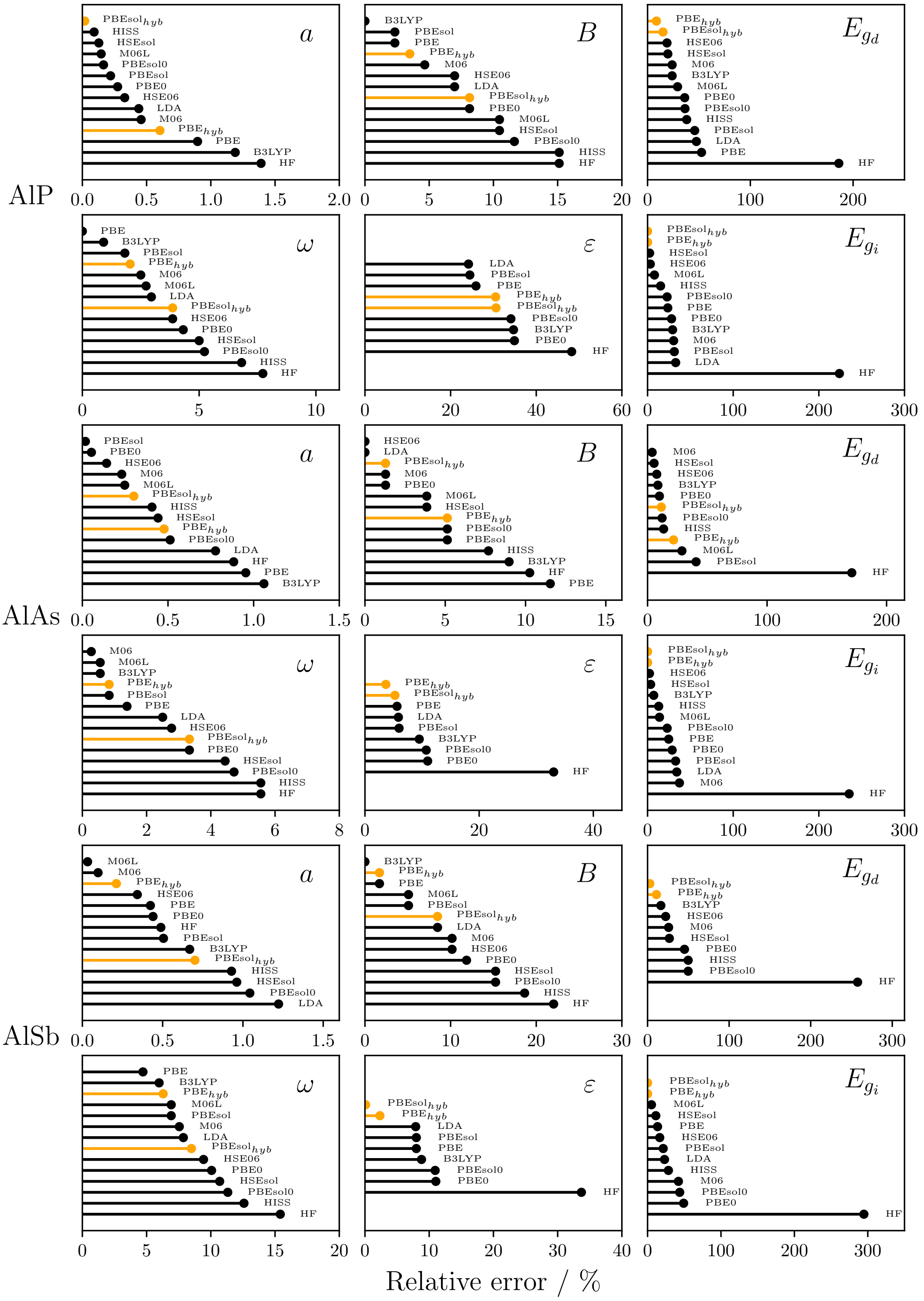

Figure 2.8 Absolute value of the relative error between calculated and experimental properties of AlP, AlAs and AlSb for each Hamiltonian.Hybrid functionals optimised for the material are displayed in orange.

this different properties and defined a global error for the structural parameters. The same procedure have been done for the other properties. Thus, we found the bulk modulus, the electrical properties corresponding to the average error for direct and indirect band gap, the dielectric properties which regroup the dielectric constant and the vibrational frequencies. Even though all this properties are not directly comparable, we summed their relative errors with experiments to have a global point of view of the functional's performances. As the hybrid functional developed in this work correctly reproduced the experimental band gap, the relative error for the electronic properties only comes from the divergence between the calculated and experimental values of the direct band gap of indirect-band gap semiconductors. This error is then extremely small compared to the other functionals from literature. We then define the measure of two distinct global errors for every Hamiltonian. The first one, called MARE_{tot}, is the average error throughout all properties. The second one, called MARE_0, is the same as MARE_{tot} without the contribution of the electronic properties' error.

As expected, the Hartree-Fock Hamiltonian leads to an overestimation of the band gap (350%) when LDA and GGA functionals underestimate its value, giving 40% and 43% respectively. PBE_{hyb} and PBEsol_{hyb} obviously give the best results for the band gap. B3LYP was created for organic molecular systems with covalent bonds. The high number of covalent materials among our test cases explains therefore that the mean B3LYP energy is low. However, B3LYP wrongly predicts the band gap to be direct for GaP and AlAs. PBEsol, HSe06 and M06 are the other functionals that lead to the lowest MARE, around 19%. When looking at the structural properties, PBE and PBEsol functionals have the lowest MARE. This is why the MARE of PBE_{hyb} and PBEsol_{hyb} is better than the majority of the other functionals with only 0.5 %. This is not the case for the precision in the bulk modulus calculation where PBE_{hyb} is in the average error of the other functionals and PBEsol_{hyb} is among those with the highest error. Just as for the lattice parameters, PBE gives the lowest MARE. Nonetheless, these results are less significant because of the experimental precision of the bulk modulus that is often of the order of several tens of percent. The dielectric properties calculated with PBE_{hyb} and PBEsol_{hyb} are very close to the experimental data with less than a 5% error. The other functionals tested give results from 10% to more than 30% for PBEsol. This comparison is not complete as the coupled-perturbed Kohn-Sham/Hartree-Fock (CPKS/HF) method is not implemented for several functionals used here. Finally, the last properties studied were the Gamma vibration frequencies of the crystal. Once again, PBE has the smallest MARE which is 0.39%. All the MARE are less or equal to 10%. In this context, the two optimised hybrid functionals do not give significant result compared to the other functionals with 3% and 5% for PBE_{hyb} and PBEsol_{hyb} respectively. The penultimate column is the average value for all the properties of each functional. Thanks to their performance for the calculation of the band gap, PBE_{hyb} and PBEsol_{hyb} give the lowest relative error. However, if we exclude the electronic properties of the mean values as in the last colum (MARE_0), these two optimised hybrid functionals are still the most accurate ones included in the tests, with relative errors of 6% and 9% just as LDA, HSE06 and the M06 functionals.

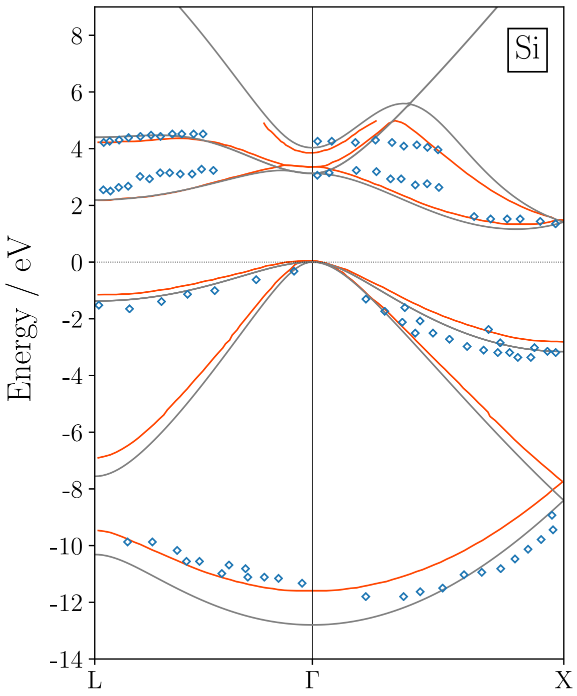

Figure 2.9 Comparison of the electronic structure computed via the PBEsol$_{hyb}$ (grey) and the *GW* calculation (red) of Rohlfing *et al.* (1993) for silicon compared to experimental data by Ortega and Himpsel (1993).

Chalcopyrite optimised hybrids

In the case of chalcopyrite, one optimised hybrid functional for every compound is not very well suited if we want to compare results throughout systems. For example, in chapter 3, alkali metals will be incorporated in the chalcopyrite for each ternary compound. We then created an optimised hybrid for the whole family by minimising the global relative error for the structural, dielectric and electrical properties of the materials. The lattice parameter, the dielectric constant and the band gap were computed for different values of α and then compared to experimental data. The performance of these hybrid functionals can be found in tables 2.7 to 2.8. The first observation is that the four ternary compounds are relatively close in term of percentage of optimised exact exchange, both for PBE$_{hyb}$ and PBEsol$_{hyb}$ as it has been seen in figure 2.4. This leads to a relatively small discrepancy between the material-optimised hybrid functionals and the one created for the family. Thus, the performances of both cases are quite similar.
Therefore, hybrid functionals which were optimised to correctly describe the experimental band gap and other main properties of materials with low mean absolute relative error compared to the Hamiltonians from literature.

2.1.3 Comparison of electronic structures from hybrid functional and from GW calculations

We just saw that the optimised hybrid functionals correctly described various types of properties for the studied semiconductors. By the procedure of tuning,

Table 2.7 Equilibrium geometry (a, b, c/a and u in Å), bulk modulus (B in GPa), band gap (E_g in eV) and dielectric properties (ε_∞^a, ε_∞^c and $\overline{\varepsilon_\infty}$) of $CuGaS_2$ and $CuGaSe_2$, calculated with different Hamiltonians and compared with experimental data.

	Hamiltonian	a	b	c/a	u	B	E_g	ε_∞^a	ε_∞^c	$\overline{\varepsilon_\infty}$
$CuGaS_2$	PBE	5.412	10.736	1.984	0.247	80.	0.61	8.06	8.12	8.08
	PBESOL	5.325	10.605	1.992	0.244	92.	0.74	8.00	8.04	8.02
	PBE0	5.403	10.609	1.963	0.254	84.	2.79	5.45	5.42	5.44
	PBESOL0	5.339	10.530	1.972	0.251	93.	2.82	5.58	5.56	5.58
	LDA	5.268	10.505	1.994	0.243	101.	0.80	8.03	8.05	8.04
	B3LYP	5.481	10.766	1.964	0.255	75.	2.10	5.69	5.67	5.68
	HSE06	5.406	10.619	1.964	0.254	84.	2.17			
	HSESOL	5.341	10.538	1.963	0.251	93.	2.21			
	HISS	5.397	10.553	1.955	0.251	86.	3.03			
	M06	5.404	10.619	1.964	0.254	90.	2.62			
	M06L	5.428	10.647	1.961	0.253	84.	1.10			
	$PBE_{22.11}$	5.403	10.622	1.966	0.253	84.	2.52	5.60	5.57	5.59
	$PBE_{22.46}$	5.403	10.622	1.966	0.255	84.	2.55	5.58	5.55	5.57
	$PBEsol_{21.74}$	5.335	10.539	1.975	0.250	93.	2.53	5.76	5.74	5.75
	$PBEsol_{22.63}$	5.336	10.540	1.975	0.251	93.	2.61	5.71	5.69	5.70
	Exp.	5.349^{a}	10.470^{a}	$1.958^{a,b}$	0.25^{a}	$94.^{c}$	2.53	6.1^{d}	6.2^{d}	6.17^{d}
		5.356^{b}	10.444^{b}		0.28^{b}	$96.^{e}$				
		5.347^{f}	10.474^{f}			$97.^{g}$				
$CuGaSe_2$	PBE	5.652	11.295	1.998	0.241	70.	0.15	12.79	16.17	13.92
	PBESOL	5.560	11.128	2.001	0.239	80.	0.25	11.62	12.42	11.89
	PBE0	5.636	11.140	1.977	0.249	75.	2.05	6.64	6.68	6.65
	PBESOL0	5.567	11.040	1.983	0.246	82.	2.07	6.79	6.83	6.80
	LDA	5.500	11.025	2.004	0.238	88.	0.08	12.02	12.91	12.32
	B3LYP	5.720	11.314	1.978	0.249	66.	1.38	7.16	7.24	7.19
	HSE06	5.638	11.154	1.978	0.248	74.	1.51			
	HSESOL	5.570	11.051	1.984	0.246	82.	1.54			
	HISS	5.628	11.074	1.967	0.251	76.	2.25			
	M06	5.624	11.148	1.982	0.248	82.	1.96			
	M06L	5.682	11.263	1.982	0.247	73.	0.62			
	$PBE_{21.18}$	5.637	11.160	1.980	0.248	74.	1.73	6.96	7.00	6.97
	$PBE_{22.46}$	5.637	11.153	1.979	0.248	74.	1.83	6.85	6.89	6.86
	$PBEsol_{20.66}$	5.565	11.051	1.986	0.245	83.	1.72	7.16	7.19	7.17
	$PBEsol_{22.63}$	5.567	11.047	1.984	0.246	83.	1.87	6.99	7.02	7.00
	Exp.	5.607^{h}	10.99^{h}	1.960^{h}	0.25^{h}	$71.^{i}$	1.73^{j}	6.8^{k}	6.6^{k}	6.7^{k}
		5.614^{l}	11.03^{l}	1.965^{l}	0.250^{l}					
		5.604^{m}	11.089^{m}							

[a] Hahn *et al.* (1953), [b] Spiess *et al.* (1974), [c] Bettini and Holzapfel (1975), [d] Baars and Koschel (1972), [e] Werner *et al.* (1981), [f] Abrahams and Bernstein (1974), [g] Tinoco *et al.* (1994), [h] Hahn *et al.* (1953), [i] Kraft *et al.* (1983), [j], [k] Márquez and Rincón (1995), [l] Spiess *et al.* (1974), [m] Rincón and Ramírez (1992)

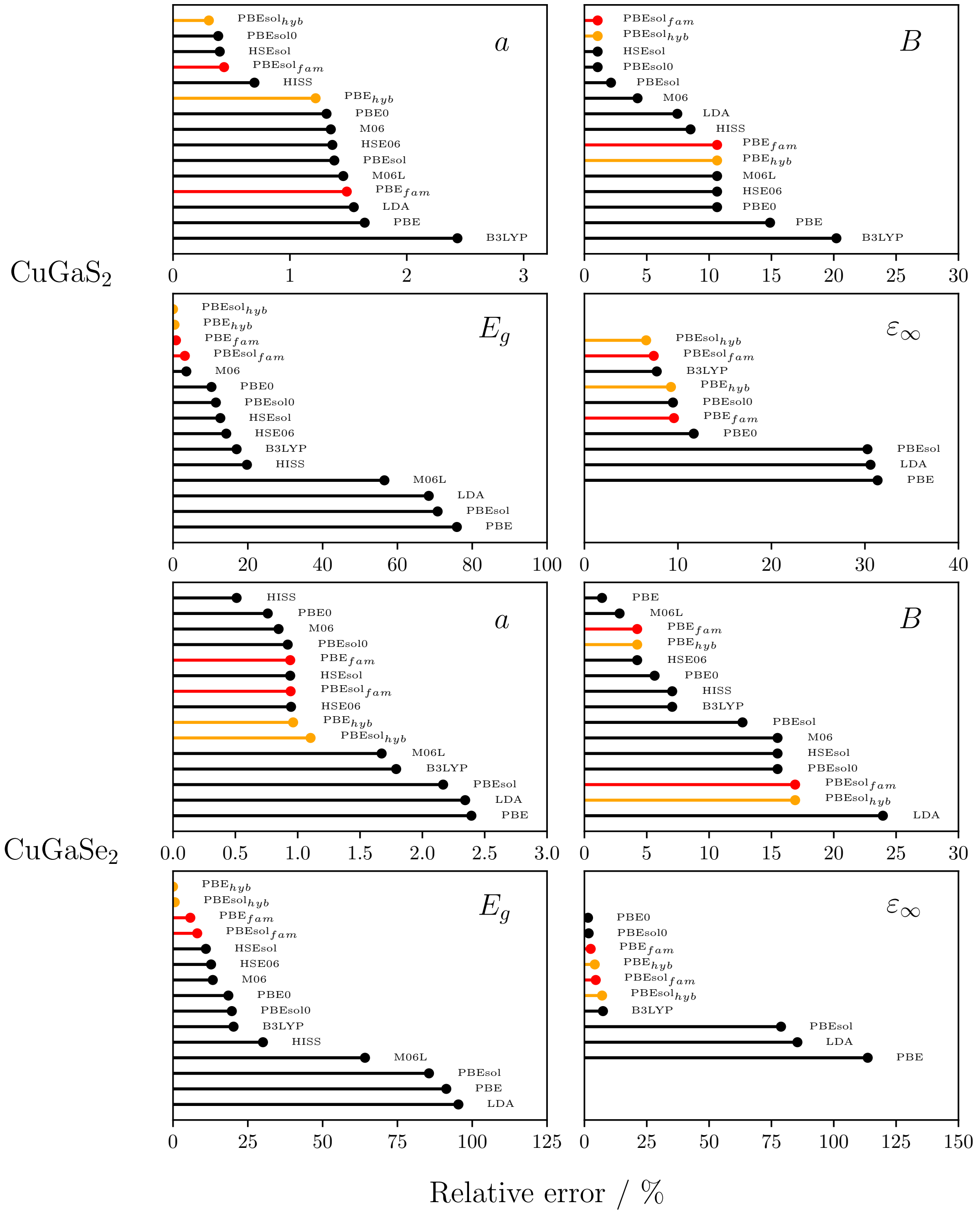

Figure 2.10 Absolute value of the relative error between calculated and experimental properties of CuGaS$_2$ and CuGaSe$_2$ for each Hamiltonian. Hybrid functionals optimised for the material are displayed in orange and the one optimised for the chalcopyrite family in red.

Table 2.8 Equilibrium geometry (a, b, c/a and u in Å), bulk modulus (B in GPa), band gap (E_g in eV) and dielectric properties (ε_∞^a, ε_∞^c and $\overline{\varepsilon_\infty}$) of CuInS$_2$ and CuInSe$_2$, calculated with different Hamiltonians and compared with experimental data.

	Hamiltonian	a	b	c/a	u	B	E_g	ε_∞^a	ε_∞^c	$\overline{\varepsilon_\infty}$
CuInS$_2$	PBE	5.614	11.325	2.017	0.218	66.	0.03	16.99	17.48	17.15
	PBESOL	5.525	11.142	2.016	0.216	77.	0.02	16.20	16.64	16.35
	PBE0	5.576	11.250	2.018	0.228	71.	1.73	5.92	5.86	5.90
	PBESOL0	5.512	11.131	2.019	0.225	80.	1.72	6.09	6.00	6.07
	LDA	5.469	11.018	2.015	0.214	85.	0.01	27.65	17.47	24.26
	B3LYP	5.674	11.392	2.008	0.229	62.	1.14	6.49	6.38	6.45
	HSE06	5.583	11.249	2.015	0.228	71.	1.14			
	HSESOL	5.517	11.134	2.018	0.225	79.	1.14			
	HISS	5.563	11.200	2.013	0.232	73.	1.90			
	M06	5.587	11.267	2.017	0.227	77.	1.59			
	M06L	5.616	11.336	2.018	0.224	70.	0.07			
	PBE$_{22.72}$	5.580	11.245	2.015	0.228	71.	1.52	6.13	6.04	6.10
	PBE$_{22.46}$	5.580	11.245	2.015	0.228	71.	1.50	6.15	6.06	6.12
	PBEsol$_{22.82}$	5.512	11.131	2.019	0.225	80.	1.53	6.29	6.19	6.26
	PBEsol$_{22.63}$	5.512	11.131	2.019	0.225	80.	1.52	6.31	6.20	6.28
	Exp.	5.517^{a}	11.06^{a}	2.005^{a}	0.20^{a}	$75.^{b}$	1.53	6.0^{d}	6.2^{d}	6.1^{d}
		5.523^{e}	11.12^{e}	2.013^{e}	0.214^{e}					
		5.523^{f}	11.133^{f}							
CuInSe$_2$	PBE	5.877	11.819	2.011	0.214	56.	0.01	31.42	21.04	27.96
	PBESOL	5.775	11.628	2.013	0.212	66.				
	PBE0	5.832	11.709	2.008	0.223	62.	1.16	7.41	7.29	7.37
	PBESOL0	5.759	11.586	2.012	0.221	69.	1.14	7.62	7.46	7.56
	LDA	5.716	11.492	2.009	0.211	73.				
	B3LYP	5.932	11.896	2.006	0.224	53.	0.62	8.61	8.40	8.54
	HSE06	5.837	11.719	2.008	0.223	61.	0.70			
	HSESOL	5.765	11.588	2.010	0.220	68.	0.68			
	HISS	5.814	11.658	2.005	0.227	63.	1.34			
	M06	5.838	11.715	2.006	0.221	68.	1.05			
	M06L	5.908	11.874	2.010	0.218	58.	0.02			
	PBE$_{23.47}$	5.834	11.715	2.008	0.223	61.	1.04	7.64	7.50	7.59
	PBE$_{22.46}$	5.835	11.718	2.008	0.222	61.	0.97	7.79	7.64	7.74
	PBEsol$_{23.79}$	5.758	11.589	2.013	0.220	69.	1.04	7.80	7.62	7.74
	PBEsol$_{22.63}$	5.759	11.589	2.012	0.220	69.	0.96	7.99	7.79	7.92
	Exp.	5.778^{h}	11.55^{h}	2.001^{h}	0.22^{h}	$72.^{i}$	1.03^{j}	7.80^{k}	7.59^{k}	7.73^{k}
		5.784^{l}	11.616^{l}	2.008^{l}	0.224^{l}					
		5.873^{m}	11.583^{m}							

[a] Hahn *et al.* (1953), [b] Tinoco *et al.* (1996), [c], [d] Márquez and Rincón (1995), [e] Spiess *et al.* (1974), [f] Abrahams and Bernstein (1974), [g], [h] Hahn *et al.* (1953), [i] Tinoco *et al.* (1996), [j], [k] Neumann (1986), [l] Spiess *et al.* (1974), [m] Rincón and Ramírez (1992),

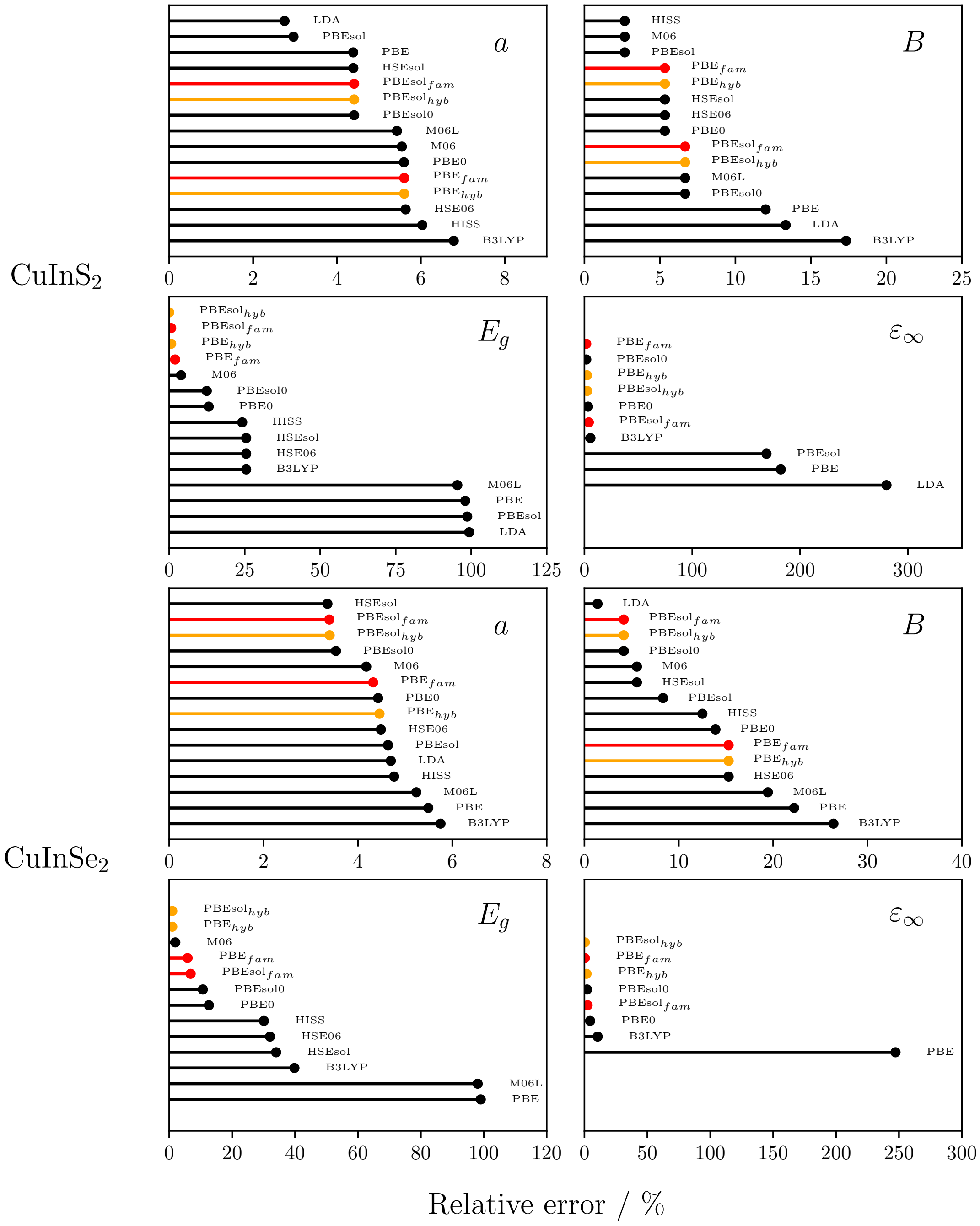

Figure 2.11 Absolute value of the relative error between calculated and experimental properties of CuInS$_2$ and CuInSe$_2$ for each Hamiltonian. Hybrid functionals optimised for the material are displayed in orange and the one optimised for the chalcopyrite family in red.

the band gaps are reproduced faithfully. However, we only looked at the smallest value of the gap, or its value at the middle of the Brillouin zone, the Γ point. In order to see the global performance of these hybrid functionals, we investigated

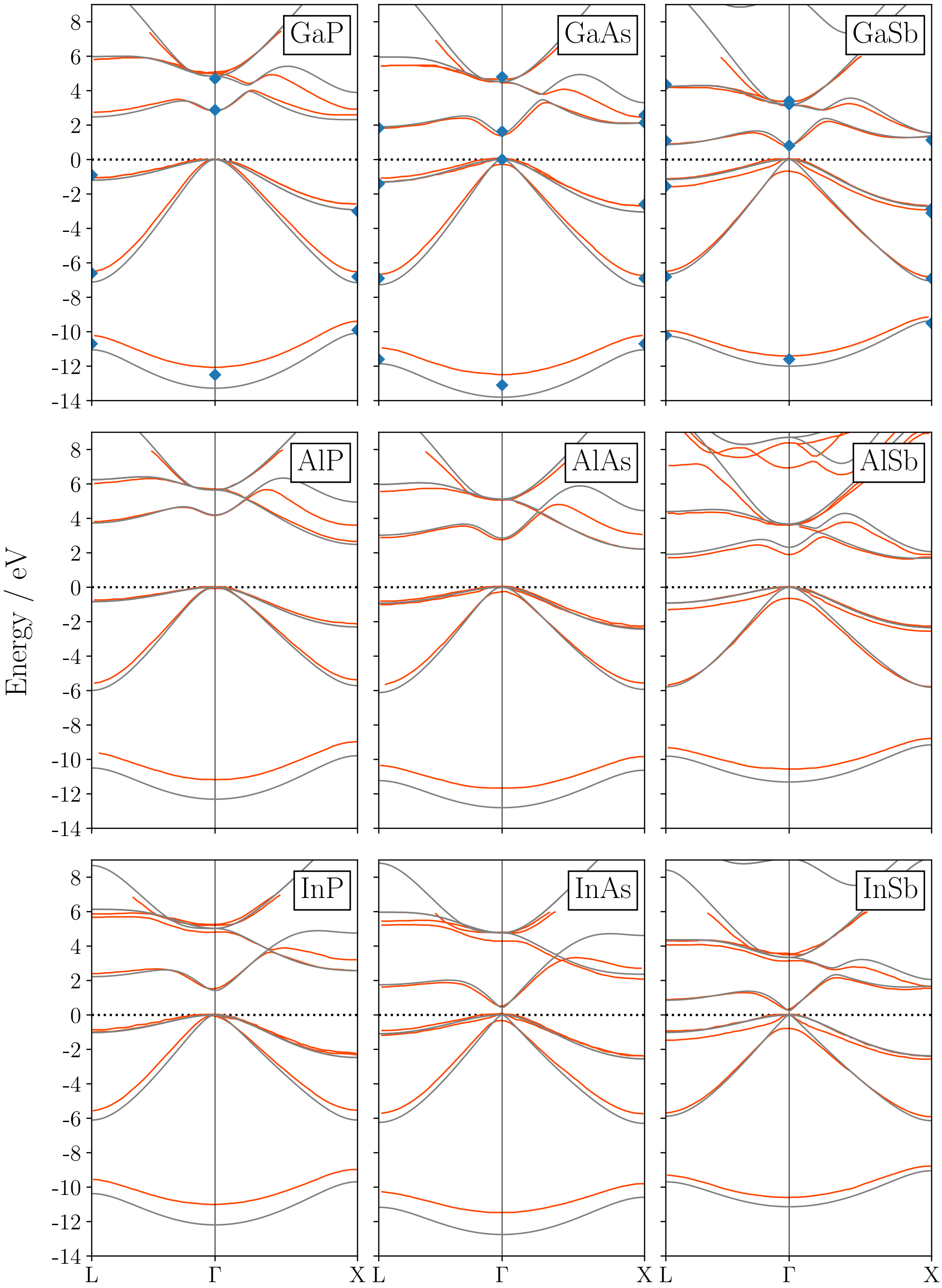

Figure 2.12 Electronic structure computed via the PBEsol$_{hyb}$ (—) and the *GW* calculation (—) of Malone and Cohen (2013) compared to experimental data for GaP, GaAs, GaSb, InP, InAs, InSb, AlP, AlAs and AlSb.

their ability to correctly describe the electronic structure of different materials and compare their results with those obtained via the more complex and time-consuming GW method.
We started by looking at the various III-V semiconductors. Silicon electronic structures calculated with PBEsol$_{12.29}$ is shown in figure 2.9. IThe comparison is done to the GW results of Rohlfing *et al.* (1993) and the experimental data by Ortega and Himpsel (1993). We can see that the hybrid functional and the GW approximation give the same description of the band structure near the band gap and close to the experimental data. The electronic structures of GaX, AlX and InX, with X=P,As and Sb, are displayed in figure 2.12. In this figure, our results

Table 2.9 Comparison of the hybrid functionals and GW+SO calculated energies Malone and Cohen (2013) at the Γ point for the III-V semiconductors. (III = Ga, In, Al and V = P, As, Sb). Experimental data are from Malone and Cohen (2013).

	GaP			GaAs			GaSb		
	Hyb.	GW+SO	Exp.	Hyb.	GW+SO	Exp.	Hyb.	GW+SO	Exp.
Γ_{1v}	−13.29	−12.14	12.5	−13.81	−12.53	−13.8/ − 13.1	−12.00	−11.47	−11.6
Γ_{15v}	0.00	−0.09, 0.00	−0.08, 0.00	0.00	−0.35, 0.00	−0.34, 0.00	0.00	−0.73, 0.00	−0.76/0.0
Γ_{1c}	2.82	2.75	2.88	1.52	1.31	1.63	0.81	0.70	0.81
Γ_{15c}	4.84	4.88, 5.05	4.7	4.53	4.38, 4.58	4.71/4.8	3.18	3.09, 3.31	
X_{1v}	−10.09	−9.47	−9.9	−11.05	−10.29	−10.7	−9.36	−9.21	−9.6/ − 9.4
X_{3v}	−7.15	−6.57	−6.8	−7.37	−6.79	−7.1/ − 6.7	−7.06	−6.86	−6.9
X_{5v}	−2.92	−2.69, −2.67	−3.0/ − 2.9	−3.05	−2.84, −2.76	−2.8/ − 2.5	−2.73	−2.96, −2.70	−3.10, −2.86
X_{1c}	2.32	2.52		2.12	2.03	2.10/2.18	1.37	1.26	1.13
X_{3c}	3.90	2.84		3.31	2.35	2.58	1.54	1.48	
L_{1v}	−11.054	−10.27	−10.7	−11.863	−10.96	−12.0/−11.24	−10.252	−9.97	−10.3/ − 10.1
L_{1v}	−7.113	−6.53	−6.6	−7.276	−6.68	−7.1/ − 6.7	−6.68	−6.51	−6.9/ − 6.6
L_{3v}	−1.198	−1.16, −1.09	−0.9	−1.313	−1.36, −1.14	−1.4/ − 1.3	−1.158	−1.60, −1.18	1.55, −1.1
L_{1c}	2.478	2.68		1.905	1.75	1.84	0.871	0.85	1.09
L_{3c}	5.981	5.75, 5.81		5.956	5.33, 5.42		4.255	4.09, 4.21	4.36, 4.49
	InP			InAs			InSb		
	Hyb.	GW+SO	Exp.	Hyb.	GW+SO	Exp.	Hyb.	GW+SO	Exp.
Γ_{1v}	−12.20	−11.04	−11.4/ − 11.0	−12.76	−11.53	−12.3	−11.14	−10.54	−11.7/ − 10.8
Γ_{15v}	0.00	−0.11, 0.00	−0.11, 0.00	0.00	−0.38, 0.00	−0.37, 0.00	0.00	−0.78, 0.00	−0.85, 0.0
Γ_{1c}	1.42	1.47	1.42	0.42	0.42	0.36	0.24	0.28	0.24
Γ_{15c}	5.03	4.78, 5.23	4.78, 5.14	4.77	4.25, 4.73	4.5	3.34	3.06, 3.50	3.14, 3.53
X_{1v}	−9.69	−9.00	−9.6/ − 8.9	−10.59	−9.84	−9.8	9.05	−8.84	−9.5
X_{3v}	−6.10	−5.55	−6.0/ − 5.9	−6.30	−5.78	−6.3/ − 6.0	6.14	−5.96	−6.4/ − 6.1
X_{5v}	−2.47	−2.36, −2.25	−2.7/ − 2.2	−2.55	−2.42	−2.7/ − 2.4	2.38	−2.60, −2.43	−2.4
X_{1c}	2.57	2.54	2.8	2.36	2.04	1.9	1.67	1.55	1.8
X_{3c}	4.76	3.18		4.62	2.67		2.06	1.65	
L_{1v}	−10.381	−9.57	−10.0	−11.174	−10.31	−10.6	−9.696	−9.38	−10.5/ − 10.0
L_{1v}	−6.106	−5.59		−6.246	−5.75		−5.88	−5.74	
L_{3v}	−1.024	−1.04, −0.92	−1.0	−1.089	−1.23, −0.96	−0.9	−1.014	−1.50, −1.01	−1.4/ − 0.9
L_{1c}	2.225	2.38	2.38	1.754	1.57		0.856	0.89	
L_{3c}	6.14	5.67, 5.84		5.972	5.20, 5.40		4.363	4.05, 4.25	4.32, 4.47
	AlP			AlAs			AlSb		
	Hyb.	GW+SO	Exp.	Hyb.	GW+SO	Exp.	Hyb.	GW+SO	Exp.
Γ_{1v}	−12.32	−11.21		−12.81	−11.73		−11.31	−10.62	
Γ_{15v}	0.00	−0.06, 0.00		0.00	−0.31, 0.00	−0.31, 0.00	0.00	−0.68, 0.00	−0.67, 0.00
Γ_{1c}	4.20	4.14		2.85	2.73	3.11	2.32	1.87	2.38
Γ_{15c}	5.65	5.66, 5.69		5.12	5.05, 5.10		3.68	3.53, 3.58	3.7
X_{1v}	−9.787	−8.99		−10.63	9.88		9.16	−8.79	
X_{3v}	−5.718	−5.38		−5.94	5.64		5.81	−5.81	
X_{5v}	−2.307	−2.17, −2.15		−2.43	−2.40, −2.27	−2.45, −2.30	2.34	−2.60, −2.30	
X_{1c}	2.49	2.63	2.5	2.22	2.19		1.69	1.62	
X_{3c}	4.951	3.56		4.45	3.06		2.07	1.85	
L_{1v}	−10.5	−9.62		−11.24	−10.40		−9.81	−9.35	
L_{1v}	−5.994	−5.58		−6.12	5.77		−5.79	−5.70	
L_{3v}	−0.837	−0.82, −0.79		−0.93			−0.92		
L_{1c}	3.732	3.79		3.03	2.85	2.49/2.54	1.91	1.68	
L_{3c}	6.251	6.01, 6.02		5.97	5.54, 5.56		4.39	4.22, 4.26	

are plotted in dark grey and the *GW* results from Malone and Cohen (2013) in red. In their article, they take into account the spin-orbit (SO) coupling. When we compare our results, there is not much difference around the band gap except for the SO that we did not look at. We have the same trends and we are even closer to the experiment value, by force of the optimisation procedure. As DFT and HF are not meant to describe excited states, our results diverge for the conduction band, even though we are still close to the results from *GW* for InSb or GaSb.

We quantified this good reproduction of *GW* electronic structures by analysing the energy band at the high symmetry point, Γ, X and L. Table 2.9 lists all these energies calculated from PBEsol$_{hyb}$ and *GW* approximation and compared to experimental data by Malone and Cohen (2013). As it was deduced from the figure 2.12, our results are sometimes closer to experimental data at the band gap. This is the case for GaP at Γ_{1c}. We obtained an energy of 2.82 eV against 2.75 eV for *GW* approximation for an experimental value of 2.88 eV. However, the spin-orbit coupling is well reproduced by the GW calculation cited, which gives accurate result for all the point observed with a maximum difference of 0.5 eV.

The same comparison was made for CuGaSe$_2$. We used the hybrid functional optimised for the chalcopyrite family and compared the electronic structure with the *GW* results of Aguilera *et al.* (2011). Even though we did not compare the energy at each point, the general trends are the same, and the gaps between occupied bands situated at about -3 and -7 eV are correctly described by our functional, which is not the case for LDA calculation (Aguilera *et al.*, 2011).

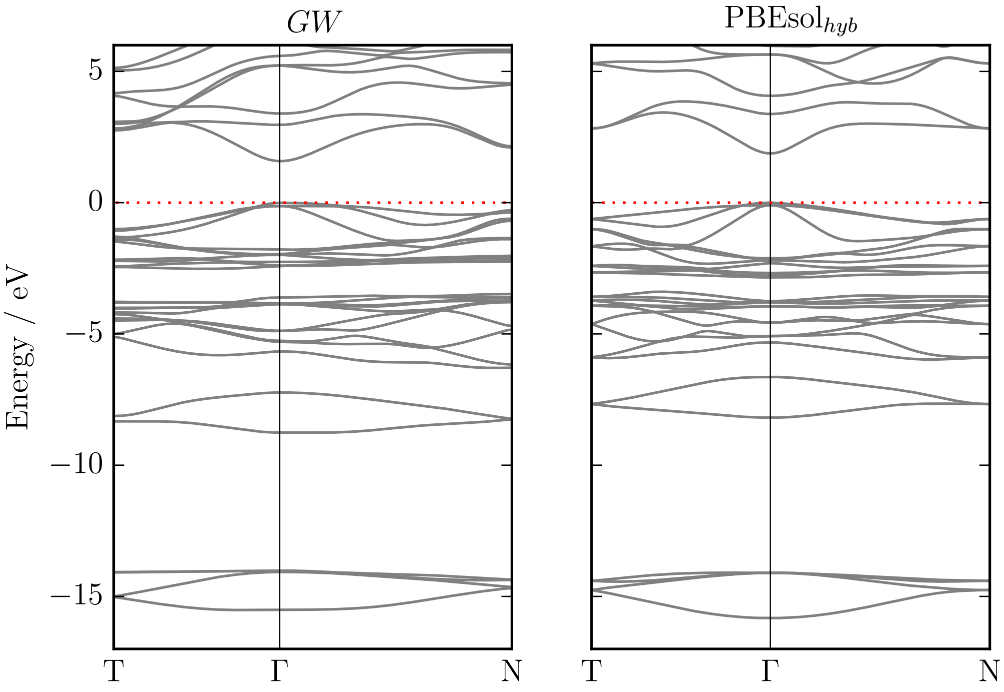

Figure 2.13 Electronic structure computed via the PBEsol$_{hyb}$ (left) and the *GW* calculation (right) of Aguilera *et al.* (2011) for CuGaSe$_2$.

Hence, the accuracy of the hybrid functional is remarkably close to the one obtained with most complex method as GW approximation. We developed hybrid functional that has the same precision on structural, mechanical and vibrational properties of other functionals in the literature, a better description of the dielectric properties and enables a very accurate reproduction of the band gap and of the electronic structure as a whole. Far less ressources-consuming than GW methods, our hybrid Hamiltonian are thus a pragmatic way to obtain quick and accurate result for semiconductors used in the photovoltaic field.

2.2 Temperature dependence of various properties

2.2.1 Structural parameters

In QHA, the effect of the temperature is directly linked to the thermal evolution of the lattice structure. Each temperature corresponds to a specific set of lattice constants. This is why the first type of properties to consider when looking at the QHA is the structural parameters and/or thermal expansion coefficient.

Figure 2.14 represents the variation of the thermal expansion coefficient α with the temperature for the set of semiconductors studied in this thesis for different Hamiltonians. These computed variations were compared to experimental data from literature. The behaviour of the calculated thermal expansion coefficient is close to the experimental ones for all the materials of figure 2.14. The only divergence is an underestimation for several III-V semiconductors (AlP, AlAs, AlSb and GaSb). We can see that we have a good description of the negative thermal expansion at low temperatures. It has been observed for various III-V semiconductors and Si and is due to the negative Grüneissen parameters of the transverse acoustical phonon branches near the limit of the Brillouin zone (Soma *et al.*, 1982; Sparks and Swenson, 1967; Gibbons, 1958; Xu *et al.*, 1991; Biernacki and Scheffler, 1989). The QHA successfully reproduces this behaviour and even has a small tendency to overestimate it as it can be seen for the Al- and In-based III-V semiconductors. The comparison of the different functionals shows similar behaviour and small dispersion. The highest difference between two functionals at a fixed temperature does not exceed 3×10^{-6} K^{-1} and is only obtained for germanium which exhibits the maximum dispersion.

We then looked at the lattice expansion of copper-based ternary chalcopyrites. In this case, the anisotropy of the system leads to two different thermal expansion coefficients α_a and α_c. Figure 2.15 shows their variation with the temperature. The Hamiltonian used is the PBEsol-based optimised one for the whole chalcopyrite family (see section 2.1.1). The above observation, concerning a good reproduction of the experimental data, applies in this case as well. However, the difference between α_a and α_c is smaller when calculated than according to experiment. This is particularly true for CuGaSe$_2$ where the two calculated curves are nearly overlapping. For this material, the negative thermal expansion is not well reproduced compared to the experimental value of Nagaoka *et al.* (2012). It is underestimated for α_c with a difference of several hundred percents whereas it is overestimated for α_a which does not show negative expansion experimentally.

The QHA leads to thermal expansion coefficients close to the experimental one for the semiconductors studied here. Even when the low temperature behaviour is not as well reproduced as in $CuGaSe_2$, the description of the values at room temperature seems satisfactory.

2.2.2 Electronic properties

After looking at the temperature dependence of the structural parameters, we turn now to the analysis of electronic properties. For the same set of materials, we calculated the band gap throughout the range of temperatures, using the QHA. Once again, the temperature here corresponds to a specific lattice param-

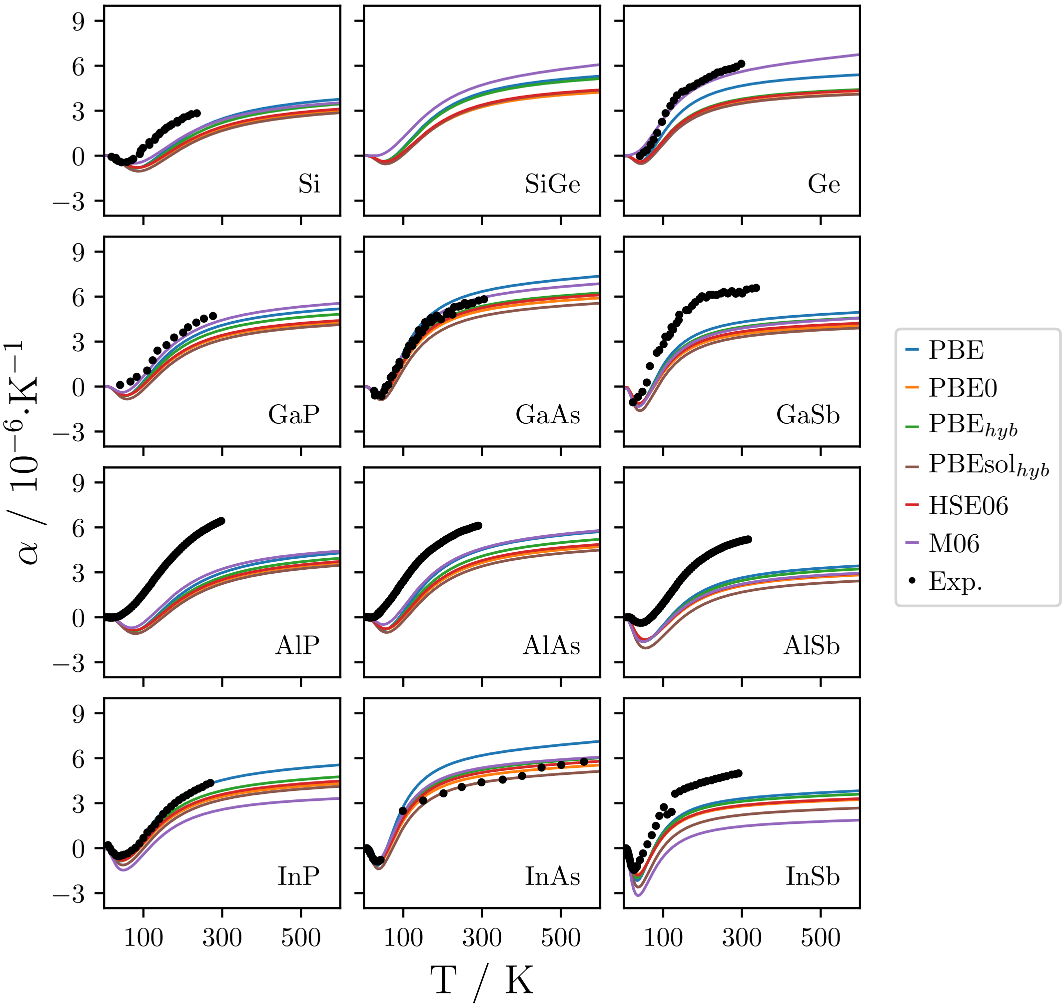

Figure 2.14 Temperature dependence of the linear thermal expansion coefficient α of various semiconductors compared to experimental data (Lyon *et al.*, 1977; Kagaya and Soma, 1987; Novikova, 1966; Deus *et al.*, 1983b; Sparks and Swenson, 1967; Ioffe Institute, 2019; Gibbons, 1958).

eter. Figure 2.16 represents the band gap variation with the temperature for different functionals. Here we can note that the calculated results quite differ from the experimental trend. For Ga and In-based III-V semiconductors and Ge, the band gap decreases with the temperature consistently with the experimental data. However, the predicted decline of the band gap with temperature turns out systematically too slow. For Si and Al-based materials it is even worse. The calculated band gap increases with the temperature whereas the experimental one declines. In reality, the main contribution to the temperature dependence comes from the electron-phonon interaction (Allen and Heine, 1976; Zollner *et al.*, 1991). However, we do not consider this type of interaction in our calculations. This might explain the discrepancies between our results and the experiments.

The same tendency as for germanium takes place for chalcopyrite. In figure 2.17, the descending variation of the band gap with temperature for the four ternary chalcopyrites is well described by the quasi-harmonic approximation for the PBEsol$_{hyb}$.

Coming back to figure 2.16, in most of the cases different functionals yield the same behaviour. Nevertheless, PBE and PBE$_{hyb}$ show some divergences for GaP and AlSb. They first vary with the temperature in the same way as the other functionals but then start to decrease. Apart from this, the choice of Hamiltonian is not especially crucial if we only looked at the variation with the temperature. PBE$_{hyb}$ or PBEsol$_{hyb}$ are still closer to the experimental variation since they start at the experimental value at 0K.

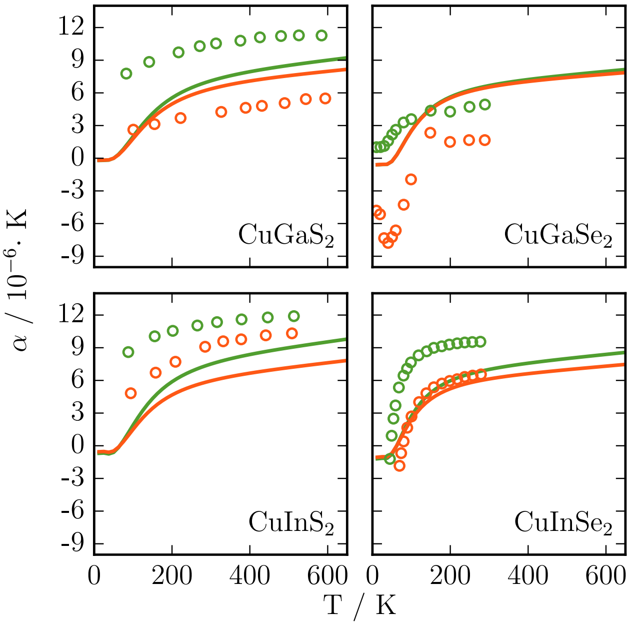

Figure 2.15 Temperature influence on the linear thermal expansion coefficient α_a (—) and α_c (—) for CuGaS$_2$, CuGaSe$_2$ CuInS$_2$ and CuInSe$_2$, calculated from the quasi-harmonic approximation with the PBEsol$_{22.63}$ functional and experimental data (Bodnar and Orlova, 1983; Nagaoka *et al.*, 2012; Deus *et al.*, 1983a).

2.2.3 Thermodynamic properties

One important feature that we want to inspect in this thesis is the variation of the defects formation energy with the temperature. We then looked at the binding energy of the perfect material and other properties such as the heat capacity at constant volume. It has been shown that HF tends to underestimate binding energies, LDA overestimate them when PBE give more accurate results (Labat *et al.*, 2007).

The formation energy of pure silicon crystal from isolated atoms is plotted in figure 2.18 between 0 and 1000 K for three different Hamiltonians, PBEsol, PBEsol0 and PBEsol$_{hyb}$. We can see that the three functionals yield the same trend in the formation energy varying with temperature. However, the corresponding curves are separated by nearly rigid shifts, occurring already at zero temperature. Compared to experimental data (Corruccini and Gniewek, 1960; Desai, 1986), the gradual decrease of the formation energy with temperature is well reproduced, especially at low temperature under 300 K. The kink at 300 K is coming from the two different experimental procedures used.

The heat capacity at constant volume for Si, GaP, GaAs and GaSb was calcu-

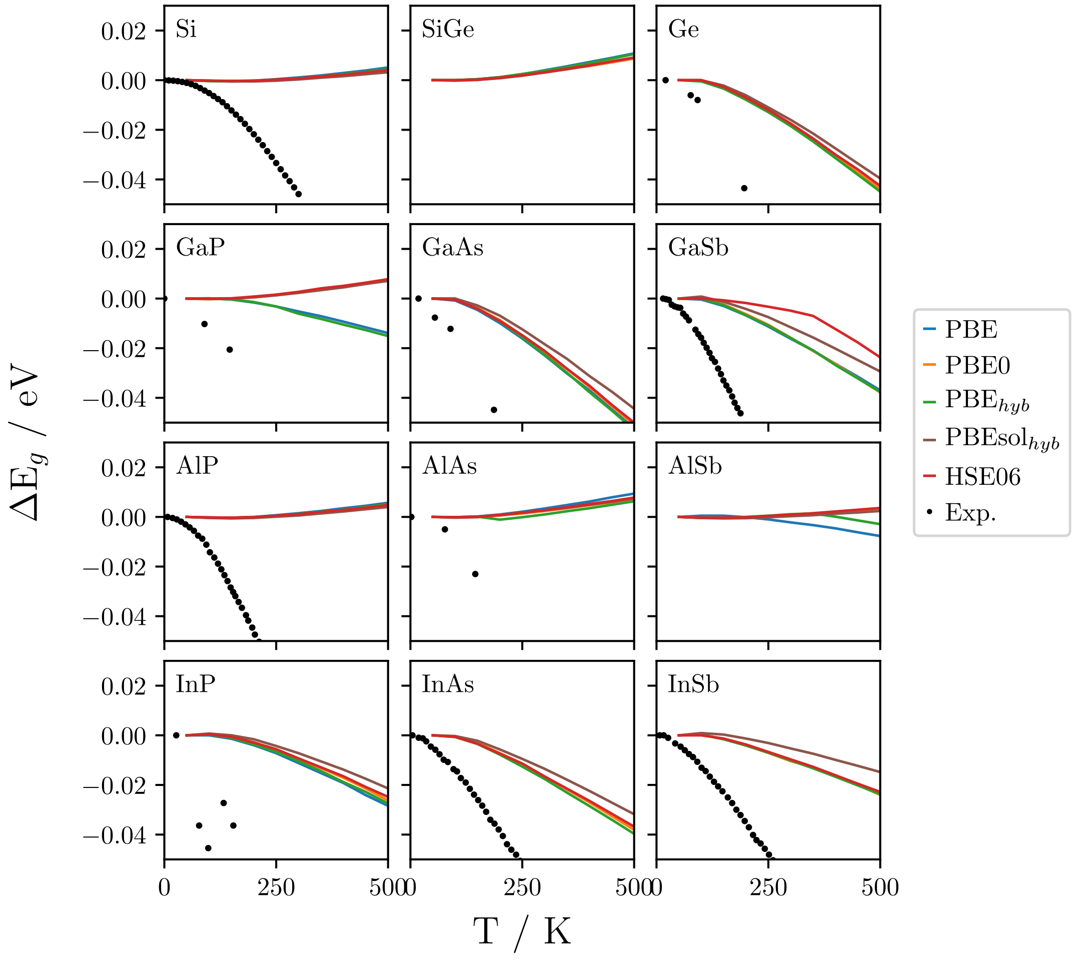

Figure 2.16 Temperature dependence of the band gap energy ΔE$_g$ of various semiconductors.

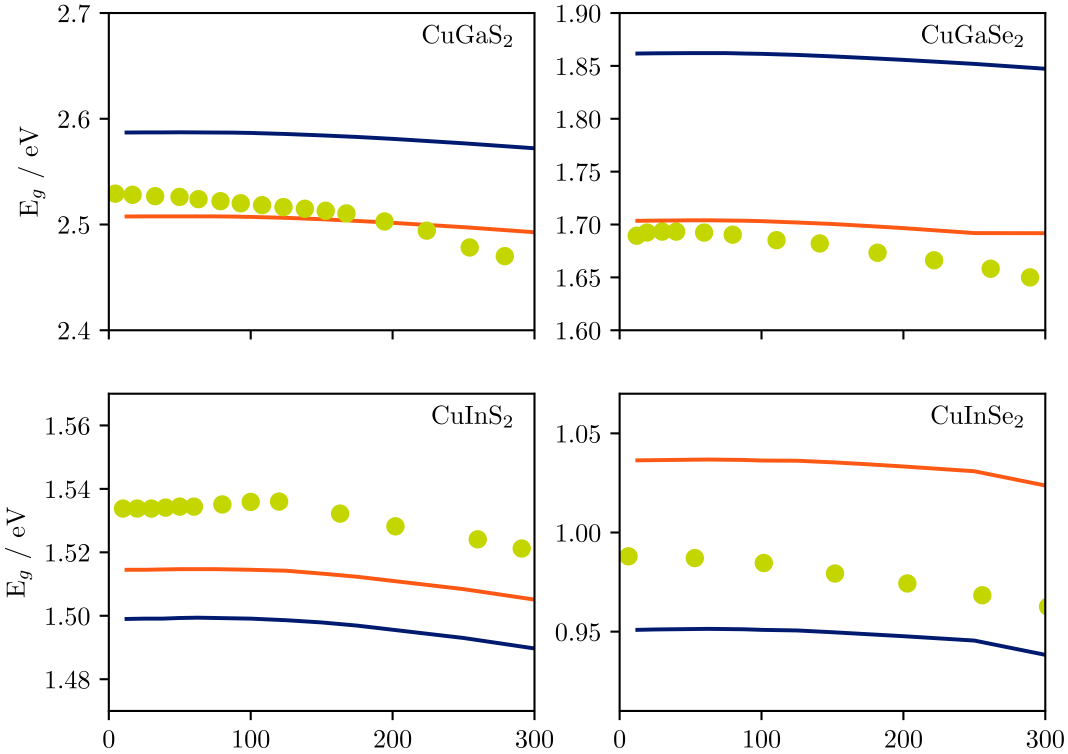

Figure 2.17 Temperature dependence of the band gap of $CuGaS_2$, $CuGaSe_2$, $CuInS_2$, and $CuInSe_2$ calculated via hybrid functional optimised for the material (red) and the chalcopyrite family (blue), compared to experimental data (green dots).

lated with PBEsol$_{hyb}$ from 0 to 600 K and is shown in the figure 2.19. The figure also reproduces the experimental data from the literature (Pässler, 2013; Glazov and Pashinkin, 2001). We have a very good agreement with the experimental data for the four materials, and this in fact independently on the functional chosen. Therefore, one can admit that the use of hybrid functionals is not imperative when thermodynamic properties are object of study; an LDA or GGA calculation would yield practically undistinguishable results in this sense. As we can see in figures 2.14 and 2.15, the thermal expansions for the studied materials are 3×10^{-6} K^{-1}. The lattice constants' variations with temperature are then negligible and as the thermodynamic properties can also be calculated from the phonon calculation, the QHA may be not necessary for the calculation of thermodynamic properties in this case. In the other cases, the QHA is a good first approximation to take into account the temperature without too much calculation time. It is not well suited for simulating the temperature variation of the band gap without the considering of electron-phonon coupling.

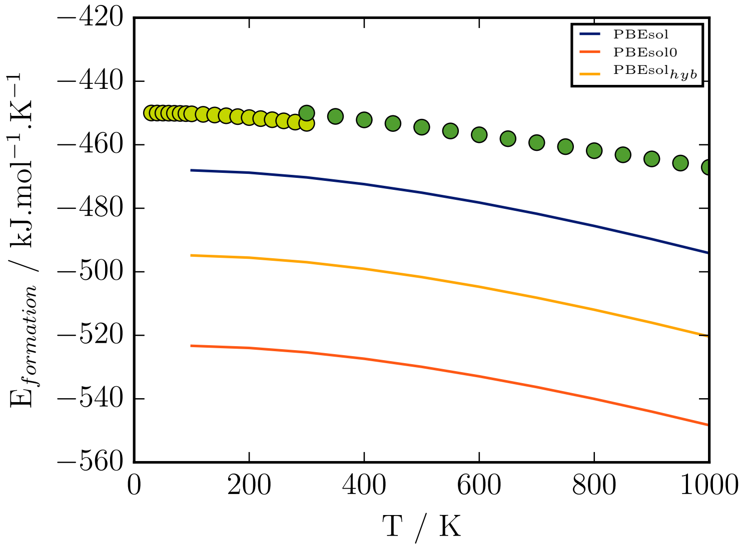

Figure 2.18 Formation energy of silicon for three different Hamiltonians compared to experimental data from Corruccini and Gniewek (1960) (●) and Desai (1986) (●).

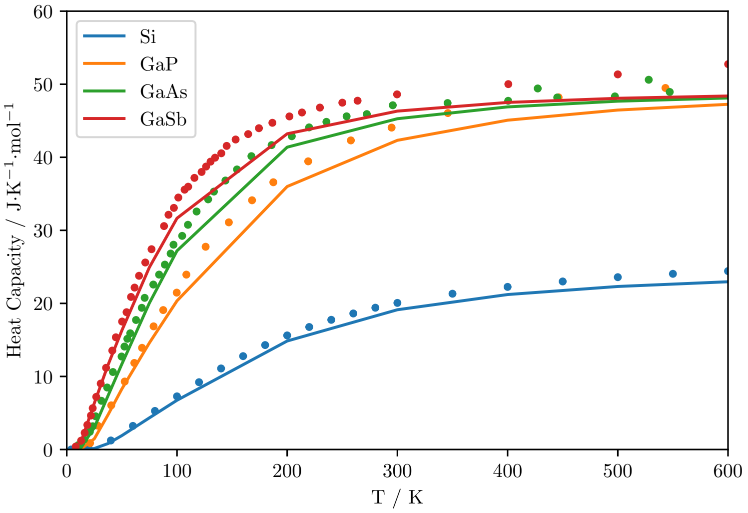

Figure 2.19 Temperature dependence of the heat capacity of Si and GaX (X = P, As and Sb) calculated with the PBEsol$_{hyb}$ compared to experimental data (Pässler, 2013; Glazov and Pashinkin, 2001).

2.3 Electrical conductivity

The last type of properties than we want to reach in this thesis are the transport properties, especially the electrical conductivity σ. This can be done from the Boltzmann transport equation (BTE). We saw in section 1.4 that there is a lot of different implementation of the BTE in the literature. Here we used `BoltzTraP2`.

Effect of the choice of functional

We first investigated the impact of the Hamiltonians on the electrical conductivity. Figure 2.20 shows the variation of the electrical conductivity, normalised by the relaxation time, with the chemical potential of silicon for different functionals. As it has been observed by Sansone *et al.* (2017), the influence of the Hamiltonian is not very important. The trends obtained in calculations using different hybrid Hamiltonians turn out to be very similar. The curves are practically the same, up to a rigid shift. However, the quantitative analysis shows variation between functionals. The lower the calculated band gap, the lower the electrical conductivity. HF has the highest electrical conductivity when PBE has the lowest. The only important aspect is the value of the band gap calculated by the functional. When defects come into play, the chemical potential moves from its value at 0 K, the Fermi level. We then need to have the most accurate description of the variation of the transport properties near the band gap. This is why the self-consistent hybrid functionals developed in this thesis are important. The accurate description of the band gap leads to the most accurate description of the electrical conductivity via the BTE.

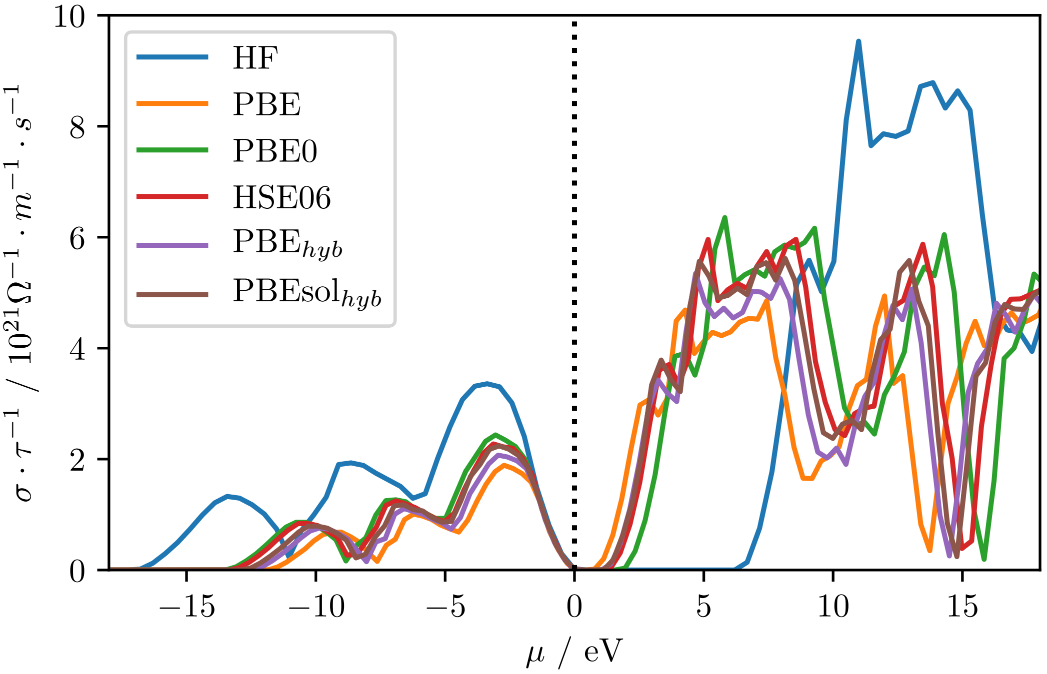

Figure 2.20 Electrical conductivity of silicon calculated with different functionals.

Effect of the temperature

The quantitative estimation of the electrical conductivity must be done at given temperature and chemical potential. The influence of temperature is shown in figure 2.21 for silicon for the PBEsol$_{12.29}$. In this case, the conductivity decreases with the temperature. Each system has a particular chemical potential, that depends on the doping. For each temperature, it is the one that yields zero net charge carrier density. For silicon, its variation is only 10^{-4} eV for 500 K. We can then consider that this value is constant with the temperature and take the chemical potential equal to the Fermi level.

Applications

We can then compare the different semiconductor materials. The electrical conductivity versus the chemical potential, normalised by the relaxation time, of different semiconductors is plotted in figure 2.22. Each material has a specific curve even though the behaviour are usually the same. The electrical conductivity is lower in the valence band compared to the one of the conduction band. The distribution of the electrical conductivity σ is directly linked to the density of state of the material. Even without looking at the quantitative data, we see that the normalisation of the electrical conductivity permits to compare materials behaviours.

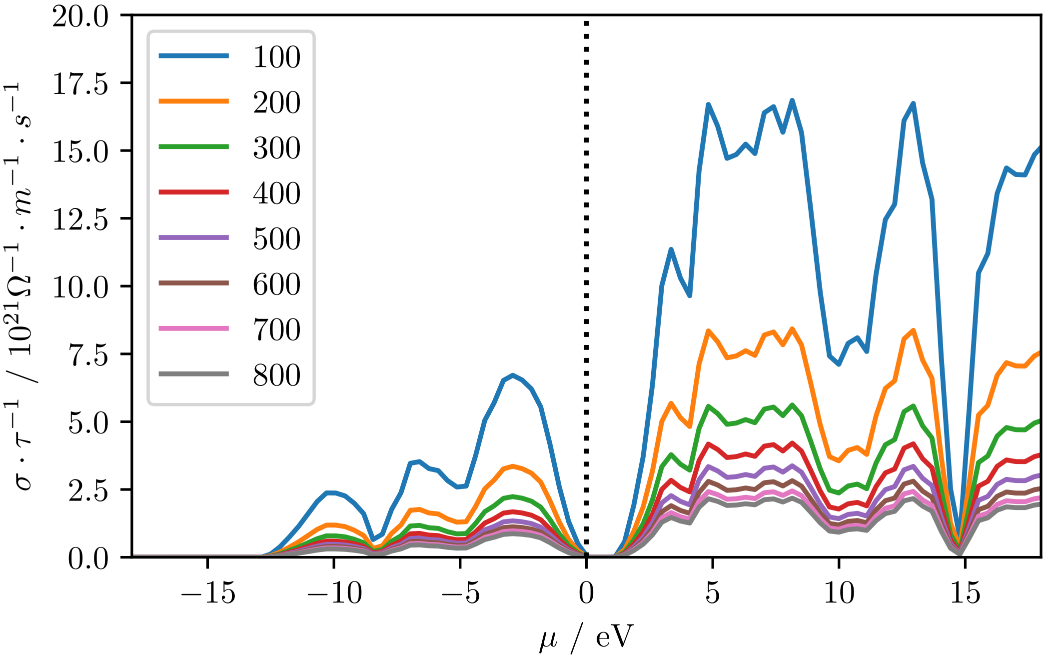

Figure 2.21 Temperature dependence of the electrical conductivity of silicon.

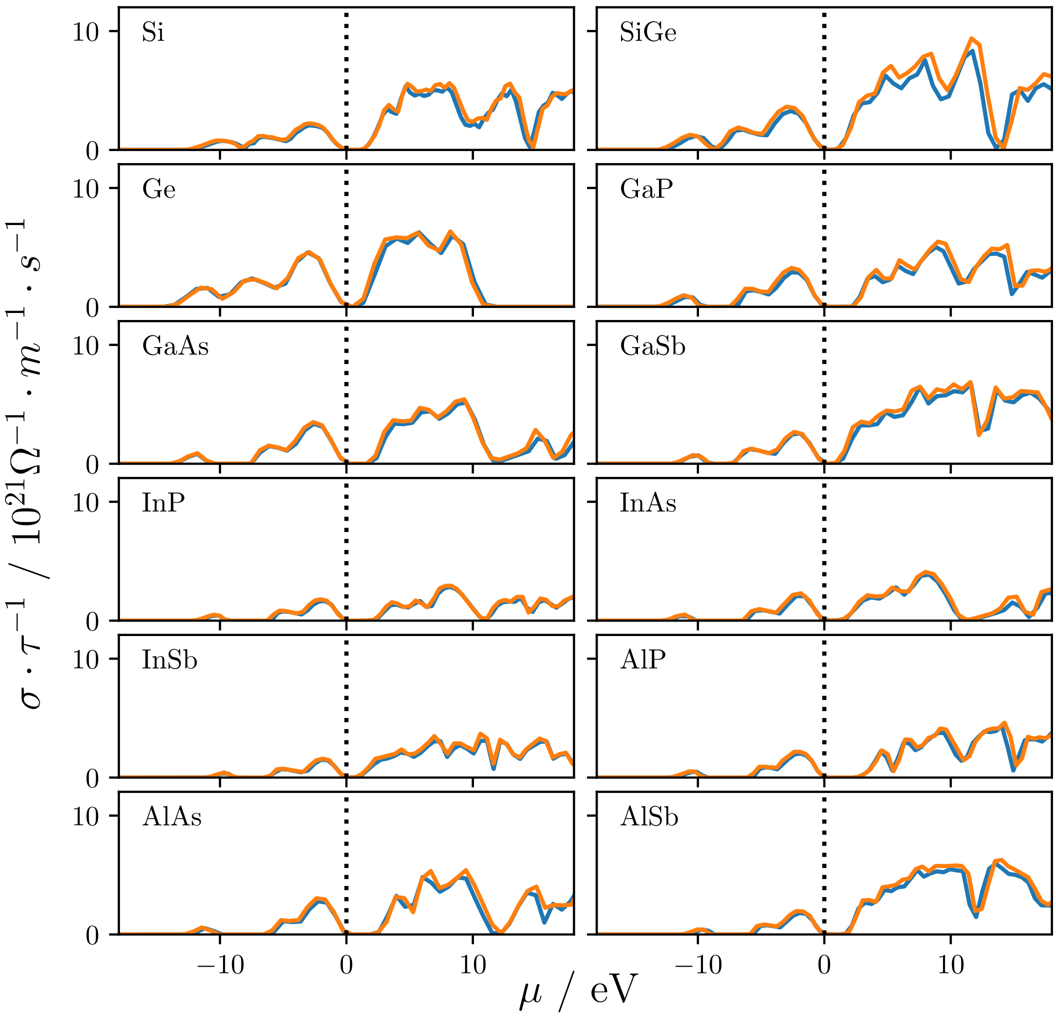

Figure 2.22 Electrical conductivity of various semiconductors calculated with the PBE$_{hyb}$ (blue) and PBEsol$_{hyb}$ (orange) functionals.

2.4 Summary and conclusion

The hybrid functionals were optimised in order to accurately describe the experimental value of the material's band gap. They were tested and compared to different types of functionals for various properties. They described the electronic structure, which matches that calculated using the GW method, but also the structural and dielectric properties. The impact of the particular Hamiltonian chosen is not significant for the description of structural properties with the temperature but it becomes crucial for the transport properties. Even though the trends are similar, the accurate description of the electronic structure of our optimised functional leads to a better description of the electrical conductivity. Thus, these approaches have been validated on pure compound, giving an accurate value of the different properties studied. We can then explore the impact of defects in the following chapters.

Chapter 3

Chalcopyrite-type compounds for tandem applications

In the previous chapters, the methodology relevant for this thesis was outlined in what regards theory foundations and practical implementation. Experimental data concerning perfect semiconductors were discussed. In the present chapter, this methodology is applied to investigate the chalcopyrite-type complex systems for tandem application. In order to use the chalcopyrite as the top cell for a silicon bottom cell, its optimal band gap must be in the range 1.5−1.7 eV. Moreover, the lattice mismatch with the silicon substrate needs to be as small as possible in order to avoid the growth of a buffer layer. In the following, two types of chalcopyrite-type compounds will be examined. We start by investigating the variation of concentrations x and y in $\mathrm{CuGa}_x\mathrm{In}_{1-x}\mathrm{S}_y\mathrm{Se}_{1-y}$ compounds and its impact on the various properties of the material. We will then look at the cation (especially copper) substitution by alkali metals in four different ternary chalcopyrites.

3.1 Doping/defect incorporation method

Some general remarks on the chalcopyrite structure might be in place here. The chalcopyrite structure can be viewed as that of II-VI zincblende in which the anions are tetrahedrally coordinated by cations. They have a tetragonal body centered Bravais lattice. Their conventional unit cell is shown in the Figure 3.1 with 16 atoms (two primitive cells). Their space group is $I\bar{4}2d$, and their structure is fully described by three crystallographic parameters: the two lattice parameters a, c and the anions fractional coordinate u. The Cu atom is always at the origin, (Ga/In) and (S/Se) atoms at the (0.5, 0.5, 0) and (u, 0.25, 0.125) positions, respectively. As shown in the Figure 3.1, the anions tetrahedra can be described by three internal parameters: d defined as the cation-anion distance, θ_1 as the (S/Se) – (Cu/Ga/In) – (S/Se) angle between atoms along the tetrahedra's basal plane, and, θ_2 as the (S/Se) – (Cu/Ga/In) – (S/Se) angle along the median of the tetrahedra.

In order to incorporate defect in the bulk material, or to tune its intrinsic composition, a procedure is adopted as outlined in figure 3.2. First of all, the

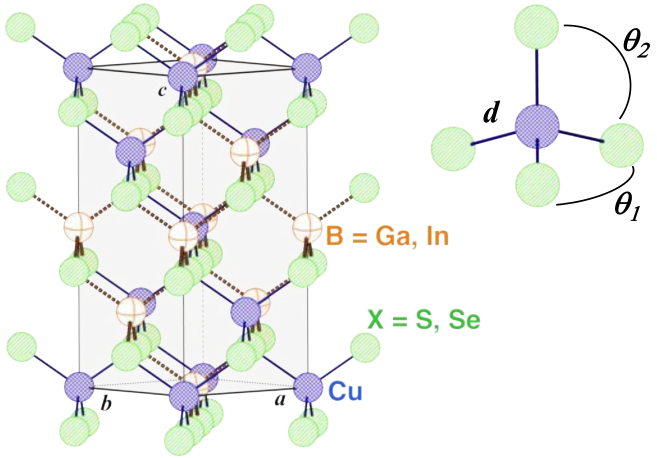

Figure 3.1 Chalcopyrite structure of $CuBX_2$ with B = Ga and In, and, X = S and Se. d, θ_1 and θ_2 stand for the cation-anion distances and the different angles in the tetrahedra, respectively.

supercell approach is used. It is mandatory for isolated defect calculation and otherwise permits to widen the range of compositions accessible. For example, in the $CuInSe_2$ primitive cell, there are two copper, two indium and four selenium atoms. If we want to substitute indium by gallium ($CuGa_xIn_{1-x}Se_2$), only three compositions are reachable: $x = 0$, 0.5 and 1, the intermediate one representing a fictitious ordered compound. A supercell containing two times the number of atoms of the primitive cell gives access to two more concentrations, $x = 0.25$ and 0.75, even if the placement of atoms over sites remains "too ordered" as compared to a genuine alloy. The bigger the supercell, the more concentrations are available and the better is the possibility, within a concentration given, to sample different distributions of atoms over the lattice sites.

Once the size of the supercell is (arbitrarily) fixed, the nominal (unperturbed) atomic positions are given, and the "commensurate" composition of choice c_n can be used to choose the placements of atoms over sites, numbered via various configurations c_{n_m}. For a given concentration, the number of configurations, given by the binomial coefficients, can be quite high. For a 64 atoms supercells with 16 indium sites, if four atoms of indium are substituted, 1820 configurations are possible, many of which will be however equivalent by symmetry. In this work, we keep only those configurations which preserve the original symmetry of the cell. This means that if two atoms are equivalent, either both of them or neither one would be substituted. This decreases the number of possible configurations and thus the calculation time. The total energy calculation for each selected configuration included the geometry optimisation, which was in all cases done within the constraints imposed by the above-mentioned preserving the supercell symmetry. This enabled to reduce ambiguity and in comparing results over different configurations. After all relaxations done, the most stable configuration c_n^0 was

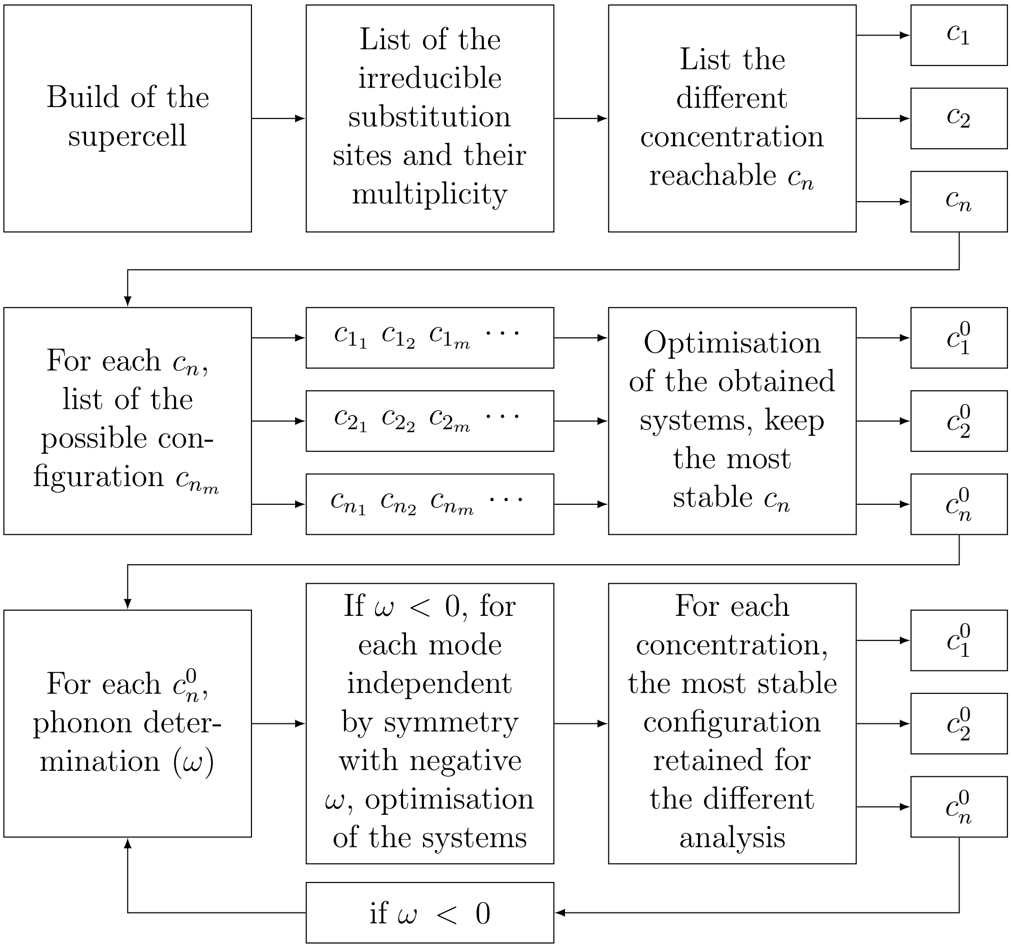

Figure 3.2 Flow chart of the method used to determine the different atomic structures associated to each concentration of complex chalcopyrites.

identified and retained for each composition. Following the static structure relaxation, the calculation of phonon frequencies around the ground-state structure thus found served to check whether all vibration frequencies are real and hence the optimised structure is dynamically stable. Imaginary vibration frequencies are then scanned and their geometry optimised within the original supercell or not.

3.2 Chalcopyrite composition

Among copper-based chalcopyrite-type materials for photovoltaic applications, the main prototype compounds are those with either Ga or In as cations and either S or Se as anions. As a throughout continuous alloying is possible on each of the respective sublattices, a general mixed chalcopyrite, in the following analysis, could be described by a general formula, $\mathrm{CuIn}_x\mathrm{Ga}_{1-x}(\mathrm{Se}_y\mathrm{S}_{1-y})_2$. We retain that x would stand for indium over gallium substitution, and y for selenium over sulphur one. The flexibility in adjusting the concentrations results in broad ranges of the band gap and lattice parameter variation. Even as separate variations of x and y were subject to a number of experimental (Roa *et al.*, 1990; Bodnar *et al.*, 1981; Bodnar and Lukomskii, 1986; Tinoco *et al.*, 1991) and theoretical (Jiang and Feng, 2008) studies, only one work, to our knowledge, addressed both substitutions simultaneously (Bär *et al.*, 2004). In this work, a model was proposed to parametrise the band gap of $\text{CuIn}_x\text{Ga}_{1-x}(\text{Se}_y\text{S}_{1-y})_2$, by extending the usual description of the band gap in binary compounds A_{1-x}B_x:

$$E_g(x) = (1-x)E_g(A) + xE_g(B) - bx(1-x)\,, \tag{3.1}$$

where b is the optical bowing constant Wei and Zunger (1995). For the penternary chalcopyrite, Bär *et al.* (2004) obtained the following band gap (in eV):

$$E_g(x,y) = 1.00 + 0.13x^2 + 0.08y^2 + 0.13xy + 0.55x + 0.54y. \tag{3.2}$$

In the present study, the band gap was probed in a series of first-principles calculations on a number of mixed structures. In particular, 81 different compositions for $\text{CuIn}_x\text{Ga}_{1-x}(\text{Se}_y\text{S}_{1-y})_2$ were analysed via the procedure described in figure 3.2. This 81-sample mesh corresponds to 9×9 trials with the values of $0, \frac{1}{8}, \frac{2}{8}, \ldots, \frac{7}{8}, 1$ over both x and y. As some concentrations could have been represented by many different configurations of atoms within the given supercell size and composition, the geometry optimisations have been performed on more than eight hundreds configurations, in order to identify the most competitive ones. In all cases, the trial systems maintained the symmetry of the chalcopyrite space group. The structural, electronic and thermodynamic properties of these compounds were then analysed under an angle of identifying the range of composition suited for tandem application.

3.2.1 The variation of the band gap with concentration

The effect of concentration on the band gap in mixed chalcopyrite-type compounds is shown at the top of figure 3.3. The four corner points of the figure are occupied by the perfect ternary compounds CuGaS_2, CuGaSe_2, CuInS_2 and CuInSe_2. The variation of the band gap is linear with both the concentration of In x and Se y, just as it was reported in the work of Bär *et al.* (2004). For a variation of x or y of 10 %, the increase of gap throughout x is ∼1 eV but throughout y only ∼0.6 eV. The whole span of the band gap variation across the diagonal of the plot goes from 1.03 eV for CuInSe_2 to 2.53 eV for CuGaS_2. Separately, both the gallium and sulphur incorporation increase the band gap value. The interesting range of 1.5-1.7 eV for tandem cells is well defined in the figure. It corresponds to the parallelepiped delimited by $(x,y) = (0.2,1); (0.4,1); (0.8,0); (1,1)$.

Whereas the inner region of this (x,y) map was not systematically investigated experimentally, the works have been done accurately exploring its four borders. A comparison of our calculations with these data are shown in figure 3.4. A very good agreement is found for all binary trends, especially for $\text{CuIn}(\text{Se}_2\text{S}_{1-x})_2$. An important conclusion from this is that our optimised hybrid functional is quite accurate throughout the whole range of substitutions and is then a reasonable compromise to use for practical predictions of electronic structure concerning this family of compounds. This conclusion gets further support from the results concerning the lattice parameters, reported in the following section.

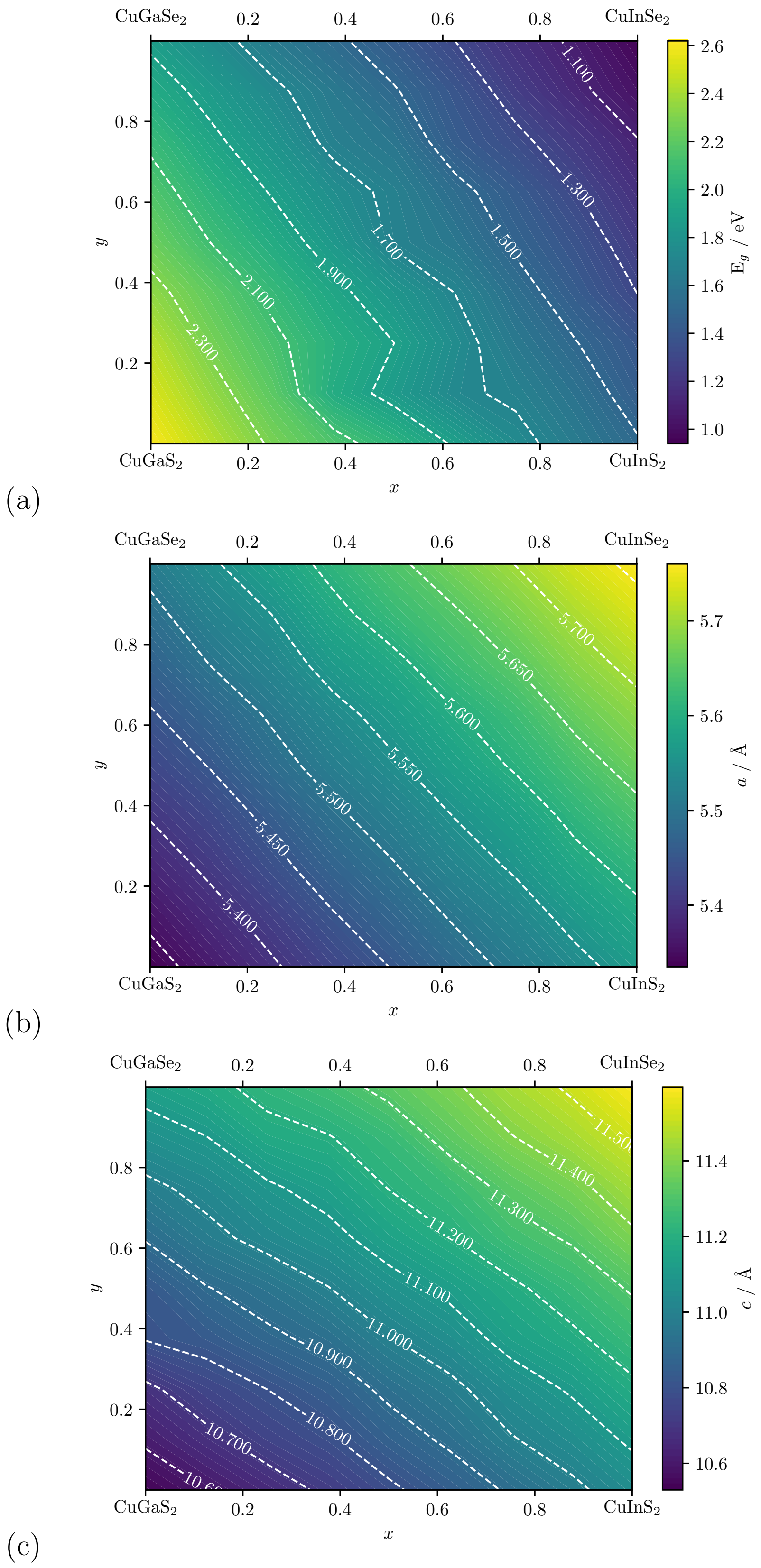

Figure 3.3 Variation with the concentration x and y for CuIn$_x$Ga$_{1-x}$(Se$_y$S$_{1-y}$)$_2$ of the band gap (a) the lattice parameter a (b) and c (c).

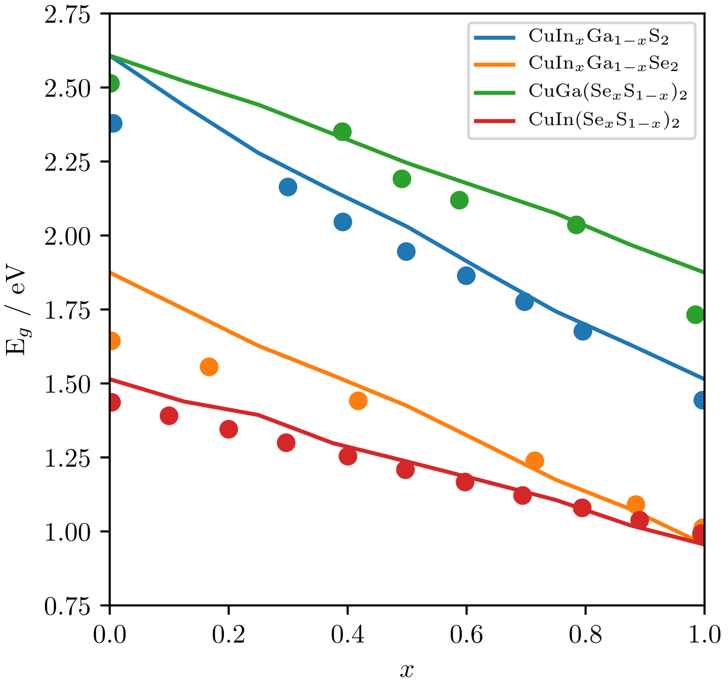

Figure 3.4 Band gap's variation with the concentration x for $CuIn_xGa_{1-x}Se_2$, $CuIn_xGa_{1-x}S_2$, $CuIn(Se_xS_{1-x})_2$ and $CuGa(Se_xS_{1-x})_2$ compared to experimental value (Roa *et al.*, 1990; Bodnar *et al.*, 1981; Bodnar and Lukomskii, 1986; Tinoco *et al.*, 1991).

3.2.2 Variation of lattice parameters with concentration

In order to grow chalcopyrite on top of silicon wafer, the lattice mismatch needs to be considered and minimised. It is then crucial to find a compromise in the choice of (x, y) concentration so that the optimal band gap would go along with acceptable levels of lattice mismatch. Unfortunately, it turns out that no easy compromise offers itself. The two lowest parts of figure 3.3 show the optimised lattice parameters a and c in their dependence on the variation of x and y. The variation is practically linear with x and y going from the smallest cell for $CuGaS_2$ with 5.336 Å and 10.540 Å for a and c respectively, to the biggest cell for $CuInSe_2$ ($a = 5.759$ Å and $c = 11.589$ Å). A change of composition, either x or y, of 20 % leads to a variation of a around 0.05 Å and c around 0.1 Å. Note that the lattice constant a of silicon is 5.430 Å. Consulting the figure 3.3, this value would correspond to mixed compounds with an important concentration of gallium, at least 60%, and more sulphur than selenium, $x \leqslant 0.5$. This combination does not correspond to the concentrations suited for the optimal band gap. The span from the line corresponding to $a \simeq 5.43$ Å in the second graph of figure 3.3 to the "parallelepiped of optimal band gaps" in the first graph of figure 3.3 defines the limits of the compromise for practical applications, the details of which have yet to be better inspected. If the band gap is a priority, an inclusion of an additional buffer layer seems to be an imposed solution, even if one of the initial motivations for this study was exactly to avoid this complication.

3.2.3 Influence of the concentration on thermodynamic properties.

We conclude our study on mixed chalcopyrite-type alloys with the analysis of alloying energetics, calculating, throughout the concentrations mesh, the binding and formation energies. Specifically, the binding energy was obtained via the equation:

$$\mathrm{Cu + In + Ga + S + Se \rightarrow CuGa}_x\mathrm{In}_{1-x}(\mathrm{S}_{1-y}\mathrm{Se}_y)_2, \tag{3.3}$$

and the formation energy by:

$$\begin{aligned} &\tfrac{1-y}{2}\mathrm{Cu_2S} + \tfrac{y}{2}\mathrm{Cu_2Se} + \tfrac{1-x}{2}\left[(1-y)\mathrm{Ga_2S_3} + y\mathrm{Ga_2Se_3}\right] \\ &\qquad + \tfrac{x}{2}\left[(1-y)\mathrm{In_2S_3} + y\mathrm{In_2Se_3}\right] \rightarrow \mathrm{CuGa}_x\mathrm{In}_{1-x}(\mathrm{S}_{1-y}\mathrm{Se}_y)_2. \end{aligned} \tag{3.4}$$

In both cases, the zero point energy was not taken into account. The contour plots of the corresponding calculated energies over the map of concentrations are shown in figures 3.5 and 3.6. The behaviours are not the same for the two reactions. When we look at the binding energy, i.e., the energy of assembling the compound (or, an alloy) from elements, the $\mathrm{CuInSe_2}$ compound is the most stable with an energy around −1.3 eV, whereas the other three ternary compounds have binding energies close to −0.4 eV or −0.5 eV. Such a difference of the order of 1 eV is quite remarkable. For the formation energy, the reference system is represented by selenide and sulphide binary compounds really used in the synthesis. Under this perspective, the selenide-based chalcopyrites are the less stable; however, the difference with the sulphur-based compound is only 0.05 eV. All these energies

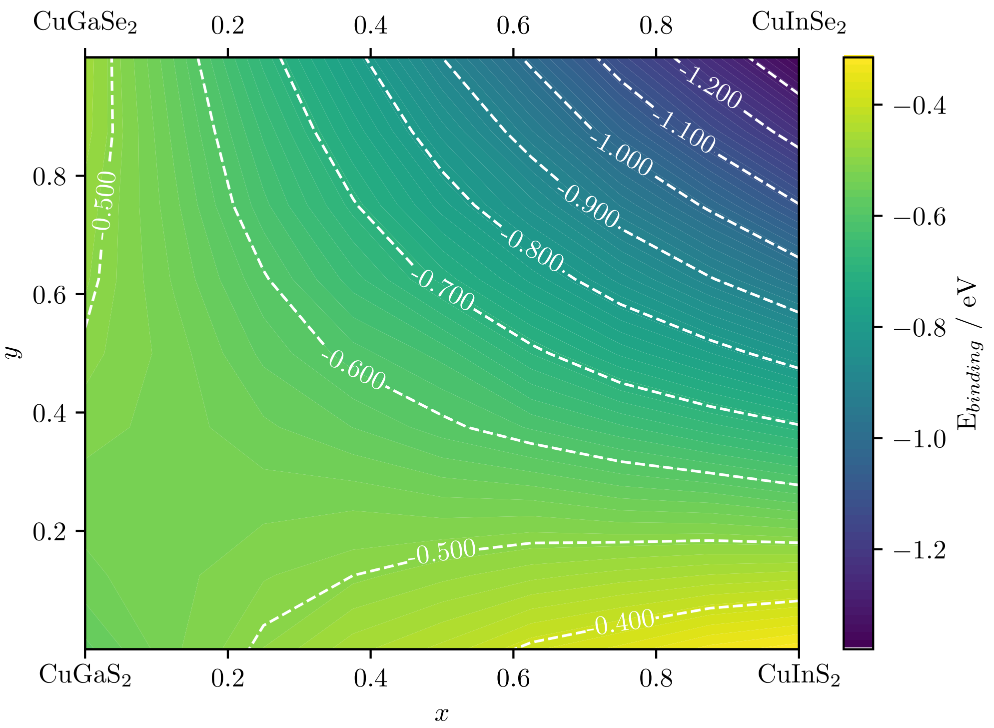

Figure 3.5 Variation of the binding energy with concentration x and y for $\mathrm{CuIn}_x\mathrm{Ga}_{1-x}(\mathrm{Se}_y\mathrm{S}_{1-y})_2$.

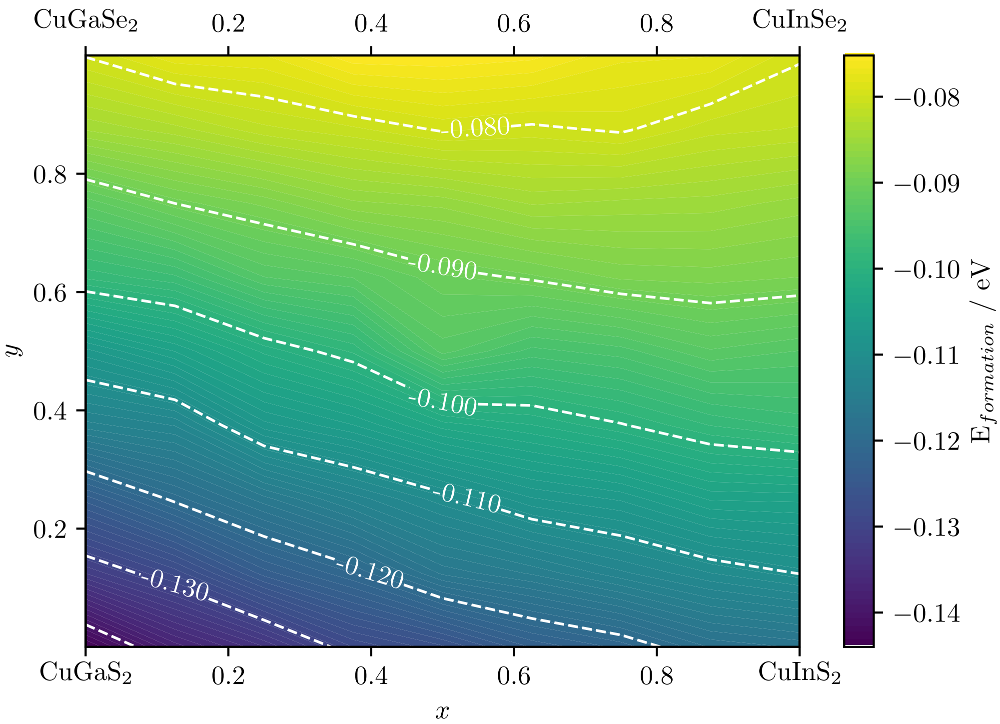

Figure 3.6 Formation energy's variation with concentration x and y for $CuIn_xGa_{1-x}(Se_yS_{1-y})_2$.

are negative, indicating that the chalcopyrite-based compounds under study are indeed stable (leaving the issue of their dynamic stability out of consideration).

3.3 Copper substitution by alkali metal

3.3.1 Review on alkali incorporation in chalcopyrite

Recently, doping with alkali metals got into the focus of studies aimed at improving the performance of the chalcopyrite-based solar cells. Their incorporation have gained attention thanks to a new post-deposition process (PDT) that led to an improved efficiency of the cell. In five years, the efficiency of thin film chalcopyrite solar cell went from 20.4 % (Chirilă *et al.*, 2013) to 23.3 % (Solar Frontier, 2019).

The beneficial impact of the alkali metal on the properties of chalcopyrite solar cell was already discovered in the mid-1990s (Hedstrom *et al.*, 1993). When comparing different types of substrate, Hedstrom *et al.* (1993) observed an improved performance of the cell grown on soda lime glass (SLG) that were later linked to the diffusion of sodium from this substrate. Investigations on heavier alkali incorporation followed. Contreras *et al.* (1997) reported that potassium and caesium-doped CIGSe absorber did not have as good efficiencies (11.4 % and 11.9 %, respectively) as sodium-doped one (13.5 %). The beneficial effects of K were brought into discussion by Wuerz *et al.* (2012) who tested a different substrate, enamelled steel sheets, and obtained better results that for SLG, due to the higher concentration of potassium. Since then, potassium, rubidium and caesium were tried, that pushed the efficiency record even further. A number of review articles summarise the influence of the alkali incorporation in chalcopyrites (Salomé *et al.*, 2015; Muzzillo, 2017; Sun *et al.*, 2017).

Sodium incorporation into CIGS absorber modifies the latter's properties in a number of ways. The major modification is the increase of the hole net concentration (Cho *et al.*, 2012; Rudmann *et al.*, 2004), whereupon follows the increase of the fill factor (FF) and the open circuit voltage (V_{oc}) (Rau *et al.*, 1998; Granath *et al.*, 2000; Cho *et al.*, 2012). The same effects, yet with superior FF and V_{oc} than with sodium doping, were observed with potassium (Pianezzi *et al.*, 2014; Khatri *et al.*, 2016; Laemmle *et al.*, 2013; Wuerz *et al.*, 2012). The exact origin of the increase of the p-doping with the increase of the net hole concentration for Na (Cho *et al.*, 2012; Rudmann *et al.*, 2004) and K (Laemmle *et al.*, 2013; Pianezzi *et al.*, 2014; Khatri *et al.*, 2016) doping is still under debate. Different hypothesis are discussed in the literature. First, Na annihilates donor states, especially In_{Cu}. When competing for a Cu site, Na or K are more likely to take the place than In or Ga, so that the alkali incorporation lowers the In_{Cu} or Ga_{Cu} concentration (Contreras *et al.*, 1997; Laemmle *et al.*, 2013; Shin *et al.*, 2016). Secondly, as proposed by Niles *et al.* (1997), Na takes the place of In or Ga in CIGS in order to create $\text{Na}_{\text{In/Ga}}$. The third hypothesis is that sodium enhanced the formation of oxyde at the surface and passivates selenium vacancies (Ruckh *et al.*, 1996; Kronik *et al.*, 1998); moreover, the oxygen substitutes for selenium vacancies. Finally, Yuan *et al.* (2016) proposed a mechanism in which sodium in copper site out-diffuses during the cooling down, thus increasing the concentration of copper vacancies (V_{Cu}) and the net hole concentrations. Furthermore, the reduction of the thickness of the CdS layer is permitted thanks to potassium incorporation with a better diffusion of Cd into the absorber (Chirilă *et al.*, 2013), that leads to a decrease of the optical loss and thus to an increase of the short circuit current. Potassium doping has an influence of the composition and structure near the surface (Muzzillo, 2017). For example, a Cu and Ga depleted zone appears (Chirilă *et al.*, 2013), or a layer of a new material containing K is formed at the interface (Handick *et al.*, 2017). The Ga gradient becomes larger while increasing the Na (Ishizuka *et al.*, 2009) or K concentration (Laemmle *et al.*, 2015; Wuerz *et al.*, 2012).

The investigation of the heaviest alkali, rubidium and caesium, began with the work of Jackson *et al.* (2016). As in the case of the lighter alkali, this resulted in an increase of the open circuit voltage (Wuerz *et al.*, 2018; Karki *et al.*, 2019; Weiss *et al.*, 2018; Schöppe *et al.*, 2017), the fill factor (Kato *et al.*, 2018; Wuerz *et al.*, 2018) and of the majority carrier concentration (Wuerz *et al.*, 2018; Karki *et al.*, 2019) of the cell. However, the gain in the open circuit voltage has been observed to be more (Wuerz *et al.*, 2018) or less (Jackson *et al.*, 2016) important than the one of the sodium post-deposition treatment. Ishizuka *et al.* (2018) found that the V_{oc} and fill factor increase whereas the short circuit current decreases for indium-based chalcopyrite, whereas they have found the opposite trends for the gallium-based compound. As Na and K (Khatri *et al.*, 2016), Rb also increases the carrier lifetime (Karki *et al.*, 2019). Just like potassium, rubidium has an important impact on the morphology and the composition of the surface. The reduction of the Cu and Ga concentration near the surface (Maticiuc *et al.*, 2018) and formation of a $RbInSe_2$ compound at the CIGS/CdS interface was directly observed using TEM measurements (Taguchi *et al.*, 2018; Maticiuc *et al.*, 2018; Kodalle *et al.*, 2018). More recently, a number of works addressed the effect of doping with caesium (Jackson *et al.*, 2016; Kim *et al.*, 2018).

As the incorporation of alkali in chalcopyrite begun with sodium and continued with heavier alkali, lithium incorporation was less studied than the rest of the family. Lithium incorporation in ternary chalcopyrites was investigated experimentally and theoretically (Maeda *et al.*, 2017; Kusumoto *et al.*, 2019; Rong-Tie *et al.*, 2017; Boehnke and Neumann, 1992). The chalcopyrite phase sustains up to 10 % of Li on Cu sites in case of $CuInS_2$ (Maeda *et al.*, 2017; Kusumoto *et al.*, 2019), 20 % for $CuGaS_2$ (Maeda *et al.*, 2017; Kusumoto *et al.*, 2019), 40 % for $Cu(In,Ga)(S,Se)_2$(Rong-Tie *et al.*, 2017) and even 50 % for $CuInSe_2$ (Boehnke and Neumann, 1992). At higher concentration, the chalcopyrite phase coexists with the orthorhombic one corresponding to the $Li(In,Ga)(S,Se)_2$ compound.

Combining different alkali offers an additional option potentially useful for better performances (Chirilă *et al.*, 2013; Kim *et al.*, 2018). However, ion exchange mechanism takes place inside the absorber. This is the case for K that tends to replace Na (Chirilă *et al.*, 2013) or Rb that pushes away lighter alkali (Jackson *et al.*, 2016; Vilalta-Clemente *et al.*, 2018; Kodalle *et al.*, 2018; Maticiuc *et al.*, 2018). That mechanism is not yet well understood.

The origin of the beneficial effect of alkali on the solar cell efficiency is still unclear (Oikkonen *et al.*, 2013; Mungan *et al.*, 2013). It seems difficult to pinpoint whether the effect primarily stems from the grain boundaries (Urbaniak *et al.*, 2014) or from inside the bulk (Yuan *et al.*, 2016; Wei *et al.*, 1999), as alkali have been found in both these locations (Laemmle *et al.*, 2014; Forest *et al.*, 2017; Cojocaru-Mirédin *et al.*, 2011; Cojocaru-Mirédin *et al.*, 2013; Schöppe *et al.*, 2017; Wuerz *et al.*, 2018; Kodalle *et al.*, 2018). The presence of different alkali plays a crucial role in the diffusivity inside the absorber as it has been proved by Wuerz *et al.* (2018) by means of secondary ion mass spectrometry.

Compositions and defects were characterised by different techniques such as scanning electron microscopy (Eid *et al.*, 2015; Kodalle *et al.*, 2018) or secondary ion mass spectrometry (Eid *et al.*, 2015). Werner *et al.* (2018) have shown that the electronic effects due to alkali doping in chalcopyrite absorbers are not characterisable today because of the strong influence of the buffer/window stack. For deeper understanding or predictions, first-principles studies have to be performed.

There are only few papers that discussed the incorporation of alkali metal on CIGS from a theoretical point of view. The majority of these papers are concerned with chalcopyrite ternary compounds and particularly $CuInSe_2$ (Oikkonen *et al.*, 2013; Ghorbani *et al.*, 2015; Malitckaya *et al.*, 2017). In order to explain the evolution of properties due to alkali doping, different parameters are calculated such as the band gap, lattice constants, or the absorption coefficient. The properties of the major interest for us will be the formation energies for different incorporations possible like $\mathrm{Alk}_{\mathrm{Cu}}$, $\mathrm{Alk}_{\mathrm{In/Ga}}$, Alk_i etc. with Alk = (Li,Na,K,Rb,Cs).

First of all, alkali metals substitute either the cation or the anion. In all the calculation done, the anion substitution has a very high formation energy [higher than 1.2 eV -see Malitckaya *et al.* (2017)] that makes it very unlikely to occur, except maybe at considerable anion deficiency. An alkali element would therefore substitute either copper or indium/gallium. In the first case, the formal valence state is not changed on substitution, whereas in the second case the univalent Cu will substitute an atom with three valent electrons, thus resulting in two electrons missing and effectively a +2-charged defect. In all previous studies, the neutral copper substitution was found to be the most favourable event. This can be attributed to the covalent bond linking the anion and the copper atom being relatively weak (Oikkonen *et al.*, 2013). The dumbbell configuration was found possible only for Li and Na at the copper site (Malitckaya *et al.*, 2017). The indium-based chalcopyrite has lower substitution energy than the gallium-based one. This is the case for the substitution of In compared to the one of Ga but also when copper is substituted: $\mathrm{Na}_{\mathrm{Cu}}$ has a higher formation energy in CuGaSe_2 compared to CuInSe_2 (Maeda *et al.*, 2015). This substitution does not directly explain the observed increase of the net hole concentration on the chalcopyrite compound after alkali-fluoride PDT. $\mathrm{Alk}_{\mathrm{In/Ga}}$ could explain this increase of concentration but it is not the preponderant defect in the material. However, the substitution energy of indium in copper site by sodium is lower than the one of copper, so that sodium may first decrease the concentration of $\mathrm{In}_{\mathrm{Cu}}$ defects and thus increase the net hole concentration (Wei *et al.*, 1999). On the contrary, if the alkali take the place of copper vacancies, this decreases the net hole concentration.

An interstitial incorporation of the alcali metal atoms was also investigated and found possible in the ternary compounds. Sodium (Oikkonen *et al.*, 2013; Malitckaya *et al.*, 2017) and heavier alkali (Malitckaya *et al.*, 2017) occupied preferably the tetrahedral sites whereas lithium prefers octahedral sites. Ghorbani *et al.* (2015) added that Na is more likely to go to the tetrahedral site surrounded by two cations and two anions, whereas K prefers the one completely surrounded by cations. Yet, all these interstitial incorporations have higher formation energy than the copper substitution, and thus less likely to happen. The diffusion mechanisms of these point defects inside the bulk were also discussed but are beyond the scope of the present work.

All the theoretical investigations cited were performed on isolated point defects, and the effect of concentration was extrapolated. In the following, we systematically and explicitly investigate the impact of alkali concentration inside the bulk. That leads to a more detailed picture of the alkali incorporation throughout a broad range of composition. We start with the most stable defect on the literature, the neutral substitution of copper by alkali metals.

3.3.2 Influence of the substitutions on the crystals structures

The methodology used to generate the different substitutions have been discussed in details in the previous section. The table 3.1 summarises the different initial supercells used in this work. It gives their lattice parameters, the supercell expansion matrices with respect to the primitive cell, the list of the irreducible Cu sites and the number of sites equivalent by symmetry for each of them, as well as the Monkhorst-Pack k-points meshes (Monkhorst and Pack, 1976) applied in each case. Except for the primitive cell (space group $I\bar{4}2d$), the space group of each supercell is $P\bar{4}$. In total, 12 different concentrations have been probed for a total of 50 configurations of different symmetries. In the following, the obtained results are discussed in terms of pseudo-conventional tetragonal parameters evolution and tetrahedra's deformation.

The Figure 3.8 shows the relative modifications of the lattice parameters (a/a_0, b/b_0, c/c_0) induced by the copper substitution by alkali metals. The obtained trends are in good agreement with experimental data, when available, as illustrated by the Figure 3.7: for $Cu_{1-x}Li_x(Ga/In)(S/Se)_2$, with $0 < x < 0.60$, our calculated lattice deformation are compared to the results of Kusumoto *et al.* (2019), Rong-Tie *et al.* (2017) and Maeda *et al.* (2017) on $CuGaS_2$, $CuInS_2$ and $CuInSe_2$ respectively. The absolute error between our theoretical and experimental data is less than 1 % for these three compounds. Other alkali incorporation at these ranges of concentration has not yet been done experimentally, to our best knowledge.

In general, with the rate of substitution, the lattice parameters vary in a not trivial way. For K, Na, Rb and Cs substituted chalcopyrite, the lattice parameters a and b increase when c decreases as the alkali metal concentration grows. This is also true for $CuGa(S/Se)_2$ substituted with Li; however, it is not the case for the two indium-based compounds, in which, as copper is replaced by lithium, the c parameters grows as well, albeit less pronouncedly than a and b (within 1 %).

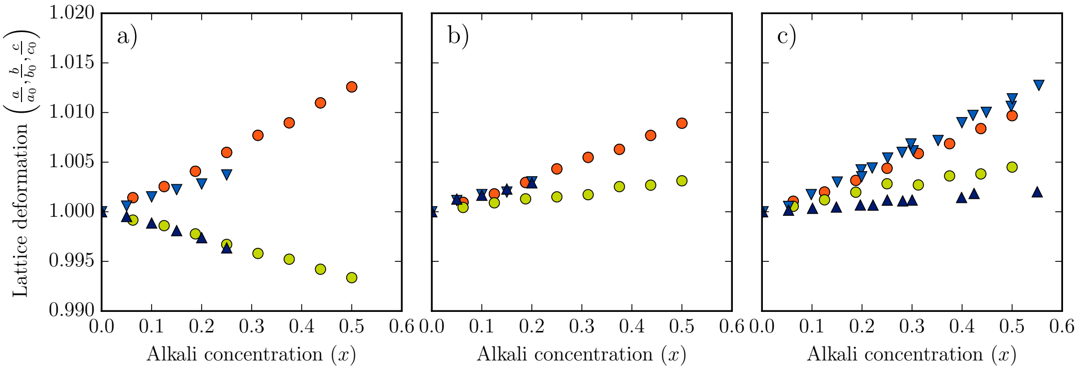

Figure 3.7 Comparison between the calculated and experimental(Kusumoto *et al.*, 2019; Rong-Tie *et al.*, 2017; Maeda *et al.*, 2017) lattice deformations, $\frac{a}{a_0}$ (●), $\frac{b}{b_0}$ (●) and $\frac{c}{c_0}$ (●) of a) $Cu_{1-x}Li_xGaS_2$, b) $Cu_{1-x}Li_xInS_2$ and c) $Cu_{1-x}Li_xInSe_2$. The experimental $\frac{a}{a_0}$ and $\frac{c}{c_0}$ are represented by ▼ and by ▲, respectively.

Table 3.1 Construction of the supercells used in the calculations. The indices P and C stand for primitive and conventional, respectively. The supercell expansion matrices refer to the primitive lattice vectors. The fractional coordinates (x, y, z) of the irreducible sites of copper as well as their multiplicity (M, number of equivalent sites) in the supercells are given. The Monkhorst-Pack k-points meshes (Monkhorst and Pack, 1976) (k) to realise the optimisation of the structures are also provided.

Number of atoms	Space group	Lattice parameter	Supercell expansion matrix	Irreducible Cu sites (x, y, z)	M.	k
8	$I\bar{4}2d$	$a = b = c = a_P$ $\alpha = \beta = \alpha_P$ $\gamma = \gamma_P$	$\begin{pmatrix} 1 & 0 & 0 \\ 0 & 1 & 0 \\ 0 & 0 & 1 \end{pmatrix}$	1 - $(0, 0, 0)$	2	18
16	$P\bar{4}$	$a = a_C$ $c = c_C$	$\begin{pmatrix} 0 & 1 & 1 \\ 1 & 0 & 1 \\ 1 & 1 & 0 \end{pmatrix}$	1 - $(0, 0, 0)$	1	12
				2 - $(\frac{1}{2}, \frac{1}{2}, \frac{1}{2})$	1	
				3 - $(\frac{1}{2}, 0, \frac{1}{4})$	2	
32	$P\bar{4}$	$a = \sqrt{2} \cdot a_C$ $c = c_C$	$\begin{pmatrix} 1 & 1 & 2 \\ 1 & -1 & 0 \\ 1 & 1 & 0 \end{pmatrix}$	1 - $(0, 0, 0)$	1	10
				2 - $(\frac{1}{2}, \frac{1}{2}, 0)$	1	
				3 - $(\frac{1}{2}, 0, \frac{1}{2})$	2	
				4 - $(\frac{3}{4}, \frac{1}{4}, \frac{3}{4})$	4	
64	$P\bar{4}$	$a = 2 \cdot a_C$ $c = c_C$	$\begin{pmatrix} 2 & 0 & 2 \\ 0 & -2 & -2 \\ 1 & 1 & 0 \end{pmatrix}$	1 - $(0, \frac{1}{2}, 0)$	2	8
				2 -$(\frac{1}{2}, \frac{1}{2}, 0)$	1	
				3 - $(0, 0, 0)$	1	
				4 - $(\frac{3}{4}, \frac{1}{4}, \frac{1}{2})$	4	
				5 - $(\frac{1}{2}, \frac{3}{4}, \frac{3}{4})$	4	
				6 - $(0, \frac{1}{4}, \frac{3}{4})$	4	
128	$P\bar{4}$	$a = 2 \cdot a_C$ $c = 2 \cdot c_C$	$\begin{pmatrix} 0 & 2 & 2 \\ 2 & 0 & 2 \\ 2 & 2 & 0 \end{pmatrix}$	1 - $(0, 0, 0)$	1	6
				2 - $(0, 0, \frac{1}{2})$	1	
				3 - $(0, \frac{1}{2}, 0)$	2	
				4 - $(0, \frac{1}{2}, \frac{1}{2})$	2	
				5 - $(\frac{1}{2}, \frac{1}{2}, 0)$	1	
				6 - $(\frac{1}{2}, \frac{1}{2}, \frac{1}{2})$	1	
				7 - $(\frac{3}{4}, \frac{1}{4}, \frac{1}{4})$	4	
				8 - $(\frac{3}{4}, \frac{1}{4}, \frac{3}{4})$	4	
				9 - $(\frac{1}{4}, 0, \frac{7}{8})$	4	
				10 - $(\frac{1}{4}, 0, \frac{3}{8})$	4	
				11 - $(\frac{1}{4}, \frac{1}{2}, \frac{7}{8})$	4	
				12 - $(\frac{1}{4}, \frac{1}{2}, \frac{3}{8})$	4	

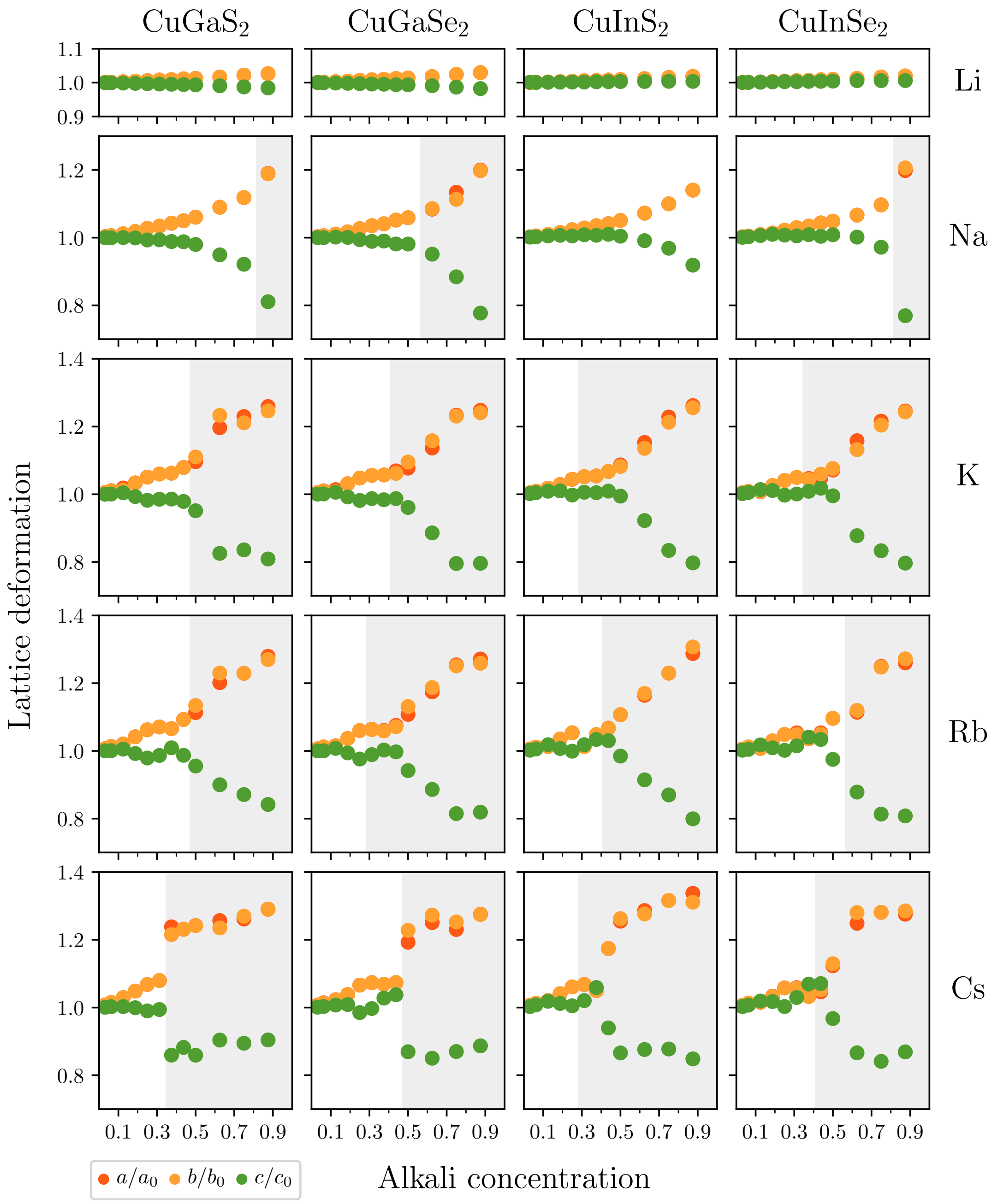

Figure 3.8 Lattice deformations $\frac{a}{a_0}$ (●), $\frac{b}{b_0}$ (●) and $\frac{c}{c_0}$ (●) of $Cu_{1-x}Alk_x(Ga,In)(S,Se)_2$ in function of the alkali concentration (x) with Alk = Li, Na, K, Rb, Cs. a_0, b_0 and c_0 refer to the lattice parameters of $Cu(Ga,In)(S,Se)_2$ as given in Tables 2.7 and 2.8. When available, the comparisons with experimental data (dotted square) are given in Figure 3.7.

Whatever the materials, these lattice parameters variations induce an increase of the volume of the cell, as shown in the table C.1 of the appendix C. The induced lattice distortion are strongly depending of the substituted crystal and the size of the inserted ions:

1 – The maximal lattice parameters distortion are 3 % for the Li substitution up to 35 % for the other alkali, as Cs.

Table 3.2 Evolution of the average structure of the anions tetrahedra associated to each alkali. d (in Å), θ_1 and θ_2 (in degree) stand for the cation-anion distances and the different angles in the tetrahedra, respectively as defined in Fig. 3.1. The data of the Cu tetrahedra in Cu(Ga/In)(S/Se)$_2$ (referenced as *Cu*) are given for comparison. The different parameters are obtained for the crystals with the $P\bar{4}$ space group; the ones in italic correspond to the $C2/c$ type crystals.

Alk.	$CuGaS_2$			$CuInS_2$			$CuGaSe_2$			$CuInSe_2$		
	d	θ_1	θ_2	d	θ_1	θ_2	d	θ_1	θ_2	d	θ_1	θ_2
Cu	2.30	109.	110.	2.32	106.	111.	2.39	109.	110.	2.40	110.	111.
Li	2.35	108.	112.	2.38	109.	111.	2.45	109.	111.	2.48	109.	111.
Na	2.60	107.	116.	2.63	107.	113.	2.70	108.	116.	2.72	107.	114.
K	2.86	106.	128.	2.86	109.	115.	2.95	106.	129.	2.98	109.	119.
	3.00	*98.*	*144.*	*2.97*	*102.*	*131.*	*3.10*	*99.*	*142.*	*3.12*	*100.*	*138.*
Rb	3.02	103.	121.	3.06	104.	118.	3.08	106.	127	3.21	100.	128.
	3.16	*97.*	*146.*	*3.19*	*99.*	*132.*	*3.21*	*97.*	*135.*	*3.36*	*96.*	*131.*
Cs	3.15	107.	117.	3.18	107.	117.	3.31	102.	121.	3.35	102.	124.
	3.41	*92.*	*142.*	*3.38*	*98.*	*128.*	*3.55*	*92.*	*147.*	*3.50*	*94.*	*132.*

2 – As shown by the gray area in Figure 3.8, except for Li (whatever the chalcopyrite) and Na in CuInS$_2$, whatever the alkali, for a given threshold concentration, the substitution brings about a phase transition. The obtained phase can be described as derived from the $C2/c$ Alk$_2$(Ga/In)(S/Se)$_2$ crystal. These phase transitions explain the sudden change of slope or discontinuity of the curves $a(x)/a_0$ and $c(x)/c_0$.

3 – At the phase transition, the main trend is a dilatation in the (a, b) plane accompanied by a compression along the c axis.

Lithium and sodium in CuInS$_2$ have specific behaviour: whatever the concentration, the crystal maintains its $P\bar{4}$ symmetry though the (Li/Na)(Ga/In)(S/Se)$_2$ crystal have a $C2/c$ space group. This behaviour is probably linked to a weakness of the used method in this work. Since it is based on the determination of unstable phonons, if the configuration correspond to a local energy minimum (or metastable state), the phase transition cannot be determined by this way. The phase transitions are influenced by the nature of the different cations. Na, K, Rb and Cs in Cu(Ga/in)S$_2$ and Cu(Ga/In)Se$_2$ have the same trend: the concentration needed to reach the transition is smaller in the In-based materials than in the Ga-based ones. It can be explained by the evolution of the local structure in the respective compounds. The tables 3.2 and 3.3 give the average structure of the tetrahedra surrounding the alkali and (Ga/In) cations, respectively (the tables giving the evolution of the tetrahedra structure with the alkali concentration can be found in the table C.2 of the appendix C). It can be noticed that, for each alkali, the cation-anion distances d are equal in Cu(Ga/In)S$_2$ and Cu(Ga/In)Se$_2$, whereas the θ_1 and θ_2 angles (cf. figure 3.1) are equal in CuGa(S/Se)$_2$ and CuIn(S/Se)$_2$. In comparison, the local structures of the tetrahedra surrounding Ga and In are less influenced by the substitution, as shown

Table 3.3 Evolution with the alkali of the average structure of the anions tetrahedra associated to Ga and In. d (in Å), θ_1 and θ_2 (in degree) stand for the cation-anion distances and the different angles in the tetrahedra, respectively as defined in Fig. 3.1. The data of the Ga and In tetrahedra in Cu(Ga/In)(S/Se)$_2$ (referenced as *Cu*) are given for comparison. The different parameters are obtained for the crystals with the $P\bar{4}$ space group; the ones in italic correspond to the $C2/c$ type crystals.

Alk.	$CuGaS_2$			$CuInS_2$			$CuGaSe_2$			$CuInSe_2$		
	d	θ_1	θ_2	d	θ_1	θ_2	d	θ_1	θ_2	d	θ_1	θ_2
Cu	2.30	109.	110.	2.48	108.	112.	2.42	109.	110.	2.60	108.	112.
Li	2.30	109.	110.	2.47	108.	112.	2.42	109.	110.	2.60	108.	112.
Na	2.30	108.	113.	2.48	107.	114.	2.42	107.	113.	2.60	107.	114.
K	2.30	107.	117..	2.48	106.	115.	2.42	106.	115.	2.61	106.	116.
	2.30	*104.*	*119.*	*2.48*	*106.*	*115.*	*2.42*	*104.*	*120.*	*2.60*	*104.*	*120.*
Rb	2.30	106.	117.	2.48	105.	118.	2.42	106.	115.	2.60	105	119.
	2.30	*105.*	*119.*	*2.48*	*105.*	*120.*	*2.42*	*105.*	*119.*	*2.59*	*103.*	*126.*
Cs	2.31	105.	117.	2.48	105.	117.	2.43	105.	119.	2.61	104.	120.
	2.30	*105.*	*121.*	*2.48*	*104.*	*123.*	*2.42*	*105.*	*124.*	*2.61*	*104.*	*123.*

by the table 3.3: the main changes concern θ_2 with a variation of ± 4 % with respect to the pure compounds. The d values grow from Li to Cs which is linked to the more ionic character of the alkali – anions bonds, as will be evidenced by the Mulliken population analysis in the next section. The phase transitions seem to be mainly explained by a strong variation of θ_2 of about + 20 % with respect to the tetragonal phase (the average variation of d and θ_1 are +8 and -9 %, respectively) which explains the increase of a and b, and the decrease of c.

Now, the evolution of the electronic structure with the alkali concentration will be described.

3.3.3 Electronic structures

Mulliken population analysis

The Mulliken net atomic charges and the overlap populations of the bonds between alkali and the sulfur and selenium are collected in table 3.4. The detailed table of the variation of these date with the alkali concentration is given in appendix C. Even if this analysis tends to overestimate the covalence contributions in chemical bonding, it provides reasonable trends, especially for comparisons between similar materials as it is the case in the present work.

For the pure chalcopyrites, the Cu-(S/Se) bonds have a iono-covalent character: first, the net charge of Cu is +0.4 and +0.1 for the sulfur and the selenium based on chalcopyrite (to compare to the nominal charge of the Cu cation +1), and, second, the populations of the Cu-(S/Se) bonds are near to 0.4 (to compare to a pure ionic bond with a population near to 0., and, a covalent bond, such as H-O in H_2O, with a population of 0.7).

Table 3.4 Average Mulliken net atomic charges of alkali (q) and Alk-(S/Se) bond populations ($b_{Alk-(S/Se)}$) for the different chalcopyrites. The data for Cu in Cu(Ga/In)(S/Se)$_2$ (referenced as Cu) are given for comparison.

Alk.	CuGaS$_2$		CuGaSe$_2$		CuInS$_2$		CuInSe$_2$	
	q	b_{Alk-S}	q	b_{Alk-S}	q	b_{Alk-S}	q	b_{Alk-S}
Cu	0.377	0.306	0.141	0.372	0.357	0.356	0.139	0.414
Li	0.390	0.193	0.205	0.210	0.391	0.231	0.209	0.287
Na	0.414	0.170	0.261	0.217	0.420	0.201	0.273	0.241
K	0.682	0.037	0.595	0.061	0.713	0.047	0.632	0.078
Rb	1.028	−0.037	1.016	−0.027	1.023	−0.033	1.108	−0.013
Cs	1.006	−0.036	0.995	−0.044	1.011	−0.051	0.998	−0.035

As concerns the Mulliken net atomic charges of alkali metals, they are higher than those of Cu, thus revealing a more ionic character of their bonding. These charges moreover increase from +0.4 to +1.0 when going from Li to Cs, which is characteristic of the reinforcement of the ionicity of the Alk-(S/Se) bonds. As for the pure chalcopyrite, the Alk-(S/Se) bonds have a more iono-covalent character for the selenium than the sulfur based on chalcopyrites.

These different trends are confirmed by the bond population analysis: from Li to Cs, the bond populations decrease from +0.2 to near to 0., which characterises an increase of the bonding's ionicity. These findings correlate with the increase of the Alk-(S/Se) bond lengths, discussed in the previous section (see table 3.2).

To conclude, the Mulliken population analysis show that the different compounds become more ionic with the incorporation of alkali which will have some impacts on the band structures of the obtained materials.

Band structures and densities of states

Table 3.5 and figure 3.9 summarise the results obtained on the effects of the copper substitution by the different alkali. The results obtained are coherent with the conclusions of the previous sections: the substitution increases the band gap of the different materials. They are also in a good agreement with experimental data when available (notably for the substitution of Cu by Li and K in CuInS$_2$ and CuInSe$_2$), and other theoretical works (Kusumoto *et al.*, 2019; Rong-Tie *et al.*, 2017; Maeda *et al.*, 2017, 2015; Muzzillo and Anderson, 2018): the error on the calculated data is less than 10%.

When the compound does not exhibit a phase transition such as for Li or Na in CuInS$_2$, the band gaps vary linearly with the concentration. When the phase transition occurs, there is a clear change in the slope of the band gaps variation with the concentration due to the more ionic nature of the Alk(Ga/In)(S/Se)$_2$ compounds.

In the chalcopyrite phase, due to the iono-covalent character of chemical bonding involving lighter alkali, such as Li and Na, the variation of the band gap is

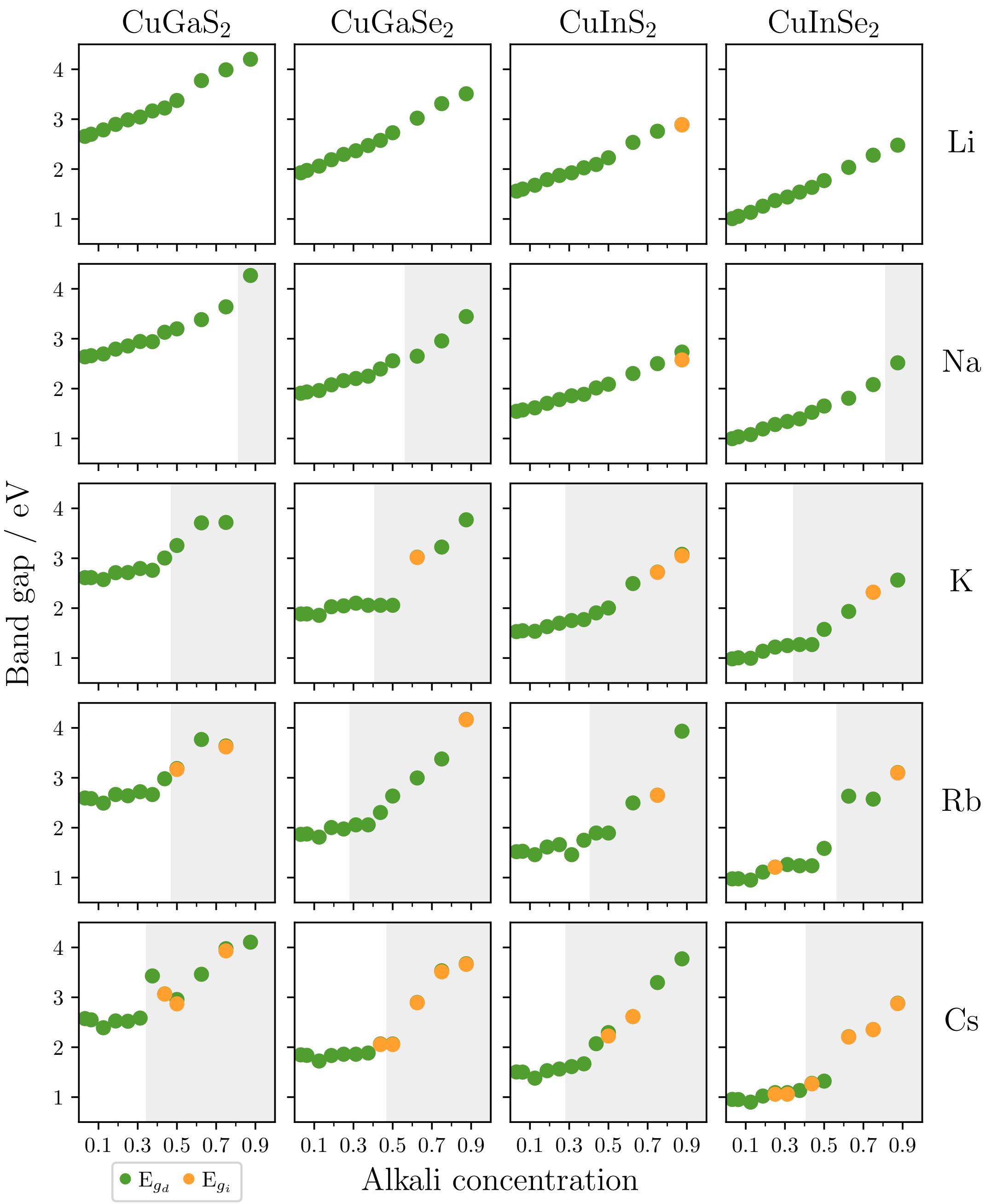

Figure 3.9 $Cu_{1-x}Alk_x(Ga,In)(S,Se)_2$ (Alk = Li, Na, K, Rb, Cs) band gap evolution (in eV) with the concentration of alkali (x). ● and ● give the direct and indirect band gaps, respectively. The gray area mark the concentrations for which the obtained phases can be described as derived from the $C2/c$ type crystals of Alk(Ga, In)(S, Se)$_2$.

more important than for the heavier alkali metals, such as K, Rb and Cs: in that way, $Cu_{1-x}Li_xGaS_2$ band gap goes from 2.6 eV to more than 3.0 eV for x between 6 % and 31 % whereas $Cu_{1-x}Cs_xGaS_2$ band gap is constant in the same range of concentration. The band gap can remain direct or become indirect with concentration, namely for the heavier alkali like caesium in CuGaSe$_2$ and CuInSe$_2$, but already for potassium in CuInS$_2$ as well.

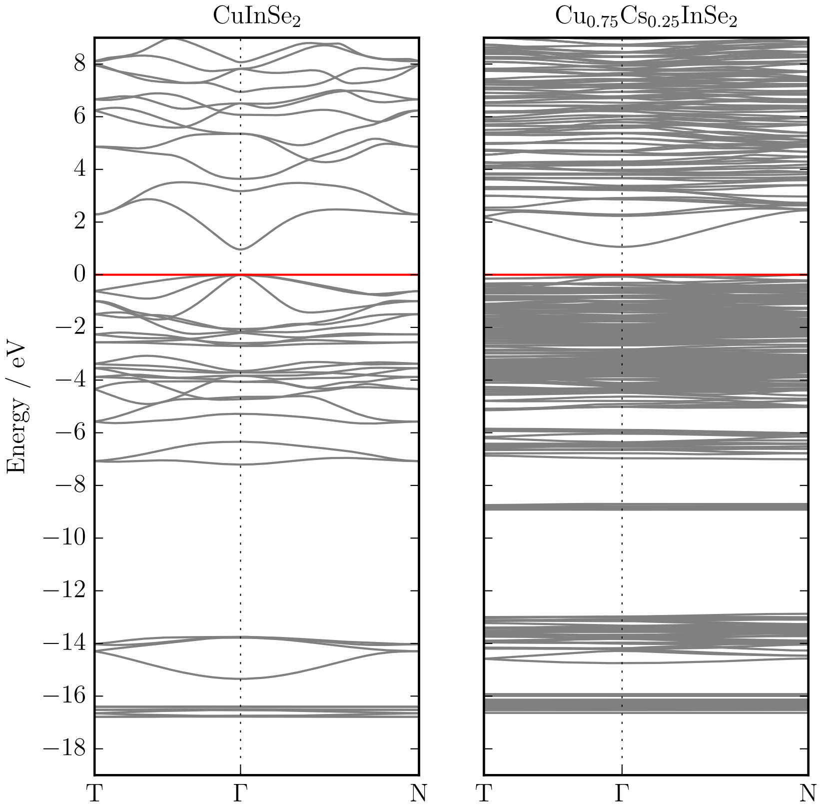

Figure 3.10 Bands structures of CuInSe$_2$ and Cu$_{0.75}$Cs$_{0.25}$InSe$_2$ in their tetragonal phases. The red line represents the Fermi level.

The figures 3.10 and 3.11 summarise the main features of the band structures and density of states with the Cu substituted by 25 % of Cs in CuInSe$_2$. The alkali-free ternary compound have been studied since the 1970s, and their electronic structure are well known (Jaffe and Zunger, 1983). Among their peculiar features one can point out a gap at about −3 eV within the occupied states, in between the bunch of bands stemming from Cu 3d hybridising with the p orbital of the anion. The lower states of the conduction bands are mainly composed by

Table 3.5 Variation of the Cu$_{1-x}$Alk$_x$(Ga/In)(S/Se)$_2$ (with Alk = Li, Na, K, Rb and Cs) band gap (in eV) with x varying from $\frac{1}{16}$ to (→) $\frac{7}{8}$. The band gaps of Cu(Ga/In)(S/Se)$_2$ (referenced as *Cu*) are given for comparison.

Alk.	CuGaS$_2$	CuGaSe$_2$	CuInS$_2$	CuInSe$_2$
Cu	2.61	1.87	1.52	0.96
Li	2.66 → 4.20	1.93 → 3.51	1.56 → 2.89	1.01 → 2.46
Na	2.64 → 4.27	1.91 → 3.44	1.54 → 2.73	1.00 → 2.52
K	2.61 → 4.75	1.88 → 3.77	1.53 → 3.08	0.98 → 2.56
Rb	2.49 → 4.70	1.81 → 4.17	1.46 → 3.93	0.95 → 3.10
Cs	2.39 → 4.11	1.72 → 3.67	1.38 → 3.77	0.90 → 2.88

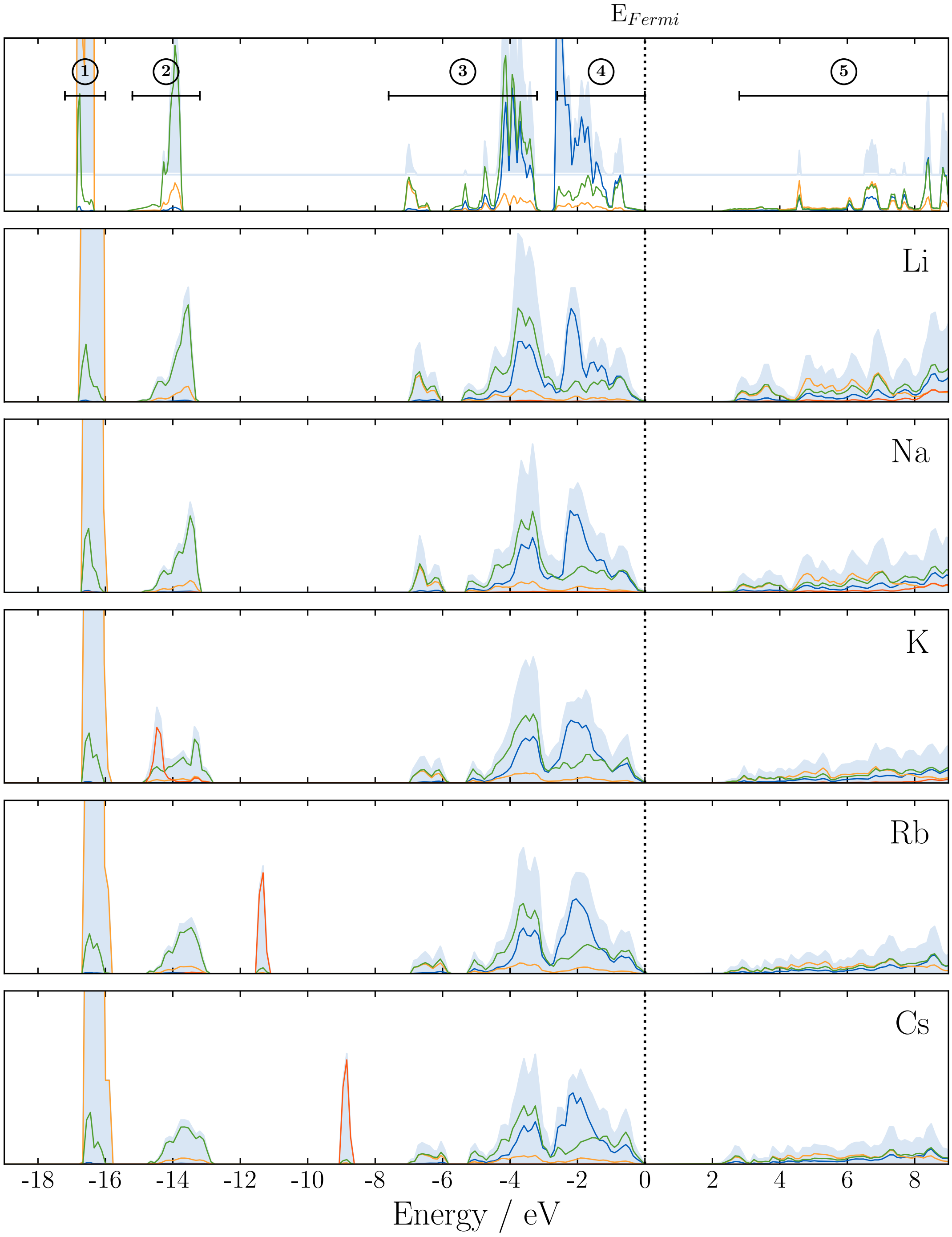

Figure 3.11 DOS of Cu$_{0.75}$Alk$_{0.25}$InSe$_2$. At the top, the CuInSe$_2$ DOS is given as reference. The grey background is the total DOS; the different lines represent the projected DOS on the states associated to Cu (▬), In (▬), Se (▬) and the alkline (▬) atoms. For the valence states, ① is mainly composed of the 4*d* orbitals of In; ② are the 4*s* of Se; ③ are the states associated to the Cu–Se bond (hybridisation of the 4*s* of Cu with the 4*p* of Se); ④ are the 3*d* of Cu and 4*p* of Se. The contribution of K, Rb and Cs appearing in the valence states correspond to their *np* orbitals with $n = 3, 4, 5$, respectively; the different states associated to Li and Na are lower in energy. For the conduction bands, the lower states ⑤ are mainly composed of the *ns* orbitals of the alkali (with $n = 2, 3, 4, 5$ 6 for Li, Na, K, Rb and Cs, respectively, and, the 4 and 5 *s* orbitals of Cu and In, respectively.

the empty *s* orbitals of Cu, Ga and In.

The use of supercells with a partial loss of symmetry lifts the degeneracy of different bands. The main effects on the substitution is the appearance of an isolated state associated to the *p* orbitals of K, Rb, Cs at -9, -11 and -14 eV, respectively; the *s* orbital of Li and *p* orbitals are deeper at -30 eV. The change of bonding, depending on the concentration, can lead to the disappearance of the gap between the *p* orbitals of S/Se and the *d* orbitals of Cu. The increase of the band gap is mainly due to the shift towards higher energies of the lowest conduction bands, linked to the increase of the empty *s* alkali's orbitals rate to these bands.

Recollecting that the target of this work is the design of materials for tandem application with an optimal band gap in the range 1.5 – 1.7 eV, we note that only the indium-based chalcopyrites reach this criteria. Let's consider now their thermodynamical properties.

3.3.4 Thermodynamical properties of the substituted chalcopyrites

Energies of copper substitution by alkali metals

In order to evaluate the feasibility of the copper substitution by alkali metals, the corresponding energy needs to be evaluated as a function of x. In our case, the following chemical reactions have been considered to determine the substitution energy of copper:

$$x\mathrm{Alk} + \mathrm{CuAB}_2 \rightarrow x\mathrm{Cu} + \mathrm{Cu}_{1-x}\mathrm{Alk}_x\mathrm{AB}_2, \tag{3.5}$$

with Alk = Li, Na, K, Rb and Cs; A = Ga and In, and, B = S and Se. The substitution energy is then

$$E_f = E_{\mathrm{tot}}^{\mathrm{Cu_{1-x}Alk_xAB_2}} + x \times E_{\mathrm{Cu}} - E_{\mathrm{tot}}^{\mathrm{CuAB_2}} - x \times E_{\mathrm{Alk}}, \tag{3.6}$$

where $E_{\mathrm{tot}}^{\mathrm{Cu_{1-x}Alk_xAB_2}}$ is the total energy of the defective supercell normalised by the number of CuAB_2 moities in the cell, $E_{\mathrm{tot}}^{\mathrm{CuAB_2}}$ is the total energy of one CuAB_2, and E_{Cu} and E_{Alk} the total energies of the isolated atoms in their fundamental states. The zero point energy was taken into account here, differently from the energy calculations reported in section 3.2. The calculated substitutions energies are plotted in figure 3.12.

For all substituting alkali metals, the formation energy exhibits the same trend: it initially increases until it reaches a maximum around 10 %, and then decreases. At low concentration, it is more difficult to substitute copper by an alkali metal, whereas at high concentration, with the joint effect of the cell expansion and phase transitions, the incorporation is easier.

Two groups of alkali metals can be distinguished: whereas the lighter ones (Li, Na and K) are characterised by formation energies lower than 2 eV, the formation energy of the heavier ones (Rb and Cs) is above 3 eV. The substitution energies for

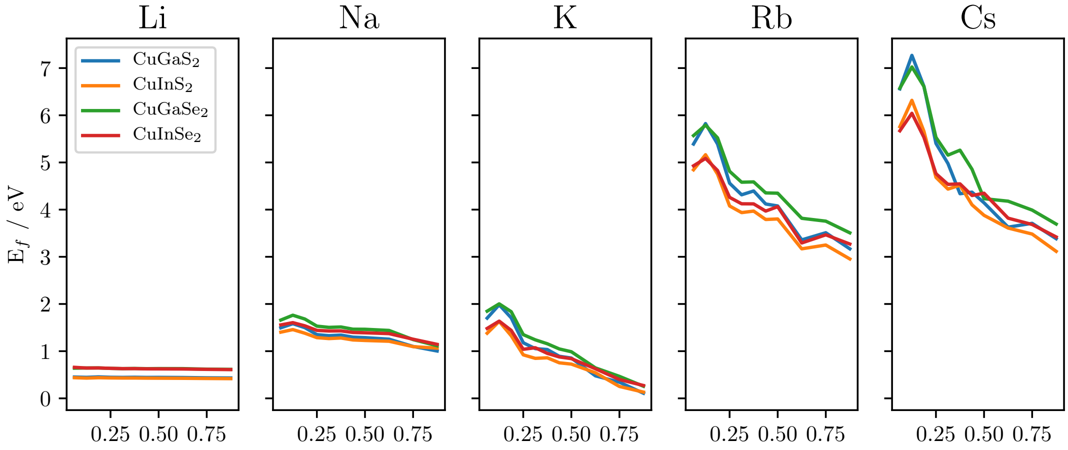

Figure 3.12 Substitution energy of Cu by the different alkali (E_f, in eV), as determined with equation (3.5), including the zero point energy.

the different alkali are in good agreement with previous theoretical work realised with the PBE (Maeda *et al.*, 2015) or HSE06 (Malitckaya *et al.*, 2017) functionals. Whatever the concentration, the lithium incorporation is easier in the sulfur-based compounds whereas for Na, K, Rb and Cs, the distinction is between Ga- and In-based compounds, with more favorable formation energy occurring for In-based chalcopyrites. However, none of these energies are negative, so that the reaction (3.5) is not spontaneous.

Experimentally, during the process of synthesis of these materials, some secondary phases can appear which could stabilise the different compounds. These possible mechanisms will be explored in the next section.

Thermodynamical stability of secondary phases

In this section, the possible mechanisms leading to secondary phases is investigated following the approach of Malitckaya *et al.* (2017). Our interest focuses on the $\mathrm{Alk_2(S/Se)}$ reactions with the ternary compound $\mathrm{Cu(Ga/In)(S/Se)_2}$ through these two following mechanisms:

$$\frac{x}{2}\mathrm{Alk_2B} + \mathrm{CuAB_2} \rightarrow \frac{x}{2}\mathrm{Cu_2B} + \mathrm{Cu}_{1-x}\mathrm{Alk}_x\mathrm{AB_2}, \tag{3.7}$$

and

$$\frac{x}{2}\mathrm{Alk_2B} + \mathrm{CuAB_2} \rightarrow x\mathrm{AlkAB_2} + (1-x)\mathrm{CuAB_2} + \frac{x}{2}\mathrm{Cu_2B}, \tag{3.8}$$

with Alk = Li, Na, K, Rb and Cs; A = Ga and In, and, B = S and Se. The obtained energies of reactions are

$$E_A = E_{\mathrm{tot}}^{\mathrm{Cu_{1-x}Alk_xAB_2}} + \frac{x}{2} \times E_{\mathrm{tot}}^{\mathrm{CuB_2}} - \frac{x}{2} \times E_{\mathrm{tot}}^{\mathrm{Alk_2B}} - E_{\mathrm{tot}}^{\mathrm{CuAB_2}}, \tag{3.9}$$

and

$$E_B = x \times E_{\mathrm{tot}}^{\mathrm{AlkAB_2}} + (1-x) \times E_{\mathrm{tot}}^{\mathrm{CuAB_2}} + \frac{x}{2} \times E_{\mathrm{tot}}^{\mathrm{CuB_2}} - \frac{x}{2} \times E_{\mathrm{tot}}^{\mathrm{Alk_2B}} - E_{\mathrm{tot}}^{\mathrm{CuAB_2}}, \tag{3.10}$$

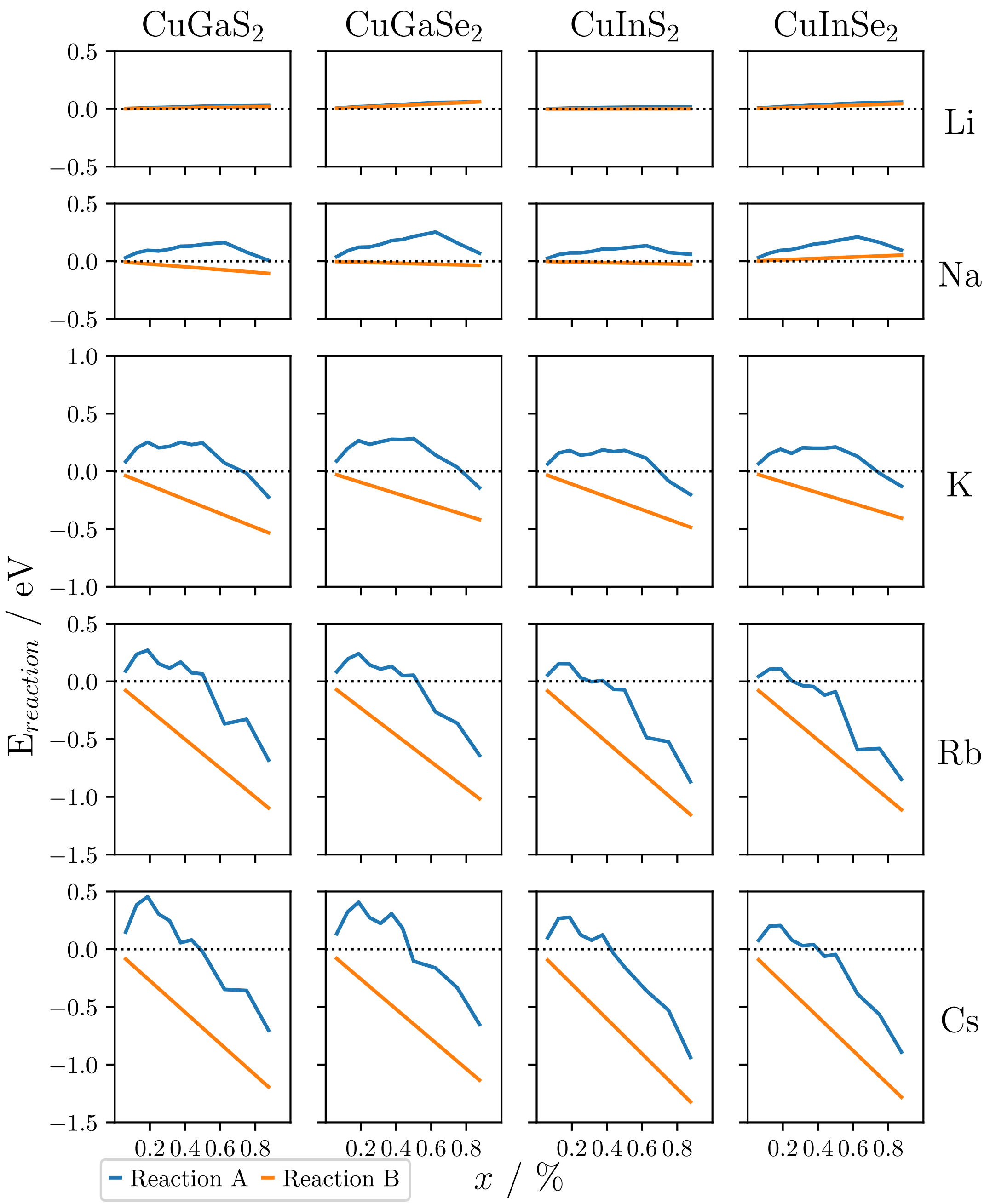

Figure 3.13 Formation energies of the mixed phases as given by the reactions A and B corresponding to the equations (3.7) and (3.8), respectively, including the zero point energy.

for the reactions (3.7) and (3.8), respectively. $E_{\mathrm{tot}}^{\mathrm{Cu_{1-x}Alk_xAB_2}}$ is the total energy of the defective supercell normalised by the number of CuAB$_2$ moities in the cell, $E_{\mathrm{tot}}^{\mathrm{CuAB_2}}$, $E_{\mathrm{tot}}^{\mathrm{Cu_2B}}$ $E_{\mathrm{tot}}^{\mathrm{Alk_2B}}$ $E_{\mathrm{tot}}^{\mathrm{AlkAB_2}}$ are the total energy of one CuAB$_2$, Cu$_2$B, Alk$_2$B and AlkAB$_2$, respectively. The zero point energy was taken into account. The figure 3.13 represents the obtained energies for both reactions.

The reaction energies for lithium substituted compounds are positive but close to zero. This is coherent with the experimental observation which show stable

Table 3.6 Formation energies (in eV) of Alk(Ga/In)(S/Se)$_2$ with (①) or without (②) secondary phases from the reactions (3.11) and (3.12), respectively. The energies include the zero point energy. The space group of the Li(Ga/In)(S/Se)$_2$ phases is $Pna2_1$; whereas for Na, K, Rb and Cs, the space group of Alk(Ga/In)(S/Se)$_2$ is $C2/c$.

Alk.	$AlkGaS_2$		$AlkGaSe_2$		$AlkInS_2$		$AlkInSe_2$	
	①	②	①	②	①	②	①	②
Li	0.02	−0.43	0.07	−0.31	0.00	−0.22	0.05	−0.20
Na	−0.12	−0.57	−0.04	−0.42	−0.03	−0.25	0.06	−0.19
K	−0.61	−1.06	−0.48	−0.86	−0.55	−0.77	−0.46	−0.71
Rb	−1.25	−1.71	−1.16	−1.54	−1.32	−1.54	−1.27	−1.52
Cs	−1.37	−1.82	−1.30	−1.68	−1.56	−1.73	−1.47	−1.72

chalcopyrite phases with x values up to ∼0.5, as mentioned by Maeda *et al.* (2015).

For Na and K, the reaction (3.8) is the most favourable which means that thermodynamically the system will be a mix of the three (Na/K)(Ga/In)(S/Se)$_2$, Cu(Ga/In)(S/Se)$_2$ and Cu$_2$(S/Se) phases.

For Rb and Cs, the situation is more complicated: at low concentration till x =0.5, only the reaction (3.8) is the favourable; but for $x > 0.5$, the energy of the reaction (3.7) becomes negative as well. Since the energy difference between these two reactions is about 0.5 eV only this means that the four phases can coexist, thermodynamically.

Alternatively, the formation of the compounds AlkAB$_2$ with or without precipitates can be considered through the reactions of Alk$_2$B with the adsorber CuAB$_2$ or A$_3$B$_2$ via the equations (3.11) and (3.12), respectively

$$\frac{1}{2}\mathrm{Alk_2B} + \mathrm{CuAB_2} \rightarrow \frac{1}{2}\mathrm{Cu_2B} + \mathrm{AlkAB_2}, \tag{3.11}$$

and

$$\frac{1}{2}\mathrm{Alk_2B} + \mathrm{A_3B_2} \rightarrow \mathrm{AlkAB_2}. \tag{3.12}$$

The energies of these reactions are summarised in the table 3.6. The obtained results for the reaction (3.11) are coherent with the ones of (3.7) and (3.8): except for the lithium and sodium for which the energies are closed to 0 eV, this reaction have negative energies whatever the materials of reference. The reaction (3.12) is always favourable with energies of the same order of magnitude than the ones of the previous reactions.

In conclusion, except for the lithium, from the thermodynamical point of view, the substitution of Cu by alkali metals seems likely to lead to the appearance of the secondary phases via one or the other of the mechanisms discussed.

3.4 Summary and conclusion

One of the key advantages of CIGS for photovoltaics is a possibility to control their composition that leads to a tunability of different properties such as the lattice parameter or the band gap. This feature makes chalcopyrite system promising candidates for tandem application. At the beginning of this chapter, the influence of the penternary chalcopyrite $\mathrm{CuIn}_x\mathrm{Ga}_{1-x}(\mathrm{Se}_y\mathrm{S}_{1-y})_2$'s composition on different properties was investigated. A complete mapping of the lattice parameters, band gap and formation energy with the two concentrations x and y was made. The target band gap values for photovoltaic applications are accessible for higher concentration of indium than gallium. However, in this very range of concentrations, the lattice mismatch with silicon is quite appreciable, whereas a good matching with the silicon lattice parameter correspond to chalcopyrite with higher concentration of gallium and sulphur. Throughout these relevant compositions, the system stays in the chalcopyrite symmetry, and its energy of formation is negative, thus the system remains thermodynamically stable.

In a similar method, alkali incorporation by means of cation substitution was simulated. The first observation is that alkali metals increase the volume of the cell with an expansion of the lattice parameter a and a contraction of c. However, the system goes from the $P\bar{4}$ symmetry at lowest concentration to $C2/c$ for the highest one, except in the case of doping with lithium and most of the cases concerning sodium; however, this might be due to an intrinsic issue of the method. This deformation is purely due to the local deformation of the tetrahedra around the substituted atoms. The calculation of electronic properties were then performed. The Mulliken population analysis shows that the different compounds become more ionic with the incorporation of alkali. As for the band gap, it increases with the concentration of alkali metal. That is not a good news for gallium-based ternary chalcopyrites that have band gap already larger than the target value, however might be useful for indium-based chalcopyrites to reach the target value. Different energy relations were then calculated corresponding to various chemical reactions. The main conclusion is that alkali metals incorporation is not easy in chalcopyrite. Even if Li, Na and K have substitution energy lower than 2 eV and hence much lower than Rb and Cs whose substitution energy is around 4 – 5 eV, all these energies are positive, and the substitution reaction is not spontaneous. Moreover, except for the lithium, thermodynamically, the substitution of the Cu by a alkali metals will lead to the appearance of the secondary phases whatever the considered mechanisms.

Chapter 4

Point defects in crystalline silicon for ageing investigation

Thin-film solar cells like those based on chalcopyrite-type compounds represent only a few percent of the photovoltaic market, which is otherwise dominated by silicon cells. An important issue regarding these latter is ageing due to exposition to light and elevated temperatures. At the microscopic scale, this comes down to the study of point defects, their creation and interaction, hence the problems related to those covered by the previous chapter. For the present work, the study of defects in silicon has a somehow subordinated character. In fact the ongoing Ph.D. work of Elisa Tejeda Zacarias (under direction of Holger Vach and Philippe Baranek), whose preliminary studies, in the framework of the master internship of Boris Belin, were supervised by me and Philippe Baranek, is expected to reveal this problematics in much more completed form. In the present chapter, I concentrate on results which are marked by my essential contribution and offer sometimes an interesting comparison with the other topics covered by my thesis. In particular, the impact of three point defects well-known in the literature, the incorporation of hydrogen, boron and iron, is considered. The goal is to validate our method via comparison with the literature and to prepare considering the point defects in combination, e.g., the Fe-B complex.

4.1 Context

Even if the works dealing with silicon solar cells are innumerable, not everything in the latters' behaviour is yet fully understood, so that some hard cases persist. One of them is the light induced degradation (LID). This effect was reported for panels tested in real conditions (Osterwald *et al.*, 2002) which suffer from a major decrease of their efficiency during the first hours following their installation. This degradation was linked to boron-oxyde defects. Oxygen atoms or molecules trapped in the silicon bulk are excited and migrate until they reach a boron atom with whom they will form a complex that acts as a recombinaison center (Schmidt *et al.*, 1997). Both explication of, and countermeasures against, the LID have been found since, the latter being the hydrogenation of the material that leads to the recovery of the degradation by the passivation of BO defect (Wilking *et al.*, 2013; Hallam *et al.*, 2013; Nampalli *et al.*, 2015). The process can be decomposed into three steps (Herguth *et al.*, 2006) : (1) the creation of the recombination inactive defect precursors (2) activation of the defect that degrade the material (3) restauration of the defect. Further on, the light-and elevated temperature-induced degradation (LeTID) was discovered in 2012 (Ramspeck *et al.*, 2012). Whereas the LID sets on already in the first few hours of the installation, the LeTID is a much slower process which can take several thousands of hours. Unfortunately, the solutions found for the LID do not work for the LeTID. For example, the three-stage process is not fully repeatable so that it would gradually suppress the degradation at each cycle (Fung *et al.*, 2018). Following the implementation of the notion of the *hydrogen reservoir* by Fung *et al.* (2018), Wenham *et al.* (2018) introduced the *"Bucket Theory"*. This theory suggests a picture of three buckets in a vertical row, each bucket able to be emptied into those below. This picture of buckets implies that the hydrogen flow occurs in one main direction, the reverse flaw being negligible. The first step consists of trapping hydrogen in the bulk to create defects (bucket two) and a reservoir of defect through firing (bucket one). In the LeTID condition, the weak bonds that holds the hydrogen atoms are broken, so that hydrogen “falls into the bucket 3”, that corresponds to the degradation of the cell. The third bucket then starts to empty as hydrogen passivates other defects, or gets dispersed in the bulk. After a while, when the three buckets are empty, the system has recovered and all hydrogen atoms are in stable bonds, strong enough to resist new LeTID conditions. The hydrogen diffusion plays therefore the crucial role in these phenomena (Chen *et al.*, 2018; Lindroos and Savin, 2016).

Hydrogen integration inside silicon have been simulated, mainly by Van de Walle and his team (Van de Walle *et al.*, 1989; Van de Walle, 1994; Herring *et al.*, 2001; Van de Walle and Neugebauer, 2006). In their works, they identify the most stable position for the neutral and charge hydrogen point defect. H^- was found at the center of the tetrahedral site of the silicon cell, region with the lowest electronic density, as H_2, whereas H^+ was stable in the bond center, midway between two Si atoms, as for H^0. H^0 was found to be a transition state, thermodynamically unstable in silicon (Van de Walle and Neugebauer, 2006).

Boron is intentionally used to dope silicon into a p-type semiconductor. Iron is a defect that may appear depending on the growth condition of silicon. It tends to deteriorate the silicon cells’ properties. Iron preferably occupies a tetrahedral interstitial and can then form a complex with the boron atom in the silicon site (Brotherton *et al.*, 1985).

4.2 Defect incorporation

4.2.1 Silicon vacancies

Before investigating extrinsic defects in silicon, silicon vacancies were analysed. One atom of silicon, not linked to any other atom in the cell to keep the highest symmetry possible, was removed from the bulk. Four different states were investigated: the metallic one and three silicon configuration with spin angular

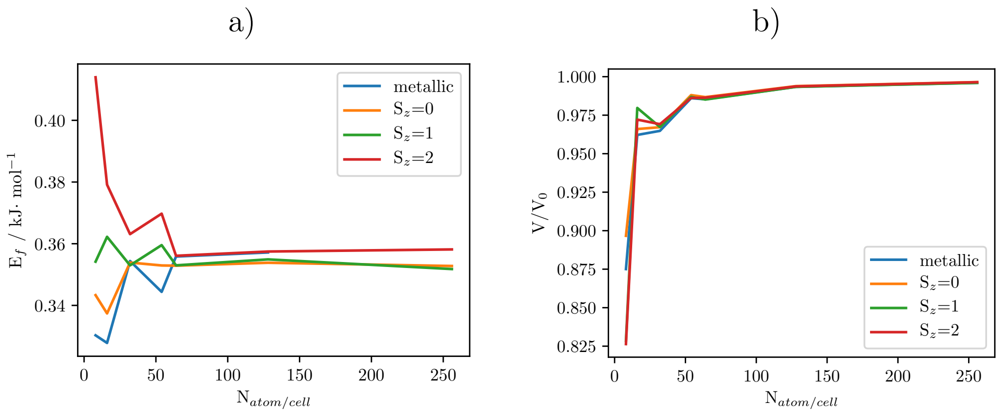

Figure 4.1 a) Formation energy of the bulk silicon b) Structural deformation of the bulk silicon (V/V_0) with one vacancy per supercells of different sizes, probing four different silicon vacancy corresponding to the metallic state and to three non-metallic ones, with spin ($S_z = 0$, 1, 2).

momentum S_z equal to 0, 1 and 2. For a charged system, `CRYSTAL` uses a uniform charged background of opposite sign in order to counteract the charge. To simulate an isolated defect, the supercell approach was used in order to sufficiently separate the defect from its translated replicas. The influence of the size of the supercell was examined so as to reach the convergence of different properties with the smallest cell possible. Thus, the structural deformation and the formation energy of the defective system was plotted for different size of the cell as can be seen in figure 4.1. The size is indicated by the number of atoms per cell, the higher the number is, the lower the defect concentration. The structural deformation corresponds to the ratio of the defective system's volume V over the one of the perfect system V_0. Since the Gaussian-type basis sets are not complete and pinned on atoms, they suffer from the basis set superposition error (BSSE). The BSSEis taken care of in the course of estimating of the formation energy according to the counterpoise method by Boys and Bernardi (1970). It was evaluated from the energy of an isolated silicon at the center of a cluster of ghost atoms.

At higher concentration, defects interact with each other. For insufficiently large supercells, a spurious interaction between translated defects leads to large unphysical variations of the calculated properties (shown in figure. 4.1) with the supercell size. The results become reasonably stabilised from the 64-atom cell on. For instance, the modification of volume does not exceed 2%. In this case, the deformation created by an isolated vacancy does not spread to reach its image on the neighbouring cells. The formation energy then converges to the formation energy of the isolate vacancy in silicon.

Even though the structural and thermodynamic properties are considered converged from a theoretical part of view, it is not the case for the band structures, as evidenced by figure 4.2. It is important to note that the distance between the high symmetry point are not the same since the symmetry of the cell differs from one supercell to the other. However, we are interested here in the (unoccupied) levels in the band gap induced by silicon vacancies. As the vacancy concentration effectively decreases on increase of the supercell size, these band flatten tending

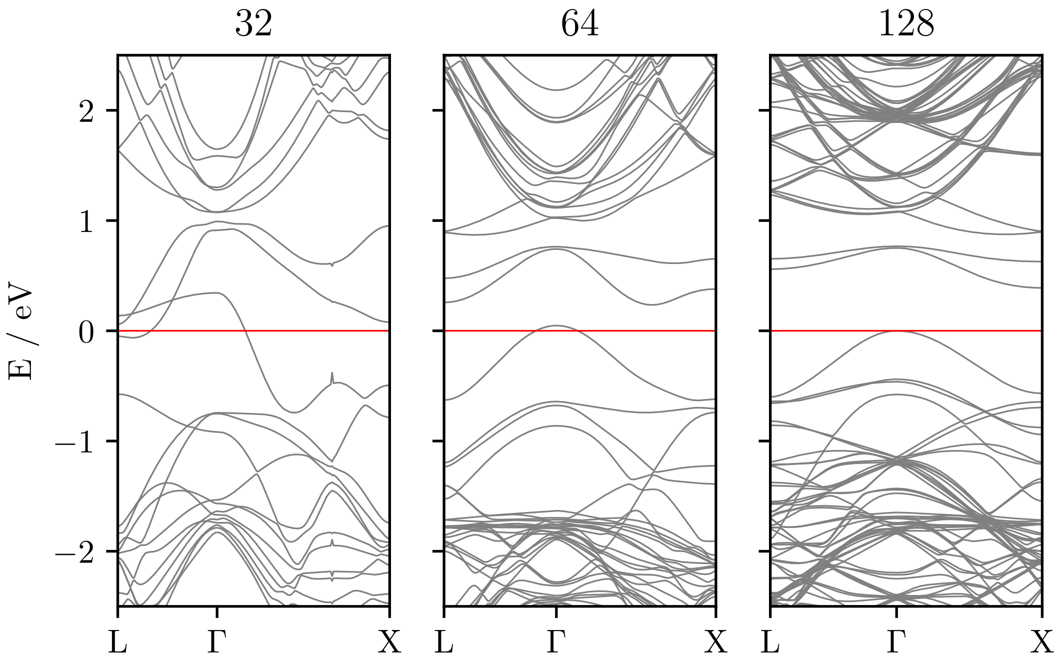

Figure 4.2 Band structures of Si supercells with originally 32, 64 and 128 atoms, from which one atom has been removed.

to become non-dispersive in the limit of an isolated defect. This is not yet the case even for the supercell size of 128 minus 1 atoms. For the rest of the study concerning the defects in silicon, in order to stay within reasonable computational time, we performed the calculations for the 64-atom supercells, except for the cases when the use of 128-atom cells was explicitly indicated.

4.2.2 Hydrogen point defects

The first type of extrinsic defect studied for silicon was the (obviously, interstitial) hydrogen impurity. Three different interstitial positions were investigated as represented in figure 4.3: the tetrahedral position and the bond-center position. The last position concerns dissociated H_2 with one atom lying in a bond center when the second is in a antibonding-typeposition (Chang and Chadi, 1989).

In table 4.1, the formation energy and the band gap values of the H_0, H^-, H^+ and H_2 at the different interstitial positions are shown for supercells containing 64 atoms. The values in the table are listed for defects being in their respective most stable configurations. H^+ stable position is the bond center where the electronic density is the highest, as it was found by Van de Walle *et al.* (1989). At the opposite, H^- prefers the tetrahedral position in the low density region of the cell.

The variation of the formation energy of the last two charged defects with the chemical potential μ is shown if figure 4.4, following the equation:

$$E_f(\mathrm{H}^{\pm}) = E_{\mathrm{Si+H}^{\pm}} - E_{\mathrm{Si}} - \frac{1}{2}E_{\mathrm{H}_2} \pm \mu, \tag{4.1}$$

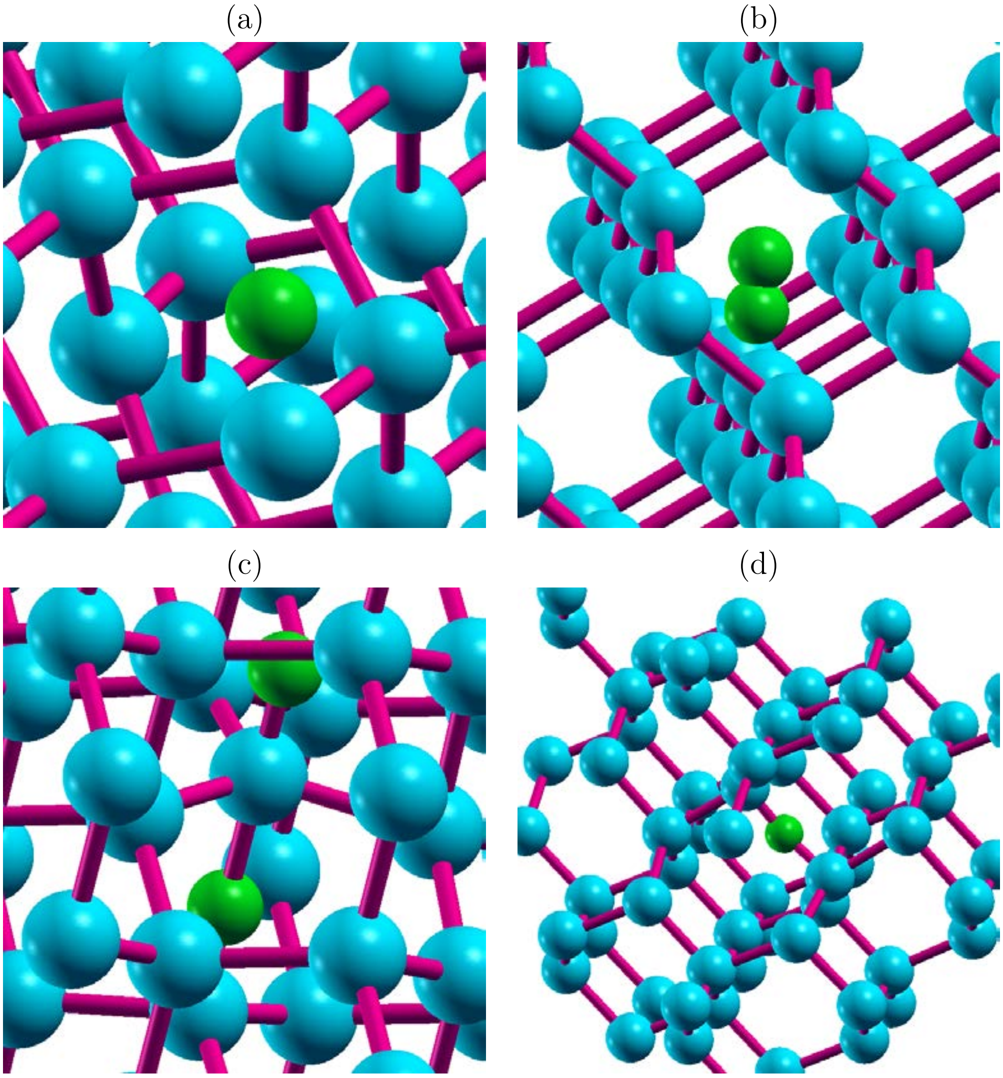

Figure 4.3 Different positions of hydrogen point defects (in green) in silicon bulk (blue) : (a) Tetrahedral (b) H_2 (c) Dissociated H_2 (d) Bond centered.

where $Ef(\mathrm{H}^{\pm})$ being the formation energy of the defect $\mathrm{H}^{\pm}$, $E_{\mathrm{Si+H}^{\pm}}$ the energy of the crystal with the defect, E_{Si} the energy of the equivalent pure crystal, E_{H_2}

Table 4.1 Band gap and formation energy (in eV) of different impurities after relaxation. T stands for tetrahedral, BC for the bond center position and D for dissociated H_2 dissociated with one electron in the tetrahedral position and the other on one of the closest bond centered position.

Defect	Site	E_g	E_f
H_2	T	1.19	1.18
H^0	BC	1.2/0.4	−0.8
H^-	T	1.06	−0.03
H^+	BC	0.85	−1.77
H_2	D	1.20	1.50

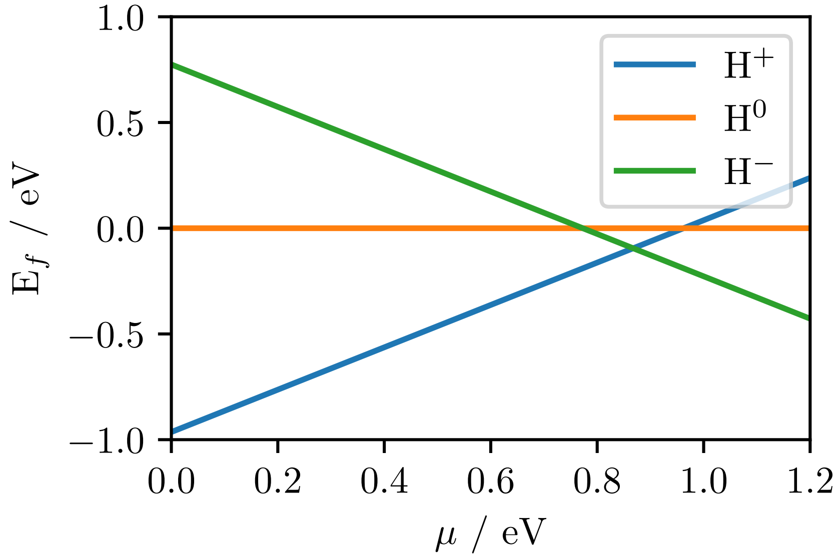

Figure 4.4 Variation of the formation energy of H^+, H^0 and H^- with the chemical potential in silicon.

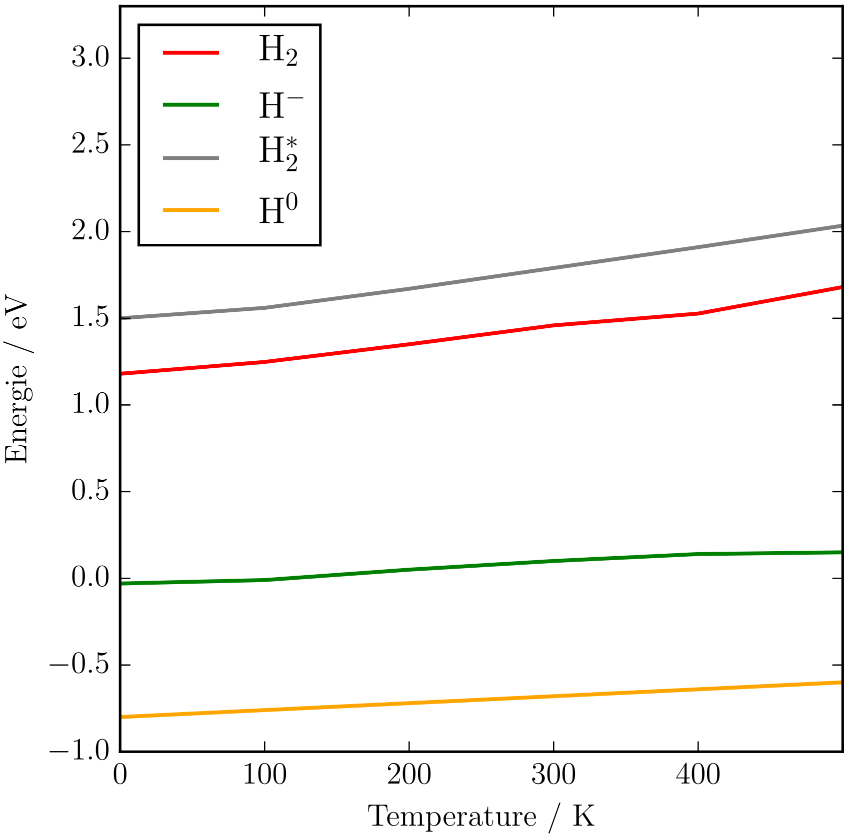

Figure 4.5 Temperature dependence of the formation energy of H^+, H^0, H^- and H_2^* in silicon calculated in the QHA.

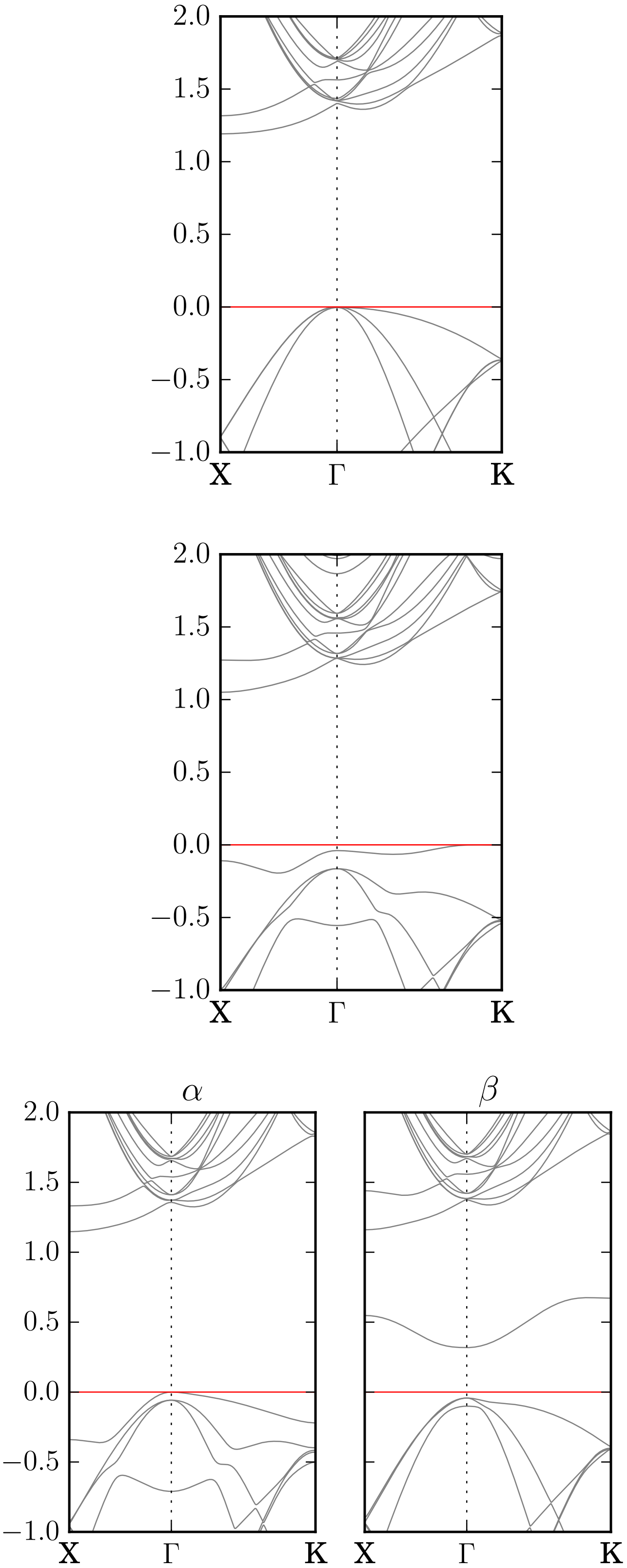

a)

b)

c)

Figure 4.6 Electronic structure of silicon with a) H_2 defect b) H^- defect c) H^0 defect.

the binding energy of H_2 taken as a reference and μ the chemical potential of the electron reservoir, allowing to add or remove an electron to simulate the doped (p or n) crystal. In agreement with the literature (Van de Walle and Neugebauer, 2006), H^+ is more stable than H^- for chemical potential energies comprise between the Fermi level and 0.8 eV. Hydrogen then acts as donor in the p-type Si and as acceptor in the n-type Si.

The temperature dependence, from QHA calculation, of the formation energy of the three states of the monoatomic hydrogen defect has been plotted in figure 4.5. The formation energy increases with temperature for the four types of defects. Finally, electronic structure calculations were performed for the hydrogen point defects. The figure 4.6 represents the band structures of H_2, H^- and H_0 interstitial in silicon along the X-Γ-K path in the Brillouin zone. Whereas H_2 slightly increases the band gap value, the H^- partially closes it due to a presence of an additional band in the band gap at the top of the valence band. The energy level associated with the s orbital of hydrogen defects is not visible for H_2, because it falls deep into the valence bond. However, such levels are placed near the band gap for H^- and H_0 with spin α and even in the middle of it, around 0.5 eV, for the β spin of H_0. We can see that the electronic structure is not fully converged with the supercell size, that is especially visible for H^0 where the band at 0.5 eV is not flat as it is supposed to be for the case of an isolated defect.

4.2.3 Fe, B and FeB complex

The same type of simulation as for hydrogen has been also performed for Fe and B impurities, as well as for the FeB complex. The energy formation calculation confirms the observation of the literature (Brotherton *et al.*, 1985) that Fe tends to go interstitial whereas B substitutes silicon. From there, we simulate FeB complex as a boron in a silicon position bonded with iron inside a tetrahedra. Other configurations were not considered. Different types of oxydation were investigated, FeB, FeB^+ and FeB^-, to find that the neutral complex is the most stable. The band structures of the three defect-containing systems are on display in figures 4.7. Silicon cells doped with boron exhibit the metallic behaviour. For interstitial iron, the band structure is available for α and β spin. In the minority-spin, the band gap additionally opens due to a lower placed valence bond, whereas in the majority-spin channel the band gap decreases due to a presence of a split-off occupied band. At more realistic lower concentration, these effects would eventually disappear. Finally, the FeB electronic structure clearly shows the formation of an additional isolated band in the middle of the gap, responsible for the recombination behaviour of this defect. Both in Fe and FeB electronic structure, the energy level in the middle of the gap or near the Fermi energy are due to the d orbitals of iron.

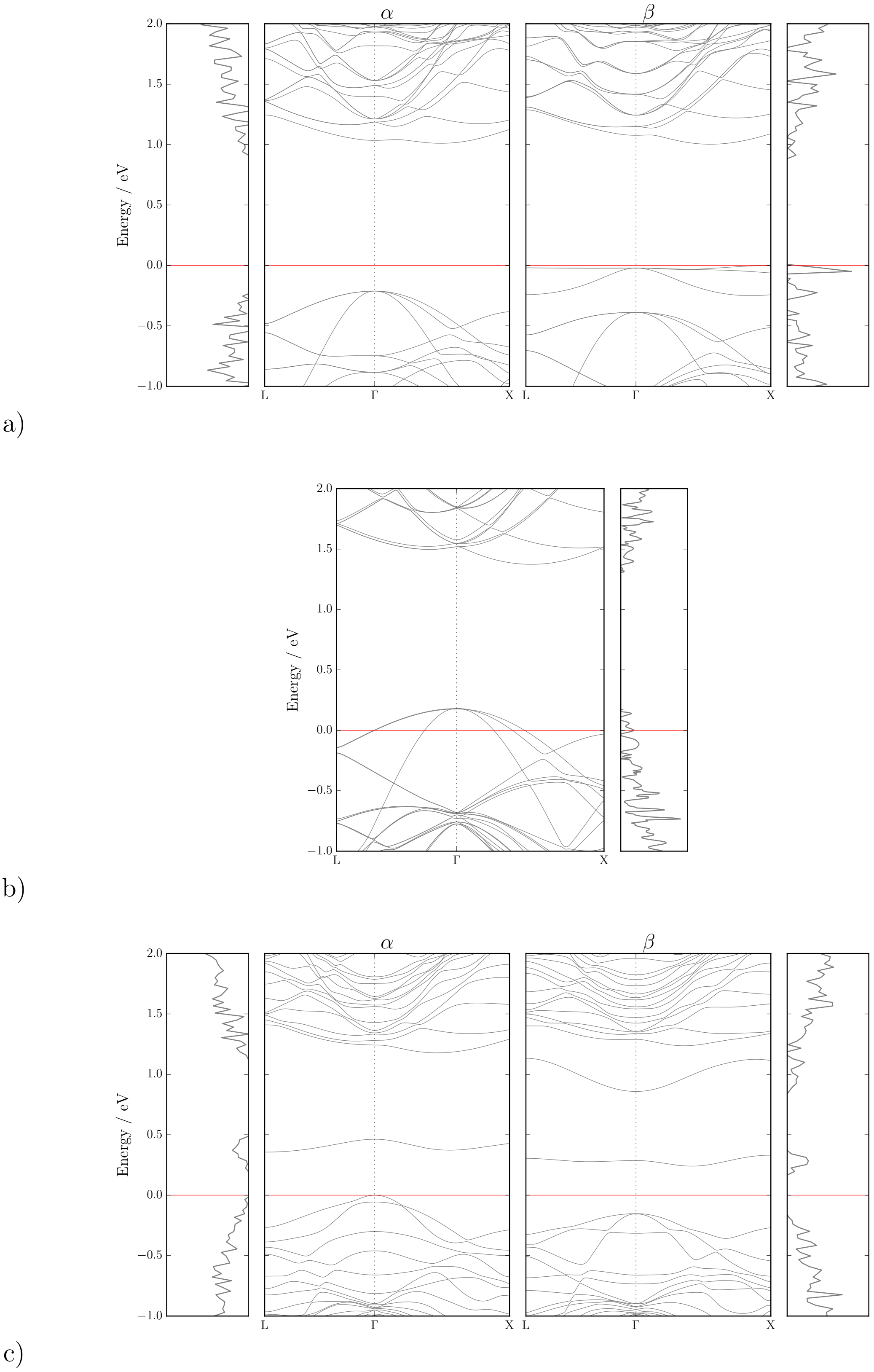

Figure 4.7 Electronic structure and density of states of silicon with a) interstitial Fe at the tetrahedral position, b) substitutional B at the Si site, c) the FeB complex combining the a) and b) defects in adjacent positions.

4.3 Summary and conclusion

Isolated point defects in silicon have been studied in this chapter. For hydrogen incorporation, the neutral defect is less stable than H^- and H^+. Preferential position of iron and boron defect in silicon that have been identified correspond to those earlier suggested in the literature (Brotherton *et al.*, 1985). At high concentration, boron atom in silicon tends to make the compound metallic. Fe does not change the electronic structure except when it forms a complex with B, thus creating a recombination center. Those preliminary results verify our method against earlier known results from the literature and start the work on the silicon cell ageing. In the future work, different type of defect and their combination will be tested.

General conclusion

In solid state physics in general and in the photovoltaic industry in particular, dopants and defects have a major impact on the properties of the material. In order to control them, the comprehension of the atomic behaviour is crucial.

In this thesis, a methodology was adopted to perform quick yet accurate simulation of complex system. The main feature is the use of hybrid functional approach that was optimised in order to correctly describe the experimental value of the band gap. PBE and PBEsol-based hybrid functionals were optimised for various materials used in photovoltaic field: silicon, germanium, SiGe, III-V semiconductors (with III = Ga, In, Al and V = P, As, Sb) and quaternary copper-based chalcopyrite $\mathrm{CuAB_2}$ (with A = In, Ga and B = Se, S). The optimisation scheme employed here was compared to the self-consistent hybrid functional in which the percentage α of the Hartree-Fock exact exchange is linked to the inverse of the high-frequency dielectric constant. Even though the dielectric procedure is a good approximation for α, it does not always describe the electronic properties correctly. For example, small-gap semiconductors such as $\mathrm{CuInSe_2}$ turn out metallic with this approach. The direct optimisation of α for the description obviously does not suffer from this problem and is more pertinent in the context where the correct description of electronic properties is crucial, as in photovoltaic. The PBE and PBEsol-based optimised hybrid functionals were compared to their different counterparts from literature. Their performances on structural, vibrational, mechanical, dielectric and electronic properties were investigated, and the mean absolute relative errors with the experimental data were calculated. The hybrid functional optimised in this work logically gives better result for the electronic properties, but also other properties, especially the structural ones, are well described for the compounds studied in this work. In general, the optimised functionals have the lowest relative errors compared to the other functionals.

GW calculation are time-consuming but very accurate method to obtain the complete electronic structure of a material. Electronic structures of several compounds have been computed via the PBEsol_{hyb} and compared with the results obtained within the GW approximation. In the vicinity of the band gap, the energy bands calculated with the optimised hybrid functional are very close to those obtained within the GW approximation. They are even sometimes better since they are optimised to correspond to the exact experimental band gap. Thus, optimised hybrid functionals are then a very interesting tool to calculate the electronic properties accurately, with precision close to that attainable within the GW, at least in the vicinity of the band gap, in significantly shorter calculation time.

The effect of temperature was then tested with the quasi-harmonic approximation. The variation of the thermal expansion, the heat capacity and the band gap with the temperature show different behaviour compared to experimental data. The first two properties are well described with the temperature variation, but the band gap dependence does not correspond to experimental trends. The inclusion of the electron-phonon coupling in the calculations might be necessary in order to provide the essential correction. Nevertheless, the choice of particular functional does not seem to be very important for estimating the temperature dependence of properties, the resulting behaviour comes out about the same. For thermodynamic study, the optimised hybrid functional is then not markedly better than the other functionals.

Finally, the influence of the choice of functional on the electrical conductivity was studied. Once again, thanks to the correct description of the band gap, optimised hybrid functional give the most accurate result. The larger the fraction of the HF-exact exchange, the higher the calculated electrical conductivity. At this point the methodology have been validated for pure material and ready to use on more complex systems.

The first complex systems investigated were chalcopyrite compounds. One of the key features of CIGSSe is the control of their composition that leads to a tunability of different properties, such as the lattice parameter or the band gap. This feature makes chalcopyrite system promising candidates for applications in tandem cells. In this work, two separate studies on CIGSSe were performed In the first study, the influence of composition for the penternary chalcopyrite $\mathrm{CuIn}_x\mathrm{Ga}_{1-x}(\mathrm{Se}_y\mathrm{S}_{1-y})_2$ on different properties was investigated. A complete mapping of the lattice parameters, band gap and formation energy with the two concentrations x and y was done. The variation of the first properties was practically linear with the concentration and was in agreement with the experimental data. The "optimal" band gap values of $1.5 - 1.7$ eV are accessible for higher concentration of indium than gallium. However, the lattice mismatch with the lattice parameter of silicon in this range of concentrations becomes more important. Even if the lattice mismatch is low, the epitaxy of chalcopyrite on top of a silicon wafer might be difficult. The silicon lattice parameter corresponds to that of chalcopyrite with higher concentration of gallium and sulphur. In all the compositions studied, the system stays in the chalcopyrite symmetry and the energies of formation are negative, thus the system is thermodynamically stable and no secondary phases appear.

In the second study, alkali incorporation by means of cation substitution were performed by a similar method. As alkali post-deposition treatment has been shown in the last five years to be able to importantly increase the efficiency of CIGSSe solar cells, the understanding of the origin of this effect is of great interest. In a few theoretical works so far done on the simulation of point defects, the copper site was identified as the most favorable incorporation site. In this work, we substituted copper by alkali metal for a broad range of concentration, in order to grasp their influence of these dopants on the bulk. The first observation is that alkali metal atoms increase the volume of the cell with an expansion of the lattice parameter a but a contraction of c. However, the system goes from the

$P\bar{4}$ symmetry at lowest concentration to $C2/c$ for the highest one, except for the case of doping with lithium and most of the cases concerning sodium; however, this might be due to an intrinsic issue of the method. This deformation is purely due to the local deformation of the tetrahedra around the substituted atoms. The calculation of electronic properties were then performed. The Mulliken population analysis shows that the different compounds become more ionic with the incorporation of alkali As for the band gap, it increases with the concentration of alkali metal. That is not a good news for gallium-based ternary chalcopyrites that have band gap already larger than the target value, however might be useful for indium-based chalcopyrites to reach the target value. Different energy relations were then calculated corresponding to various chemical reactions. The main conclusion is that the alkali metals incorporation is not easy in chalcopyrite. Even if Li, Na and K have substitution energy lower than 2 eV and hence much lower than Rb and Cs whose substitution energy is around $4 - 5$ eV, all these energies are positive, and the substitution reaction is not spontaneous. Moreover, except for the lithium, thermodynamically, the substitution of the Cu by a alkali metals will lead to the appearance of the secondary phases whatever the considered mechanisms.

Finally, the second complex system studied was silicon with various point defects. In the context of a global project working on the ageing of silicon solar cell, the light and elevated temperature induced degradation (LeTID) might be the consequence of atomic effect linked to hydrogen trapped in the bulk and interacting with defect (iron) or dopant (boron). In this thesis, we performed preliminary calculation of H, Fe, B point defects and FeB complex. Even though these defects are well known in the literature, they served excellent benchmarks to test and validate the calculation method. The most stable position of the different charge states of the point defect correspond to the knowledge from the literature. Now that the simulation of simple isolated defects have been demonstrated to be reliable, the combination of defects can be probed, and the way opened to simulations of the defects' interaction among themselves and e.g. with dislocations.

Bibliography

Abou-Ras, D., S. Wagner, B. J. Stanbery, H.-W. Schock *et al.* (2017). Innovation highway: Breakthrough milestones and key developments in chalcopyrite photovoltaics from a retrospective viewpoint. *Thin Solid Films* **633**, 2.

Abrahams, S. C. and J. L. Bernstein (1974). Piezoelectric nonlinear optic $CuGaSe_2$ and $CdGeAs_2$: Crystal structure, chalcopyrite microhardness, and sublattice distortion. *The Journal of Chemical Physics* **61**(3), 1140. URL http://scitation.aip.org/content/aip/journal/jcp/61/3/10.1063/1.1681987.

Adachi, S. (1985). GaAs, AlAs, and $Al_xGa_{1-x}As$: Material parameters for use in research and device applications. *Journal of Applied Physics* **58**(3), R1. URL http://aip.scitation.org/doi/10.1063/1.336070.

Adamo, C. and V. Barone (1999). Toward reliable density functional methods without adjustable parameters: The PBE0 model. *The Journal of Chemical Physics* **110**(13), 6158. URL http://aip.scitation.org/doi/10.1063/1.478522.

Aguilera, I., J. Vidal, P. Wahnòn, L. Reining *et al.* (2011). First-principles study of the band structure and optical absorption of $CuGaS_2$. *Physical Review B* **84**(8). URL https://link.aps.org/doi/10.1103/PhysRevB.84.085145.

Alkauskas, A., P. Broqvist, F. Devynck and A. Pasquarello (2008). Band Offsets at Semiconductor-Oxide Interfaces from Hybrid Density-Functional Calculations. *Physical Review Letters* **101**(10). URL https://link.aps.org/doi/10.1103/PhysRevLett.101.106802.

Alkauskas, A., P. Broqvist and A. Pasquarello (2011). Defect levels through hybrid density functionals: Insights and applications. *physica status solidi (b)* **248**(4), 775. URL http://doi.wiley.com/10.1002/pssb.201046195.

Alkauskas, A. and A. Pasquarello (2011). Band-edge problem in the theoretical determination of defect energy levels: The O vacancy in ZnO as a benchmark case. *Physical Review B* **84**(12). URL https://link.aps.org/doi/10.1103/PhysRevB.84.125206.

Allen, P. (1996). Boltzmann theory and resistivity of metals. *Kluwer International Series in Engineering and Computer Science* 219–250.

Allen, P. B. and V. Heine (1976). Theory of the temperature dependence of electronic band structures. *Journal of Physics C: Solid State Physics* **9**(12), 2305. URL https://doi.org/10.1088%2F0022-3719%2F9%2F12%2F013.

Alonso, M. I. and K. Winer (1989). Raman spectra of c–$Si_{1-x}Ge_x$ alloys. *Physical Review B* **39**(14), 10056. URL https://link.aps.org/doi/10.1103/PhysRevB.39.10056.

Aryasetiawan, F. and O. Gunnarsson (1998). The GW method. *Reports on Progress in Physics* **61**(3), 237. URL https://doi.org/10.1088/0034-4885/61/3/002.

Aspnes and Studna (1972). Direct observation of the E_0 and E_0+$\delta 0$ transition in silion. *Solid State Communications* **11**(10), 1375.

Azuhata, T., T. Sota and K. Suzuki (1995). Second-order Raman spectra and lattice dynamics in AlAs. *Journal of Physics: Condensed Matter* **7**(9), 1949. URL https://doi.org/10.1088%2F0953-8984%2F7%2F9%2F018.

Baars, J. and W. H. Koschel (1972). Dielectric dispersion of $CuGaS_2$ by infrared reflectivity analysis. *Solid State Communications* **11**(11), 1513. URL http://www.sciencedirect.com/science/article/pii/003810987290511X.

Bär, M., W. Bohne, J. Röhrich, E. Strub *et al.* (2004). Determination of the band gap depth profile of the penternary $Cu(In_{1-x}Ga_x)(S_ySe_{1-y})_2$ chalcopyrite from its composition gradient. *Journal of Applied Physics* **96**(7), 3857. URL http://aip.scitation.org/doi/10.1063/1.1786340.

Barker, A. S. (1968). Dielectric Dispersion and Phonon Line Shape in Gallium Phosphide. *Physical Review* **165**(3), 917. URL https://link.aps.org/doi/10.1103/PhysRev.165.917.

Becke, A. D. (1993a). Density functional thermochemistry. III. The role of exact exchange. *The Journal of Chemical Physics* **98**(7), 5648. URL http://aip.scitation.org/doi/10.1063/1.464913.

Becke, A. D. (1993b). A new mixing of Hartree–Fock and local density functional theories. *The Journal of Chemical Physics* **98**(2), 1372. URL http://aip.scitation.org/doi/10.1063/1.464304.

Beer, S., J. Jackovitz, D. Feldman and J. Parker (1968). Raman and infrared active modes of aluminium phosphide. *Physics Letters A* **26**(7), 331. URL https://linkinghub.elsevier.com/retrieve/pii/0375960168906804.

Bettini, M. and W. B. Holzapfel (1975). Grüneisen parameters of τ phonons in $CdSiP_2$, $CuAlS_2$ and $CuGaS_2$. *Solid State Communications* **16**(1), 27. URL http://www.sciencedirect.com/science/article/pii/0038109875907814.

Betzinger, M. (2007). Efficient Implementation of the Non–Local Exchange Potential within the FLAPW Method. Ph.D. thesis, Diplomarbeit, RWTH Aachen, Institut für Festkörperphysik, Forschungszentrum Jülich.

Biernacki, S. and M. Scheffler (1989). Negative thermal expansion of diamond and zinc-blende semiconductors. *Physical Review Letters* **63**(3), 290. URL `https://link.aps.org/doi/10.1103/PhysRevLett.63.290`.

Birch, F. (1947). Finite Elastic Strain of Cubic Crystals. *Physical Review* **71**(11), 809. URL `https://link.aps.org/doi/10.1103/PhysRev.71.809`.

Bludau, W., A. Onton and W. Heinke (1974). Temperature dependence of the band gap of silicon. *Journal of Applied Physics* **45**(4), 1846. URL `http://aip.scitation.org/doi/10.1063/1.1663501`.

Bodnar, I. V., B. V. Korzun and A. I. Lukomskii (1981). Composition dependence of the band gap of $\mathrm{CuInS}_{2x}\mathrm{Se}_{2(1-x)}$. *physica status solidi (b)* **105**(2), K143. URL `http://onlinelibrary.wiley.com/doi/abs/10.1002/pssb.2221050259`.

Bodnar, I. V. and A. I. Lukomskii (1986). The concentration dependence of the band gap $\mathrm{CuGa}_x\mathrm{In}_{1-x}\mathrm{S}_2$ and $\mathrm{AgGa}_x\mathrm{In}_{1-x}\mathrm{S}_2$ solid solutions. *physica status solidi (a)* **98**(2), K165. URL `http://onlinelibrary.wiley.com/doi/abs/10.1002/pssa.2210980255`.

Bodnar, I. V. and N. S. Orlova (1983). X-ray study of the thermal expansion in CuAlS_2, CuGaS_2, and CuInS_2 compounds over the temperature range from 90 to 650 K. *Physica Status Solidi (a)* **78**(1), K59. URL `http://doi.wiley.com/10.1002/pssa.2210780155`.

Boehnke, U. and H. Neumann (1992). $\mathrm{Cu}_{1-x}\mathrm{Li}_x\mathrm{InSe}_2$. *Journal of Alloys and Compounds* **190**(1).

Bolef, D. I. and M. Menes (1960). Elastic Constants of Single–Crystal Aluminum Antimonide. *Journal of Applied Physics* **31**(8), 1426. URL `http://aip.scitation.org/doi/10.1063/1.1735857`.

Born, M. and R. Oppenheimer (1927). Zur Quantentheorie der Molekeln. *Annalen der Physik* **389**(20), 457. URL `https://onlinelibrary.wiley.com/doi/abs/10.1002/andp.19273892002`.

Boyle, W. F. and R. J. Sladek (1975). Elastic constants and lattice anharmonicity of GaSb and GaP from ultrasonic-velocity measurements between 4.2 and 300 K. *Physical Review B* **11**(8), 2933. URL `https://link.aps.org/doi/10.1103/PhysRevB.11.2933`.

Boys, S. (1950). Electronic wave functions. I. A general method of calculation for the stationary states of any molecular system. *Proceeding of the Royal Society of London* **200**.

Boys, S. and F. Bernardi (1970). The calculation of small molecular interactions by the differences of separate total energies. Some procedures with reduced errors. *Molecular Physics* **19**(4), 553. URL `http://www.tandfonline.com/doi/full/10.1080/00268977000101561`.

Broqvist, P., A. Alkauskas and A. Pasquarello (2008). Defect levels of dangling bonds in silicon and germanium through hybrid functionals. *Physical Review B* **78**(7). URL `https://link.aps.org/doi/10.1103/PhysRevB.78.075203`.

Brotherton, S. D., P. Bradley and A. Gill (1985). Iron and the iron-boron complex in silicon. *Journal of Applied Physics* **57**(6), 1941. URL `http://aip.scitation.org/doi/10.1063/1.335468`.

Cardona, M., F. H. Pollak and K. L. Shaklee (1966). Electroreflectance in AlSb: Observation of the Direct Band Edge. *Physical Review Letters* **16**(15), 644. URL `https://link.aps.org/doi/10.1103/PhysRevLett.16.644`.

Carles, R., N. Saint-Cricq, J. B. Renucci, M. A. Renucci *et al.* (1980). Second-order Raman scattering in InAs. *Physical Review B* **22**(10), 4804. URL `https://link.aps.org/doi/10.1103/PhysRevB.22.4804`.

Carr, J. A. and S. Chaudhary (2013). The identification, characterization and mitigation of defect states in organic photovoltaic devices: a review and outlook. *Energy & Environmental Science* **6**(12), 3414. URL `http://xlink.rsc.org/?DOI=c3ee41860j`.

Chang, K. J. and D. J. Chadi (1989). Hydrogen bonding and diffusion in crystalline silicon. *Physical Review B* **40**(17), 11644. URL `https://link.aps.org/doi/10.1103/PhysRevB.40.11644`.

Chen, D., P. G. Hamer, M. Kim, T. H. Fung *et al.* (2018). Hydrogen induced degradation: A possible mechanism for light- and elevated temperature-induced degradation in n-type silicon. *Solar Energy Materials and Solar Cells* **185**, 174. URL `https://linkinghub.elsevier.com/retrieve/pii/S0927024818302617`.

Chirilă, A., P. Reinhard, F. Pianezzi, P. Bloesch *et al.* (2013). Potassium-induced surface modification of Cu(In,Ga)Se$_2$ thin films for high-efficiency solar cells. *Nature Materials* **12**(12), 1107.

Cho, D.-H., K.-S. Lee, Y.-D. Chung, J.-H. Kim *et al.* (2012). Electronic effect of Na on Cu(In,Ga)Se$_2$ solar cells. *Appl. Phys. Lett.* 5.

Cojocaru-Mirédin, O., P.-P. Choi, D. Abou-Ras, S. S. Schmidt *et al.* (2011). Characterization of Grain Boundaries in Cu(In,Ga)Se$_2$ Films Using Atom-Probe Tomography. *IEEE Journal of Photovoltaics* **1**(2), 207.

Cojocaru-Mirédin, O., T. Schwarz, P.-P. Choi, M. Herbig *et al.* (2013). Atom probe tomography studies on the Cu(In,Ga)Se$_2$ grain boundaries. *Journal of Visualized Experiments : JoVE* **74**. URL `https://www.ncbi.nlm.nih.gov/pmc/articles/PMC3667468/`.

Conesa, J. C. (2012). Modeling with Hybrid Density Functional Theory the Electronic Band Alignment at the Zinc Oxide–Anatase Interface. *The Journal of Physical Chemistry C* **116**(35), 18884. URL `http://pubs.acs.org/doi/10.1021/jp306160c`.

Contreras, M. A., B. Egaas, P. Dippo, J. Webb *et al.* (1997). On the role of na and modifications to Cu(In,Ga)Se_2 absorber materials using thin-MF (M= Na, K, Cs) precursor layers [solar cells]. In *Conference Record of the Twenty Sixth IEEE Photovoltaic Specialists Conference-1997*, 359–362. IEEE.

Corruccini, R. J. and J. J. Gniewek (1960). Specific heats and enthalpies of technical solids at low temperatures. A compilation from the literature. Technical Report NBS-Mon-21, National Bureau of Standards, Washington, D.C. URL `https://www.osti.gov/biblio/4803576`.

Cottam, R. I. and G. A. Saunders (1973). The elastic constants of GaAs from 2 K to 320 K. *Journal of Physics C: Solid State Physics* **6**(13), 2105. URL `http://stacks.iop.org/0022-3719/6/i=13/a=011?key=crossref.f69af4617f3239c6ea359f866ce8a29d`.

Coughlan, C., M. Ibáñez, O. Dobrozhan, A. Singh *et al.* (2017). Compound copper chalcogenide nanocrystals. *Chemical Reviews* **117**(9), 5865. URL `http://pubs.acs.org/doi/10.1021/acs.chemrev.6b00376`.

CRYSTAL17 (2019). `CRYSTAL` - basis sets library. URL `http://www.crystal.unito.it/basis-sets.php`.

Deák, P., A. Gali, A. Sólyom, A. Buruzs *et al.* (2005). Electronic structure of boron-interstitial clusters in silicon. *Journal of Physics: Condensed Matter* **17**(22), S2141. URL `http://stacks.iop.org/0953-8984/17/i=22/a=001?key=crossref.c6b31286fe557d1278163f8e2c06d3ce`.

Desai, P. D. (1986). Thermodynamic Properties of Iron and Silicon. *Journal of Physical and Chemical Reference Data* **15**(3), 967. URL `http://aip.scitation.org/doi/10.1063/1.555761`.

Deus, P., H. Neumann, G. Kühn and B. Hinze (1983a). Low-temperature thermal expansion in $CuInSe_2$. *Physica Status Solidi (a)* **80**(1), 205. URL `http://doi.wiley.com/10.1002/pssa.2210800122`.

Deus, P., U. Voland and H. A. Schneider (1983b). Thermal expansion of GaP within 20 to 300 K. *Physica Status Solidi (a)* **80**(1), K29. URL `http://doi.wiley.com/10.1002/pssa.2210800152`.

Dirac, P. A. M. (1930). Note on Exchange Phenomena in the Thomas Atom. *Mathematical Proceedings of the Cambridge Philosophical Society* **26**(03), 376. URL `http://www.journals.cambridge.org/abstract_S0305004100016108`.

Dismukes, J. P., L. Ekstrom and R. J. Paff (1964). Lattice Parameter and Density in Germanium-Silicon Alloys. *Journal of Physicsal Chemistry* **437**(10), 3021.

Dovesi, R., B. Civalleri, R. Orlando, C. Roetti *et al.* (2005). *Ab initio* quantum simulation in solid state chemistry. *Reviews in computational chemistry* **21**, 1.

Dovesi, R., A. Erba, R. Orlando, C. M. Zicovich-Wilson *et al.* (2018). Quantum-mechanical condensed matter simulations with CRYSTAL. *Wiley Interdisciplinary Reviews: Computational Molecular Science* **8**(4).

Dovesi, R., E. Ermondi, E. Ferrero, C. Pisani *et al.* (1983). Hartree-Fock study of lithium hydride with the use of a polarizable basis set. *Phys. Rev. B* **29**, 3591. URL `https://doi.org/10.1103/PhysRevB.29.3591`.

Dovesi, R., C. Roetti, C. Freyria Fava and V. Prencipe, M.and Saunders (1991). On the elastic properties of lithium, sodium an potassium oxide. An *ab initio* study. *Chem. Phys.* **156**, 11.

Dziedzic, J., Q. Hill and C.-K. Skylaris (2013). Linear-scaling calculation of Hartree-Fock exchange energy with non-orthogonal generalised Wannier functions. *The Journal of Chemical Physics* **139**(21), 214103. URL `http://aip.scitation.org/doi/10.1063/1.4832338`.

Eid, J., H. Liang, I. Gereige, S. Lee *et al.* (2015). Combinatorial study of NaF addition in CIGSe films for high efficiency solar cells. *Progress in Photovoltaics: Research and Applications* **23**(3), 269.

Eifler, A., V. Riede, J. Brückner, S. Weise *et al.* (2000). Band Gap Energies and Lattice Vibrations of the Lithium Ternary Compounds $LiInSe_2$, $LiInS_2$, $LiGaSe_2$ and $LiGaS_2$. *Japanese Journal of Applied Physics* **39**(S1), 279. URL `http://stacks.iop.org/1347-4065/39/279`.

Erba, A. (2014). On combining temperature and pressure effects on structural properties of crystals with standard *ab initio* techniques. *The Journal of Chemical Physics* **141**(12), 124115. URL `http://aip.scitation.org/doi/10.1063/1.4896228`.

Erba, A. (2017). Self-consistent hybrid functionals for solids: a fully-automated implementation. *Journal of Physics: Condensed Matter* **29**(31), 314001. URL `http://stacks.iop.org/0953-8984/29/i=31/a=314001?key=crossref.688c4f145cedf8f27dc556a5cff87ee4`.

Faghaninia, A. (2016). Theory of Carrier Transport From First Principles: Applications in Photovoltaic and Thermoelectric Materials. Ph.D. thesis, Washington University.

Faghaninia, A., J. W. Ager and C. S. Lo (2015). *Ab initio* electronic transport model with explicit solution to the linearized Boltzmann transport equation. *Phys. Rev. B* **91**(23).

Faghaninia, A., G. Yu, U. Aydemir, M. Wood *et al.* (2017). A computational assessment of the electronic, thermoelectric, and defect properties of bournonite ($CuPbSbS_3$) and related substitutions. *Physical Chemistry Chemical Physics* **19**(9), 6743.

Fang, Z. M., K. Y. Ma, D. H. Jaw, R. M. Cohen *et al.* (1990). Photoluminescence of InSb, InAs, and InAsSb grown by organometallic vapor phase epitaxy. *Journal of Applied Physics* **67**(11), 7034. URL `http://aip.scitation.org/doi/10.1063/1.345050`.

Faulkner, R. A. (1969). Higher donor excited states for prolate-spheroid conduction bands: A reevaluation of silicon and germanium. *Physical Review* **184**(3), 713. URL `https://link.aps.org/doi/10.1103/PhysRev.184.713`.

Feng, K., D. Mei, L. Bai, Z. Lin *et al.* (2012). Synthesis, structure, physical properties, and electronic structure of $KGaSe_2$. *Solid State Sciences* **14**(8), 1152. URL `https://linkinghub.elsevier.com/retrieve/pii/S1293255812001914`.

Ferrero, M., M. Rérat, R. Orlando and R. Dovesi (2008). Coupled perturbed Hartree-Fock for periodic systems: The role of symmetry and related computational aspects. *The Journal of Chemical Physics* **128**(1), 014110. URL `http://aip.scitation.org/doi/10.1063/1.2817596`.

Fine, M. E. (1955). Elastic Constants of Germanium between 1.7 and 80 K. *Journal of Applied Physics* **26**(7), 862. URL `http://aip.scitation.org/doi/10.1063/1.1722110`.

Fock, V. (1930). Näherungsmethode zur Lösung des quantenmechanischen Mehrkörperproblems. *Zeitschrift für Physik* **61**(1–2), 126. URL `http://dx.doi.org/10.1007/BF01340294`.

Forest, R. V., B. E. McCandless, X. He, A. A. Rockett *et al.* (2017). Diffusion of sodium in single crystal $CuInSe_2$. *Journal of Applied Physics* **121**(24), 245102.

Friedrich, D., M. Schlosser, M. Etter and A. Pfitzner (2017a). Influence of Alkali Metal Substitution on the Phase Transition Behavior of $CsGaQ_2$ ($Q = S, Se$). *Crystals* **7**(12), 379. URL `http://www.mdpi.com/2073-4352/7/12/379`.

Friedrich, D., M. Schlosser and A. Pfitzner (2017b). Synthesis and Structural Characterization of the layered Selenogallate $RbGaSe_2$. *Zeitschrift für anorganische und allgemeine Chemie* **643**(21), 1589. URL `http://onlinelibrary.wiley.com/doi/abs/10.1002/zaac.201700288`.

Fritsch, D., B. J. Morgan and A. Walsh (2017). Self-Consistent Hybrid Functional Calculations: Implications for Structural, Electronic, and Optical Properties of Oxide Semiconductors. *Nanoscale Research Letters* **12**(1). URL `http://nanoscalereslett.springeropen.com/articles/10.1186/s11671-016-1779-9`.

Fung, T. H., M. Kim, D. Chen, C. E. Chan *et al.* (2018). A four-state kinetic model for the carrier-induced degradation in multicrystalline silicon: Introducing the reservoir state. *Solar Energy Materials and Solar Cells* **184**, 48. URL `https://linkinghub.elsevier.com/retrieve/pii/S0927024818301995`.

Garland, C. W. and K. C. Park (1962). Low Temperature Elastic Constants of Gallium Arsenide. *Journal of Applied Physics* **33**(2), 759. URL `http://aip.scitation.org/doi/10.1063/1.1702519`.

Gerlich, D. (1963). Elastic Constants of Single–Crystal Indium Arsenide. *Journal of Applied Physics* **34**(9), 2915. URL `http://aip.scitation.org/doi/10.1063/1.1729833`.

Gerlich, D. (1964). Low–Temperature Elastic Constants of Indium Arsenide. *Journal of Applied Physics* **35**(10), 3062. URL `https://aip-scitation-org.bases-doc.univ-lorraine.fr/doi/10.1063/1.1713174`.

Ghorbani, E., J. Kiss, H. Mirhosseini, G. Roma *et al.* (2015). Hybrid-functional calculations on the incorporation of na and k impurities into the $CuInSe_2$ and $CuIn_5Se_8$ solar-cell materials. *The Journal of Physical Chemistry C* **119**(45), 25197. URL `http://pubs.acs.org/doi/10.1021/acs.jpcc.5b07639`.

Gibbons, D. F. (1958). Thermal Expansion of Some Crystals with the Diamond Structure. *Physical Review* **112**(1), 136. URL `https://link.aps.org/doi/10.1103/PhysRev.112.136`.

Glazov, V. M. and A. S. Pashinkin (2001). The Thermophysical Properties (Heat Capacity and Thermal Expansion) of Single-Crystal Silicon. *High Temperature* **39**(3), 413. URL `https://doi.org/10.1023/A:1017562709942`.

Granath, K., M. Bodegard and L. Solt (2000). The effect of NaF on $Cu(In,Ga)Se_2$ thin film solar cells. *Solar Energy Materials & Solar Cells* **60**.

Hahn, H., G. Frank, W. Klingler, A.-D. Meyer *et al.* (1953). Untersuchungen über ternäre Chalkogenide. V. Über einige ternäre Chalkogenide mit Chalkopyritstruktur. *Zeitschrift für anorganische und allgemeine Chemie* **271**(3-4), 153. URL `http://onlinelibrary.wiley.com/doi/abs/10.1002/zaac.19532710307`.

Hall, J. J. (1967). Electronic effects in the elastic constants of n-type silicon. *Phys. Rev.* **161**(1961), 756. URL `https://link.aps.org/doi/10.1103/PhysRev.161.756http://link.aps.org/doi/10.1103/PhysRev.161.756`.

Hallam, B. J., S. R. Wenham, P. G. Hamer, M. D. Abbott *et al.* (2013). Hydrogen Passivation of B-O Defects in Czochralski Silicon. *Energy Procedia* **38**, 561. URL `https://linkinghub.elsevier.com/retrieve/pii/S1876610213014033`.

Handick, E., P. Reinhard, R. G. Wilks, F. Pianezzi *et al.* (2017). Formation of a K—In—Se Surface Species by NaF/KF Postdeposition Treatment of Cu(In,Ga)Se_2 Thin-Film Solar Cell Absorbers. *ACS Applied Materials & Interfaces* **9**(4), 3581.

Hartree, D. R. (1928a). The Wave Mechanics of an Atom with a Non-Coulomb Central Field. Part I. Theory and Methods. *Mathematical Proceedings of the Cambridge Philosophical Society* **24**(1), 89.

Hartree, D. R. (1928b). The Wave Mechanics of an Atom with a Non-Coulomb Central Field. Part II. Some Results and Discussion. *Mathematical Proceedings of the Cambridge Philosophical Society* **24**(1), 111.

Hass, M. and B. Henvis (1962). Infrared lattice reflection spectra of III-V compound semiconductors. *J. Phys. Chem. Solids* **23**, 1099.

Hay, P. and W. Wadt (1985a). *Ab initio* effective core potentials for molecular calculations. Potentials for K to Au including the outermost orbitals. *J. Chem. Phys.* **82**, 299.

Hay, P. and W. Wadt (1985b). *Ab initio* effective core potentials for molecular calculations. Potentials for main group elements Na to Bi. *J. Chem. Phys.* **82**, 284.

Hedstrom, J., H. Ohlsen, M. Bodegard, A. Kylner *et al.* (1993). ZnO/CdS/Cu(In,Ga)Se_2 thin film solar cells with improved performance. In *Conference Record of the Twenty Third IEEE Photovoltaic Specialists Conference - 1993 (Cat. No.93CH3283-9)*, 364–371. IEEE, Louisville, KY, USA.

Hehre, J., L. Radom, P. Schleyer and J. Pople (1986). *Ab initio molecular orbital theory*. John Wiley & Sons.

Henderson, T. M., A. F. Izmaylov, G. E. Scuseria and A. Savin (2007). The importance of middle-range Hartree-Fock-type exchange for hybrid density functionals. *The Journal of Chemical Physics* **127**(22), 221103. URL `http://aip.scitation.org/doi/10.1063/1.2822021`.

Henderson, T. M., A. F. Izmaylov, G. E. Scuseria and A. Savin (2008). Assessment of a Middle-Range Hybrid Functional. *Journal of Chemical Theory and Computation* **4**(8), 1254. URL `http://pubs.acs.org/doi/abs/10.1021/ct800149y`.

Herguth, A., G. Schubert, M. Kaes and G. Hahn (2006). A New Approach to Prevent the Negative Impact of the Metastable Defect in Boron Doped CZ Silicon Solar Cells. In *2006 IEEE 4th World Conference on Photovoltaic Energy Conference*, 940–943. IEEE, Waikoloa, HI. URL `http://ieeexplore.ieee.org/document/4059784/`.

Herring, C., N. M. Johnson and C. G. Van de Walle (2001). Energy levels of isolated interstitial hydrogen in silicon. *Physical Review B* **64**(12). URL `https://link.aps.org/doi/10.1103/PhysRevB.64.125209`.

Heyd, J., J. E. Peralta, G. E. Scuseria and R. L. Martin (2005). Energy band gaps and lattice parameters evaluated with the Heyd-Scuseria-Ernzerhof screened hybrid functional. *The Journal of Chemical Physics* **123**(17), 174101. URL https://aip-scitation-org.bases-doc.univ-lorraine.fr/doi/10.1063/1.2085170.

Heyd, J., G. E. Scuseria and M. Ernzerhof (2003). Hybrid functionals based on a screened Coulomb potential. *The Journal of Chemical Physics* **118**(18), 8207. URL http://aip.scitation.org/doi/10.1063/1.1564060.

Heyd, J., G. E. Scuseria and M. Ernzerhof (2006). Erratum: Hybrid functionals based on a screened Coulomb potential [J. Chem. Phys. 118, 8207 (2003)]. *The Journal of Chemical Physics* **124**(21), 219906. URL http://aip.scitation.org/doi/10.1063/1.2204597.

Hickernell, F. S. and W. R. Gayton (1966). Elastic Constants of Single–Crystal Indium Phosphide. *Journal of Applied Physics* **37**(1), 462. URL http://aip.scitation.org/doi/10.1063/1.1707886.

Hinuma, Y., Y. Kumagai, I. Tanaka and F. Oba (2017). Band alignment of semiconductors and insulators using dielectric-dependent hybrid functionals: Toward high-throughput evaluation. *Physical Review B* **95**(7). URL https://link.aps.org/doi/10.1103/PhysRevB.95.075302.

Hohenberg, P. and W. Kohn (1964). Inhomogeneous Electron Gas. *Physical Review* **136**(3B), 8.

Holt, D. B. and B. G. Yacobi (2007). *Extended Defects in Semiconductors by D. B. Holt*. Cambridge University Press. URL /core/books/extended-defects-in-semiconductors/F94B911A858720A2B44C32F5CBC0CAFD.

Huang, F. Q., B. Deng, D. E. Ellis and J. A. Ibers (2005). Preparation, structures, and band gaps of $RbInS_2$ and $RbInSe_2$. *Journal of Solid State Chemistry* **178**(6), 2128. URL http://linkinghub.elsevier.com/retrieve/pii/S0022459605001581.

Ioffe Institute (2019). NSM Archive - Physical Properties of Semiconductors. URL http://www.ioffe.ru/SVA/NSM/Semicond/.

Isaenko, L., A. Yelisseyev, S. Lobanov, A. Titov *et al.* (2003). Growth and properties of $LiGaX_2$ (X = S, Se, Te) single crystals for nonlinear optical applications in the mid-IR. *Crystal Research and Technology* **38**(35), 379. URL http://doi.wiley.com/10.1002/crat.200310047.

Ishizuka, S., N. Taguchi, J. Nishinaga, Y. Kamikawa *et al.* (2018). Group III Elemental Composition Dependence of RbF Postdeposition Treatment Effects on $Cu(In,Ga)Se_2$ Thin Films and Solar Cells. *The Journal of Physical Chemistry C* **122**(7), 3809.

Ishizuka, S., A. Yamada, M. M. Islam, H. Shibata *et al.* (2009). Na-induced variations in the structural, optical, and electrical properties of Cu(In,Ga)Se_2 thin films. *Journal of Applied Physics* **106**(3), 034908.

Jackson, P., R. Wuerz, D. Hariskos, E. Lotter *et al.* (2016). Effects of heavy alkali elements in Cu(In,Ga)Se_2 solar cells with efficiencies up to 22.6%. *physica status solidi (RRL) - Rapid Research Letters* **10**(8), 583.

Jaffe, J. E. and A. Zunger (1983). Electronic structure of the ternary chalcopyrite semiconductors $CuAlS_2$, $CuGaS_2$, $CuInS_2$, $CuAlSe_2$, $CuGaSe_2$, and $CuInSe_2$. *Phys. Rev. B* **28**(10), 5822.

Jiang, F. D. and J. Y. Feng (2008). Electronic modification of cu-based chalcopyrite semiconductors induced by lattice deformation and composition alchemy. *Semiconductor Science and Technology* **23**(2), 025001. URL `http://stacks.iop.org/0268-1242/23/i=2/a=025001?key=crossref.fd5db77c8022d5f52cbb3808b64f74ac`.

Kagaya, H. M. and T. Soma (1987). Specific heat and thermal expansion coefficient of AlP, AlAs and AlSb. *Solid State Communications* **62**(10), 707. URL `http://www.sciencedirect.com/science/article/pii/0038109887904133`.

Kamijoh, T. and K. Kuriyama (1981). Single crystal growth and characterization of $LiInSe_2$. *Journal of Crystal Growth* **51**(1), 6. URL `http://www.sciencedirect.com/science/article/pii/0022024881900038`.

Karki, S., P. Paul, G. Rajan, B. Belfore *et al.* (2019). Analysis of Recombination Mechanisms in RbF-Treated CIGS Solar Cells. *IEEE Journal of Photovoltaics* **9**(1), 313.

Kato, T., J.-L. Wu, Y. Hirai, H. Sugimoto *et al.* (2018). Record Efficiency for Thin-Film Polycrystalline Solar Cells Up to 22.9% Achieved by Cs-Treated Cu(In,Ga)$(Se,S)_2$. *IEEE Journal of Photovoltaics* 1–6.

Khatri, I., H. Fukai, H. Yamaguchi, M. Sugiyama *et al.* (2016). Effect of potassium fluoride post-deposition treatment on Cu(In,Ga)Se_2 thin films and solar cells fabricated onto sodalime glass substrates. *Solar Energy Materials and Solar Cells* **155**, 280.

Kiefer, W., W. Richter and M. Cardona (1975). Second-order Raman scattering in InSb. *Physical Review B* **12**(6), 2346. URL `https://link.aps.org/doi/10.1103/PhysRevB.12.2346`.

Kim, S., H. Tampo, H. Shibata, K. Matsubara *et al.* (2018). Effect of Combined Alkali (KF + CsF) Post-Deposition Treatment on Cu(InGa)Se_2 Solar Cells. *physica status solidi (RRL) – Rapid Research Letters* **12**(10), 1800372.

Kish, Z. (1985). Synthesis and Crystal Structure of Lithium Thioindate $LiInS_2$. *Doklady Akademii nauk SSSR* **280**(2).

Kittel, C. (2004). *Introduction to solid state physics.*. Wiley, 8 edition. URL https://www.osti.gov/etdeweb/biblio/7307886.

Kodalle, T., M. D. Heinemann, D. Greiner, H. A. Yetkin *et al.* (2018). Elucidating the Mechanism of an RbF Post Deposition Treatment in CIGS Thin Film Solar Cells. *Solar RRL* **2**(9), 1800156.

Kohn, W. and L. J. Sham (1965). Self-Consistent Equations Including Exchange and Correlation Effects. *Physical Review* **140**(4A), A1133. URL https://link.aps.org/doi/10.1103/PhysRev.140.A1133.

Kraft, A., G. Kühn and W. Möller (1983). Untersuchung von $CuGaSe_2$ und $CuGaTe_2$ unter hohem Druck. *Zeitschrift für anorganische und allgemeine Chemie* **504**(9), 155. URL http://onlinelibrary.wiley.com/doi/abs/10.1002/zaac.19835040920.

Krebs, B. (2006). Thio- und Selenoverbindungen von Hauptgruppenelementen - neue anorganische Oligomere und Polymere. *Angewandte Chemie* **95**(2), 113. URL http://doi.wiley.com/10.1002/ange.19830950206.

Krishnan, R. and N. Krishnamurthy (1965). The Raman spectrum of gallium phosphide. *Journal de Physique* **26**(11), 630. URL http://www.edpsciences.org/10.1051/jphys:019650026011063000.

Kronik, L., D. Cahen and H. W. Schock (1998). Effects of Sodium on Polycrystalline Cu(In,Ga)Se_2 and Its Solar Cell Performance. *Advanced Materials* **10**(1), 31.

Kuriyama, K. and T. Nozaki (1981). Single–crystal growth and characterization of $LiGaSe_2$. *Journal of Applied Physics* **52**(10), 6441. URL http://aip.scitation.org/doi/10.1063/1.328553.

Kusumoto, T., A. Kai, T. Maeda and T. Wada (2019). Crystallographic, optical, and electronic properties of (Cu, Li)GaS_2. *Thin Solid Films* **672**, 192.

Labat, F., P. Baranek, C. Domain, C. Minot *et al.* (2007). Density functional theory analysis of the structural and electronic properties of TiO_2 rutile and anatase polytypes: Performances of different exchange-correlation functionals. *The Journal of Chemical Physics* **126**(15), 154703. URL http://aip.scitation.org/doi/10.1063/1.2717168.

Laemmle, A., R. Wuerz and M. Powalla (2013). Efficiency enhancement of Cu(In,Ga)Se_2 thin-film solar cells by a post-deposition treatment with potassium fluoride. *physica status solidi (RRL) - Rapid Research Letters* **7**(9), 631.

Laemmle, A., R. Wuerz and M. Powalla (2015). Investigation of the effect of potassium on Cu(In,Ga)Se_2 layers and solar cells. *Thin Solid Films* **582**, 27.

Laemmle, A., R. Wuerz, T. Schwarz, O. Cojocaru-Mirédin *et al.* (2014). Investigation of the diffusion behavior of sodium in Cu(In,Ga)Se_2 layers. *Journal of Applied Physics* **115**(15), 154501.

Leach, A. R. (2001). *Molecular Modelling: Principles and Applications*. Pearson Education.

Leal-Gonzalez, J., S. A. Melibary and A. J. Smith (1990). Structure of lithium gallium sulfide, $LiGaS_2$. *Acta Crystallographica Section C: Crystal Structure Communications* **46**(11), 2017. URL `//scripts.iucr.org/cgi-bin/paper?hu0307`.

Lee, C., W. Yang and R. G. Parr (1988). Development of the Colle-Salvetti correlation-energy formula into a functional of the electron density. *Physical Review B* **37**(2), 785. URL `https://link.aps.org/doi/10.1103/PhysRevB.37.785`.

Lemoine, P., D. Carré and M. Guittard (1984). Structure du sulfure de gallium et de potassium, $KGaS_2$. *Acta Crystallographica Section C: Crystal Structure Communications* **40**(6), 910. URL `//scripts.iucr.org/cgi-bin/paper?a23628`.

Levinshtein, M. E., S. L. Rumyantsev and M. S. Shur (2001). *Properties of Advanced Semiconductor Materials: GaN, AIN, InN, BN, SiC, SiGe*. John Wiley & Sons.

Lindroos, J. and H. Savin (2016). Review of light-induced degradation in crystalline silicon solar cells. *Solar Energy Materials and Solar Cells* **147**, 115. URL `https://linkinghub.elsevier.com/retrieve/pii/S0927024815006406`.

Lockwood, D., G. Yu and N. Rowell (2005). Optical phonon frequencies and damping in AlAs, GaP, GaAs, InP, InAs and InSb studied by oblique incidence infrared spectroscopy. *Solid State Communications* **136**(7), 404. URL `https://linkinghub.elsevier.com/retrieve/pii/S0038109805007398`.

Lorenz, M., R. Chicotka, G. Pettit and P. Dean (1970). The fundamental absorption edge of AlAs and AlP. *Solid State Communications* **8**(9), 693. URL `https://linkinghub.elsevier.com/retrieve/pii/0038109870901973`.

Lorenz, M. R., G. D. Pettit and R. C. Taylor (1968). Band gap of gallium phosphide from 0 to 900 K and light emission from diodes at high temperatures. *Physical Review* **171**(3), 876. URL `https://doi.org/10.1103/PhysRev.171.876`.

Lowe-Ma, C. K., D. O. Kipp and T. A. Vanderah (1991). On the Crystal Structure of $KInS_2$-I. *Journal of Solid State Chemistry* **92**, 520.

Lyon, K. G., G. L. Salinger, C. A. Swenson and G. K. White (1977). Linear thermal expansion measurements on silicon from 6 to 340 K. *Journal of Applied Physics* **48**(3), 865. URL `https://aip-scitation-org.bases-doc.univ-lorraine.fr/doi/10.1063/1.323747`.

Madsen, G. K., J. Carrete and M. J. Verstraete (2018). BoltzTraP2, a program for interpolating band structures and calculating semi-classical transport coefficients. *Computer Physics Communications* **231**, 140. URL https://linkinghub.elsevier.com/retrieve/pii/S0010465518301632.

Madsen, G. K. and D. J. Singh (2006). BoltzTraP. A code for calculating band-structure dependent quantities. *Computer Physics Communications* **175**(1), 67. URL http://linkinghub.elsevier.com/retrieve/pii/S0010465506001305.

Maeda, T., A. Kawabata and T. Wada (2015). First-principles study on alkali-metal effect of Li, Na, and K in $CuInSe_2$ and $CuGaSe_2$. *Japanese Journal of Applied Physics* **54**(8S1), 08KC20.

Maeda, T., C. Zhao and T. Wada (2017). Crystallographic, optical, and electronic properties of (Cu,Li)InS2 system. *Thin Solid Films* **633**, 172.

Mahajan, S. (2000). Defects in semiconductors and their effects on devices. *Acta Materialia* **48**(1), 137. URL http://www.sciencedirect.com/science/article/pii/S135964549900292X.

Malitckaya, M., H.-P. Komsa, V. Havu and M. J. Puska (2017). Effect of Alkali Metal Atom Doping on the $CuInSe_2$ -Based Solar Cell Absorber. *The Journal of Physical Chemistry C* **121**(29), 15516.

Malone, B. D. and M. L. Cohen (2013). Quasiparticle semiconductor band structures including spin–orbit interactions. *Journal of Physics: Condensed Matter* **25**(10), 105503. URL http://stacks.iop.org/0953-8984/25/i=10/a=105503?key=crossref.998cacdca004cef48338d1ab204a9349.

Marques, M. A. L., J. Vidal, M. J. T. Oliveira, L. Reining *et al.* (2011). Density-based mixing parameter for hybrid functionals. *Physical Review B* **83**(3). URL https://link.aps.org/doi/10.1103/PhysRevB.83.035119.

Márquez, R. and C. Rincón (1995). On the Dielectric Constants of $A^IB^{III}C$ Chalcopyrite Semiconductor Compounds. *physica status solidi (b)* **191**(1), 115. URL http://doi.wiley.com/10.1002/pssb.2221910112.

Maticiuc, N., T. Kodalle, J. Lauche, R. Wenisch *et al.* (2018). In vacuo XPS investigation of $Cu(In,Ga)Se_2$ surface after RbF post-deposition treatment. *Thin Solid Films* **665**, 143.

McSkimin, H. J. and P. Andreatch (1972). Elastic moduli of diamond as a function of pressure and temperature. *Journal of Applied Physics* **43**(7), 2944.

Meillaud, F., A. Shah, C. Droz, E. Vallat-Sauvain *et al.* (2006). Efficiency limits for single-junction and tandem solar cells. *Solar Energy Materials and Solar Cells* **90**(18), 2952. URL https://linkinghub.elsevier.com/retrieve/pii/S0927024806002029.

Monemar, B. (1973). Fundamental Energy Gaps of AlAs and Alp from Photoluminescence Excitation Spectra. *Physical Review B* **8**(12), 5711. URL `https://link.aps.org/doi/10.1103/PhysRevB.8.5711`.

Monkhorst, H. J. and J. D. Pack (1976). Special points for Brillouin-zone integrations. *Physical Review B* **13**(12), 5188. URL `https://link.aps.org/doi/10.1103/PhysRevB.13.5188`.

Mooradian, A. and G. B. Wright (1966). First Order Raman Effec in III-V Compounds. *Solid State Communications* **4**, 431.

Moore, W. J. and R. T. Holm (1996). Infrared dielectric constant of gallium arsenide. *Journal of Applied Physics* **80**(12), 6939. URL `http://aip.scitation.org/doi/10.1063/1.363818`.

Muñoz, M., F. H. Pollak, M. B. Zakia, N. B. Patel *et al.* (2000). Temperature dependence of the energy and broadening parameter of the fundamental band gap of GaSb and $Ga_{1-x}In_xAs_ySb_{1-y}$/GaSb (0.07<x<0.22, 0.05<y<0.19) quaternary alloys using infrared photoreflectance. *Physical Review B* **62**(24), 5.

Müller, D., F. E. Poltmann and H. Hahn (2014). Notizen: Zur Struktur ternärer Chalkogenide des Thalliums mit Aluminium, Gallium und Indium, XXII* / On the Structure of Ternary Thalliumchalkogenides with Aluminium, Gallium and Indium, XXII*. *Zeitschrift für Naturforschung B* **29**(1-2), 117. URL `https://www.degruyter.com/view/j/znb.1974.29.issue-1-2/znb-1974-1-237/znb-1974-1-237.xml`.

Mungan, E. S., X. Wang and M. A. Alam (2013). Modeling the Effects of Na Incorporation on CIGS Solar Cells. *IEEE Journal of Photovoltaics* **3**(1), 451.

Murnaghan, F. D. (1944). The Compressibility of Media under Extreme Pressures. *Proceedings of the National Academy of Sciences of the United States of America* **30**(9), 244. URL `https://www.ncbi.nlm.nih.gov/pmc/articles/PMC1078704/`.

Muzzillo, C. P. (2017). Review of grain interior, grain boundary, and interface effects of K in CIGS solar cells: Mechanisms for performance enhancement. *Solar Energy Materials and Solar Cells* **172**, 18.

Muzzillo, C. P. and T. J. Anderson (2018). Surface and bulk effects of K in $Cu_{1-x}K_xIn_{1-y}Ga_ySe_2$ solar cells. *Solar Energy Materials and Solar Cells* **179**, 362.

Nagaoka, A., K. Yoshino, T. Taniyama and H. Miyake (2012). Temperature Dependence of Linear Thermal Expansion of $CuGaSe_2$ Crystals. *Materials Science Forum* URL `https://www.scientific.net/MSF.725.171`.

Nampalli, N., B. Hallam, C. Chan, M. Abbott *et al.* (2015). Role of hydrogen in the permanent passivation of boron-oxygen defects in czochralski silicon. In

2015 IEEE 42nd Photovoltaic Specialist Conference (PVSC), 1–3. IEEE, New Orleans, LA. URL http://ieeexplore.ieee.org/document/7356404/.

Neumann, H. (1986). Lattice vibrational, thermal and mechanical properties of $CuInSe_2$. *Solar Cells* **16**, 399.

Nichols, D. N., D. S. Rimai and R. J. Sladek (1980). Elastic anharmonicity of InP: Its relationship to the high pressure transition. *Solid State Communications* **36**(8), 667. URL http://www.sciencedirect.com/science/article/pii/0038109880902057.

Niles, D., K. Ramanathan, F. Hasoon, R. Noufi *et al.* (1997). Na impurity chemistry in photovoltaic. *Journal of Vacuum Science & Technology A* **15**(6), 3044.

Novikova, S. (1966). Chapter 2 Thermal Expansion. In *Semiconductors and Semimetals*, volume 2, 33–48. Elsevier. URL https://linkinghub.elsevier.com/retrieve/pii/S008087840860160X.

Oikkonen, L. E., M. G. Ganchenkova, A. P. Seitsonen and R. M. Nieminen (2013). Effect of sodium incorporation into $CuInSe_2$ from first principles. *Journal of Applied Physics* **114**(8), 083503.

Olego, D. and M. Cardona (1982). Pressure dependence of Raman phonons of Ge and 3C–SiC. *Physical Review B* **25**(2), 1151. URL https://link.aps.org/doi/10.1103/PhysRevB.25.1151.

Ortega, J. E. and F. J. Himpsel (1993). Inverse-photoemission study of Ge(100), Si(100), and GaAs(100): Bulk bands and surface states. *Physical Review B* **47**(4), 2130. URL https://link.aps.org/doi/10.1103/PhysRevB.47.2130.

Osterwald, C., A. Anderberg, S. Rummel and L. Ottoson (2002). Degradation analysis of weathered crystalline-silicon PV modules. In *Conference Record of the Twenty-Ninth IEEE Photovoltaic Specialists Conference, 2002.*, 1392–1395. ISSN: 1060-8371.

Paier, J., R. Hirschl, M. Marsman and G. Kresse (2005). The Perdew–Burke–Ernzerhof exchange-correlation functional applied to the G2-1 test set using a plane-wave basis set. *The Journal of Chemical Physics* **122**(23), 234102. URL http://aip.scitation.org/doi/10.1063/1.1926272.

Paier, J., M. Marsman, K. Hummer, G. Kresse *et al.* (2006). Screened hybrid density functionals applied to solids. *The Journal of Chemical Physics* **124**(15), 154709. URL http://aip.scitation.org/doi/10.1063/1.2187006.

Palmer, D. (2019). Properties of III-V Semiconductors. URL http://www.semiconductors.co.uk/propiiiv5653.htm.

Parker, J. H., D. W. Feldman and M. Ashkin (1967). Raman scattering by silicon and germanium. *Physical Review* **155**(3), 712. URL http://link.aps.org/doi/10.1103/PhysRev.155.712.

Pässler, R. (2013). Non-Debye heat capacity formula refined and applied to GaP, GaAs, GaSb, InP, InAs, and InSb. *AIP Advances* **3**(8), 082108. URL `http://aip.scitation.org/doi/10.1063/1.4818273`.

Pavesi, L., F. Piazza, A. Rudra, J. F. Carlin *et al.* (1991). Temperature dependence of the InP band gap from a photoluminescence study. *Physical Review B* **44**(16), 9052. URL `https://link.aps.org/doi/10.1103/PhysRevB.44.9052`.

Perdew, J. P., K. Burke and M. Ernzerhof (1996a). Generalized Gradient Approximation Made Simple. *Physical Review Letters* **77**(18), 3865. URL `https://link.aps.org/doi/10.1103/PhysRevLett.77.3865`.

Perdew, J. P., M. Ernzerhof and K. Burke (1996b). Rationale for mixing exact exchange with density functional approximations. *The Journal of Chemical Physics* **105**(22), 9982. URL `http://aip.scitation.org/doi/10.1063/1.472933`.

Perdew, J. P., A. Ruzsinszky, G. I. Csonka, O. A. Vydrov *et al.* (2008). Restoring the Density-Gradient Expansion for Exchange in Solids and Surfaces. *Physical Review Letters* **100**(13). URL `https://link.aps.org/doi/10.1103/PhysRevLett.100.136406`.

Pianezzi, F., P. Reinhard, A. Chirilă, B. Bissig *et al.* (2014). Unveiling the effects of post-deposition treatment with different alkaline elements on the electronic properties of CIGS thin film solar cells. *Physical Chemistry Chemical Physics* **16**(19), 8843.

Pizzi, G., D. Volja, B. Kozinsky, M. Fornari *et al.* (2014). BoltzWann: A code for the evaluation of thermoelectric and electronic transport properties with a maximally-localized Wannier functions basis. *Computer Physics Communications* **185**(1), 422. URL `http://arxiv.org/abs/1305.1587`. ArXiv: 1305.1587.

Potter, R. F. (1956). Elastic Moduli of Indium Antimonide. *Physical Review* **103**(1), 47. URL `https://link.aps.org/doi/10.1103/PhysRev.103.47`.

Ramspeck, K., S. Zimmermann, H. Nagel, A. Metz *et al.* (2012). Light induced degradation of rear passivated mc-Si solar cells. In *Proc. 27th Eur. Photovolt. Sol. Energy Conf. Exhib.*, volume 1, 861–865.

Rau, U., M. Schmitt, F. Engelhardt, O. Seifert *et al.* (1998). Impact of Na and S incorporation on the electronic transport mechanisms of Cu(In, Ga)Se_2 solar cells. *Solid State Communications* **107**(2), 59.

Reeber, R. R. and K. Wang (1995). Thermal Expansion of β–Sic, Gap and Inp. *MRS Online Proceedings Library Archive* **410**. URL `https://www.cambridge.org/core/journals/mrs-online-proceedings-library-archive/article/thermal-expansion-of-sic-gap-and-inp/EFCF795C2635DCC96887769824FB8392`.

Reining, L. (2018). The GW approximation: content, successes and limitations. *Wiley Interdisciplinary Reviews: Computational Molecular Science* **8**(3), e1344. URL `http://onlinelibrary.wiley.com/doi/abs/10.1002/wcms.1344`.

Rincón, C. and F. J. Ramírez (1992). Lattice vibrations of $CuInSe_2$ and $CuGaSe_2$ by Raman microspectrometry. *Journal of Applied Physics* **72**(9), 4321. URL `http://aip.scitation.org/doi/10.1063/1.352195`.

Roa, L., C. Rincón, J. González and M. Quintero (1990). Analysis of direct exciton transitions in $CuGa(S_xSe_{1-x})_2$ alloys. *Journal of Physics and Chemistry of Solids* **51**(6), 551. URL `http://www.sciencedirect.com/science/article/pii/0022369790901629`.

Rode, D. L. (1970). Electron Mobility in Direct-Gap Polar Semiconductors. *Physical Review B* **2**(4), 1012. URL `https://link.aps.org/doi/10.1103/PhysRevB.2.1012`.

Rohlfing, M., P. Krüger and J. Pollmann (1993). Quasiparticle band-structure calculations for C, Si, Ge, GaAs, and SiC using Gaussian-orbital basis sets. *Physical Review B* **48**(24), 17791. URL `https://link.aps.org/doi/10.1103/PhysRevB.48.17791`.

Rong-Tie, H., Z. Ming, S. Li-Fang, C. Chuan-Bing *et al.* (2017). Synthesis and Physical Properties of Solar Material $Cu_xLi_{1-x}InSe_2$. *Journal of Inorganic Materials* **32**(1), 101.

Ruckh, M., D. Schmid, M. Kaiser, R. Schaffler *et al.* (1996). Influence of substrates on the electrical properties of Cu(In,Ga)Se_2 thin films. *Solar Energy Materials and Solar Cells* **41-42**, 335.

Rudmann, D., A. F. da Cunha, M. Kaelin, F. Kurdesau *et al.* (2004). Efficiency enhancement of Cu(In,Ga)Se_2 solar cells due to post-deposition Na incorporation. *Applied Physics Letters* **84**(7), 1129.

Saarinen, K., T. Laine, S. Kuisma, J. Nissilä *et al.* (1997). Observation of native Ga vacancies in GaN by positron annihilation. *MRS Online Proceedings Library Archive* **482**. URL `https://www.cambridge.org/core/journals/mrs-online-proceedings-library-archive/article/observation-of-native-ga-vacancies-in-gan-by-positron-annihilation/BD4C0A534F4DE0BF4BA220C3F907BF8C`.

Salomé, P., H. Rodriguez-Alvarez and S. Sadewasser (2015). Incorporation of alkali metals in chalcogenide solar cells. *Solar Energy Materials and Solar Cells* **143**, 9.

Sansone, G., A. Ferretti and L. Maschio (2017). *Ab initio* electronic transport and thermoelectric properties of solids from full and range-separated hybrid functionals. *The Journal of Chemical Physics* **147**(11), 114101. URL `http://aip.scitation.org/doi/10.1063/1.4986398`.

Scheidemantel, T. J., C. Ambrosch-Draxl, T. Thonhauser, J. V. Badding *et al.* (2003). Transport coefficients from first-principles calculations. *Physical Review B* **68**(12). URL `https://link.aps.org/doi/10.1103/PhysRevB.68.125210`.

Schimka, L., J. Harl and G. Kresse (2011). Improved hybrid functional for solids: The HSEsol functional. *The Journal of Chemical Physics* **134**(2), 024116. URL `http://aip.scitation.org/doi/10.1063/1.3524336`.

Schmidt, J., A. Aberle and R. Hezel (1997). Investigation of carrier lifetime instabilities in Cz-grown silicon. In *Conference Record of the Twenty Sixth IEEE Photovoltaic Specialists Conference - 1997*, 13–18. ISSN: 0160-8371.

Schöppe, P., S. Schönherr, R. Wuerz, W. Wisniewski *et al.* (2017). Rubidium segregation at random grain boundaries in Cu(In,Ga)Se_2 absorbers. *Nano Energy* **42**, 307.

Schubert, H. and R. Hoppe (1970). Zur Kenntnis der $RbInS_2$-Strukturfamilie. *Z. Naturforsch* **25b**, 886.

Seeger, A. (1974). The study of defects in crystals by positron annihilation. *Applied physics* **4**(3), 183. URL `https://doi.org/10.1007/BF00884229`.

Sekine, T., K. Uchinokura and E. Matsuura (1976). Two-phonon Raman scattering in GaSb. *Solid State Communications* **18**(9-10), 1337.

Shimazaki, T. and Y. Asai (2008). Band structure calculations based on screened Fock exchange method. *Chemical Physics Letters* **466**(1-3), 91. URL `https://linkinghub.elsevier.com/retrieve/pii/S0009261408013717`.

Shimazaki, T. and Y. Asai (2009). First principles band structure calculations based on self-consistent screened Hartree–Fock exchange potential. *The Journal of Chemical Physics* **130**(16), 164702. URL `https://aip-scitation-org.bases-doc.univ-lorraine.fr/doi/10.1063/1.3119259`.

Shimazaki, T. and T. Nakajima (2014). Dielectric-dependent screened Hartree–Fock exchange potential and Slater-formula with Coulomb-hole interaction for energy band structure calculations. *The Journal of Chemical Physics* **141**(11), 114109. URL `http://aip.scitation.org/doi/10.1063/1.4895623`. Citation Key Alias: shimazaki.nakajima_2014_Dielectricdependenta.

Shin, D., J. Kim, T. Gershon, R. Mankad *et al.* (2016). Effects of the incorporation of alkali elements on Cu(In,Ga)Se_2 thin film solar cells. *Solar Energy Materials and Solar Cells* **157**, 695.

Singh, J. (1992). *Physics of Semiconductors and Their Heterostructures*, volume 84. McGraw-Hill New York.

Skone, J. H., M. Govoni and G. Galli (2014). Self-consistent hybrid functional for condensed systems. *Physical Review B* **89**(19). URL `https://link.aps.org/doi/10.1103/PhysRevB.89.195112`.

Slater, J. C. (1929). The Theory of Complex Spectra. *Physical Review* **34**(10), 1293. URL https://link.aps.org/doi/10.1103/PhysRev.34.1293.

Slutsky, L. J. and C. W. Garland (1959). Elastic Constants of Indium Antimonide from 4.2K to 300K. *Physical Review* **113**(1), 167. URL https://link.aps.org/doi/10.1103/PhysRev.113.167.

Solar Frontier (2019). Solar frontier achieves world record thin-film solar cell efficiency of 23.35%. URL http://www.solar-frontier.com/eng/news/2019/0117_press.html. [Online; accessed 5-March-2019].

Soma, T., J. Satoh and H. Matsuo (1982). Thermal expansion coefficient of GaAs and InP. *Solid State Communications* **42**(12), 889. URL https://linkinghub.elsevier.com/retrieve/pii/0038109882902332.

Sommer, H. and R. Hoppe (1977). Die Kristallstruktur von Cs_2S, mit einer Bemerkung über Cs_2Se, Cs_2Te, Rb_2Se und Rb_2Te. *Zeitschrift für anorganische und allgemeine Chemie* **429**(1), 118. URL http://doi.wiley.com/10.1002/zaac.19774290116.

Sopori, B. (1999). Impurities and defects in photovoltaic si devices: A review. Technical Report NREL/CP-520-27524, National Renewable Energy Lab., Golden, CO (US). URL https://www.osti.gov/biblio/753811.

Sparks, P. W. and C. A. Swenson (1967). Thermal Expansions from 2 to 40 K of Ge, Si, and Four III-V Compounds. *Physical Review* **163**(3), 779. URL https://link.aps.org/doi/10.1103/PhysRev.163.779.

Spiess, H. W., U. Haeberlen, G. Brandt, A. Räuber *et al.* (1974). Nuclear Magnetic Resonance in I_B–III–VI_2 Semiconductors. *physica status solidi (b)* **62**(1), 183. URL http://onlinelibrary.wiley.com/doi/abs/10.1002/pssb.2220620118.

Staroverov, V. N., G. E. Scuseria, J. Tao and J. P. Perdew (2004). Tests of a ladder of density functionals for bulk solids and surfaces. *Physical Review B* **69**(7). URL https://link.aps.org/doi/10.1103/PhysRevB.69.075102.

Straumanis, M. E. and C. D. Kim (1965). Lattice Parameters, Thermal Expansion Coefficients, Phase Width, and Perfection of the Structure of GaSb and InSb. *Journal of Applied Physics* **36**(12), 3822. URL http://aip.scitation.org/doi/10.1063/1.1713955.

Sturge, M. D. (1962). Optical absorption of gallium arsenide between 0.6 and 2.75 eV. *Physical Review* **127**(3), 768.

Sun, Y., S. Lin, W. Li, S. Cheng *et al.* (2017). Review on Alkali Element Doping in $Cu(In,Ga)Se_2$ Thin Films and Solar Cells. *Engineering* **3**(4), 452.

Taguchi, N., S. Tanaka and S. Ishizuka (2018). Direct insights into $RbInSe_2$ formation at $Cu(In,Ga)Se_2$ thin film surface with RbF postdeposition treatment. *Applied Physics Letters* **113**(11), 113903.

Tiginyanu, I. M. (1999). Raman Modes in Porous GaP under Hydrostatic Pressure. *Physica Status Solidi (b)* **211**, 6.

Tinoco, T., J. P. Itié, A. Polian, A. San Miguel *et al.* (1994). Combined x-ray absorption and x-ray diffraction studies of $CuGaS_2$, $CuGaSe_2$, $CuFeS_2$ and $CuFeSe_2$ under high pressure. *Le Journal de Physique IV* **04**(C9), C9. URL `http://www.edpsciences.org/10.1051/jp4:1994923`.

Tinoco, T., A. Polian, D. Gómez and J. P. Itié (1996). Structural Studies of $CuInS_2$ and $CuInSe_2$ under High Pressure. *physica status solidi (b)* **198**(1), 433. URL `http://onlinelibrary.wiley.com/doi/abs/10.1002/pssb.2221980156`.

Tinoco, T., M. Quintero and C. Rincón (1991). Variation of the energy gap with composition in $A^{I}B^{III}C_2^{VI}$ chalcopyrite-structure alloys. *Physical Review B* **44**(4), 1613. URL `https://link.aps.org/doi/10.1103/PhysRevB.44.1613`.

Urbaniak, A., M. Igalson, F. Pianezzi, S. Bücheler *et al.* (2014). Effects of Na incorporation on electrical properties of Cu(In,Ga)Se_2-based photovoltaic devices on polyimide substrates. *Solar Energy Materials and Solar Cells* **128**, 52.

Van de Walle, C. G. (1994). Energies of various configurations of hydrogen in silicon. *Physical Review B* **49**(7), 4579. URL `https://link.aps.org/doi/10.1103/PhysRevB.49.4579`.

Van de Walle, C. G., P. J. H. Denteneer, Y. Bar-Yam and S. T. Pantelides (1989). Theory of hydrogen diffusion and reactions in crystalline silicon. *Physical Review B* **39**(15), 10791. URL `https://link.aps.org/doi/10.1103/PhysRevB.39.10791`.

Van de Walle, C. G. and J. Neugebauer (2006). Hydrogen in semiconductors. *Annual Review of Materials Research* **36**(1), 179. URL `https://doi.org/10.1146/annurev.matsci.36.010705.155428`.

Varshni, Y. P. (1967). Temperature dependence of the energy gap in semiconductors. *Physica* **34**(1), 149. URL `http://www.sciencedirect.com/science/article/pii/0031891467900626`.

Vilalta-Clemente, A., M. Raghuwanshi, S. Duguay, C. Castro *et al.* (2018). Rubidium distribution at atomic scale in high efficient Cu(In,Ga)Se_2 thin-film solar cells. *Applied Physics Letters* **112**(10), 103105.

Vosko, S. H., L. Wilk and M. Nusair (1980). Accurate spin-dependent electron liquid correlation energies for local spin density calculations: a critical analysis. *Canadian Journal of Physics* **58**(8), 1200. URL `http://www.nrcresearchpress.com/doi/10.1139/p80-159`.

Vurgaftman, I., J. R. Meyer and L. R. Ram-Mohan (2001). Band parameters for III-V compound semiconductors and their alloys. *Journal of Applied Physics* **89**(11 I), 5815.

Ward, M. D., E. A. Pozzi, R. P. Van Duyne and J. A. Ibers (2014). Syntheses, structures, and optical properties of the indium/germanium selenides $Cs_4in_8gese_{16}$, $CsInSe_2$, and $CsInGeSe_4$. *Journal of Solid State Chemistry* **212**, 191. URL https://linkinghub.elsevier.com/retrieve/pii/S0022459614000279.

Weber, J. and M. I. Alonso (1989). Near-band-gap photoluminescence of Si-Ge alloys. *Physical Review B* **40**(8), 5683. URL https://link.aps.org/doi/10.1103/PhysRevB.40.5683.

Wei, S. and A. Zunger (1995). Band offsets and optical bowings of chalcopyrites and Zn–based II–VI alloys. *Journal of Applied Physics* **78**(6), 3846. URL http://aip.scitation.org/doi/10.1063/1.359901.

Wei, S.-H., S. B. Zhang and A. Zunger (1999). Effects of Na on the electrical and structural properties of $CuInSe_2$. *Journal of Applied Physics* **85**(10), 7214.

Weil, R. and W. O. Groves (1968). The Elastic Constants of Gallium Phosphide. *Journal of Applied Physics* **39**(9).

Weiss, T. P., S. Nishiwaki, B. Bissig, R. Carron *et al.* (2018). Injection Current Barrier Formation for RbF Postdeposition-Treated Cu(In,Ga)Se_2 -Based Solar Cells. *Advanced Materials Interfaces* **5**(4), 1701007.

Wenham, A. C. n., S. Wenham, R. Chen, C. Chan *et al.* (2018). Hydrogen-Induced Degradation. In *2018 IEEE 7th World Conference on Photovoltaic Energy Conversion (WCPEC) (A Joint Conference of 45th IEEE PVSC, 28th PVSEC & 34th EU PVSEC)*, 0001–0008. IEEE, Waikoloa Village, HI. URL https://ieeexplore.ieee.org/document/8548100/.

Werner, A., H. D. Hochheimer and A. Jayaraman (1981). Pressure-induced phase transformations in the chalcopyrite-structure compounds: $CuGaS_2$ and $AgGaS_2$. *Physical Review B* **23**(8), 3836. URL https://link.aps.org/doi/10.1103/PhysRevB.23.3836.

Werner, F., M. H. Wolter, S. Siebentritt, G. Sozzi *et al.* (2018). Alkali treatments of Cu(In,Ga)Se_2 thin-film absorbers and their impact on transport barriers. *Progress in Photovoltaics: Research and Applications* **26**(11), 911.

Wilking, S., A. Herguth and G. Hahn (2013). Influence of hydrogen on the regeneration of boron-oxygen related defects in crystalline silicon. *Journal of Applied Physics* **113**(19), 194503. URL http://aip.scitation.org/doi/10.1063/1.4804310.

Wu, M. and C. Chen (1992). Photoluminescence of high–quality GaSb grown from Ga– and Sb–rich solutions by liquid–phase epitaxy. *Journal of Applied Physics* **72**(9), 4275. URL http://aip.scitation.org/doi/10.1063/1.352216.

Wuerz, R., A. Eicke, F. Kessler, S. Paetel *et al.* (2012). CIGS thin-film solar cells and modules on enamelled steel substrates. *Solar Energy Materials and Solar Cells* **100**, 132.

Wuerz, R., W. Hempel and P. Jackson (2018). Diffusion of Rb in polycrystalline Cu(In,Ga)Se_2 layers and effect of Rb on solar cell parameters of Cu(In,Ga)Se_2 thin-film solar cells. *Journal of Applied Physics* **124**(16), 165305.

Xu, C., C. Wang, C. Chan and K. Ho (1991). Theory of the thermal expansion of Si and diamond. *Phys. Rev. B* **43**(6).

Yu, P. and M. Cardona (2010). *Fundamentals of Semiconductors: Physics and Materials Properties*. Graduate Texts in Physics. Springer-Verlag, Berlin Heidelberg, 4 edition. URL `https://www.springer.com/gp/book/9783642007095`.

Yuan, Z.-K., S. Chen, Y. Xie, J.-S. Park *et al.* (2016). Na-Diffusion Enhanced p-type Conductivity in Cu(In,Ga)Se_2 : A New Mechanism for Efficient Doping in Semiconductors. *Advanced Energy Materials* **6**(24), 1601191.

Zeng, H.-Y., F.-K. Zheng, R.-P. Chen, Z.-C. Dong *et al.* (2007). Reactive flux syntheses, crystal structures and band gaps of $AInS_2$ (A=Rb, Cs). *Journal of Alloys and Compounds* **432**(1-2), 69. URL `http://linkinghub.elsevier.com/retrieve/pii/S0925838806007109`.

Zhao, Y. and D. G. Truhlar (2006). A new local density functional for main-group thermochemistry, transition metal bonding, thermochemical kinetics, and noncovalent interactions. *The Journal of Chemical Physics* **125**(19), 194101. URL `http://aip.scitation.org/doi/10.1063/1.2370993`.

Zhao, Y. and D. G. Truhlar (2008). The M06 suite of density functionals for main group thermochemistry, thermochemical kinetics, noncovalent interactions, excited states, and transition elements: two new functionals and systematic testing of four M06-class functionals and 12 other functionals. *Theoretical Chemistry Accounts* **120**(1-3), 215. URL `http://link.springer.com/10.1007/s00214-007-0310-x`.

Zintl, E., A. Harder and B. Dauth (1934). Gitterstruktur der Oxyde, Sulfide, Selenide und Telluride des Lithiums, Natriums und Kaliums. *Zeitschrift für Elektrochemie und angewandte physikalische Chemie* **40**(8), 588. URL `https://onlinelibrary.wiley.com/doi/abs/10.1002/bbpc.19340400811`.

Zollner, S., S. Gopalan and M. Cardona (1991). The temperature dependence of the band gaps in InP, InAs, InSb, and GaSb. *Solid State Communications* **77**(7), 485. URL `https://linkinghub.elsevier.com/retrieve/pii/003810989190725B`.

List of Contributions and Awards

Awards

Best poster presented in symposium A
"First-Principles Investigation of Chemical Composition Effects on Thermodynamic and Optoelectronic Properties of Chalcopyrites"
F. Lafond, Ph. Baranek, A. Postnikov
E-MRS 2018 Spring Meeting, Strasbourg, France

Paper

"Effects of the Copper Substitution by Alkali Metals on the Properties of Chalcopyrites for Tandem Applications: Insights from Theory."
F. Lafond, Ph. Baranek, A. Postnikov
Submitted to Inorganic Chemistry

Contributions to conferences

Talk
"First-Principles Approach of the Structural, Electronic, Dynamical and Thermodynamic Properties of Defective Silicon: Influence of the Temperature on the Formation Energy of Defect."
F. Lafond, Ph. Baranek, A. Postnikov
E-MRS 2017 Fall Meeting, Warsaw, Poland

Talk
"First-Principles Investigation of Chemical Composition Effects on Thermodynamic and Optoelectronic Properties of Chalcopyrites"
F. Lafond, Ph. Baranek, A. Postnikov
International Conference on Ternary and Multinary Compounds (ICTMC-21), Boulder, Colorado, USA

Poster
"First-Principles Approach of the Structural, Electronic and Dynamical Properties of Si_xGe_{1-x} *(*$0 \leq x \leq 1$*), SiC, GaX (with* $X = P, As, Sb$*): A Study of the Hybrid Functionals Performance."*

F. Lafond, Ph. Baranek, A. Postnikov
XXIX IUPAP Conference in Computational Physics (CCP2017), Paris, France

Poster
"Hybrid Functionals Approach of the Structural, Electronic and Dynamical Properties of Semiconductors for Photovoltaic Applications."
F. Lafond, B. Civalleri, Ph. Baranek, A. Postnikov
11th Triennial Congress of the World Association of Theoretical and Computational Chemists (WATOC), Munich, Germany

Poster
"First-Principles Investigation of Chemical Composition Effects on Thermodynamic and Optoelectronic Properties of Chalcopyrites"
F. Lafond, Ph. Baranek, A. Postnikov
E-MRS 2018 Spring Meeting, Strasbourg, France

Summary

The electrical properties of semiconductors, such as concentrations and mobilities of charge careers, are strongly influenced by the types of dopants and defects inserted or formed during the synthesis of materials. In the field of photovoltaics, these defects lead to various perturbations (distortions of the phase stability, appearance of supplementary energy levels in the band gap, *etc.*) and can degrade the efficiency and durability of solar cells. In this context, *ab initio* simulation methods, such as Hartree-Fock (HF) or those implemented in the framework of density functional theory (DFT), are relevant to understand these behaviours and thus improve and optimise the photovoltaic materials. However, a qualitative and quantitative description of properties, such as the electronic structures, requires sophisticated but time consuming techniques, implementing, e.g., the *GW* approximation. An interesting alternative to this can be provided by hybrid functionals, which combine a certain percentage of the HF exact exchange with the exchange-correlation provided by functionals from the various realisations of the DFT.

Firstly, hybrid functionals were optimised in order to accurately describe the band gap for different compounds by carefully adjusting the percentage of the HF exact exchange in the exchange part of the PBE and PBEsol functionals, suggested within the generalised gradient approximation of the DFT. The materials investigated were Si, Ge, SiGe, III-V and the chalcopyrite-type compounds. The results obtained by this approach were compared to those available from the literature, paying particular attention to the *GW* calculation results. The description of the electronic properties, such as the band structures, with the hybrid functional turns out to generally match that from the *GW* calculations. Structural and dielectric properties were also in good agreement with the experimental data. The temperature evolution of various thermodynamic properties, like the heat capacity, was calculated via the quasi-harmonic approximation (QHA). In this latter approximation and for the range of studied materials, optimised hybrid functionals however do not bring any noticeable improvement against the existing functionals. Nevertheless, they bring about a coherent description of the materials.

Secondly, these optimised hybrid functionals were used to systematically describe the impact of chemical composition on chalcopyrite's properties for tandem solar cells. First, they enable the determination of the compositions, structural and electrical properties of $\mathrm{CuGa}_x\mathrm{In}_{1-x}(\mathrm{S}_y\mathrm{Se}_{1-y})_2$ for band gap specific to this kind of application. Then, the effect of alkali metals incorporations into the chalcopyrite-type bulk materials was addressed. Doping with alkali metals leads to a major

enhancement of the photovoltaic efficiency of the chalcopyrite-type compounds. Interesting results have been obtained concerning the substitution of copper by Li, Na, K, Rb and Cs. The impact of these dopants on the band gap was interpreted via the structural evolution and the thermodynamic stability of the different crystallines phases that can exist within the material.

Finally, hydrogen, iron and boron point defects in silicon were simulated as a part of a preliminary study on the *light and elevated temperature induced degradation* (LeTID) which is among the major challenges in the study of the ageing process of the silicon solar cells.

Résumé en français

Introduction

Les propriétés électriques des semi-conducteurs sont fortement influencées par le type de dopants et défauts (ponctuels ou étendus) insérés ou formés lors de leur synthèse. Dans le domaine du photovoltaïque, ces défauts, sources de nombreuses métastabilités (perturbation de la stabilité des phases cristallines, apparition de niveau électronique dans la bande interdite, *etc.*), vont fortement dégrader l'efficacité et la durabilité des cellules solaires, mais restent difficile à caractériser expérimentalement. Dans ce contexte de défauts nanoscopiques, les méthodes de simulation *ab initio* sont nécessaires afin de comprendre leur influence sur divers matériaux.
Les approches de type Hartree-Fock (HF) ou celles utilisées dans le cadre de la théorie de la fonctionnelle de la densité (DFT), sont pertinentes pour une compréhension de ces différents effets nécessaire à l'optimisation et l'amélioration des matériaux pour le photovoltaïque. L'approximation HF détermine la fonction d'onde de l'état fondamental en utilisant le principe variationnel sur un modèle purement mono-électronique où chaque électron est sous l'influence du champ moyen crée par les autres électrons, mais ne prend pas en compte la corrélation entre électrons autre que le principe d'exclusion de Pauli. Pour prendre en compte la corrélation Coulombienne, la DFT abandonne la fonction d'onde pour la densité électronique. Néanmoins, les approches HF et DFT sont connues pour respectivement surestimer et sous-estimer la valeur de l'énergie de bande interdite, définie à leurs façons, par référence aux valeurs propres des équations respectives. L'obtention d'une description aussi bien qualitative que quantitative de propriétés, comme les structures en bandes électroniques, requiert alors l'utilisation d'approches sophistiquées, comme les méthodes de type GW, coûteuses en temps de calcul. Ainsi, les approches pragmatiques basées sur les fonctionnelles hybrides, combinant un certain pourcentage (α) d'échange HF (E_x^{HF}) avec les échanges issus des différentes approximations de la DFT (E_x^{DFT} et E_c^{DFT}), représentent une alternative intéressante pour explorer les propriétés de systèmes complexes. Les fonctionnelles hybrides à un seul paramètre sont définies par l'équation suivante :

$$E_{xc}^{Hyb} = \alpha \times E_x^{HF} + (1 - \alpha) \times E_x^{DFT} + E_c^{DFT}. \tag{4.2}$$

Fonctionnelles hybrides optimisées

Performances des fonctionnelles hybrides

Le pourcentage α a d'abort été maintenu constant dans la littérature (Adamo and Barone, 1999), puis les fonctionnelles ont été optimisées grâce au calcul de la constante diélectrique qui est directement proportionnelle au pourcentage α Alkauskas *et al.* (2008). Cependant, on montre ici que cette méthode peut converger sur des solutions métalliques pour des matériaux à faible valeur d'énergie de bande interdite, comme pour le $CuInSe_2$ par exemple. Dans la première partie de cette thèse, les fonctionnelles hybrides ont été optimisées afin d'avoir une bonne description de l'énergie de bande interdite pour différents composés en faisant varier le pourcentage d'échange HF dans le terme d'échange des fonctionnelles de type PBE et PBEsol de l'approximation GGA de la DFT. Les matériaux considérés étaient le Si, Ge, SiGe, les III-V et quatre composés chalcopyrites (CIGSSe), $CuGaS_2$, $CuInS_2$, $CuGaSe_2$ et $CuInSe_2$. Les résultats obtenus avec cette approche semi-empirique ont été confrontés à ceux de la littérature et notamment à ceux obtenus au niveau GW. De manière générale, les fonctionnelles hybrides optimisées ici permettent d'obtenir des valeurs calculées des différentes propriétés avec des erreurs relatives par rapport aux valeurs expérimentales les plus faibles, comparables à celle d'HSE06 ou de M06. Pour la famille des chalcopyrites, une fonctionnelle hybride a été optimisée pour les quatre composés en trouvant la valeur de α minimisant l'erreur relative globale par rapport à l'expérience. La valeur de l'énergie de bande interdite correspondant à celle expérimentale par définition, la bonne reproduction du reste de la structure électronique fut étudiée. La description des propriétés électroniques, comme les structures en bandes, est similaire à celle obtenue au niveau GW comme on peut le voir sur la figure i pour les trois semiconducteurs III-V à base de gallium. Cette optimisation des fonctionnelles hybrides permet donc une bonne description des propriétés électroniques

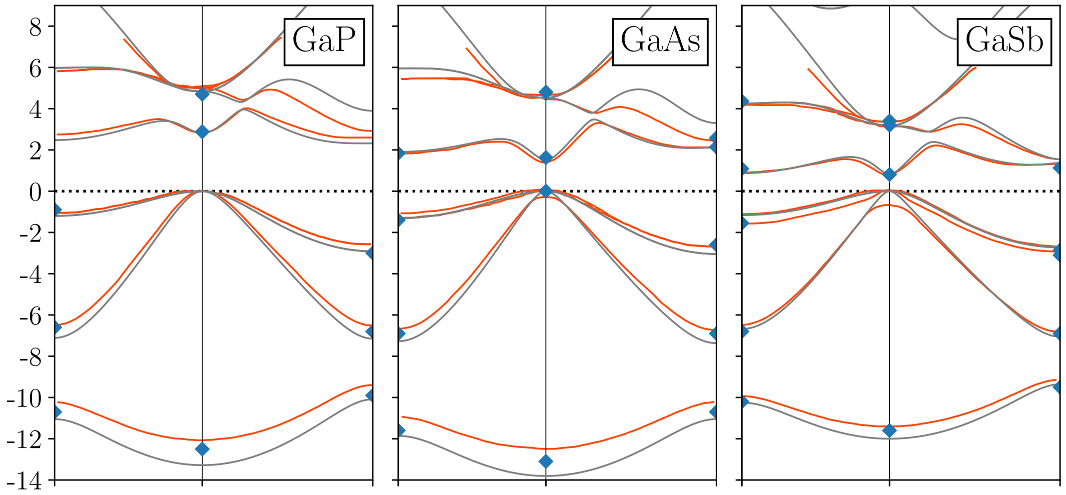

Figure i Bandes d'énergie calculées via la fonctionnelle hybride optimisée $PBEsol_{hyb}$ (—) et des calculs GW (—) de Malone and Cohen (2013) comparées aux valeurs expérimentales (♦) pour le GaP, GaAs et GaSb.

pour des temps de calculs beaucoup plus raisonnables que ceux nécessaires lors de calcul GW.

Influence de la température et propriétés de transport

L'utilisation des approches *ab initio* ne permet pas la prise en compte direct des effets de température sur les systèmes étudiés. Pour cela, l'approximation quasi-harmonique (QHA) fut utilisée. Via cette approximation, l'évolution en température de différentes données thermodynamiques a été abordée comme le montre la figure ii. Les variations du coefficient d'expansion thermique et des chaleurs spécifiques en fonction de la temperature pour différents matériaux sont comparées et correspondent aux données expérimentales. Parmis les propriétés étudiées, la variation en température de l'énergie de bande interdite de certains matériaux, comme le silicium, ne correspond pas aux tendances observées dans la littérature. Le couplage électron-phonon doit alors être pris en compte. Pour l'ensemble des matériaux étudiés, les approches hybrides n'apportent pas d'amélioration par rapport aux fonctionnelles existantes. Néanmoins, elles permettent une description cohérente des matériaux.
Enfin, l'obtention de la conductivité électrique par les fonctionnelles hybrides optimisées fut comparée à celle de diverses autres fonctionnelles. Les différentes fonctionnelles donnent une même tendance générale pour la variation de la conductivité électrique avec le potentiel chimique. Cependant, les fonctionnelles hybrides optimisées donnent les tendances les plus cohérentes avec leurs énergies de bande interdite correspondantes aux valeurs expérimentales.

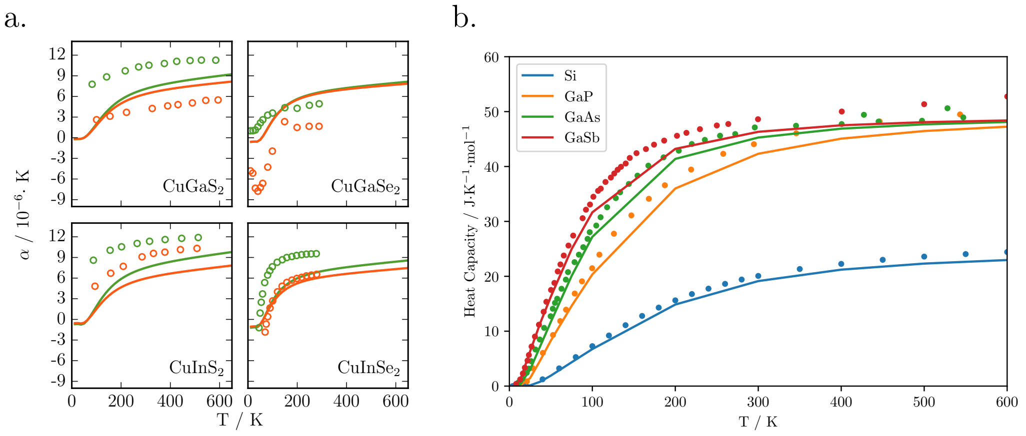

Figure ii a. Variation du coefficient de dilatation linéaire a (—) et c (—) en fonction de la température du Cu(In,Ga)(S,Se)$_2$ comparé aux données experimentales (Bodnar and Orlova, 1983; Nagaoka *et al.*, 2012; Deus *et al.*, 1983a) b. Variation de la capacité thermique en fonction de la température du Si et du GaX (X = P, As and Sb) calculée avec la fonctionnelle hybride optimisée PBEsol comparée à l'experience (Pässler, 2013; Glazov and Pashinkin, 2001).

Composition des matériaux chalcopyrites pour cellules tandem

Dans une seconde partie, ces fonctionnelles ont été utilisées pour réaliser une étude systématique de l'impact de la composition chimique sur les propriétés des chalcopyrites (CIGSSe) pour des cellules solaires de type tandem en complément de cellule silicium.

Compositions des composés chalcopyrites

Tout d'abord, elles ont permis de déterminer les compositions, propriétés structurales et électroniques des $CuGa_xIn_{1-x}(S_ySe_{1-y})_2$ avec des gaps donnés compatibles à leur utilisation en tant que cellule supérieure dans une cellule tandem. Le but de cette étude est de cartographier les différentes compositions possibles afin de déterminer celles ayant une énergie de bande interdite proche de 1.7 eV, valeur optimale pour la cellule supérieure complémentaire à une cellule à base de silicium. 81 compositions ont été modélisées et ont permis d'obtenir les graphiques de la figure iii représentant les variations de l'énergie de bande interdite et du paramètre de maille a en fonction des concentrations x et y. Ainsi, le paramètre de maille des compositions ayant une énergie de bande interdite de 1.7 eV sont directement comparables à celui du silicium pour déceler d'éventuel problémes structuraux. Les deux critères n'étant pas remplis dans les mêmes conditions, des compromis doivent être fait comme par exemple avoir une énergie de bande interdite supérieure à 1.7 eV ou alors utiliser une couche tampon entre les deux matériaux.

Substitution du cuivre par des métaux alcalins

Après avoir étudié l'impact de la concentration, l'effet de l'insertion des alcalins dans les chalcopyrites a été abordé. En effet, cette voie permet de nettes améliorations des rendements de ces matériaux (Salomé *et al.*, 2015; Muzzillo, 2017;

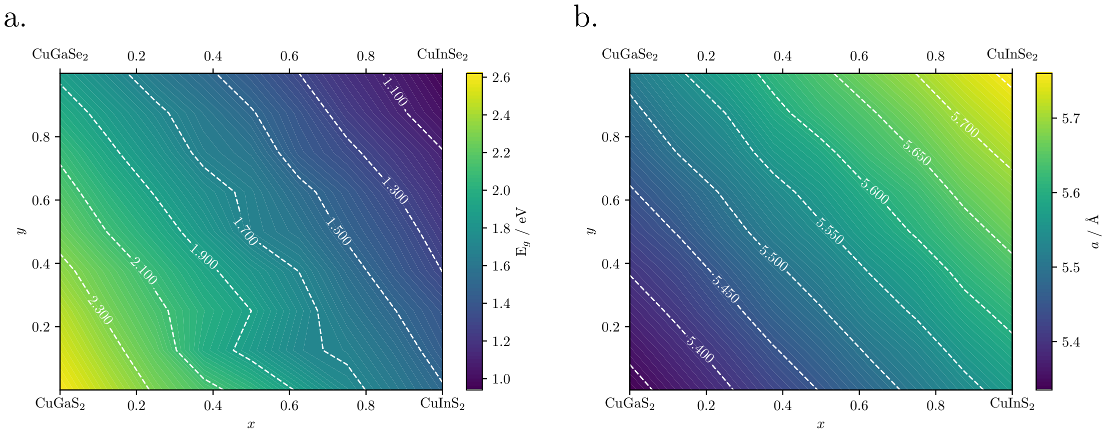

Figure iii Variation en fonction des concentrations x et y pour le $CuIn_xGa_{1-x}(Se_yS_{1-y})_2$ des a. énergies de bande interdite E_g et b. des paramètres de maille a.

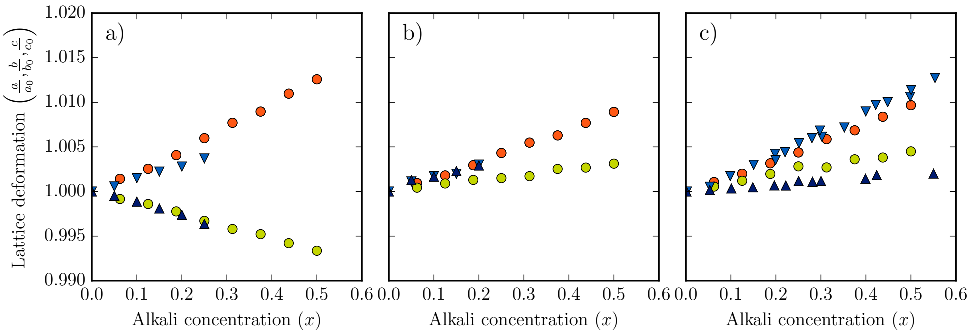

Figure iv Comparaison entre les valeurs expérimentales et calculées de la déformation du paramètre de maille des chalcopyrites ternaires dopés (a. $CuGaS_2$ b. $CuInS_2$ c. $CuInSe_2$) avec du Li.

Sun *et al.*, 2017). Divers sites d'incorporation existent mais aux vues de la littérature, l'accent a été mis sur la substitution du cuivre par le Li, Na, K, Rb et Cs. Il existe peu de données expérimentales sur des composés chalcopyrites mixés avec des alcalins. Cependant, les valeurs calculées dans cette thèse correspondent aux rares données trouvées dans la littérature comme le montre la figure iv pour les déformations structurelles découlant de l'ajout de lithium dans des chalcopyrites ternaires. Ainsi, l'impact sur les déformations structurelles, sur l'évolution de l'énergie de bande interdite ou encore les énergies de subsitution ont été déterminées. La figure v montre par exemple l'évolution de l'énergie de bande interdite des quatre chalcopyrites ternaires en fonction de la concentration de césium incorporé. Les zones grisées dans cette figure correspondent à une nouvelle phase. En effet, on montre ici que pour K, Rb et Cs, pour des compositions seuils allant de 30 % à plus de 80 %, le composé chalcopyrite passe d'un groupe d'espace P2 à un dérivé du $C/2c$. En plus de ce changement structural, l'incorporation de métaux alcalins augmente la valeur de l'énergie de bande interdite. De ce fait, les composés à base de gallium ne permettent pas d'obtenir une énergie de bande interdite de 1.7 eV, au contraire de $CuInSe_2$ et $CuInS_2$. On montre enfin que l'incorporation des alcalins dans les CIGSSe n'est pas favorable et tend énergétiquement vers une séparation de phase.

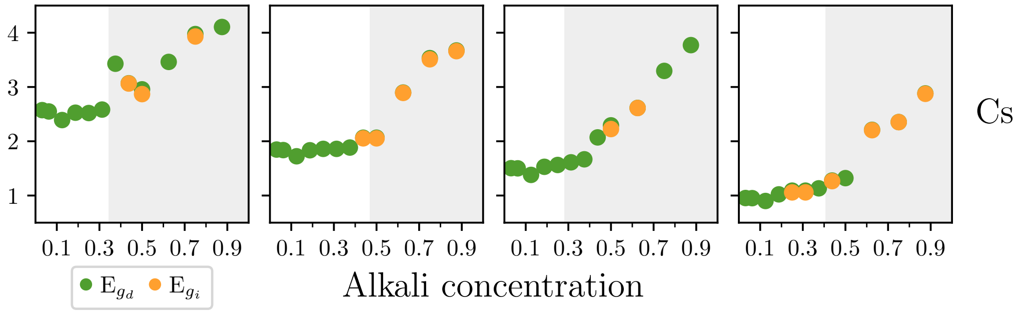

Figure v Évolution de l'énergie de bande interdite (en eV) du $Cu_{1-x}Alk_x(Ga,In)(S,Se)_2$ avec la concentration en césium (x).

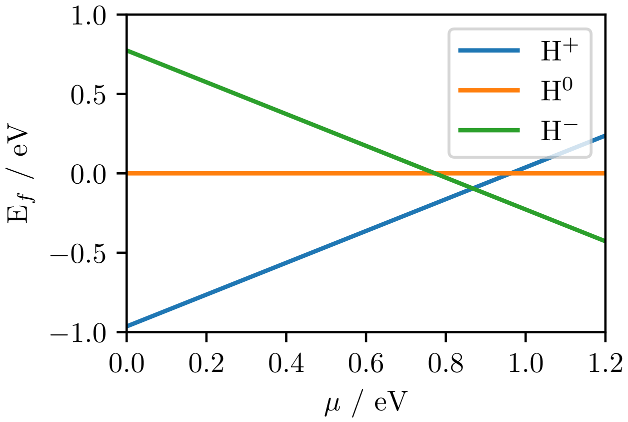

Figure vi Variation de l'énergie de formation du H^+, H^0 et H^- dans le silicium avec le potentiel chimique.

Étude du vieillissement des cellules silicium: importance des défauts ponctuels

Enfin, les défauts ponctuels d'hydrogène, de fer et de bore dans le silicium ont été modélisés dans le cadre d'une étude préliminaire sur le thème de la dégradation induite par la lumière à haute temperature (LeTID) qui est l'un des mécanismes de vieillissement des cellules à base de silicium. Cette première étude des défauts ponctuels dans le silicium par des fonctionelles hybrides optimisées confirment les résultats de la littérature (Van de Walle *et al.*, 1989; Brotherton *et al.*, 1985). Pour les défauts d'hydrogène, H^+ préfère se placer au centre d'une liaison Si-Si alors que H^- se glisse dans les tetrahèdres de la maille. En faisant varier le potentiel chimique comme sur la figure vi, et comme montré par Van de Walle and Neugebauer (2006), l'hydrogène réagit comme accepteur dans le silicium dopé n et donneur dans celui dopé p. H^0 correspond quand à lui à un état de transition, instable thermodynamiquement. Le fer et le bore forment de leur côté un centre de recombinaison avec l'apparition d'un niveau d'énergie au centre de la bande interdite.

Conclusion

Dans cette thèse, une méthodologie a été adoptée afin d'obtenir des résultats rapide et précis pour des systèmes complexes. Elle repose sur l'utilisation de fonctionnelles hybrides optimisées afin de reproduire les valeurs expérimentales des énergies de bandes interdites des matériaux étudiés. Cette approche pragmatique permet de réduire les erreurs relatives par rapport à l'expérience au niveau caractéristique standard lors de l'usage des fonctionnelles HSE06 ou M06. Les propriétés électroniques, telle que les structures en bandes, obtenues via cette approche sont comparables à celle calculées par des calculs GW. Cette méthode a par la suite été mise en application pour deux cas concrets relatifs au monde du photovoltaïque: l'utilisation de matériaux chalcopyrites pour des cellules tandem et le vieillissement des cellules à base de silicium. Pour une application tandem, la composition des chalcopyrites ainsi que l'incorporation de métaux alcalins en substitution du cuivre ont été étudiées dans le but d'obtenir un matériau ayant une énergie de bande interdite d'environ 1.7 eV. En jouant sur la concentration du gallium et du souffre, les énergies souhaitées entrainent un décalage des paramètres de mailles avec la cellule silicium en dessous, et nécessitent donc des compromis. L'incorporation d'alcalins entraine une augmentation de l'énergie de bande interdite. Les chalcopyrites à base d'indium sont alors les seuls à permettre une énergie de bande interdite de 1.7 eV. Cependant, ces incorporations ne sont pas stables et amènent à des séparations de phases. Enfin, en vue de comprendre les phénomènes de dégradation liés à la lumière et aux hautes températures des cellules silicium, diverses défauts ponctuels relatifs à l'hydrogène, au fer et au bore, ont été analysés. Les principaux résultats de la littérature ont été retrouvés, comme la formation de complexe Fe-B, centre de recombinaison néfaste pour la cellule solaire. La simulation des défauts ponctuels étant fiable, de futurs travaux se tourneront sur l'intéraction de ces défauts, entre eux mais également avec d'autres éléments comme des dislocations.

List of Figures

List of Tables

Appendices

Appendix A

Basis set

Table A.1 Exponents of the uncontracted GTFs of Li, Na, K, Rd and Cs – see Dovesi *et al.* (1983, 1991); CRYSTAL17 (2019) for a complete set of data. The K, Rb and Cs basis sets are used in conjunction with the Hay-Wadt small-core pseudoptentials (Hay and Wadt, 1985b,a) .

Atom	Shell	Expt.	Coeff.	
			$s(d)$	p
Li	*sp*	1.466596	1.	1.
	sp	0.463406	1.	1.
	sp	0.092101	1.	1.
	d	0.447768	1.	
Na	*sp*	0.517941	1.	1.
	sp	0.089944	1.	1.
	d	0.162856	1.	
K	*sp*	0.310588	1.	1.
	sp	0.101487	1.	1.
	d	0.525	1.	
Rb	*sp*	0.227558	1.	1.
	d	0.521716	1.	
Cs	*sp*	0.162258	1.	1.
	d	0.490609	1.	

Appendix B

Structural data

Table B.1 Reference crystal structure data and the band gap values for the compounds used for the tests in the present work the substitution energy and their structural properties.

Name	Space group		E_g	a	b	c	α
Cu_2S	$P2_1/c$	Calc.	1.65	15.027	11.805	13.272	116.
		Exp.		15.246	11.884	13.494	116.
Cu_2Se	$P2_1/c$	Calc.	1.23	6.993	4.277	6.823	70.
Li_2S	$Fm\bar{3}m$	Calc.	4.97	5.649			
		Exp.		5.708[a]			
Li_2Se	$Fm\bar{3}m$	Calc.	4.34	5.942			
		Exp.		6.005[a]			
Na_2S	$Fm\bar{3}m$	Calc.	4.27	6.472			
		Exp.		6.526[a]			
Na_2Se	$Fm\bar{3}m$	Calc.	3.72	6.735			
		Exp.		6.809[a]			
K_2S	$Fm\bar{3}m$	Calc.	4.54	7.224			
		Exp.		7.391[a]			
K_2Se	$Fm\bar{3}m$	Calc.	4.15	7.452			
		Exp.		7.676[a]			
Rb_2S	$Fm\bar{3}m$	Calc.	13.48	7.503			
		Exp.		7.650[a]			
Rb_2Se	$Fm\bar{3}m$	Calc.	12.53	7.670			
		Exp.		8.019[b]			
Cs_2S	$Pnma$	Calc.	11.27	8.628	5.183	10.383	
		Exp.		8.571[b]	5.383[b]	10.39[b]	
Cs_2Se	$Pnma$	Calc.	10.73	8.770	5.257	10.657	
		Exp.		8.79[b]	5.55[b]	10.78[b]	
$LiGaS_2$	$Pna2_1$	Calc.	5.22	6.520	7.802	6.197	
		Exp.	3.62[c]	6.519[d]	7.872[d]	6.238[d]	
				6.513[e]	7.863[e]	6.218[e]	
$LiGaSe_2$	$Pna2_1$	Calc.	3.69	6.070	10.206	6.097	
		Exp.	3.13[c]	6.833[f]	8.227[f]	6.541[f]	
				6.832[e]	8.237[e]	6.535[e]	

Continued on next page

Continuation of TABLE

Name	Space group		E_g	a	b	c	α
$LiInS_2$	$Pna2_1$	Calc.	3.88	6.884	8.002	6.457	
		Exp.	3.56[c]	6.887[g]	8.050[g]	6.474[g]	
$LiInSe_2$	$Pna2_1$	Calc.	2.955	7.225	9.654	6.765	
		Exp.	2.83[c]	7.218[h]	8.441[h]	6.772[h]	
$NaGaS_2$	$C2/c$	Calc.	4.658	10.188	10.189	13.430	101.
$NaGaSe_2$	$C2/c$	Calc.	3.449	10.617	10.654	14.019	105.
$NaInS_2$	$C2/c$	Calc.	3.256	10.836	10.536	13.828	104.
$NaInSe_2$	$C2/c$	Calc.	2.365	10.815	11.381	13.883	94.
$KGaS_2$	$C2/c$	Calc.	4.959	10.359	10.360	14.639	100.
		Exp.	2.71[i]	14.791[i,j]	10.425[i,j]	10.424[i,j]	100.[i,j]
$KGaSe_2$	$C2/c$	Calc.	3.994	10.741	10.742	15.203	100.
		Exp.	3.14[i]	10.909[i]	10.920[i]	15.470[i]	100.[i]
			2.60[k]				
$KInS_2$	$C2/c$	Calc.	3.783	10.911	10.875	14.934	100.
		Exp.		11.003[l,m,n]	10.995[l,m,n]	15.021[l,m,n]	101.[l,m,n]
$KInSe_2$	$C2/c$	Calc.	2.943	11.281	11.230	15.378	98.
		Exp.		11.423[o]	11.428[o]	15.621[o]	101.[o]
$RbGaS_2$	$C2/c$	Calc.	5.441	10.413	10.413	15.340	100.
		Exp.	2.86[i]	10.495[i]	10.485[i]	15.432[i]	100[i]
				15.64[p]	11.10[p]	11.16[p]	100.[p]
$RbGaSe_2$	$C2/c$	Calc.	4.529	10.755	10.755	15.863	100.
		Exp.	3.16[i]	10.954[i,q]	10.949[i,q]	16.064[i,q]	100.[i,q]
$RbInS_2$	$C2/c$	Calc.	4.399	10.969	10.971	15.608	100.
		Exp.	3.3[r]	10.47[s]	10.49[s]	15.46[s]	100.[s]
				11.07[r]	11.068[r]	15.610[r]	100.[r]
$RbInSe_2$	$C2/c$	Calc.	3.674	11.298	11.282	16.062	99.
		Exp.		11.065[t]	11.064[t]	15.580[t]	100.[t]
$CsGaS_2$	$C2/c$	Calc.	5.213	10.643	10.642	16.154	99.
		Exp.	2.89[i]	10.622[i]	10.616[i]	16.170[i]	100.[i]
$CsGaSe_2$	$C2/c$	Calc.	4.459	10.948	10.949	16.744	99.
		Exp.	3.17[i]	11.046[i]	11.051[i]	16.827[i]	99.[i]
$CsInS_2$	$C2/c$	Calc.	4.429	11.149	11.147	16.491	100.
		Exp.		11.14[s]	11.31[s]	16.08[s]	101.[s]
		Exp.	3.4[r]	11.197[r]	11.158[r]	16.358[r]	100.[r]
$CsInSe_2$	$C2/c$	Calc.	3.771	11.431	11.433	17.123	100.
		Exp.		11.4467[u]	11.4530[u]	17.0338[u]	100.[u]

[a] Zintl *et al.* (1934); [b] Sommer and Hoppe (1977); [c] Eifler *et al.* (2000); [d] Leal-Gonzalez *et al.* (1990); [e] Isaenko *et al.* (2003); [f] Kuriyama and Nozaki (1981); [g] Kish (1985); [h] Kamijoh and Kuriyama (1981); [i] Friedrich *et al.* (2017a); [j] Lemoine *et al.* (1984); [k] Feng *et al.* (2012); [m] Schubert and Hoppe (1970); [n] Lowe-Ma *et al.* (1991); [o] Krebs (2006); [p] Müller *et al.* (2014); [q] Friedrich *et al.* (2017b); [r] Zeng *et al.* (2007); [s] Schubert and Hoppe (1970); [t] Huang *et al.* (2005); [u] Ward *et al.* (2014)

Appendix C

Alkali incorporation in CIGSSe: supplementary data

Table C.1 Evolution with the alkaline concentration of the average structure of the anions tetrahedra associated to each alkaline for Ga-based chalcopyrite. V (in Å^3), d (in Å), θ_1 and θ_2 (in degree) stand for the volume of the primitive cell, the cation-anion distances and the different angles in the tetrahedra, respectively as defined in Fig. 1. The different parameters are obtained for the crystals with the $P\bar{4}$ space group; the ones in italic correspond to the $C2c$ type crystals.

	$CuGaS_2$				$CuGaSe_2$			
	V	d	θ_1	θ_2	V	d	θ_1	θ_2
Li								
0.0625	301.	2.34	109.	111.	343.	2.44	109.	110
0.1875	302.	2.34	109.	111.	345.	2.44	109.	110.
0.25	303.	2.35	109.	111.	346.	2.45	109.	111.
0.3125	303.	2.35	108.	112.	347.	2.45	108.	112.
0.375	304.	2.35	109.	112.	347.	2.45	109.	111.
0.4375	305.	2.36	108.	112.	348.	2.46	108.	112.
0.5	306.	2.36	108.	112.	349.	2.46	108.	112.
0.75	309.	2.37	108.	113.	354.	2.47	108.	113.
Na								
0.0625	304.	2.54	109.	111.	346.	2.64	109.	110.
0.1875	311.	2.55	109.	111.	354.	2.65	109.	111.
0.25	315.	2.59	107.	115.	359.	2.69	109.	113.
0.3125	319.	2.60	108.	112.	363.	2.68	107.	118.
0.375	322.	2.59	108.	117.	367.	2.69	107.	120.
0.4375	327.	2.61	108.	116.	372.	2.70	106.	120.
0.5	331.	2.61	107.	118.	377.	2.72	108.	118.
0.75	346.	2.68	103.	126.	*382.*	*2.83*	*100.*	*147.*
K								
0.0625	307.	2.78	109.	111.	350.	2.88	109.	110.
0.1875	318.	2.80	107.	126.	361.	2.91	105.	130.
0.25	325.	2.86	106.	125.	369.	2.97	105.	130.
0.3125	332.	2.90	107.	119.	377.	3.00	107.	121.
0.375	334.	2.89	102.	148.	376.	3.01	100.	152.
0.4375	342.	2.93	104.	136.	*384.*	*3.06*	*102.*	*140.*
0.5	*347.*	*2.96*	*97.*	*151.*	*388.*	*3.07*	*96.*	*152.*
0.75	*373.*	*3.05*	*100.*	*137.*	*413.*	*3.17*	*98.*	*134.*
Rb								
0.0625	308.	2.92	109.	111.	350.	3.05	107.	132.
0.1875	323.	2.95	106.	129.	366.	3.06	105.	132.
0.25	332.	3.02	102.	116.	376.	3.12	106.	119.
0.3125	339.	3.08	108.	116.	*383.*	*3.17*	*106.*	*122.*
0.375	344.	3.04	91.	120.	*386.*	*3.16*	*93.*	*135.*
0.4375	354.	3.12	102.	134.	*393.*	*3.22*	*94.*	*129.*
0.5	*362.*	*3.12*	*96.*	*158.*	*404.*	*3.22*	*95.*	*159.*
0.75	*395.*	*3.19*	*99.*	*134.*	*438.*	*3.30*	*98.*	*131.*
Cs								
0.0625	310.	3.05	109.	111.	353.	3.20	108.	127.
0.1875	330.	3.09	106.	128.	372.	3.21	106.	135.
0.25	339.	3.17	103.	115.	383.	3.29	101.	115.
0.3125	348.	3.27	109.	115.	393.	3.36	108.	117.
0.375	*387.*	*3.38*	*97.*	*133.*	402.	3.32	92.	119.
0.4375	*401.*	*3.36*	*99.*	*119.*	409.	3.46	98.	115.
0.5	*398.*	*3.43*	*90.*	*166.*	*435.*	*3.54*	*92.*	*136.*
0.75	*427.*	*3.48*	*83.*	*149.*	*455.*	*3.56*	*93.*	*158.*

Table C.2 Evolution with the alkaline concentration of the average structure of the anions tetrahedra associated to each alkaline for In-based chalcopyrite. V (in Å^3), d (in Å), θ_1 and θ_2 (in degree) stand for the volume of the primitive cell, the cation-anion distances and the different angles in the tetrahedra, respectively as defined in Fig. 1. The different parameters are obtained for the crystals with the $P\bar{4}$ space group; the ones in italic correspond to the $C2c$ type crystals.

	$CuInS_2$				$CuInSe_2$			
	V	d	θ_1	θ_2	V	d	θ_1	θ_2
Li								
0.0625	339.	2.37	109.	111.	385.	2.47	109.	111.
0.1875	341.	2.37	109.	111.	388.	2.47	109.	111.
0.25	342.	2.38	109.	111.	389.	2.48	109.	111.
0.3125	342.	2.38	109.	111.	390.	2.47	109.	111.
0.375	343.	2.38	108.	112.	391.	2.47	108.	112.
0.4375	344.	2.38	109.	111.	392.	2.48	109.	112.
0.5	345.	2.38	109.	111.	394.	2.48	108.	111.
0.75	350.	2.39	109.	111.	399.	2.49	109.	111.
Na								
0.0625	342.	2.58	109.	110.	389.	2.68	109.	111.
0.1875	351.	2.60	109.	111.	399.	2.69	109.	112.
0.25	356.	2.62	109.	112.	405.	2.72	109.	112.
0.3125	361.	2.63	109.	111.	409.	2.71	108.	114.
0.375	365.	2.61	105.	115.	415.	2.72	105.	116.
0.4375	370.	2.64	107.	113.	420.	2.73	106.	117.
0.5	375.	2.64	106.	114.	426.	2.74	108.	116.
0.75	396.	2.69	105.	118.	449.	2.79	106.	118.
K								
0.0625	346.	2.82	109.	110.	393.	2.93	109.	111.
0.1875	362.	2.84	111.	112.	409.	2.95	110.	118.
0.25	368.	2.92	107.	124.	415.	3.03	107.	129.
0.3125	*377.*	*2.93*	*108.*	*118.*	424.	3.02	109.	118.
0.375	*378.*	*2.93*	*104.*	*142.*	*424.*	*3.07*	*104.*	*143.*
0.4375	*389.*	*2.95*	*106.*	*130.*	*434.*	*3.09*	*103.*	*132.*
0.5	*396.*	*2.99*	*101.*	*125.*	*441.*	*3.12*	*97.*	*128.*
0.75	*418.*	*3.07*	*98.*	*142.*	*465.*	*3.18*	*96.*	*151.*
Rb								
0.0625	348.	2.98	109.	110.	393.	3.12	108.	132.
0.1875	365.	3.01	108.	122.	411.	3.13	107.	134.
0.25	375.	3.07	108.	121.	423.	3.18	108.	123.
0.3125	384.	3.11	105.	115.	431.	3.23	102.	125.
0.375	384.	3.11	89.	121.	429.	3.23	91.	128.
0.4375	*397.*	*3.15*	*100.*	*128.*	439.	3.27	92.	127.
0.5	*408.*	*3.19*	*99.*	*125.*	450.	3.30	95.	126.
0.75	*445.*	*3.22*	*99.*	*138.*	*487.*	*3.36*	*96.*	*131.*
Cs								
0.0625	349.	3.13	109.	110.	395.	3.27	108.	133.
0.1875	371.	3.17	108.	124.	417.	3.29	107.	136.
0.25	382.	3.25	104.	112.	431.	3.37	102.	111.
0.3125	*394.*	*3.31*	*109.*	*114.*	443.	3.42	102.	113.
0.375	*395.*	*3.27*	*92.*	*124.*	435.	3.41	91.	127.
0.4375	*438.*	*3.36*	*100.*	*119.*	*453.*	*3.47*	*89.*	*119.*
0.5	*464.*	*3.52*	*91.*	*146.*	*472.*	*3.49*	*97.*	*132.*
0.75	*514.*	*3.46*	*97.*	*138.*	*530.*	*3.53*	*95.*	*144.*

Table C.3 Mulliken net atomic charges of alkali (q) and Alk-(S/Se) bond populations ($b_{Alk-(S/Se)}$) for the different chalcopyrites. The data for Cu in Cu(Ga/In)(S/Se)$_2$ (referenced as *Cu*) are given for comparison.

Alk.	$CuGaS_2$		$CuGaSe_2$		$CuInS_2$		$CuInSe_2$	
	q	b_{Alk-S}	q	b_{Alk-S}	q	b_{Alk-S}	q	b_{Alk-S}
Li								
0.0625	+0.411	+0.1883	+0.226	+0.256	+0.404	+0.228	+0.221	+0.284
0.125	+0.414	+0.1884	+0.227	+0.254	+0.405	+0.228	+0.222	+0.284
0.1875	+0.410	+0.1894	+0.224	+0.255	+0.402	+0.228	+0.220	+0.286
0.25	+0.407	+0.1926	+0.224	+0.258	+0.402	+0.229	+0.220	+0.286
0.3125	+0.386	+0.1944	+0.202	+0.258	+0.389	+0.230	+0.207	+0.286
0.375	+0.391	+0.1937	+0.205	+0.258	+0.392	+0.230	+0.210	+0.287
0.4375	+0.376	+0.1963	+0.191	+0.259	+0.383	+0.232	+0.201	+0.287
0.5	+0.381	+0.1969	+0.196	+0.259	+0.385	+0.232	+0.204	+0.287
0.625	+0.386	+0.1955	+0.201	+0.258	+0.389	+0.232	+0.207	+0.288
0.75	+0.370	+0.1985	+0.186	+0.260	+0.379	+0.234	+0.199	+0.289
0.875	+0.361	+0.1992	+0.177	+0.261	+0.373	+0.235	+0.193	+0.289
Na								
0.0625	+0.439	+0.1680	+0.284	+0.224	+0.433	+0.196	+0.283	+0.246
0.125	+0.444	+0.1622	+0.278	+0.224	+0.433	+0.196	+0.279	+0.246
0.1875	+0.438	+0.1680	+0.279	+0.225	+0.430	+0.198	+0.280	+0.247
0.25	+0.437	+0.1708	+0.289	+0.223	+0.435	+0.198	+0.291	+0.244
0.3125	+0.428	+0.1727	+0.264	+0.229	+0.432	+0.198	+0.266	+0.250
0.375	+0.412	+0.1752	+0.264	+0.227	+0.418	+0.203	+0.273	+0.249
0.4375	+0.411	+0.1777	+0.249	+0.233	+0.417	+0.204	+0.257	+0.254
0.5	+0.403	+0.1809	+0.257	+0.230	+0.408	+0.206	+0.264	+0.252
0.625	+0.411	+0.1749	+0.268	+0.218	+0.416	+0.204	+0.272	+0.249
0.75	+0.389	+0.1797	+0.225	+0.190	+0.403	+0.207	+0.267	+0.248
0.875	+0.346	+0.1485	+0.209	+0.169	+0.398	+0.205	+0.267	+0.168
K								
0.0625	+0.712	+0.0127	+0.624	+0.060	+0.734	+0.030	+0.646	+0.076
0.125	+0.717	−0.003	+0.629	+0.042	+0.731	+0.020	+0.661	+0.061
0.1875	+0.709	+0.0137	+0.619	+0.058	+0.730	+0.033	+0.649	+0.075
0.25	+0.709	+0.0319	+0.624	+0.065	+0.736	+0.041	+0.653	+0.072
0.3125	+0.702	+0.0375	+0.618	+0.070	+0.732	+0.045	+0.628	+0.088
0.375	+0.683	+0.0373	+0.591	+0.068	+0.718	+0.046	+0.639	+0.073
0.4375	+0.683	+0.0437	+0.591	+0.071	+0.719	+0.051	+0.642	+0.080
0.5	+0.655	+0.0528	+0.567	+0.075	+0.703	+0.058	+0.620	+0.083
0.625	+0.659	+0.0589	+0.589	+0.067	+0.689	+0.061	+0.619	+0.074
0.75	+0.649	+0.0628	+0.562	+0.085	+0.683	+0.062	+0.602	+0.087
0.875	+0.627	+0.0633	+0.540	+0.081	+0.671	+0.067	+0.591	+0.087
Rb								
0.0625	+1.049	−0.082	+1.035	−0.056	+1.037	−0.066	+1.027	−0.043

Continued on next page

Continuation of table C.3

Alk.	$CuGaS_2$		$CuGaSe_2$		$CuInS_2$		$CuInSe_2$	
	q	b_{Alk-S}	q	b_{Alk-S}	q	b_{Alk-S}	q	b_{Alk-S}
0.125	+1.054	−0.082	+1.044	−0.062	+1.051	−0.069	+1.039	−0.048
0.1875	+1.049	−0.073	+1.035	−0.054	+1.038	−0.060	+1.025	−0.039
0.25	+1.037	−0.042	+1.023	−0.031	+1.029	−0.034	+1.016	−0.024
0.3125	+1.032	−0.035	+1.019	−0.023	+1.026	−0.030	+1.015	−0.019
0.375	+1.029	−0.035	+1.017	−0.022	+1.027	−0.027	+1.016	−0.017
0.4375	+1.023	−0.026	+1.012	−0.018	+1.024	−0.025	+1.014	−0.013
0.5	+1.016	−0.020	+1.006	−0.013	+1.011	−0.019	+1.002	−0.015
0.625	+1.013	−0.011	+1.007	−0.010	+1.016	−0.013	+1.007	−0.004
0.75	+1.007	−0.013	+0.999	−0.006	+1.009	−0.013	+1.002	−0.005
0.875	+1.000	−0.008	+0.992	−0.004	+1.004	−0.007	+0.997	−0.004
Cs								
0.0625	+1.040	−0.134	+1.020	−0.089	+1.032	−0.108	+1.019	−0.071
0.125	+1.052	−0.139	+1.031	−0.101	+1.051	−0.117	+1.032	−0.080
0.1875	+1.040	−0.121	+1.018	−0.086	+1.033	−0.099	+1.017	−0.065
0.25	+1.022	−0.059	+1.005	−0.052	+1.018	−0.056	+1.001	−0.037
0.3125	+1.013	−0.056	+0.997	−0.038	+1.013	−0.047	+0.999	−0.032
0.375	+0.983	−0.025	+0.998	−0.038	+1.015	−0.042	+0.997	−0.026
0.4375	+0.989	−0.026	+0.983	−0.027	+1.003	−0.028	+0.993	−0.020
0.5	+0.987	−0.021	+0.977	−0.011	+1.000	−0.017	+0.982	−0.021
0.625	+0.988	−0.019	+0.977	−0.017	+0.992	−0.018	+0.982	−0.013
0.75	+0.980	−0.015	+0.972	−0.013	+0.988	−0.016	+0.978	−0.009
0.875	+0.972	−0.016	+0.963	−0.010	+0.981	−0.014	+0.973	−0.009

Table C.4 Mulliken net atomic charges of gallium (q) and Ga-(S/Se) bond populations ($b_{Ga-(S/Se)}$) for the different Ga-based chalcopyrites.

Alk.	CuGaS$_2$		CuGaSe$_2$	
	q	b_{Ga-S}	q	b_{Ga-S}
Li				
0.0625	0.4110	0.2605	0.2260	0.2557
0.125	0.4140	0.2610	0.2270	0.2566
0.1875	0.4103	0.2620	0.2243	0.2575
0.25	0.4070	0.2626	0.2240	0.2584
0.3125	0.3862	0.2634	0.2018	0.2594
0.375	0.3907	0.2643	0.2047	0.2604
0.4375	0.3757	0.2648	0.1907	0.2612
0.5	0.3805	0.2657	0.1955	0.2620
0.625	0.3856	0.2671	0.2008	0.2638
0.75	0.3698	0.2686	0.1864	0.2658
0.875	0.3606	0.2701	0.1770	0.2677
Na				
0.0625	0.4390	0.2609	0.2840	0.2560
0.125	0.4440	0.2619	0.2780	0.2571
0.1875	0.4380	0.2633	0.2790	0.2585
0.25	0.4370	0.2647	0.2890	0.2601
0.3125	0.4282	0.2663	0.2636	0.2611
0.375	0.4123	0.2667	0.2640	0.2623
0.4375	0.4110	0.2688	0.2494	0.2634
0.5	0.4025	0.2694	0.2570	0.2653
0.625	0.4108	0.2720	0.2678	0.2675
0.75	0.3888	0.2741	0.2247	0.2657
0.875	0.3457	0.2704	0.2086	0.2644
K				
0.0625	0.7120	0.2610	0.6240	0.2561
0.125	0.7170	0.2605	0.6290	0.2545
0.1875	0.7090	0.2634	0.6190	0.2581
0.25	0.7090	0.2652	0.6240	0.2600
0.3125	0.7016	0.2678	0.6178	0.2625
0.375	0.6830	0.2652	0.5910	0.2601
0.4375	0.6833	0.2690	0.5914	0.2621
0.5	0.6551	0.2668	0.5665	0.2619
0.625	0.6594	0.2666	0.5888	0.2535
0.75	0.6489	0.2618	0.5619	0.2498
0.875	0.6274	0.2687	0.5403	0.2662
Rb				
0.0625	1.0490	0.2608	1.0350	0.2558

Continued on next page

Continuation of table C.4

Alk.	$CuGaS_2$		$CuGaSe_2$	
	q	b_{Ga-S}	q	b_{Ga-S}
0.125	1.0540	0.2599	1.0440	0.2466
0.1875	1.0493	0.2628	1.0353	0.2577
0.25	1.0370	0.2655	1.0230	0.2611
0.3125	1.0316	0.2684	1.0194	0.2631
0.375	1.0290	0.2647	1.0168	0.2562
0.4375	1.0230	0.2697	1.0124	0.2598
0.5	1.0161	0.2680	1.0059	0.2643
0.625	1.0128	0.2711	1.0072	0.2643
0.75	1.0067	0.2730	0.9994	0.2534
0.875	0.9997	0.2723	0.9923	0.2664
Cs				
0.0625	1.0400	0.2604	1.0200	0.2476
0.125	1.0520	0.2587	1.0310	0.2530
0.1875	1.0400	0.2613	1.0183	0.2549
0.25	1.0220	0.2640	1.0050	0.2592
0.3125	1.0130	0.2676	0.9972	0.2624
0.375	0.9830	0.2652	0.9983	0.2579
0.4375	0.9887	0.2679	0.9829	0.2469
0.5	0.9872	0.2677	0.9770	0.2637
0.625	0.9876	0.2699	0.9770	0.2623
0.75	0.9797	0.2751	0.9717	0.2698
0.875	0.9720	0.2729	0.9626	0.2744

Table C.5 Mulliken net atomic charges of indium (q) and In-(S/Se) bond populations ($b_{In-(S/Se)}$) for the different In-based chalcopyrites.

Alk.	$CuGaS_2$		$CuGaSe_2$	
	q	b_{In-S}	q	b_{In-S}
Li				
0.0625	0.4040	0.2151	0.2210	0.2289
0.125	0.4050	0.2155	0.2220	0.2295
0.1875	0.4020	0.2162	0.2197	0.2301
0.25	0.4020	0.2166	0.2200	0.2308
0.3125	0.3892	0.2172	0.2070	0.2313
0.375	0.3920	0.2177	0.2097	0.2319
0.4375	0.3830	0.2182	0.2013	0.2324
0.5	0.3850	0.2188	0.2040	0.2330
0.625	0.3888	0.2198	0.2074	0.2343
0.75	0.3788	0.2206	0.1985	0.2354
0.875	0.3730	0.2214	0.1926	0.2365
Na				
0.0625	0.4330	0.2148	0.2830	0.2286
0.125	0.4330	0.2151	0.2790	0.2286
0.1875	0.4303	0.2153	0.2797	0.2291
0.25	0.4350	0.2157	0.2910	0.2296
0.3125	0.4318	0.2161	0.2664	0.2297
0.375	0.4177	0.2164	0.2730	0.2303
0.4375	0.4174	0.2169	0.2570	0.2306
0.5	0.4080	0.2171	0.2640	0.2311
0.625	0.4156	0.2176	0.2718	0.2321
0.75	0.4032	0.2186	0.2670	0.2333
0.875	0.3979	0.2180	0.2671	0.2224
K				
0.0625	0.7340	0.2146	0.6460	0.2283
0.125	0.7310	0.2150	0.6610	0.2203
0.1875	0.7303	0.2151	0.6493	0.2280
0.25	0.7360	0.2151	0.6530	0.2284
0.3125	0.7320	0.2161	0.6278	0.2287
0.375	0.7180	0.2153	0.6393	0.2212
0.4375	0.7191	0.2173	0.6419	0.2259
0.5	0.7027	0.2158	0.6200	0.2288
0.625	0.6888	0.2159	0.6188	0.2182
0.75	0.6826	0.2025	0.6018	0.2174
0.875	0.6710	0.2162	0.5907	0.2323
Rb				
0.0625	1.0370	0.2144	1.0270	0.2208

Continued on next page

Continuation of table C.5

Alk.	$CuInS_2$		$CuInSe_2$	
	q	b_{In-S}	q	b_{In-S}
0.125	1.0510	0.2070	1.0390	0.2192
0.1875	1.0377	0.2141	1.0250	0.2265
0.25	1.0290	0.2149	1.0160	0.2287
0.3125	1.0260	0.2161	1.0154	0.2290
0.375	1.0273	0.2141	1.0160	0.2144
0.4375	1.0239	0.2175	1.0136	0.2191
0.5	1.0111	0.2172	1.0015	0.2301
0.625	1.0162	0.2026	1.0074	0.2341
0.75	1.0091	0.2217	1.0015	0.2168
0.875	1.0041	0.2217	0.9969	0.2316
Cs				
0.0625	1.0320	0.2138	1.0190	0.2203
0.125	1.0510	0.2058	1.0320	0.2179
0.1875	1.0327	0.2124	1.0167	0.2110
0.25	1.0180	0.2135	1.0010	0.2264
0.3125	1.0132	0.2146	0.9986	0.2271
0.375	1.0153	0.1901	0.9970	0.2007
0.4375	1.0027	0.2178	0.9929	0.2031
0.5	0.9999	0.2186	0.9819	0.2217
0.625	0.9920	0.2147	0.9820	0.2245
0.75	0.9875	0.2218	0.9784	0.2373
0.875	0.9806	0.2256	0.9726	0.2404